Philipp Welker

Failure of granular assemblies

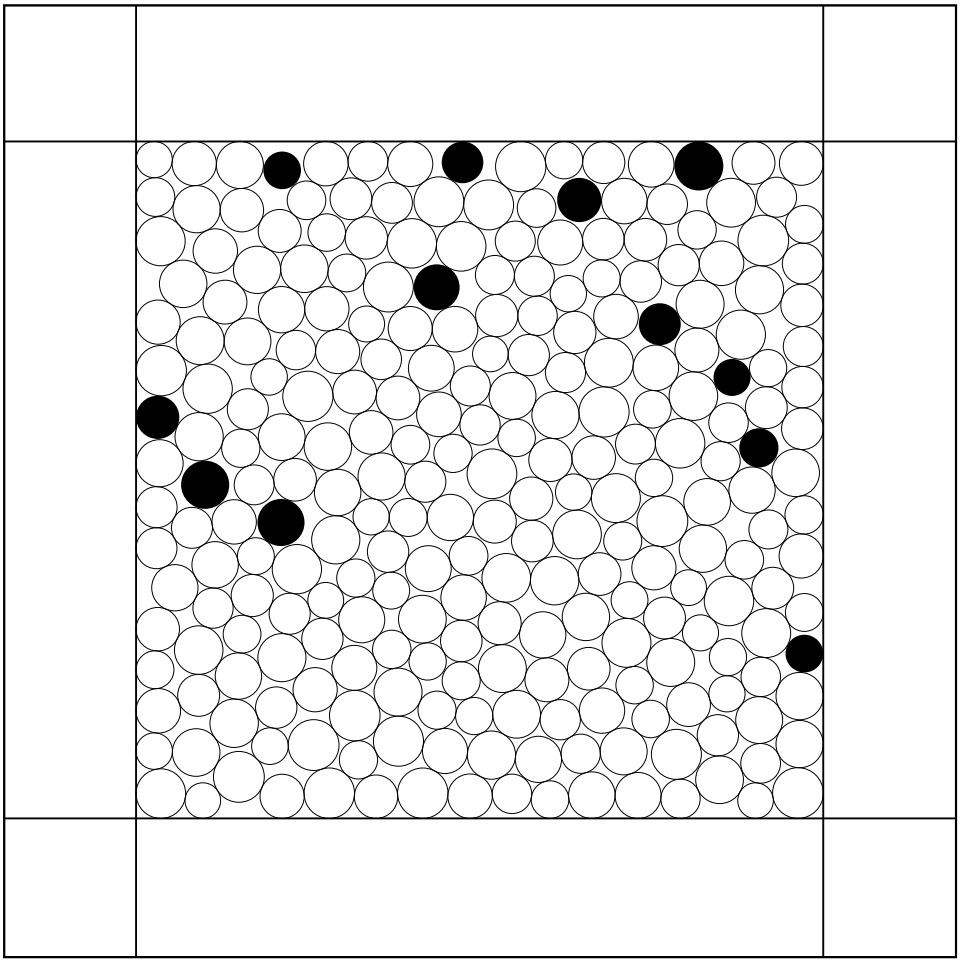

Fakultät für Mathematik und Physik
Universität Stuttgart

2011

Failure of granular assemblies

Von der Fakultät Mathematik und Physik der Universität Stuttgart
zur Erlangung der Würde eines Doktors
der Naturwissenschaften (Dr. rer. nat.) genehmigte Abhandlung

vorgelegt von

Philipp Welker

aus Nürnberg

Hauptberichter	:	Apl. Prof. Dr. Dr. Rudolf Hilfer
Zweitberichter	:	Prof. Dr. Günther Wunner
Drittberichter	:	Habil. Dr. Sean McNamara
Prüfungsvorsitzender	:	Prof. Dr. Jörg Wrachtrup

Tag der mündlichen Prüfung : 11. Januar 2011

Institut für Computerphysik der Universität Stuttgart

2011

List of publications

Articles

P. R. Welker and S. C. McNamara, "What triggers failure in frictional granular assemblies?," *Physical Review E*, vol. 79, no. 6, pp. 061305, 2009.

P. R. Welker and S. C. McNamara, "Precursors of failure and weakening in a biaxial test," *Granular Matter*, vol. 13, no. 1, pp. 93, 2010.

P. Welker and S. McNamara, "An increasing length scale associated with the failure of granular solids." submitted to Europhyics Letters (EPL), 2011.

Proceedings

P. Welker and S. McNamara, "Trigger of failure in granular assemblies," in *Tagungsband zur DPG Frhjahrstagung der Sektion Kondensierte Materie (SKM)*, 2009.

P. Welker and S. McNamara, "Failure in small granular assemblies," in *Powders and Grains* (M. Nakagawa and S. Luding, eds.), pp. 289–292, Springer, 2009.

P. Welker and S. McNamara, "Precursors of failure in granular systems," in *Tagungsband zur DPG Frhjahrstagung der Sektion Kondensierte Materie (SKM)*, 2010.

Contents

Zusammenfassung

Ziel dieser Arbeit ist die Vertiefung des fundamentalen Verständnisses von Versagen granularer Anordnungen in zwei und drei Dimensionen. Ein Granulat besteht aus einer typischerweise großen Anzahl von Konstituenten, den Körnern. Aufgrund der Größe der Körner (ab ca. $10\mu m$) hat die Temperatur keinen Einfluss auf deren Bewegungen. Die dissipativen Bewegungen werden daher alleine durch Newtonsche Kräfte gesteuert, die dem System von außen aufgeprägt werden (siehe Abb. 1). In dieser Arbeit werden sowohl kleine als auch große granulare Systeme untersucht, mit dem Ziel eine Längenskala zu identifizieren, welche bis zum Versagen so stark anwächst, dass sie der Systemgröße entspricht. Versagen ist eine plötzliche Änderung der Systemabmessungen. Methodisches Kernstück der Untersuchung ist die Steifigkeitsmatrix, welche aus der Information über alle Teilchenkontakte des Systems aufgestellt wird. Diese Matrix bestimmt das dynamische Verhalten eines granularen Systems unter langsam veränderter Belastung.

In einem ersten Schritt werden kleine granulare Systeme in zwei Dimensionen untersucht. In diesen Systemen mit nur 16 Teilchen wurden mit Hilfe der Steifigkeitsmatrix die Auslöser von Versagen identifiziert und deren relative Häufigkeit ausgewertet. Wenn Versagen auftritt, geht stets eine Kontaktstatusänderung voraus, welche eine Änderung der Systemstabilität bewirkt. Es sind drei Folgen möglich. Erstens kann die Änderung eine Systeminstabilität herbeiführen, und die kinetische Energie steigt exponentiell. Zweitens kann eine Bewegung mit Stabilität Null auftreten. Dieser Mechanismus wird allerdings nur in kleinen Systemen beobachtet. Drittens kann das System so weich bzw. schwach werden, dass schon eine kleine Zunahme der äußeren Belastung eine hohe kinetische Energie, verbunden mit weiteren Kontaktänderungen, herbeiführt. Auch in diesem Fall versagt das System. Dieser letztgenannte Mechanismus herrscht in großen System mit mehreren zehntausend Teilchen vor.

Im Bezug auf das Versagen treten weitere Fragen auf, die bislang nicht hinreichend geklärt wurden. Eine dieser Fragen betrifft die Anzahl der nötigen Stabilitätsbedingungen. Tritt Versagen genau dann auf, wenn bei Verlust eines einzelnen, beliebig wählbaren Kontaktes keine Stabilität mehr gewährleistet werden kann? Diese Untersuchung zeigt, dass dies im Allgemeinen nicht so ist. Das Resultat nährt den Verdacht, dass Versagen auf einen Teilbereich des Systems beschränkt ist. Und in der Tat findet man, dass sich sowohl Gleit- als auch Rollbewegungen in einem diagonal verlaufenden Band bei Versagen konzentrieren.

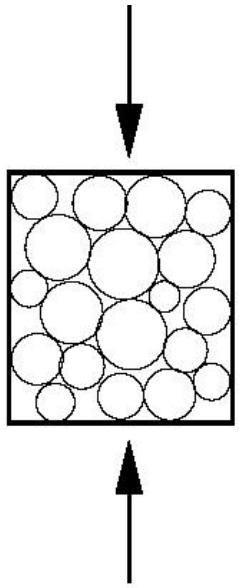

Figure 1: Beispiel eines Systems mit biaxialen Randbedingungen. Die geraden Wände sind beweglich. Auf sie wird eine Kraft ausgeübt, die zeitlich konstant (Seitenwände) bzw. zeitlich variabel (obere und untere Wand) ist. Durch Kraftzunahme (Pfeile) wird das System komprimiert.

Diese Konzentration wird ebenfalls in der vorliegenden Arbeit quantitativ erfasst und charakterisiert.

Ein weiteres bemerkenswertes Resultat ist, dass das Versagen im Mittel über viele kleine Systeme bei demselben Wert der äußeren Kräfte auftritt wie in einem großen System. Dies ist ein Beleg dafür, dass es sinnvoll ist Versagen zunächst in kleinen Systemen zu charakterisieren, weil sie sich in mancher Hinsicht den großen Systemen ähnlich verhalten, jedoch ihr Verhalten deutlich leichter zu beschreiben und zu verstehen ist.

In großen Systemen mit zehntausenden Teilchen führen einzelne Kontaktänderungen nur zu sehr kleinen Änderungen in der Systemstabilität. Auch andere Eigenschaften ändern sich fast kontinuierlich. Die Anzahl an Kontakten, an denen Teilchen aneinander entlanggleiten können, nimmt linear mit der Belastung zu bis zu einem Maximalwert. Anschließend gibt es gleich häufig Übergänge in beide Richtungen (gleitend $\leftrightarrow$ geschlossen), sodass keine neuen Gleitkontakte entstehen. Jedoch öffnen sich immer mehr Gleitkontakte, d.h. die Gesamtanzahl der Kontakte sinkt bis zum Versagen ab, wodurch das System weiter geschwächt wird. Die räumliche Verteilung der Gleitkontakte ist zu Beginn zufällig, ein zunehmendes Ordnungsverhalten zeichnet sich jedoch frühzeitig ab. Nahe dem Versagen organisieren sich Gleitkontakte schließlich in diagonal verlaufenden Bändern. Eines dieser Bänder, das sogenannte Scherband, ist bei Versagen besonders deutlich ausgeprägt.

Während der Zunahme der Ordnung von Gleitkontakten kommt es manchmal zu plötzlichen Einbrüchen in deren Anzahl. Diese Einbrüche werden mit Vorläufern von Versagen identifiziert. Es handelt sich hierbei um lokalisierte Instabilitäten im System, die zum räum-

lich begrenzen Anstieg der kinetischen Energie führen. Diese Energie wird, da der Vorläufer nur von sehr kurzer Dauer ist, rasch in Form einer Vibrationswelle in umliegende Bereiche dissipiert. Eng mit der Vibrationswelle verbunden ist der Einbruch in der Anzahl der Gleitkontakte im Bereich hoher Energie. Dieser Einbruch entsteht dadurch, dass Kontakte *schließen*, d.h. nichtlgleitend werden, und kurz darauf wieder in ihren Ursprungszustand *gleitend* zurückkehren. Signifikante bleibende „Schäden", d.h. Veränderungen in der Struktur des Granulates, die nach dem Voräufer zurückbleiben, werden nicht beobachtet.

Neben den Gleitkontakten ist das Abrollen von Teilchen an ihren Kontaktstellen ein weiterer Mechanismus, der zur Zunahme der kinetischen Energie führt. Es kann gezeigt werden, dass diese Rollbewegungen räumlich korreliert sind. Sie organisieren sich, ähnlich wie die Gleitkontakte, in diagonaler Richtung. Diese Organisation startet bereits zu Simulationsbeginn und nimmt kontinuierlich zu. Das Organisationsverhalten unterscheidet sich vom demjenigen der Gleitkontakte, die – zumindest für die einfachsten untersuchten Randbedingungen vom Typ zwei- bzw. dreiachsiger Test – nur bei Annäherung an das Versagen zunehmende Organisation zeigen. Für die Organisation der Rollkontakte wurde eine zunehmende Korrelationslänge bestimmt. Diese wird durch Approximation der Verteilung durch eine endliche Fourierreihe gewonnen. Aus der Approximation werden die Anzahl der Maxima bestimmt. Es zeigt sich, dass die Anzahl der Maxima ab einer bestimmten Anzahl an Fourier-Koeffizienten konvergiert. Diese Anzahl nimmt vom Simulationsbeginn bis zum Versagen um eine Größenordnung ab (bei Systemen mit 16384 Teilchen). Dies zeigt, dass die Korrelationslänge im selben Maße zunimmt. Ferner lässt sich zeigen, dass Gleitkontakte und die Bereiche hoher Rollgeschwindigkeiten korreliert sind. Diese Korrelation ist besonders hoch kurz nach Simulationsbeginn und bei Versagen, wo der Korrelationskoeffizient einen Wert von etwa 0.5 annimmt.

Bei Untersuchung von Systemen mit andersartigen Randbedingungen, nämlich membranartigen seitlichen Begrenzungen, zeigt sich, dass viele Eigenschaften der Materialschwächung und des Versagens von den gewählten Randbedingungen unabhängig sind. Die auffälligste Abhängigkeit zeigt sich bei der Organisation der Gleitkontakte: Bei membranartigen Rändern nimmt die Konzentration der Gleitkontakte in bestimmten Bereichen schon von Beginn an zu, wohingegen bei starren Wänden zunächst eine gleichmäßigere Verteilung beobachtet wird.

Der letzte Schritt dieser Untersuchung von Versagen ist die Erweiterung der Ergebnisse auf dreidimensionale Systeme und der Vergleich dieser Ergebnisse mit einem weiteren Simulationscode. Dieser Vergleich ist nötig, um mögliche Simulationsartefakte, die keineswegs von vornherein vollständig auszuschließen sind, als Ursache bestimmter Ergebnisse auszugrenzen. In dieser Richtung ist das erste Resultat die Beobachtung, dass Gleitkontakte auch in drei Dimensionen maßgeblich an der Materialschwächung und dem Versagen beteiligt sind. Die Entwicklung ihrer Anzahl ist ähnlich der Evolution in zwei Dimensionen. Das zweite, noch wichtigere Resultat, ist die Beobachtung des Auftretens von Vorläufern von Versagen in drei Dimensionen, die auf gleiche Weise wie in zwei Dimensionen zu charakterisieren sind. Dieses Resultat stützt die These, dass das Versagen stets durch Voräufer von Versagen angekündigt wird. Die Vorläufer von Versagen wurden auch bei der vergleichenden Simulation mit einem weiteren Simulationscode beobachtet, sodass Simulationsartefakte als

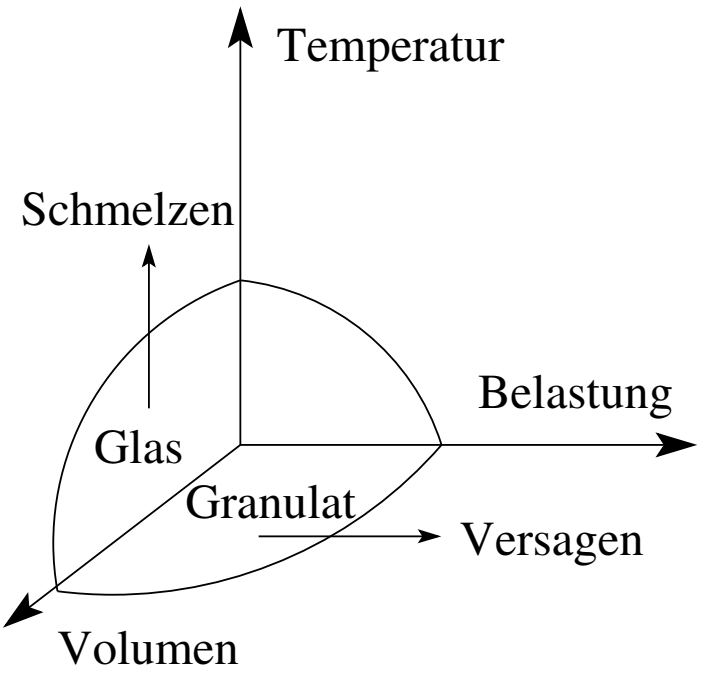

Figure 2: Schematische Darstellung des Hemmungsdiagrammes, welches von Liu und Nagel 1998 veröffentlicht wurde [1].

deren Ursache ausgeschlossen werden können.

Die vorliegende Untersuchung beinhaltet eine Reihe von Resultaten, die das fundamentale Verständnis von Versagen granular Andordnungen erweitern. Dieses Wissen ermöglicht es, die Verbindung zwischen granularem Versagen und dem Glasübergang, welche zuerst von Liu und Nagel im sogenannten *Hemmungsdiagramm* (Abb. 2) aufgestellt wurde, besser zu charakterisieren und zu verstehen.

Chapter 1

Introduction

Qui donc peut calculer le trajet d'une molécule ? Que savons-nous si des créations de monde ne sont point déterminées par des chutes de grains de sable ?

(Who ever can calculate the path of a molecule? How do we know if the worlds' creations are not uniquely determined by falling grains of sand?)
Victor Hugo, excerpt of "Les Misérables.

The above citation alludes to the observation that grains are found everywhere around us – they are ubiquitous. In everyday life, such ordinary, yet very useful things like rice, salt, sand, and marbles are among the examples. Materials such as gravel and rocks belong to the same class of systems. These and other similar materials are called *granular media* by the experts in this field. The granular media consist of the above mentioned grains, each of them having a size in the range from about 10μm to several meters. Therefore they obey the laws of classical mechanics. Usually these systems, i.e. the granular media, contain thousands, millions or more grains, and within one system, these components can have very different sizes. The grains' surfaces can be smooth or rough, and their shape can be spherical, cubic, or of any other kind.

While on the one hand the granular media are found in everyday life, these systems are also matter of current research carried out by both engineers and physicists [1–8]. The investigation of the behavior of granular media is motivated by different interests. Engineers are interested in granular materials because of a variety of different fields of application. Granular materials are needed for many processes in industry. For instance, powder handling is a very important issue, because many industrial processes involve the treatment of granular ingredients. Another important field is construction, where knowledge of granular behavior is necessary for building appropriate foundations for every single edifice. An appropriate foundation provides the framework for construction stability. Soil analysis is therefore the first step in the realization of a construction project, which, knowing the behavior of the soil, devises the further course of action. Another example where soil analysis and thus granular behavior is important are landslides. These appear when the granular soil becomes unstable and motions occur. Landslides have severe consequences when appearing close to settlements. The causes for landslides are diverse and include anthropogenic factors such as underground mining (causing the soil above to slip into the cavity) and overexploitation, such as clearance (deleting the ability of trees to keep the soil from sliding after heavy rains). Even larger effects have the motions of tectonic plates. The plates consist of many small and large rocks, and these rocks are rubbing

against each other at the joint of two plates. The rubbing in turn causes large vibrations, known as earthquakes. At the joints between two plates, a shear band forms, in which the rocks move relative to each other. Geologists draw their attention to the movement because forecasting the earthquakes is essential for evacuating nearby residents in time. Furthermore, the knowledge of the earthquake formation process and the prediction of their strength allows for the construction of adapted buildings and hence a prevention of disasters in advance.

The motivation of physicists for investigating granular behavior arises from some particular granular properties. First of all, and in contrast to many other systems, temperature is irrelevant. This means that, although temperature can be nonzero, it is not important for the motions of the grains. This is related to the energy scale introduced by temperature being much smaller than other energy scales, e.g. the potential energy of a grain; lifting a spherical grain of mass m by its diameter $d = 10\mu m$ requires the energy $mgh \approx 10^{-13}Nm$, where g is the gravitation constant. This energy is five orders of magnitude higher than the thermal energy at room temperature ($k_BT \approx 25meV \sim 10^{-18}Nm$). Therefore the grains are not sensitive to thermal fluctuations, which are relevant in many other systems. Granular media are *athermal* systems.

Furthermore energy is inherently *not* conserved in these systems [9, 10]. The underlying physical reason is that a significant amount of energy is converted to heat when particles collide, and the heat is dissipated to the surroundings. During a collision, or when touching particles move relative to each other, small deformations of the grains occur, and these elastoplastic deformations lead to a significant part of the kinetic energy being converted to heat. Thus the sum of potential and kinetic energy is not conserved, making the dynamic behavior of granular systems *irreversible*. This irreversibility, combined with the large number of thousands or even millions of particles, makes the analysis of such systems difficult.

Recently, physicists became interested in granular media because this class of systems is very different from ordinary solids [10]. The athermal nature of granular media prevents such systems from exploring phase space, and their properties consequently depend on the preparation history. Once a set of particles is put together by external forces, in order to form a stable compound, this assembly can resist large applied loads or strains in some directions, while small strains in other directions might cause the granular components to move. When this happens, the system passes from its rigid, jammed state to a fluid state. Cates and coworkers [11–13] argue that these systems feature paths of large forces, transmitted between the grains through the system. These paths of large forces appear in the direction of the principal force. They are called force chains. These force chains cannot change continuously. Instead, when the system of chains is not compatible with the external load, the existing force chains will be abandoned to form new ones, entailing dissipative, plastic reorganization. Despite significant effort, at present the behavior of granular systems, particularly at this transition from *solid* to *liquid*, is yet not understood – granular fragility remains mysterious. This thesis is aiming to contribute to uncovering the properties of this transition.

In 1998 a speculative *jamming diagram* (Fig. 1.1) has been proposed by Liu and Nagel [1]. This diagram establishes ties of the jamming transition from *fluid* to *solid* with the glass transition, which is also not fully understood. Although this diagram is speculative, it shows that granular systems and glasses might indeed share some features. The jamming diagram suggests that glass transition and the liquid-to-solid transition might be two special cases of a more fundamental jamming transition that depends on three variables: density, external load, and temperature of the system. Inside a limited region around the origin of that diagram, the system is jammed. When the surface of this area is reached, an *unjamming transition* happens, and flow of the particles is initiated. In [14] Krzakala and Kurchan suggest that the surface of this transition might also depend on the applied protocol, i.e. on

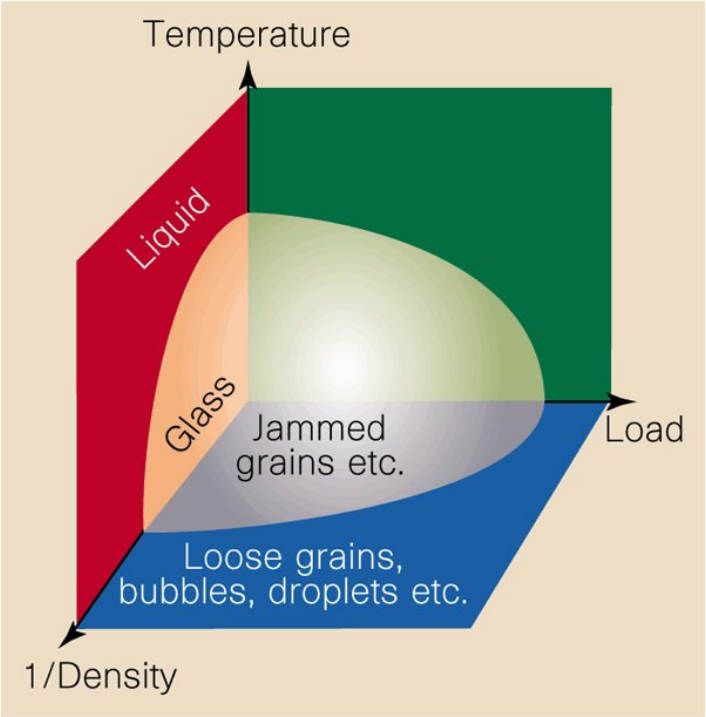

Figure 1.1: The jamming diagram as proposed in 1998 by Liu and Nagel. The figure is taken from [1]

the succession of points visited in phase space until reaching the transition surface. The jamming diagram of Liu and Nagel might therefore be misleading because more than three parameters are needed for defining a unique jamming surface.

Furthermore the concept of jamming is ambiguous, giving rise to different definitions of this term. A particularly elaborated concept is developed in [15–19] by Torquato and coworkers. The authors provide a hierarchical set of definitions for jammed states. Their concept of jamming evolved during the years and the embodied definitions were consequently more refined. Another, more fundamental concept of jamming is provided by Bagi [20]. Her concept is not only applicable to perfectly rigid spherical grains, but also to deformable grains of more general shape. Furthermore she allows for tangential forces being transmitted at the granular contacts, making the model also applicable to frictional systems. In the same paper Bagi proposes a numerical method to determine whether a given state of a system is a jammed state. The numerical analysis uses the stiffness matrix, which is also explained and applied to granular systems in this thesis (The definition of the matrix is given in Sec. 2.8). It is a useful tool for determining a system's stability. In a granular mechanics context, the notion "jamming" is frequently replaced by the term stability.

Let us see how stability can be defined by giving an example of a system for which the resistance to a load is investigated. Figure 1.2 shows such a system in two dimensions. It is made of disks with different radii that are confined in a volume by smooth walls. The walls are perpendicular to each other. This setup is called the *biaxial box*, and it is the principal system studied in this thesis. The external forces on the walls are increased in y-direction ($f_y = f_y(t)$), while they are held constant in x-direction ($f_x = f_0$), compressing the system along y. When the system keeps its shape during a

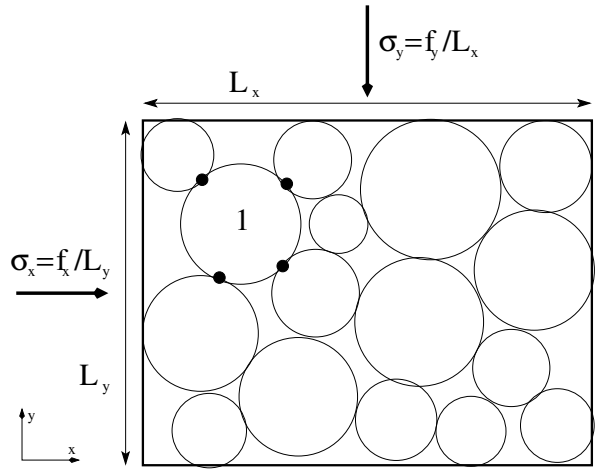

Figure 1.2: Sketch of a system with rigid wall boundary conditions. The four smooth and lightweight walls are perpendicular to each other. Each wall can move in the direction of its normal vector. The contacts of the particle labeled 1 are marked by dark spots. If the particle surfaces are smooth, that particle can rotate in place without resistance.

gentle increase, it is stable. But at a certain value of f_y the system will deform abruptly. This event is called failure of the granular system.

Instead of the control parameter force f_y, one could also consider the stress, i.e. the force per unit area. The force f_y is equivalent to an increasing stress in y-direction, $\sigma_y = f_y/L_x$. L_x is the dimension of the system in the x-direction. Similarly, the stress in x-direction is $\sigma_x = f_x/L_y$, where L_y is the system's dimension in y-direction. In a continuum theory, the stress is described by a 2×2 matrix. For the biaxial box, this matrix is diagonal, because the walls are smooth, and they are parallel to the coordinate axes. The elements on the diagonal of the matrix are σ_x and σ_y. The stress has two parts: the isotropic pressure $p = \frac{1}{2}(\sigma_x + \sigma_y)$, which does not cause failure, and the deviatoric stress

$$\sigma_{\mathrm{d}} = \frac{1}{2}(\sigma_y - \sigma_x)\,. \tag{1.1}$$

At a certain value of σ_d, failure happens, which leads to a decrease of σ_d: σ_y decreases, while σ_x increases, because L_x and L_y suddenly change.

Thanks to the simplicity, the maximum of σ_d is widely used to identify the failure. Although discussed here for one particular geometry, this criterion is applicable for all types of solids and does furthermore not depend on the microscopic structure of the material. This independence entails the disadvantage that it is difficult to predict the stability limit of granular systems, because the maximum of σ_d does depend on the microscopic variables particle roughness, number of contacts per particle (the coordination number), and particle shape. Furthermore crystallization effects, which are particularly important when the components are about equal in size, can alter the maximum level of stress.

One possibility to investigate the stability limit is to consider a system such as the one in Fig. 1.2. In a simple example, the particles interact at their points of contact via forces directed normal to their surfaces. The grains can slide along each other or rotate in place without resistance. Such systems are called frictionless, and have been studied by many authors under several conditions. These frictionless

systems are rather simple to analyze, but not very realistic. Investigating their behavior is the first step in understanding granular behavior. In the limit of vanishing particle overlaps, these frictionless systems exhibit very particular properties [4, 21–23]. Specifically, the number of contacts, which constrain the particle motions, is equal to the number of kinetic degrees of freedom (two for each particle). This is the minimum number of contacts required for stability. Small structural changes, causing the loss of just one contact, will lead to instability.

The granular behavior changes completely when a second force, tangent to the particle surfaces, is transmitted at the particle contacts sketched in Fig. 1.2. The physical meaning of the tangential force is friction, arising from the roughness of particle surfaces. Friction forces oppose relative tangent motions and rotations of the particles. In this case two independent forces oppose particle motions at every contact. Therefore the number of constraints is twice the number of contacts. It exceeds in general the number of degrees of freedom (two translations and one rotation per particle), resulting in an abundance of stable structural configurations. The system will choose one of them. Due to the large number of stable configurations, a limited number of structural changes is possible without causing failure or instability. Thus there is a certain period where material weakening occurs, and the number of contacts decreases, before the failure happens. The behavior during this period is investigated in detail in Chap. 5.

The goal of this study is to investigate the processes leading to the failure of granular assemblies. One particularly important question that is answered in this thesis is the possibility of the emergence of a characteristic length scale that increases until the failure. Such a length scale connects the failure with other phenomena in which motions are related to an increasing length scale. One such phenomenon is a phase transition.

The structure of the thesis is as follows. In the next Chapter, Chap. 2, the theoretical background and the the simulation procedure are explained in detail. They are needed for understanding the simulation results in the chapters thereafter.

The numerical and analytical investigation of failure in granular assemblies begins with small systems and the trigger that cause the failure. They are investigated in Sec. 3. Chapter 4 is a bridge between the small systems and the larger systems in later chapters. In Chap. 4 different properties of failure are discussed with respect to their dependence on system size.

Large systems are investigated in more detail in Chap. 5. In that chapter the structural weakening before the failure is inspected. Specific times during the weakening process of a granular system require special care. At that positions, localized instabilities appear. They are inspected in Sec. 6. Thereafter, in Chap. 7, we come back to the weakening process, investigating the organization of particle motions during the weakening.

The following chapters generalize the results. They consider other boundary conditions (membrane boundaries in Sec. 8), other particle roughnesses (Sec. 9), and three dimensional systems (Sec. 10). These chapters show that important findings in this thesis are not sensitive to boundary conditions, important parameters, and the dimensionality. The summary in Chapter 11 addresses the main results and reconsiders the physical meaning of the jamming diagram in Fig. 1.1.

Chapter 2

Model, theoretical analysis, and simulation procedure

In this work the granular system is described by a microscopic model. In this model each grain is one element that has a certain size and shape. This model is called the discrete element model (DEM) [24]. The boundary walls in Fig. 1.2 are also part of that system. They are interpreted as special elements with particular properties. All the grains and walls constitute the system that is analyzed. This section contains three parts that address the model and its analytical and numerical solution. The first part introduces the reader to the microscopic model (Secs. 2.1 – 2.5). The second part describes the analytical solution of that model (Secs. 2.6 – 2.8). In the third part the simulation procedure for solving the model numerically is explained (Secs. 2.9 – 2.11).

An appropriate granular model must fulfill two different demands. On the one hand, the model must capture the essential granular details. These are the disordered structure of the solid, resulting from the diversity in size of the grains, and the dissipative interactions. On the other hand, it should also be simple and get by with the smallest possible number of parameters. There are three reasons for the second requirement. It makes the model easier to understand, it facilitates the theoretical analysis of the model, and it reduces the computation costs to a minimum.

The granular model consists of two parts: the grains and the interactions of the grains. The grain model is explained in Sec. 2.1, while the interaction model is presented in Sec. 2.2. The parameters in that model are the spring constants. Their values are given in Sec. 2.5. The boundary conditions applied in the model are explained in Secs. 2.3 and 2.4. Some details of the model might depend on the boundary conditions, so we compare different boundary conditions to investigate these effects. With the definition of the grains, the interaction of the grains, and the boundary conditions, the model is complete and can now be analyzed.

One possible way to analyze granular behavior is to analytically examine the model. Specifically we are interested in deformations and the failure of a granular system. Here the stiffness matrix is the tool for investigating the system's structural stability. It is a theoretical model and it is introduced and explained in Sec. 2.8. For introducing the concept of stiffness matrix, one needs to consider some additional aspects of granular media. Thus in Sec. 2.6 the term rattler is introduced, explaining the possibility of grains not contributing to the stability of the system, because these grains flow freely in voids. And in Sec. 2.7 the *degree of hyperstaticity* is introduced and explained. This degree compares the number of stability conditions to the number of degrees of freedom of the system.

The analytical examination of the model is followed by the explanation of the simulation procedure in Secs. 2.9 – 2.11. In Sec. 2.9, the simulation method is introduced. The sections thereafter

explain important details of the simulations. Section 2.10 describes the preparation procedure to generate a granular solid. Section 2.11 introduces the reader to the subsequent loading procedure, where the forces on the walls are slowly increased until the system fails, and macroscopic deformations occur. These deformations, together with the foregoing material weakening, are investigated in Chapters 3 – 10. In this chapter the theoretical background needed to understand the results is presented.

A specific notation convention is used to distinguish between the different mathematical quantities. In some sections the matrices, vectors and scalars must be distinguished. To make this structure apparent, scalars are presented in math font, x, while vectors are distinguished by an arrow, $\vec{x}$. Finally, matrices and vectors of vectors (which themselves are vectors) are presented in boldface, $\mathbf{x}$. In the next section, the particle model is presented in this notation.

2.1 Particle model

The focus of the work is to investigate the general behavior of granular media driven towards the stability limit with a simple but sufficiently general model. A simple granular model has only a small number of parameters (or variables). One such model in three dimensions is the sphere model: the particles are considered spheres of radius r. When the mass density ρ is known, one can calculate mass, size, and surface of the individual particle from the value of r.

In two dimensions, the model of a grain is a disk (which could be considered the profile of a three dimensional sphere). This disk also has radius r and mass density ρ. In both two and three dimensions, we allow for polydispersity by varying the radii in a continuous range [0.7r$_{max}$,r$_{max}$]. The individual radius is chosen at random. The same density ρ applies to all grains of the system.

2.2 The 'linear spring' contact model

Two grains that come in touch interact with each other. In classical mechanics, this interaction is described by forces that are exerted by the particles. The forces between the grains can be modeled in different ways. Here they are modeled by springs, and the elongation of a spring is proportional to the force. In this spring model, two independent forces arise at each point of contact. One is directed normal to the particles' surfaces, and one is tangent to the surfaces. Both forces are proportional to particle deformations, arising at the point of contact. In normal direction, this deformation is equal to the particle overlap D_n defined in Fig. 2.1, while the tangent deformation is given by the stretching of a fictitious spring which connects the initial position of the contact point on the surface of particle 1 to the initial position of the contact point on the surface of particle 2. This spring is considered to be tangent to the particles' surfaces.

The normal force F_n at the contact is calculated from the elongation D_n of a linear dissipative spring with length independent stiffness k_n:

$$F_n = -k_n D_n - \gamma_n \dot{D}_n. \tag{2.1}$$

The damping coefficient γ_n controls the dissipation. The overlap distance D_n is calculated from the radii r_i and r_j of the touching particles and the positions $\mathbf{x}_i$ and $\mathbf{x}_j$ of their centers of mass,

$$D_n = |\mathbf{x}_i - \mathbf{x}_j| - r_i - r_j. \tag{2.2}$$

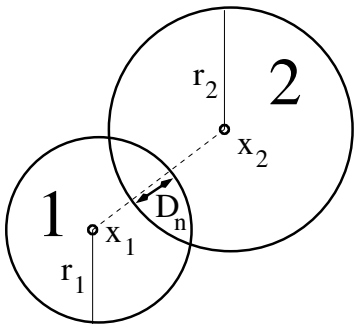

Figure 2.1: An illustration of the contact model. When two particles touch, deformations arise at the point of contact. But in the model, the particles are always circles, and deformations are modeled by the overlap of the circles. D_n denotes the particle overlap along a line through the particles' centers, which is indicated by the dashed line.

When the surfaces of the two touching disks move relative to each other, a second force F_t arises, directed tangent to the particle surfaces. In analogy with the normal force defined in Eq. 2.1 we have

$$F_t = -k_t D_t - \gamma_t \dot{D}_t. \tag{2.3}$$

To reduce the number of parameters we set $k_t = k_n$ and $\gamma_t = \gamma_n$. This choice might not be realistic, but it is a sufficiently accurate 'first guess' and simplifies the model. The change in the tangential spring length $\dot{D}_t$ involves both translational motions and rotations of the two touching particles i and j,

$$\dot{D}_t = -r_i\omega_i - r_j\omega_j + \left(1 + \frac{D_n}{r_i + r_j}\right)(\mathbf{v}_i - \mathbf{v}_j)\cdot\mathbf{t}\,. \tag{2.4}$$

Here, ω_i and ω_j are the angular velocities of the touching particles, and $\mathbf{t}$ is a vector tangent to the particle surfaces at the point of contact. The factor in front of the last term is needed to account for the overlap of the particles. As there is no attraction in the system, all forces are positive, thus indicating repulsion:

$$F_n > 0. \tag{2.5}$$

We also enforce the Coulomb condition at each contact.

$$\mu F_n \geq |F_t|. \tag{2.6}$$

At a given moment, contacts where the strict inequality holds are nonsliding contacts, whereas contacts with $\mu F_n = |F_t|$ are sliding. The condition *sliding* means that the particles can move relative to each other in tangent direction without changing F_t.

Note that F_n and F_t are in principle vectors. In two dimensions F_n is oriented along the line connecting the particle centers in Fig. 2.1, and F_t is perpendicular to that direction. In three dimensions F_t looses its uniqueness. Besides its length one also needs to know its orientation in the plane tangent to the particle surfaces.

2.3 Boundary conditions

Next it is important to define the boundary conditions of the granular model. These boundary conditions will have an effect on theoretical and simulation results. Thus they have to be chosen with care.

To identify the significance of boundary conditions and to discern boundary dependent behavior from more general observations, different boundary conditions will be investigated in this thesis. There are two boundary conditions in two dimensions and one in three dimensions. In two dimensions we have

- **rigid walls boundary conditions**
  The granular assembly is delimited by straight walls that are perpendicular to each other, resulting in a rectangular box wherein the grains are located (Fig. 2.2(a)). Either constant or time dependent forces are exerted onto the walls from the outside.

- **membrane like boundary conditions (floppy boundaries)**
  The sidewalls from the rigid walls boundaries are replaced by flexible strings that are at the ends attached to specific positions. These strings are called membranes. They can be elongated, and the stretching depends on the strength of the membrane and the applied forces. The membranes are defined in more detail in Sec. 2.4.

In three dimensions the systems have

- **triaxial boundary conditions**
  This setup resembles the triaxial test in soil mechanics. Here, the system occupies a volume in three dimensional space. It is limited by straight walls that are perpendicular to each other, like the rigid walls in 2 dimensions. Similarly, forces are exerted onto the walls in order to compress the system. While forces in two of the three directions are constant, the forces in the third direction are increased with time in the same manner as in two dimensions. The aim of this setup is to compare the behavior of two to three dimensional systems with straight walls at the boundaries.

In Chaps. 5, 6 the results will be compared to findings from the literature, which are obtained with another, frequently used type of boundary conditions. This is the

- **inclined surface**
  These boundary conditions are not used in this thesis, but many works on granular avalanches use them [25–33]. Specifically, precursors of failure have been observed in granular avalanches. These precursors will be compared to the precursor findings in Sec. 6 for the case of rigid wall boundaries.

2.4 Setting up membrane like boundary conditions

We now discuss the model for the membrane boundaries. Although we implement a rather simple model, the definition of the membrane and the derivation of the forces from the potential energy stored in the membrane requires some work. Those readers who are not interested in these details might skip the section and continue with Sec. 2.5. Although there might be innumerably many ways to implement membranes, some of which can be found in the literature [34–37], possibly the simplest way is to think of a membrane as an infinitely thin strap that exerts a force on the particles in touch with it. Given the force law is known, one can directly calculate the forces on the grains. Thus there is no need to introduce a new sort of elastic boundary in the simulations, because the particles at the boundaries (considered to be boundary grains) will do this job just as well.

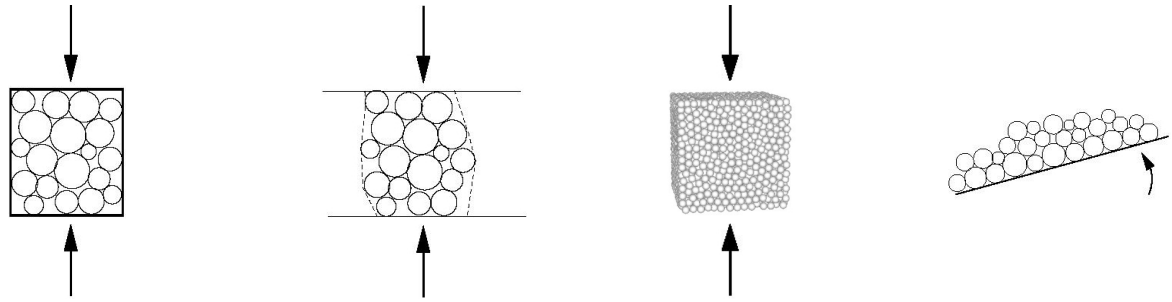

Figure 2.2: Boundary conditions: (1a) rigid wall boundaries, (1b) membrane like boundaries, (1c) triaxial boundary conditions (particles at the surface touch the boundary walls, which are not shown in the figure), (2) inclined surface. The arrows in Figs. (1a – c) indicate the direction of increasing external force $f(t)$. The arrow in Fig. (2) indicates the increasing angle of inclination.

Usually the forces from the membrane on the particles depend on the membrane's length L. Hence, the potential energy of the membrane must be some function of the stretching $L - L_0$ of the membrane, relative to its passive state at length L_0, where all forces from the membrane are zero. One simple way to construct a membrane is to think of it as a very long spring that is bended at the positions of the grains. In this model, the potential energy is proportional to the square of the elongation $L - L_0$ from a length of reference L_0, and the prefactor is the spring stiffness k_{mem}:

$$E_{\mathrm{pot}} = k_{\mathrm{mem}} \left(L - L_0\right)^2 . \tag{2.7}$$

When calculating the forces from the derivative of the potential energy in Eq. 2.7, the forces are linear in L. On the other hand, the forces at rigid wall boundaries are constant. Therefore it will be difficult to compare results for systems with membrane boundary conditions to systems with rigid wall boundary conditions. This problem can be solved by making E_{pot} in Eq. 2.7 linear in L. In that way the derivative of E_{pot} is L-independent. So, we set:

$$E_{\mathrm{pot}} = k_{\mathrm{mem}} \left(L - L_0\right) . \tag{2.8}$$

Still the membrane will try to shrink to the shortest length L possible. This length is defined to be the sum of the distances between the particles at the membrane (Fig. 2.3). A distance here is defined as the position difference of the centers of mass of two particles. Thus the distance between particles i and $i + 1$ is

$$L_{i,i+1} = |\vec{x}_{i+1} - \vec{x}_i|. \tag{2.9}$$

Here, $\vec{x}_i$ is the position of the center of mass of particle i. The length L of the membrane can thus be written as a sum over segments $L_{i,i+1}$ that connect the two nearby grains i and $i + 1$,

$$L = \sum_{j=0}^{N} L_{j,j+1}. \tag{2.10}$$

Here, N is the number of particles of the membrane. Their number is determined by evaluating a condition which is presented in Sec. 2.4.1. The ends of the membrane are fixed to positions which

will be defined in Sec. 2.4.2. Assuming that the membrane is well defined, we want to construct the forces on the grains. Differentiating $E_{\rm pot}$ with respect to the particle position $\vec{x}_i$ gives

$$\vec{F}_i = -\frac{\delta E_{\rm pot}}{\delta \vec{x}_i} = -k_{\rm mem}\left(\frac{\vec{x}_i - \vec{x}_{i-1}}{L_{i,i-1}} + \frac{\vec{x}_i - \vec{x}_{i+1}}{L_{i,i+1}}\right) . \tag{2.11}$$

Equation 2.11 is a local force condition, i.e. in the calculation only the particle position and the ones of its nearest neighbors enter. With the definition of the unit vectors

$$\vec{n}_i := \frac{\vec{x}_i - \vec{x}_{i-1}}{L_{i,i-1}} \tag{2.12}$$

we can rewrite Eq. 2.11 to read

$$\vec{F}_i = k_{\rm mem}\left(\vec{n}_{i+1} - \vec{n}_i\right) . \tag{2.13}$$

Now we should give a condition when grain i is a boundary grain. As membrane forces oppose the attempt to elongate the membrane, for the grains at the left membrane in Fig. 2.2(c), the horizontal or x-component of the force in Eq. 2.11 must be positive. Thus the force $\vec{F}_i$ on grain i is

$$\vec{F}\,(\text{grain } i) = \begin{cases} \vec{F}_i & for\left(\vec{F}_i\right)_x > 0 \quad (< 0 \text{ at the right boundary}) , \\ \vec{0} & \text{otherwise.} \end{cases} \tag{2.14}$$

This condition simply assures that the surface defined by a membrane is convex. Note that $\vec{F}_i$ depends on the direction of the line segments, and not on their length (see Eq. 2.13). Thus the force on a particle depends on the local curvature of the membrane only.

2.4.1 Which grains are part of the boundary?

Equation 2.14 gives a condition that the grains of the membrane must fulfill. This equation is evaluated for the membrane grains. But how do we get to know these grains? We introduce here a rigorous condition for a grain i to be part of the boundary, which is the following

Definition Grain i is a *left side (right side) boundary grain* if and only if $\forall$ grains j, k with $y_j < y_i < y_k : \frac{1}{2}(x_k + x_j) - x_i > 0\,(< 0)$.

This definition means that a grain i is part of the left membrane when the expression in Eq. 2.14, evaluated for all neighbor grains j at a smaller y-coordinate and all neighbor grains k at a larger y-coordinate, the Eq. 2.11 always evaluates to positive x-components of the force $\vec{F}_i$. As mentioned above, this condition guarantees that the membranes have a convex shape at both sides of the system.

In the simulations one needs to have a more *local condition* that is easier to calculate. As a prerequisite, one has therefore to decide which of the grains could possibly become part of the boundary. Candidates are the ones that are at the boundary of the packing. Hence, we will determine them with the following procedure, restricting the discussion to the left sidewall (the right sidewall is analogous). To determine the grains at the left side of the packing, the system is divided in small horizontal stripes that are not wider than one particle's thickness. These boxes all contain the particle with the leftmost position of all particles in the box. For the procedure to work, the boxes have to be so small that adjacent boundary particles are contained in different boxes. If the sidewall were straight, then a box width of $\leq 2r_{min}$ would be sufficient. But this is not the case, and the membrane is rather bended,

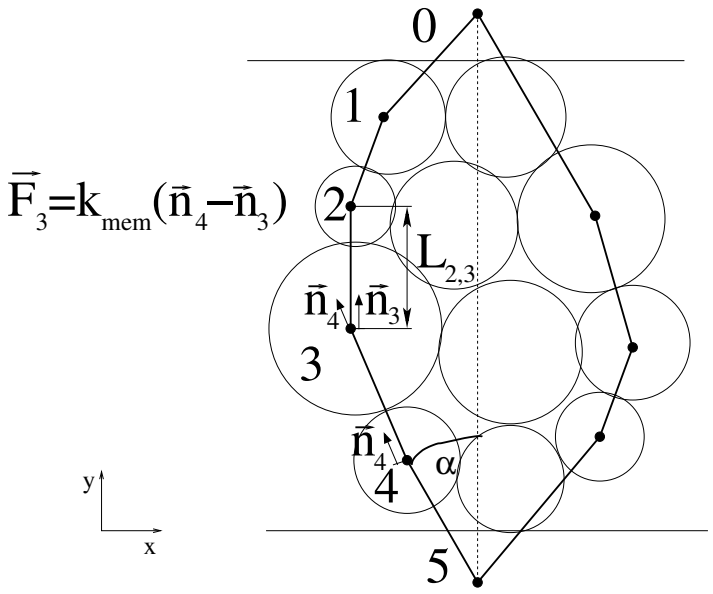

Figure 2.3: Construction of the membrane. The grains of the left side membrane are numbered. The membranes start at some point outside the system and end at another point on the other side of the system. These points are defined in Sec. 2.4.1. Angle α defines the maximum inclination from the vertical axis that the membrane can take at some position. The force on a grain of the membrane is proportional to the difference between two unit vectors $\vec{n}$. These vectors point to the neighbor particles.

with some maximum angle α relative to the vertical axis in Fig. 2.3. The maximum acceptable box width will depend on this angle. Thus we set

$$\text{BoxSize} = 1.9\ \mathrm{r}_{\mathrm{min}}\ \cos(\alpha)\ . \tag{2.15}$$

While the minimum diameter of a grain is $2r_{\min}$, the somewhat smaller prefactor 1.9 accounts for the fact that in molecular dynamics simulations the particles do overlap. But what is the value of α one has to put in Eq. 2.15? Extensive tests have shown that for $\alpha > 40°$ there are no more constitutive changes in the membrane for small size packings. However, in larger packings the membrane resembles a circle segment, and therefore a larger maximum angle has to be chosen to get the membrane stable. Tests showed that

$$\alpha = 60° \tag{2.16}$$

is a good choice for this angle. Note that with this choice, a significant number of boxes don't contain any grain, therefore the assumption that the boxes are chosen sufficiently small seems valid.

The left side membrane can now be constructed in the following way (the right side is analogous). Each box contains one particle from the left boundary, or no particle. For every particle in a box the definition given in the beginning of this section is evaluated. However, the neighbor grains j, k are not all grains in the packing, but only the grains in the other boxes. By construction, these grains are all at the left side of the system. Thus these grains are also candidates for becoming part of the membrane. The advantage is therefore that only a number of grains proportional to the length of the membrane are considered. This number is $\sim \sqrt{N}$, where N is the number of particles. Thus, for large N, the time required for determining the membrane grains is small.

2.4.2 Fixing the membrane

To prevent the membrane particles from moving around, the membrane has to be attached to some point on top and bottom of the simulation box. One simple way is to trace a vertical line through the geometric center of the simulation box (see left side of Fig. 2.4) and take the intersection with the top and bottom limit of the simulation box as membrane endpoints in the calculation of the forces in Eq. 2.11. To do so, the list containing the membrane particles is enlarged at its beginning and its end by one element.

Note that the forces on the membrane grains are bounded. Equation 2.11 together with Eq. 2.14 tells us that the x-component of the force is in the range

$$0 \leq \left| \left(\vec{F}_{\vec{x}_i} \right)_x \right| \leq 2k_{\mathrm{mem}}\ . \tag{2.17}$$

The same boundary values apply for the y-component. For large numbers of particles N, the polygonal boundary, defined by the membrane particles, approaches a smooth curve. This curve has the shape found in the right side system in Fig. 2.4. Since the shape is independent of N, the local curvature of the membrane is constant.

The total force exerted by the membrane is also insensitive to the number of particles. This finding can be explained in the following way. The force on each particle of the membrane is proportional to the difference between two normal vectors. These vectors are normal to the line segments which connect a membrane grain to the two adjacent membrane particles. The difference in the direction of the two normal vectors is proportional to the distance between adjacent membrane particles. But since the system size is independent of the number of particles, the size of one particle decreases proportional to $1/\sqrt{N}$. Thus two adjacent membrane particles are closer. Consequently, the directions of

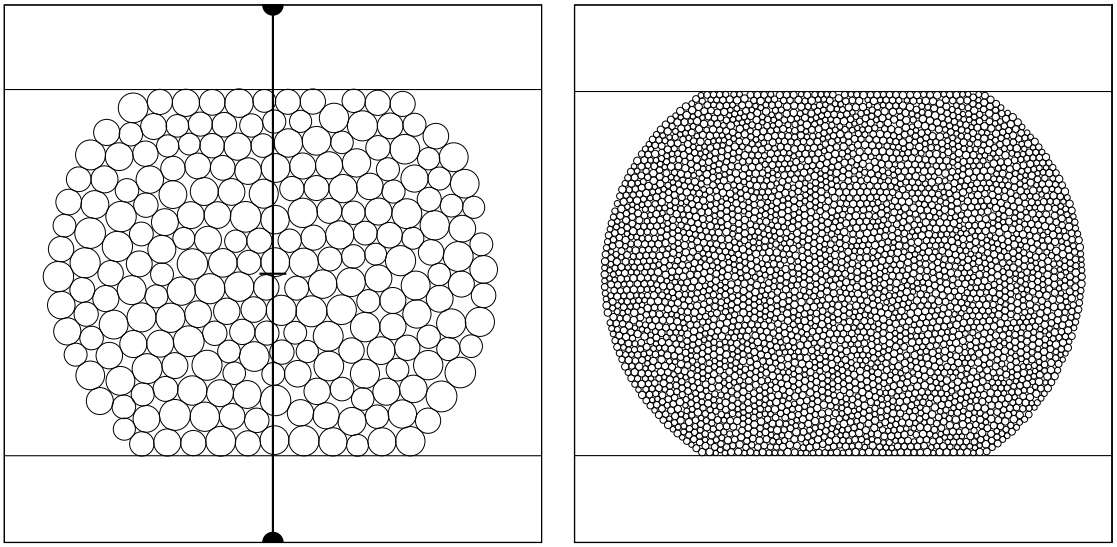

Figure 2.4: Examples of systems with membrane boundary conditions. In each figure, on top and on bottom a moving wall exerts a force $f_y = f(t)$ on the particles of the system. This force corresponds to a pressure. left: example of a packing with 225 particles; right: example of a packing with 4096 particles. In the left figure, the endpoints of the membrane are indicated by black spots at the upper and lower end of the simulation box. At these points the line through the geometric center of the box intersects the box boundaries.

the two normal vectors are also closer to each other. Since the force is proportional to the difference between these vectors, it decreases $\sim 1/\sqrt{N}$. On the other hand, the number of membrane particles increases $\sim \sqrt{N}$. Thus the sum of all membrane forces is independent of N.

2.5 Units and Parameters

The units and parameter values presented here are used throughout the thesis. While most of them are important for the numerical description, the parameter *Coulomb friction coefficient* is also important for the theoretical analysis.

There are three parameters which are set to unity: the particle density $\hat{\rho}$, the initial system length $\hat{L}$, and the pressure $\hat{p}$. This defines our system of units. In two dimensions, the unit of force is $\hat{f} = \hat{p}\hat{L}$, and the unit of energy is $\hat{E} = \hat{p}\hat{L}^2$. The unit of mass is $\hat{m} = \hat{\rho}\hat{L}^2$, whereas the time is measured in units of $\hat{t} = \hat{L}\sqrt{\hat{\rho}/\hat{p}}$. The spring stiffness, which is an important parameter, has a value of $k_{n,t} = 1600\hat{p}$. The average particle overlap $\overline{D}_n$ in this case is around 0.3% of the average particle radius r_{av}. The coefficient for critical damping at a contact depends on the number of particles. Because the length of the system $\hat{L}$ and the density ρ are fixed, the mass of a particle decreases with increasing number of particles N. The damping coefficient is set to 9/10th of the value for critical damping. For example, in $N = 16$ particles systems, the damping coefficient is $\gamma_{n,t} = 6\hat{m}/\hat{t}$. Some more details on the damping are given at the end of Sec. 2.10. The Coulomb friction coefficient for the friction between particles is $\mu = 0.25$, while the walls are frictionless, $\mu_{\mathrm{wall}} = 0$. No gravity is applied to the system.

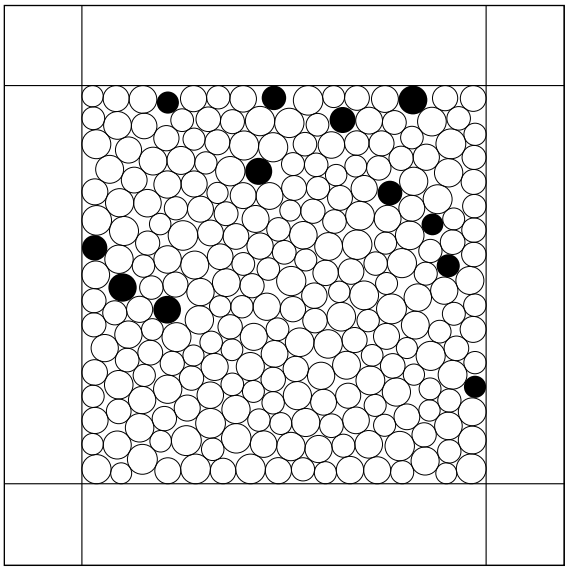

Figure 2.5: Rattlers in a 256 particles system with rigid walls at the boundaries. The rattlers are the black grains.

2.6 Rattlers

Let us begin the analysis of the model which has been presented above by discussing a simple but frequent event that can complicate the analysis: it is possible for a grain to float inside a void, occasionally colliding with its neighbors. Such grains are called *rattlers* [38]. An example of a system with rattlers is shown in Fig. 2.5. On the one hand, rattlers contribute like other grains to some granular properties, e.g. the packing fraction of the granular system. On the other hand, rattlers do not transmit forces, and thus do not contribute to the load-bearing properties of the granular system. Let us give an example: The stiffness of the granular assembly relates the change in external forces to the displacements of the walls. If rattlers are removed from the packing, then the stiffness will not change. Since rattlers do not contribute to the stiffness, they are removed whenever the assembly's stability is discussed. In the following, the remaining number of grains is referred to as $\tilde{N}$.

2.7 Global hyperstatic number

Hyperstaticity is defined as the difference between the number of contact forces (constraints) and the number of particle forces (degrees of freedom) [21, 39]. Here *contact forces* mean the normal and tangential forces at the contacts, and *particle forces* mean the total forces and torques exerted on the particles. In static equilibrium, the particle forces vanish, hence the contact forces must balance each other. When the number of contact forces is larger than the number of particle forces, there is some freedom to choose a specific set of contact forces. The possible ways to choose these forces form a set whose dimension is called global hyperstatic number $\mathcal{H}$. A naive expectation is that $\mathcal{H}$ decreases as the external load increases, and finally $\mathcal{H}$ vanishes at the time when the failure happens. The simulation results on this question will be discussed in Sec. 4.1. In this section the theoretical background, necessary to understand the results in Sec. 4.1, is presented.

When the granular system is stable, the particles are bound to each other in a way that only center of mass movements are possible. To clarify this idea, we will begin with a convenient representation of the forces. Although explained for two dimensions, the generalization to three dimensions is straightforward. First, one groups the forces in x and y-direction, f_x and f_y, and the torque τ, exerted on particle i, into a vector f_i. Then, one also groups the normal and tangent contact forces at one contact α, $F_{\alpha,n}$ and $F_{\alpha,t}$, into a vector $\vec{F}_\alpha$:

$$\vec{f_i} = \begin{pmatrix} f_{i,x} \\ f_{i,y} \\ \tau_i/r_i \end{pmatrix} \quad , \qquad \vec{F}_\alpha = \begin{pmatrix} F_{\alpha,n} \\ F_{\alpha,t} \end{pmatrix} \quad . \tag{2.18}$$

Now one gathers these quantities into a vector $\mathbf{f}$ for all $\tilde{N}$ grains and walls and another vector $\mathbf{F}$ for all M contacts,

$$\mathbf{f} = \begin{pmatrix} f_1 \\ f_2 \\ \vdots \\ f_{\tilde{N}} \end{pmatrix} = \begin{pmatrix} f_{1,x} \\ f_{1,y} \\ \tau_1/r_1 \\ \vdots \\ f_{\tilde{N},x} \\ f_{\tilde{N},y} \\ \tau_{\tilde{N}}/r_{\tilde{N}} \end{pmatrix} \tag{2.19}$$

and

$$\mathbf{F} = \begin{pmatrix} F_1 \\ F_2 \\ \vdots \\ F_M \end{pmatrix} = \begin{pmatrix} F_{1,n} \\ F_{1,t} \\ \vdots \\ F_{M,n} \\ F_{M,t} \end{pmatrix} . \tag{2.20}$$

In Eq. 2.19, all entries have the unit of a force, because the torques τ are divided by the particle radius r. Note that the f_i are linearly related to the F_α, thus $\mathbf{f}$ is linearly related to $\mathbf{F}$,

$$\mathbf{f} = \mathbf{c}\mathbf{F}, \tag{2.21}$$

where $\mathbf{c}$ is a matrix that maps the contact forces onto the particle forces. In other words, for each particle the matrix $\mathbf{c}$ maps the forces transmitted at the points of contact onto the total amount of force acting on this particle. Matrix $\mathbf{c}$ contains the information about the orientation of the contacts. Specifically, for a given contact α, $\mathbf{c}_\alpha$ contains the contact normal $\vec{n}_\alpha$ and the contact tangent $\vec{t}_\alpha$:

$$\mathbf{c}_{i\alpha} = \begin{pmatrix} \chi_{i\alpha}\vec{n}_\alpha & \chi_{i\alpha}\vec{t}_\alpha \\ 0 & 1 \end{pmatrix} . \tag{2.22}$$

$\mathbf{c}_{i\alpha}$ is the part of matrix $\mathbf{c}_\alpha$ which deals with the mapping of the contact forces transmitted to particle i. If $\vec{n}_\alpha$ is pointing towards particle i, then $\chi_{i\alpha} = +1$, otherwise $\chi_{i\alpha} = -1$. Matrix $\mathbf{c}$ contains therefore two columns for every contact α, and three rows for every particle i. The dimensions of this matrix are thus $2M \times 3\tilde{N}$, where M is the number of contacts and $\tilde{N}$ the number of particles.

In equilibrium, the particle forces $\mathbf{f}$ will balance the externally imposed forces $\mathbf{f}_{\text{ext}}$, $\mathbf{f} - \mathbf{f}_{\text{ext}} = 0$. In other words, the packing is stable when the equation

$$\mathbf{f}_{\text{ext}} = \mathbf{c}\mathbf{F}. \tag{2.23}$$

has at least one solution. If the external forces are given, then Eq. 2.23 is simply a system of linear equations from which one can attempt to calculate the contact forces $\mathbf{F}$. If there is a solution, then the contact forces balance the external load, and the system is in equilibrium. Otherwise the constraints set by the right side of the equation are not sufficient for achieving equilibrium, and the assumption of force balance, required for Eq. 2.23, is not valid any more. Instead a resulting force initiates a specific motion of the particles. This motion corresponds to one unconstrained degree of freedom. Let us now investigate the possibility of solving Eq. 2.23. We begin by comparing the number of unknowns $\mathbf{F}$ with the number of degrees of freedom, represented by the number of particle forces $\mathbf{f}$. On the left side of the equation one has 3 force components for each of the $\tilde{N}$ particles (rattlers are not considered). The total number of particle forces to be determined from Eq. 2.23 is thus

$$\mathcal{E}_p = 3\tilde{N} - 2. \tag{2.24}$$

This equation refers to the number of internal kinetic degrees of freedom. The two global kinetic degrees of freedom (the two linear displacement modes) of the system are subtracted at the right side. The number of kinetic degrees of freedom is the total number of all linearly independent directions of particle motions in the vector space of particle movements. Now let us consider the number of contact forces. When all contacts are nonsliding, it is $\mathcal{E}_c = 2M$. But, when a contact becomes sliding, Eq. 2.6 tells us that $|F_t| = \mu F_n$, and the number of independent contact forces is reduced by one, because the tangential force can be derived from the normal one. Thus the number of independent contact forces is reduced by the number of sliding contacts M_s,

$$\mathcal{E}_c = 2M - M_s. \tag{2.25}$$

The number of independent contact forces gives us the number of force constraints on the particle motions. Hence, the dimension of the solution space of Eq. 2.23 is given by the number of contact forces exceeding the number of particle forces to be determined. The *degree of hyperstaticity* can be calculated as:

$$\mathcal{H} = \mathcal{E}_c - \mathcal{E}_p\,. \tag{2.26}$$

When $\mathcal{H} > 0$, the granular assembly is hyperstatic, and the solution of Eq. 2.23 is not unique [21]. If $\mathcal{H} = 0$, the assembly is isostatic and the solution must be unique. On the other hand, if $\mathcal{H} < 0$, the assembly is hypostatic, and a solution of Eq. 2.23 does in general not exist.

It has been shown by other authors [40] that assemblies of frictionless grains are isostatic in the limit of very low external forces, or equivalently very high stiffnesses. The behavior of frictional assemblies, however, is different. In the most common case they are hyperstatic. However, the degree of hyperstaticity strongly depends on the formation procedure applied to form a granular solid. In a recent work, Agnolin et al. [39] show that it is also possible to produce isostatic frictional granular assemblies. But does $\mathcal{H}$ attain a specific value at the failure of the system? The history-dependent dynamic behavior of granular systems suggests there is no unique value. We will come back to this question when the simulation results are presented in Sec. 4.1.

2.8 The stiffness matrix

The stiffness matrix relates the velocities of the particles to the changes of the forces at the grains' contacts. The changes in these forces cause the grains' velocities. In the literature this relation, the stiffness matrix, is often called dynamical matrix, because it predicts the dynamical behavior

by means of the knowledge of the contact forces [6, 8, 41–43]. In the following subsection we will develop the concept of this matrix for the contact model introduced in Sec. 2.2 and explain the components of this matrix. When having accomplished this task, we present an alternative derivation of the stiffness matrix in Sec. 2.8.2, starting from the equations of motion of the particles. Thereafter stability is discussed in Secs. 2.8.3, 2.8.4. In the Section 2.8.5 we discuss the inversion of the stiffness matrix for determining the particle velocities. The subsection is followed by an examination of the energy contributions to the rise of the kinetic energy at the failure, which is carried out in Sec. 2.8.6.

2.8.1 Definition

We start the construction of the stiffness matrix with the contact model introduced in Sec. 2.2, and we include in the end a discussion of the components of the stiffness matrix. We can put Eqs. 2.1, 2.3 together to form one matrix equation for contact α. Neglecting the damping contributions, one obtains

$$\vec{F}_\alpha = \mathbf{K}_\alpha \vec{D}_\alpha \,. \tag{2.27}$$

In this equation, $\vec{F}_\alpha$ is a vector containing F_n and F_t, and $\vec{D}_\alpha$ contains D_n and D_t. The matrix $\mathbf{K}_\alpha$ is a 2×2 diagonal matrix containing the spring stiffnesses k_n, k_t in normal and tangent direction at the contact.

The derivative of $\vec{D}_\alpha$ with respect to time is

$$\dot{\vec{D}}_\alpha = \mathbf{S}_\alpha \vec{V}_\alpha \tag{2.28}$$

The vector $\vec{V}_\alpha$ contains the relative velocities of the particles in normal and tangent direction at contact α. Matrix $\mathbf{S}_\alpha$ contains the status of the contact. Before explaining this matrix in more detail, we make use of Eq. 2.28 for writing the derivative of Eq. 2.27 with respect to time:

$$\dot{\vec{F}}_\alpha = \mathbf{K}_\alpha \mathbf{S}_\alpha \vec{V}_\alpha \,. \tag{2.29}$$

When the tangential component $F_{t,\alpha}$ of $\vec{F}_\alpha$ is not restricted by the Coulomb condition in Eq. 2.6, matrix $\mathbf{S}_\alpha$ is a 2×2 identity matrix. If on the other hand we have equality in Eq. 2.6, the contact starts to slide and matrix $\mathbf{S}_\alpha$ must be adjusted, because $F_{t,\alpha}$ is set by the value of $F_{n,\alpha}$. Therefore, depending on the status of contact α, matrix $\mathbf{S}_\alpha$ is

$$\text{contact } \alpha \text{ is nonsliding}: \quad \mathbf{S}_{\alpha,C} = \begin{pmatrix} 1 & 0 \\ 0 & 1 \end{pmatrix}. \tag{2.30}$$

$$\text{contact } \alpha \text{ is sliding with } F_t = \pm\mu F_n: \quad \mathbf{S}_{\alpha,S\pm} = \begin{pmatrix} 1 & 0 \\ \mp\mu\frac{k_t}{k_n} & 0 \end{pmatrix}. \tag{2.31}$$

The second index of matrix $\mathbf{S}_\alpha$ indicates nonsliding (index 'C') or sliding in positive or negative direction (indexes 'S+' and 'S-'). When a sliding movement occurs, the stiffness will decrease on average [44].

The velocity $\vec{V}_\alpha$ at the contact can be calculated from the particle velocities. Assuming particles i and j touch at contact α, one obtains

$$V_n = (\vec{v}_i - \vec{v}_j)\vec{n}_\alpha \tag{2.32}$$

$$V_t = (\vec{v}_i - \vec{v}_j)\vec{t}_\alpha + \omega_i r_i + \omega_j r_j \,. \tag{2.33}$$

Having a look at Eq. 2.22, one notices that these equations can be put into one equation by making use of the transposed $\mathbf{c}_{i\alpha}$ [40]:

$$\vec{V}_\alpha = \mathbf{c}_{i\alpha}^T \vec{v}_i + \mathbf{c}_{j\alpha}^T \vec{v}_j \,. \tag{2.34}$$

Next we construct such an equation for each contact and put them all together in one. This is done by merging Eq. 2.29 of all contacts α into a single matrix equation. To do so, we construct large matrices $\mathbf{K}, \mathbf{S}$ whose diagonals consist of the matrices $\mathbf{K}_\alpha, \mathbf{S}_\alpha$ of all contacts α. Their off-diagonal elements are all zero. Then we gather all vectors $\vec{V}_\alpha$ in a vector $\mathbf{V}$. In that way one obtains one equation for all contacts:

$$\dot{\mathbf{F}} = \mathbf{KSV} = \sum_{\alpha=1}^{M} \mathbb{1}_\alpha \mathbf{K}_\alpha \mathbf{S}_\alpha \vec{V}_\alpha. \tag{2.35}$$

Here, M is the number of contacts in the system, and $\mathbb{1}_\alpha$ is a $M \times 1$ matrix (M being the number of contacts). This matrix has only one nonzero element, a 2×2 identity matrix, at $(\alpha, 1)$. Taking into account Eq. 2.23, one obtains

$$\dot{\mathbf{f}}_{\text{ext}} = \mathbf{cKSc}^T \mathbf{v} =: \mathbf{kv} \,. \tag{2.36}$$

Matrix $\mathbf{k} := \mathbf{cKSc}^T$ is called the stiffness matrix. It establishes a linear relation between the velocities of the particles and the change in the external forces. At constant $\dot{\mathbf{f}}_{\text{ext}}$, a contact change altering $\mathbf{k}$ leads to a discontinuous change of $\mathbf{v}$. But $\mathbf{v}$ actually changes continuously, because inertia effects become important. The inertia term is part of the equations of motion of the particles. In the next subsection, the stiffness matrix is derived from these equations.

2.8.2 Derivation from the equations of motion

The stiffness matrix can also be derived as an approximation to the full equations of motion. In this section, first the equations governing particle motions are presented. Then the approximations necessary to result in the matrix description of Eq. 2.36 are detailed.

In the equations of motion, the particle inertia terms are equal to the difference of external forces $\mathbf{f}_{\text{ext}}$ and particle forces $\mathbf{f}$:

$$\mathbf{m}\ddot{\mathbf{x}} = \mathbf{f}_{\text{ext}} - \mathbf{f}. \tag{2.37}$$

$\mathbf{x}$ is a vector containing the positions of the centers of mass of the particles. In two dimensions, it contains three components for each grain: horizontal, vertical and angular position. As the grains are circular with uniform density, positions $\mathbf{x}$ coincide with the grains' center positions. $\mathbf{m}$ is a $3N \times 3N$ diagonal matrix containing the particle masses and moments of inertia:

$$\mathbf{m} = \begin{pmatrix} \mathbf{m}_1 & \cdots & 0 \\ 0 & \ddots & \vdots \\ 0 & \cdots & \mathbf{m}_N \end{pmatrix}, \tag{2.38}$$

$$\mathbf{m}_i = \begin{pmatrix} m_i & 0 & 0 \\ 0 & m_i & 0 \\ 0 & 0 & I_i/r_i \end{pmatrix}. \tag{2.39}$$

m_i is the mass of particle i and I_i is its moment of inertia. Vector $\mathbf{f}$ can be expressed in the contact forces:

$$\mathbf{f} = \mathbf{cF} = \mathbf{cKSD} - \mathbf{c\Gamma c}^T \mathbf{v}. \tag{2.40}$$

The second term on the right side arises when passing from the static case (Eq. 2.27) to dynamic granular behavior. It contains the damping terms in the contact equations 2.1 and 2.3. The diagonal matrix $\mathbf{\Gamma}$ contains for each contact a 2×2 diagonal matrix, whose nonzero elements are the damping coefficients γ_n, γ_t.

In the next step we take the derivative of Eq. 2.40. Neglecting damping derivatives proportional to $\dot{\mathbf{c}}$ leads to

$$\dot{\mathbf{f}} = \dot{\mathbf{c}}\mathbf{F} + \mathbf{c}\dot{\mathbf{F}} = \dot{\mathbf{c}}\mathbf{F} + \mathbf{c}\mathbf{K}\mathbf{S}\dot{\mathbf{D}} - \mathbf{c}\mathbf{\Gamma}\mathbf{c}^T\dot{\mathbf{v}}. \tag{2.41}$$

Inserting this result in the derivative of Eq. 2.37 gives [45]:

$$\mathbf{m}\ddot{\mathbf{v}} = \dot{\mathbf{f}}_{\text{ext}} + \mathbf{c}\mathbf{\Gamma}\mathbf{c}^T\dot{\mathbf{v}} - \dot{\mathbf{c}}\mathbf{F} - \mathbf{k}\mathbf{v}. \tag{2.42}$$

The left hand side is the accelerations of the particles, differentiated once with respect to time.

On the right hand side are the forces, again differentiated with respect to time. The first term is the change in the external forces, and the second arises from the damping forces. The last two terms express the change of the contact forces due to the change in position of the particles. A change in the geometry of the contact alters the direction of force transmission, and this is described by the third term which constitutes the *geometric stiffness* of the assembly. The change in geometry is contained in the derivative of matrix $\mathbf{c}$ which contains all the information about contact positions and orientations. The contribution of this term to the system's stability is discussed in Sec. 2.8.3. The last term is the change in contact forces due to the change in spring lengths, and constitutes the *mechanical stiffness*.

Eq. 2.42 reduces to Eq. 2.36 under two assumptions. First, emerging vibrations should give a negligible contribution to Eq. 2.42. This assumption is valid if vibrations are much smaller than the contribution from the external force. Alternatively, the lifetime of vibrations has to be significantly smaller than the time scale introduced by the change in external force, which is defined by the frequency of contact changes. In this case the vibrations can be separated from the slow deformation of the packing [45]. When this assumption, the so called *quasi-static limit*, is fulfilled, the inertia term ($\mathbf{m}\ddot{\mathbf{v}}$) and the damping contribution ($\mathbf{c}\mathbf{\Gamma}\mathbf{c}^T\dot{\mathbf{v}}$) can be neglected. Second, in the case of hard particles, the typical deformation D is much smaller than the average particle radius r, $D \ll r$. This defines the so called *quasi-rigid limit*. In this limit the geometric contribution to the stiffness ($\dot{\mathbf{c}}\mathbf{F}$) becomes irrelevant. In these two limits, quasi-static and quasi-rigid, the last term on the right side of Eq. 2.42 is dominant, and balances the change in external load:

$$\dot{\mathbf{f}}_{\text{ext}} = \mathbf{k}\mathbf{v}. \tag{2.43}$$

In the remaining part of this subsection, we will examine the quasi-rigid limit in more detail. Our starting point is the configuration matrix $\mathbf{c}_{i\alpha}$, introduced in Eq. 2.22. First, its derivative is calculated, and the result is generalized to all contacts. Then, an expression for estimating the quasi-rigid limit is developed.

The derivative of $\mathbf{c}_{i\alpha}$ quantifies the change in contact direction $\vec{n}_\alpha$. Introducing the particle center distance $\vec{X}_{ij} = \vec{x}_i - \vec{x}_j$, its length $X_{ij} = |\vec{X}_{ij}|$, and its derivative $\vec{V}_{ij} = \vec{v}_i - \vec{v}_j$, one gets

$$\dot{\vec{n}}_\alpha = \frac{d}{dt}\frac{\vec{X}_{ij}}{X_{ij}} = \frac{\vec{V}_{ij}}{X_{ij}} - \frac{\vec{n}_\alpha\left(\vec{n}_\alpha \cdot \vec{V}_{ij}\right)}{X_{ij}} = \frac{\vec{t}_\alpha\left(\vec{t}_\alpha \cdot \vec{V}_{ij}\right)}{X_{ij}}\,. \tag{2.44}$$

The vector $\dot{\vec{t}}_\alpha$ is then obtained from the relation

$$\dot{\vec{t}}_\alpha = \vec{e}_z \times \dot{\vec{n}}_\alpha = -\vec{n}_\alpha\frac{\left(\vec{t}_\alpha \cdot \vec{V}_{ij}\right)}{X_{ij}}\,, \tag{2.45}$$

where $\vec{e}_z$ is the unit vector along z and orthogonal to both $\vec{n}_\alpha$ and $\vec{t}_\alpha$. The quantity in brackets is the tangential velocity V_{ij}^t at the contact. The derivative of $\mathbf{c}_{i\alpha}$ is linear in this quantity,

$$\dot{\mathbf{c}}_{i\alpha} = \frac{V_{ij}^t}{X_{ij}} \begin{pmatrix} \vec{t}_\alpha & -\vec{n}_\alpha \\ 0 & 0 \end{pmatrix} . \tag{2.46}$$

We see that $\dot{\mathbf{c}}_{i\alpha} \sim O\left(\frac{V_{ij}}{X_{ij}}\right)$. This result can be generalized to all contacts: $\dot{\mathbf{c}} \sim O\left(\frac{V}{X}\right)$. Here, V is the average relative velocity at a contact, and $X \approx 2r$ is the average particle distance, which is about twice the average particle radius r. Furthermore, if all contacts are nonsliding, $\mathbf{S} = \mathbb{1}$, and thus $\mathbf{F} = \mathbf{KD} \sim O(kD)$, where D is the average particle overlap. One therefore obtains $\dot{\mathbf{c}}\mathbf{F} \sim \left(Vk\frac{D}{r}\right)$ for the geometric stiffness. On the other hand, an estimate for the mechanical stiffness is $\mathbf{kv} \sim kV$. In the quasi-rigid limit the overlap D is much smaller than a particle radius $D \ll r$, thus the geometric stiffness becomes irrelevant.

2.8.3 Stability

On a macroscopic level, stability is guaranteed when the dimensions of the system are constant. For the system introduced in Fig. 1.2, this means that the walls do not move upon a small variation of the external forces. The system can also be considered stable if, when increasing the external forces $\mathbf{f}_{\text{ext}}$ on the walls to compress the system, all walls move in the direction of the force, i.e., inwards. Therefore $\mathbf{v}^T\dot{\mathbf{f}}_{\text{ext}} > 0$ signals stability. On the other hand, $\mathbf{v}^T\dot{\mathbf{f}}_{\text{ext}} < 0$ would signal instability. Assuming Eq. 2.43 is valid, we can alternatively write

$$\mathbf{v}^T\mathbf{kv} > 0\,. \tag{2.47}$$

Note that this equation contains not only the velocities of the walls, but also the motions of all the particles in the system. Whenever this inequality is violated, instability will occur. When this happens, we have to re-evaluate the assumptions leading to Eq. 2.43. But let us first see which types of instability can occur. One condition is

$$\mathbf{v}^T\mathbf{kv} < 0\,. \tag{2.48}$$

When this relation is satisfied, a small displacement in the direction of $\mathbf{v}$ leads to a force that amplifies this displacement. A particular clear discussion of this is given in Ref. [20]. Another type of instability occurs when

$$\mathbf{v}^T\mathbf{kv} = 0. \tag{2.49}$$

As discussed in Sec. 2.8.5, Eq. 2.49 always holds for some motions. It is therefore necessary to inspect the vectors $\mathbf{v}$. If they correspond to trivial motions, such as the uniform translation of all the particles, Eq. 2.49 does not signal failure, but simply expresses the translation invariance of space. On the other hand, if vectors $\mathbf{v}$ correspond to non-trivial motions, then Eq. 2.49 indicates that the packing is unstable and fails.

The numerical results in Chapter 3 show that these statements must be nuanced. The reason for this is that the criteria in Eqs. 2.48 and 2.49 are based on Eq. 2.43, which in turn is based on the dominance of $\mathbf{kv}$ over the other terms in Eq. 2.42. But as the load increases, $\mathbf{kv}$ decreases, so that other terms may become important.

In the most common case the geometric stiffness becomes significant. In Eq. 2.42, it is written as $\dot{\mathbf{c}}\mathbf{F}$, but since $\dot{\mathbf{c}}$ is proportional to $\mathbf{v}$, it can be rewritten [20]:

$$\dot{\mathbf{c}}\mathbf{F} = \mathbf{k}_{\text{geo}}\mathbf{v}. \tag{2.50}$$

The stability of the packing depends on the total stiffness $\mathbf{k}_{\rm tot} = \mathbf{k} + \mathbf{k}_{\rm geo}$, and not just on the mechanical stiffness $\mathbf{k}$. Thus, Eq. 2.48 should be modified to read

$$\mathbf{v}^T\mathbf{k}_{\rm tot}\mathbf{v} = \mathbf{v}^T\mathbf{k}\mathbf{v} + \mathbf{v}^T\mathbf{k}_{\rm geo}\mathbf{v} < 0. \tag{2.51}$$

The geometric stiffness is usually much smaller than the mechanical one, as discussed in Sec. 2.8.2. Why $\mathbf{k}_{\rm geo}$ reduces the stability of packings of circular grains is explained in the remaining part of this subsection.

Starting from Eq. 2.46, the contribution to the geometric stiffness of particle i at contact α is

$$\vec{v}_i^T\dot{\mathbf{c}}_{i\alpha}\vec{F}_\alpha = \frac{V_{ij}^t}{X_{ij}}\left(v_i^t F_\alpha^n - v_i^n F_\alpha^t\right) . \tag{2.52}$$

Now we include the contribution from particle j at contact α. Noting that $\dot{\mathbf{c}}_{j\alpha} = -\dot{\mathbf{c}}_{i\alpha}$, we get

$$\left(\vec{v}_i^T\dot{\mathbf{c}}_{i\alpha} + \vec{v}_j^T\dot{\mathbf{c}}_{j\alpha}\right)\vec{F}_\alpha = \frac{V_{ij}^t}{X_{ij}}\left(V_{ij}^t F_\alpha^n - V_{ij}^n F_\alpha^t\right) . \tag{2.53}$$

X_{ij} and F_α^n are always positive, the other quantities can be either positive or negative. Thus the second term can be either negative or positive, and averaging over a large number of contacts leads to many cancellations. On the other hand, the first term is always positive. Hence $\mathbf{v}\dot{\mathbf{c}}\mathbf{F} > 0$ for assemblies of circular grains.

For stiff circular grains, the geometric stiffness is negligible in comparison to the mechanical part. The argument in Sec. 2.8.2 for this statement can now be refined, because now a true scalar stiffness is defined. The ratio estimate is

$$\frac{\mathbf{v}^T\dot{\mathbf{c}}\mathbf{F}}{\mathbf{v}^T\mathbf{k}\mathbf{v}} \propto \frac{v\frac{v}{d}F}{v^2 k_n} \propto \frac{\frac{1}{d}\left(f_{\rm ext}\frac{d}{L}\right)}{k_n} = \frac{f_{ext}}{k_n L} = \frac{p}{k_n} . \tag{2.54}$$

Here, L is the length of the simulation box. The average contact force is denoted by F, and $p = f_{\rm ext}/L$ is the pressure. Presuming pressure is around unity, the particle stiffness k_n can be tuned to a sufficiently high value (10^3, for instance).

This equation holds when there are no sliding contacts. The ratio can become significantly larger when their number increases. At failure, the geometric stiffness $\mathbf{v}\dot{\mathbf{c}}\mathbf{F}$ can even surpass the mechanical contribution.

The other term that can become important as $\mathbf{v}\mathbf{k}\mathbf{v}$ decreases is the inertia term on the left hand side of Eq. 2.42. This always happens at contact status changes. When the assembly is stable, this is the signature of vibrations. We will come back to this in Sec. 3.3.

2.8.4 Closer inspection of the stability limit

In the last subsection we have seen that the mechanical stiffness is the main contribution to the total stiffness. But the mechanical stiffness decreases, and the geometric stiffness becomes more important close to the failure. But what are the processes that decrease the mechanical stiffness, and how can it become negative? These two questions are answered in this subsection. Particularly important for the change of the mechanical stiffness are the contact changes. First the number of contacts decreases with increasing load. Second, each contact can also change its status, for example from nonsliding to sliding. But sliding contacts allow for a free tangent motion at the contact, i.e. a motion that corresponds to zero resistance.[1] For the definiteness of the mechanical stiffness, the sliding contacts

[1] Eq. 2.6 assures the tangential force F_t never exceeds the value required for the sliding condition. Thus the contact force cannot increase when the particles slide along each other at the point of contact.

play a central role.

Contact statuses

Granular contacts can be in two states: *nonsliding* ($F_t < \mu F_n$) or *sliding* ($F_t = \mu F_n$). Enlarging this concept of contact states by introducing a further, *open* status ($F_n = F_t = 0$), opening and closing contacts can also be inspected. The open state appears when a contact (nonsliding or sliding) is lost. We expect the weakening of the system to happen through two different mechanisms:

1. A nonsliding contact becomes sliding ('C' $\rightarrow$ 'S').
2. A nonsliding or sliding contact disappears ('C/S' $\rightarrow$ 'O').

Note that the first process does not always entail softening of the system [44]. In fact it can increase or decrease the stiffness, and the change will depend on the local structure of the system. But at sliding contacts particles get an additional possibility to move, namely to slide. This additional motion usually makes the system softer. We will investigate the rates of contact status transitions in the simulations in Sec. 5.4.3.

Definiteness of $\mathbf{k}$

A slightly modified view in terms of stiffness is connected with the question whether or not the stiffness matrix $\mathbf{k}$ is positive definite. If it is positive definite, small particle velocities move the particles back to the equilibrium positions. When, on the other hand, $\mathbf{k}$ is not positive definite, the assembly is either not "jammed", i.e. the grains can displace more or less independently of each other, or the current position is not a stable one, and small displacements entrain forces that push the particles further away.

Let us now investigate which part of $\mathbf{k}$ does determine the definiteness. As we are interested in positive semi-definiteness[2], we should identify whether a vector $\mathbf{v}$ exists such that

$$\mathbf{v}^T\mathbf{k}\mathbf{v} \geq 0\,. \tag{2.55}$$

is violated. Here, $\mathbf{v}$ can for now be any velocity vector, not just one compatible with the boundary conditions. Next we will define the velocities $\mathbf{V}$ in contact space, i.e. the relative particle velocities at their point of contact:

$$\mathbf{V} = \mathbf{c}^T\mathbf{v}\,. \tag{2.56}$$

With this definition, Eq. 2.55 writes

$$\mathbf{VKSV} \geq 0\,. \tag{2.57}$$

Note that the indicative of the transpose is omitted for better readability. Usually one wants the contacts to have the same stiffness. Then, $\mathbf{K}$ is just proportional to the identity matrix, $\mathbf{K} = k\mathbb{1}$. Thus the definiteness of $\mathbf{k}$ solely depends on matrix $\mathbf{S}$, which carries the information whether contacts are sliding or nonsliding. We will first discuss the contribution of one contact α. Its contribution to $\mathbf{vkv}$ is:

$$\vec{V}_\alpha\mathbf{K}_\alpha\mathbf{S}_\alpha\vec{V}_\alpha = \begin{cases} k(V_n^2 + V_t^2) & (nonsliding)\,, \\ k(V_n^2 \pm \mu V_n V_t) & (sliding)\,. \end{cases} \tag{2.58}$$

[2] As we will see in Sec. 3.4.2, there are under certain circumstances motions which correspond to a stiffness that is zero. These motions do not necessarily change the system's stability. The motions can for instance be particle rotations. One such example is shown in Fig. 3.9.

It should be noted that both the normal V_n and the tangential V_t part of the relative velocity $\vec{V}_\alpha$ at contact α can be positive or negative. When the contact is nonsliding, its contribution to the stiffness is always positive according to Eq. 2.58. Hence it is only the sliding contacts that can cause the stiffness to become negative. To counterbalance the positive contribution of the normal component, the condition $\mp V_t = V_n/\mu$ is necessary. Hence $|V_t| > |V_n|/\mu$ is required for a velocity vector $\mathbf{v}$ with negative $\mathbf{vkv} < 0$ to exist.

Furthermore the definiteness can change in two ways: by passing through a *null-mode*, i.e. $\mathbf{vkv} = 0$, or abruptly, i.e. that $\mathbf{vkv}$ suddenly changes its sign through a contact status change. The magnitude of the sudden change will depend on the size of the assembly, and become negligibly small in the large particle number limit. Hence $\mathbf{vkv}$ will, as long as $\mathbf{vkv} > 0$, always change smoothly in sufficiently large granular assemblies. It is therefore expected that $\mathbf{vkv}$ tends to zero in large assemblies at the time of failure. To be precise, the total stiffness matrix $\mathbf{k_{tot}} = \mathbf{k} + \mathbf{k_{geo}}$ will be such that the *total* stiffness $\mathbf{v}\mathbf{k}_{\mathrm{tot}}\mathbf{v}/\mathbf{vv}$ vanishes at the failure, $\mathbf{vk_{tot}v} \to 0$. Here, $\mathbf{k}_{\mathrm{geo}}$ denotes the contribution of the geometric stiffness, introduced in Eq. 2.50.

2.8.5 Inversion and particle velocities

If Eq. 2.43 could be solved for $\mathbf{v}$, the validity of the theory could be proven by comparing the result with the simulation velocities. But more fundamentally, the theoretical value only depends on $\mathbf{k}$, and it is completely independent of the grains' masses. Since $\dot{\mathbf{f}}_{ext}$ is constant and $\mathbf{k}$ only changes when a status change arises, the impact of such a contact status change can be noticed in a simultaneous, sudden change in the velocity.

However, $\mathbf{k}$ has no inverse, because certain motions, such as a translation of the system, do not lead to changes in the forces. Nevertheless, a pseudo-inverse $\tilde{\mathbf{k}}$ of the stiffness matrix can be defined that disregards these movements. We require that $\tilde{\mathbf{k}}\mathbf{kv} = \mathbf{v}$ if $\mathbf{v}$ is orthogonal to the kernel of $\mathbf{k}$, and $\tilde{\mathbf{k}}\mathbf{kv} = 0$ if $\mathbf{v}$ belongs to the kernel of $\mathbf{k}$. Then $\tilde{\mathbf{k}}$ can be used to predict the velocities $\mathbf{v}$:

$$\mathbf{v}_{\mathrm{th}} := \tilde{\mathbf{k}}\dot{\mathbf{f}}_{\mathrm{ext}}. \tag{2.59}$$

The index "th" indicates that the velocities are predicted theoretically. The construction of $\tilde{\mathbf{k}}$ is as follows: first we decompose $\mathbf{k}$ into a diagonal matrix $\mathbf{s}$ and two orthonormal matrices $\mathbf{u}$ and $\mathbf{w}$,

$$\mathbf{usw}^T = \mathbf{k}\,. \tag{2.60}$$

This reduction is called *singular value decomposition* and is always possible, with $\mathbf{s}$ containing the (non-negative) real *singular values* on the diagonal. Note that $\mathbf{k}$ is not symmetric, so it can in general not be diagonalized over the field of real numbers (some of the eigenvalues would be complex). To define a matrix that acts as an inverse of $\mathbf{k}$, we first define

$$\tilde{s}_{ij} := \begin{cases} 1/s_{ii} & \text{if } i = j \text{ and } s_{ii} \neq 0, \\ 0 & \text{otherwise.} \end{cases} \tag{2.61}$$

Then the "inverse" of the stiffness matrix is defined as

$$\tilde{\mathbf{k}} := \mathbf{w}\tilde{\mathbf{s}}\mathbf{u}^T\,. \tag{2.62}$$

Note that, by definition, the kernel dimensions of $\mathbf{k}$ and $\tilde{\mathbf{k}}$ are identical.

We now turn to the investigation of the energy contribution to the kinetic and the potential energy.

2.8.6 Inspection of energy terms in kinetic and potential energy

The energy injected by the forcing at the boundaries will be distributed among the kinetic and the potential energy of the particles. When the system is stable, most of the energy is converted to potential energy, and the kinetic energy remains small. We would like to analyze the different contributions to the kinetic and potential energy. Let us begin by writing the expressions for these two types of energy:

$$E_{\mathrm{kin}} = \frac{\mathbf{vmv}}{2}, \quad E_{\mathrm{pot}} = \frac{\mathbf{DKD}}{2}. \tag{2.63}$$

We will consider the first and second derivatives of these quantities with respect to time. In addition, we will make use of Eq. 2.42, and Eq. 29 from [45], writing Newton's second law as

$$\mathbf{m}\dot{\mathbf{v}} = \mathbf{cF} + \mathbf{f}_{\mathrm{ext}}, \tag{2.64}$$

To simplify the following calculations, we will neglect the damping ($\mathbf{\Gamma} = \mathbf{0}$ in Eq. 2.42). The first two derivatives of E_{kin} are then

$$\begin{aligned} \dot{E}_{\mathrm{kin}} &= \mathbf{vm}\dot{\mathbf{v}} = \mathbf{v}(\mathbf{f}_{\mathrm{ext}} + \mathbf{cF}), \\ \ddot{E}_{\mathrm{kin}} &= \dot{\mathbf{v}}\mathbf{m}\dot{\mathbf{v}} + \mathbf{vm}\ddot{\mathbf{v}}. \end{aligned} \tag{2.65}$$

With Eqs. 2.42 and 2.64, the second derivative of the kinetic energy can be written

$$\begin{aligned} \ddot{E}_{\mathrm{kin}} \quad = \quad & (\mathbf{f}_{\mathrm{ext}} + \mathbf{cF})\mathbf{m}^{-1}(\mathbf{f}_{\mathrm{ext}} + \mathbf{cF}) \\ & + \mathbf{v}\dot{\mathbf{f}}_{\mathrm{ext}} - \mathbf{vkv} + \mathbf{v}\dot{\mathbf{c}}\mathbf{F}. \end{aligned} \tag{2.66}$$

The first term is the contribution from the force imbalance and will be explained in more detail below. The second term is the contribution from the increase in the external forces. The last two terms are related to the geometric and mechanical stiffnesses. This can be seen by comparing Eq. 2.66 with Eq. 2.42.

The force imbalance is quadratic in $(\mathbf{f}_{\mathrm{ext}} + \mathbf{cF})$ and thus nonnegative. When it is nonzero, the difference between the external forces $\mathbf{f}_{\mathrm{ext}}$ and the contact forces $\mathbf{F}$ leads to significant particle motions, pushing the system towards force equilibrium. Equation 2.64 shows that the increase in the particle motions is proportional to the force imbalance, i.e. it is proportional to the separation from the equilibrium (force) configuration. Thus if the force imbalance contributes significantly to $\ddot{E}_{\mathrm{kin}}$, the system is actually far from equilibrium, which means that the quasi-static assumption, which is part of the basis of the stiffness matrix ansatz, is not valid any more. The break down of quasi-staticity is equivalent to the particle inertia becoming important in the equations of motion (Eq. 2.42). When this happens, failure might be under way, and the system might envisage a new equilibrium configuration very different from the old one.

If one calculates the second derivative of the potential energy, and assumes all the contacts are non-sliding, one obtains

$$\ddot{E}_{\mathrm{pot}} = -(\mathbf{cF})\mathbf{m}^{-1}(\mathbf{f}_{\mathrm{ext}} + \mathbf{cF}) + \mathbf{vkv} - \mathbf{v}\dot{\mathbf{c}}\mathbf{F}. \tag{2.67}$$

The first term is part of the force imbalance term which appears in the kinetic energy in Eq. 2.66. In the potential energy this term does not have a quadratic form. Thus it can be either positive or negative, meaning that the force imbalance can either lead to an increase or a decrease of the potential energy. The first possibility signals the system is stable, while the second possibility means it is

	term	dependence	key relation
force imbalance	$\dot{\mathbf{v}}\mathbf{m}\dot{\mathbf{v}}$	$\sim \mathbf{vv}$	$\dot{\mathbf{v}}/\mathbf{v} = const$
change in load	$\mathbf{v}\dot{\mathbf{f}}_{\text{ext}}$	$\sim \mathbf{v}$	-
mech. stiffness	$-\mathbf{vkv}$	$\sim \mathbf{vv}$	-
geometric stiffness	$\mathbf{v}\dot{\mathbf{c}}\mathbf{F}$	$\sim \mathbf{vv}$	$\dot{\mathbf{c}} \sim \mathbf{v}$

Table 2.1: Dependence of the energy contributions on $\mathbf{v}$ during failure, when the kinetic energy rises exponentially. We used Eq. 2.64 to write $\mathbf{m}\dot{\mathbf{v}}$ for the forces appearing in the first line.

unstable, and large deformations will occur. The other two terms in Eq. 2.67 are the contributions from the mechanical and geometric stiffnesses and they are the same as in Eq. 2.66, but the signs are reversed. Thus the decrease in the stiffness ($\mathbf{vkv} - \mathbf{v}\dot{\mathbf{c}}\mathbf{F}$) leads to a conversion of energy from the potential energy to the kinetic energy. We can combine Eqs. 2.66 and 2.67 to obtain

$$\ddot{E}_{\text{kin}} + \ddot{E}_{\text{pot}} = \mathbf{v}\dot{\mathbf{f}}_{\text{ext}} + \dot{\mathbf{v}}\mathbf{f}_{\text{ext}}. \tag{2.68}$$

This is simply a statement of the conservation of energy in the absence of dissipation ($\mathbf{\Gamma} = 0$); the amount of energy injected into the system is equal to the changes in kinetic and potential energy. What happens when the system fails, i.e. when it deforms macroscopically? In the introduction, failure was associated with a sudden change of the system's dimension. Thus the kinetic energy must increase. But which of the terms in Eq. 2.66 causes the rise?

We observe from the simulation results presented in Sec. 3.9.1 that E_{kin} always rises exponentially during failure: $E_{\text{kin}} \sim e^{\alpha t}$. This means that the velocities must also increase exponentially. Failure is a collective rearrangement process, hence we can substitute the velocity vector by its length $|\mathbf{v}|$. Its time dependence is $|\mathbf{v}| \sim e^{\alpha t/2}$.

Now we can determine which of the terms in Eq. 2.66 can drive the increase in kinetic energy during the failure. An exponential rise in E_{kin} is possible only if the dominant term on the right hand side increases proportionally to E_{kin}, i.e. if it is proportional to $\mathbf{vv}$. Tab. 2.1 shows which terms are proportional to $\mathbf{vv}$ and thus are candidates for driving failure: the force imbalance, the mechanical stiffness, and the geometric stiffness. The last is proportional to E_{kin} because the change $\dot{\mathbf{c}}$ in the contact orientations is proportional to the particle velocities, which is shown for one contact in Eq. 2.46. The term $\mathbf{v}\dot{\mathbf{f}}_{\text{ext}}$, arising from the change in the external load, is proportional to $|\mathbf{v}|$ only, and thus is not capable of sustaining the exponential growth of the kinetic energy. In Sec. 3.9.1 we will see that the main contribution to $\ddot{E}_{\text{kin}}$ at the failure comes from the force imbalance.

2.9 Simulation Method

Why is it necessary to do simulations? Can't we just do experiments, and compare results with theoretical predictions? Although seemingly simple to answer, it is yet a question one should bring up before carrying out simulations, because there might be other, better ways to model granular behavior. However, microscopic variables, i.e. variables for which each grain contributes one value, are difficult to access experimentally. Two simple examples are the positions and the velocities of the grains. While in experiments it is easy to track motions next to the boundary of a solid, it is difficult to inspect particles in the bulk. Although not completely impossible, accessing the internal structure

is difficult. For crystalline solids, methods like x-ray diffraction allow for a detailed analysis of the bulk. But these techniques are difficult to apply to the disordered structure of granular materials. Simulations are an appropriate means to access the internal structure and microscopic quantities, because many of these quantities are stored in the computer's cache and just have to be read out.

But which is the best way to investigate numerically granular materials? In the beginning of this chapter, the discrete element model (DEM) has been introduced as our theoretical model of granular systems. Within the DEM, different ways of modeling numerically granular motions are possible. One of them is the contact dynamics method (CD) [46], which considers a set of hard, undeformable particles interacting at contacts j for which the forces are not known. Thus the forces have to be constructed or chosen from a variety of sets of forces which are compatible with the boundary conditions. Another possibility is to consider a set of deformable particles, as we have done in Secs. 2.1, 2.2, and integrate the equations governing their motions, Eq. 2.37. Therefrom one deduces the forces at the contacts. This approach is implemented in the molecular dynamics method (MD) [47, 48]. In this approach, there is no freedom to choose between different sets of forces, but the set is unique; as mentioned in the introduction, granular media are athermal. Therefore the system cannot explore phase space, and the set of forces follows from the history, i.e. it depends on the preparation of the system.

The molecular dynamics method is used in this thesis, and the equations of motion are numerically integrated using the *velocity Verlet* algorithm. It is similar to the Verlet algorithm [49], but it explicitly incorporates velocity:

$$\mathbf{x}(t+\Delta t) = \mathbf{x}(t) + \mathbf{v}(t)\Delta t + \frac{1}{2}\mathbf{a}(t)(\Delta t)^2, \tag{2.69}$$

$$\mathbf{v}(t+\Delta t) = \mathbf{v}(t) + \frac{1}{2}\left(\mathbf{a}(t) + \mathbf{a}(t+\Delta t)\right)\Delta t. \tag{2.70}$$

In these equations, $\mathbf{a}(t)$ is a vector containing the accelerations of the particles at time t, organized in the same way as $\mathbf{f}$ in Eq. 2.19. The accelerations $\mathbf{a}$ are calculated from the forces $\mathbf{f}$. The integration time step is Δt. With the MD simulation technique we can now prepare the sample systems.

2.10 Sample preparation

The granular systems are made of disks (2D) or spheres (3D) with radii r uniformly distributed within the range $[0.7r_{\max}, r_{\max}]$ and having initial velocities in the range $v_x, v_y \in [-0.5, 0.5]$. The radii and initial velocities are chosen using a random number generator. A series of packings is generated by changing the initial *seed* of this random number generator. The resulting assemblies essentially differ in contact topology and the spatial distribution of the grain sizes.

The frictionless particles are initially separated, but a constant external force $f_0 = 0.8\hat{f}$ is applied to each of the light-weight ($m = 0.01\hat{m}$) boundary walls, so that they move inward and compress the grains into a packing. This type of preparation is also reported in the literature [34]. The preparation procedure lasts from $t = -50\hat{t}$ until $t = 0\hat{t}$, the latter marking the start of the loading procedure described in Sec. 2.11. The approximate size of the packing is $0.8\hat{L}$ at the end of preparation. The density of the systems is close to the value believed to be the *random close packing density* [18, 22, 50], i.e. the most dense packing one can create without crystallization of the system. However, in small systems boundary effects are very important, and they lead to a significantly smaller packing density. This can be seen in Tab. 2.2 which shows the packing fraction of different system sizes in two and three dimensions.

2 dimensions			3 dimensions		
N (number of systems)	ϕ	σ_ϕ	N (number of systems)	ϕ	σ_ϕ
16 (26)	0.711	0.012	64 (8)	0.514	0.005
256 (256)	0.815	0.003	512 (128)	0.575	0.002
1024 (64)	0.830	0.001	1100 (64)	0.590	0.001
4096 (16)	0.837	$5\ 10^{-4}$	4352 (16)	0.608	0.001
16384 (4)	0.841	$2\ 10^{-4}$	16875 (4)	0.620	$3\ 10^{-4}$
65536 (1)	0.843	-			

Table 2.2: Packing fractions of two and three dimensional packings with rigid wall (2D) and triaxial (3D) boundary conditions. Voids close to the walls, which are smaller than a particle, lead to smaller packing fractions than one would obtain in infinitely large systems. Boundary effects decrease with increasing system size. The large two dimensional systems have packing fractions $\phi \approx 0.84$, which is believed to be the value for random close packing [22, 50, 51]. In three dimensions, the investigated systems are not large enough to reach the asymptotic limit. Thus the packing fractions are smaller than the random close packing value in the literature, which is $\phi \approx 0.64$ [18, 50]. Boundary effects are still an important issue for the three dimensional systems with $N = 16875$ particles. σ_ϕ is the standard deviation of ϕ.

During the compression process, kinetic energy is removed by the damping at particle contacts. Certain motions, however, require special care. For example, the velocity of the center of mass cannot be removed by the damping at particle contacts, and thus a global viscous damping is applied for $-50\hat{t} < t < -40\hat{t}$. Through this procedure, the kinetic energy decreases by several orders of magnitude. For example, in 16 particle packings it decreases to $(6.9 \pm 0.1) \times 10^{-8}\hat{E}$ (average over 26 configurations). The main reservoir of remaining kinetic energy are particles without contacts. To remove their energy, a viscous damping force opposing the individual grain movement is applied until $t = 0\hat{t}$. The remaining kinetic energy in the 16 particles packings is $(3.0 \pm 6.1) \times 10^{-9}\hat{E}$.[3] At the end of the preparation, friction is turned on.

The contact structure obtained turns out not to depend much on the contact damping. When γ_n in Eq. 2.2 is set to the aperiodic limit value $\gamma_{n,aperiodic} = \sqrt{k_n \bar{m}}$ ($\bar{m}$ is the mean particle mass), the number of contacts decreases only by 0.1% in comparison with a preparation where $\gamma_{n,low} = 0.25\gamma_{n,aperiodic}$. Therefore, a comparatively high value $\gamma_{n,default} = 0.9\gamma_{n,aperiodic}$ was taken. This permits to keep vibrations as small as possible, but on the other hand does not lead to overdamping at a significant number of contacts.

2.11 Loading the sample

The configurations obtained are submitted to an increasing external force along the vertical axis, whereas the horizontally applied forces remain unchanged (Fig. 2.6). The vertical external force increases linearly,

$$f_y(t) = f_0 + \alpha t \tag{2.71}$$

[3] Each of the damping terms increases the simulation time by approximately 15%.

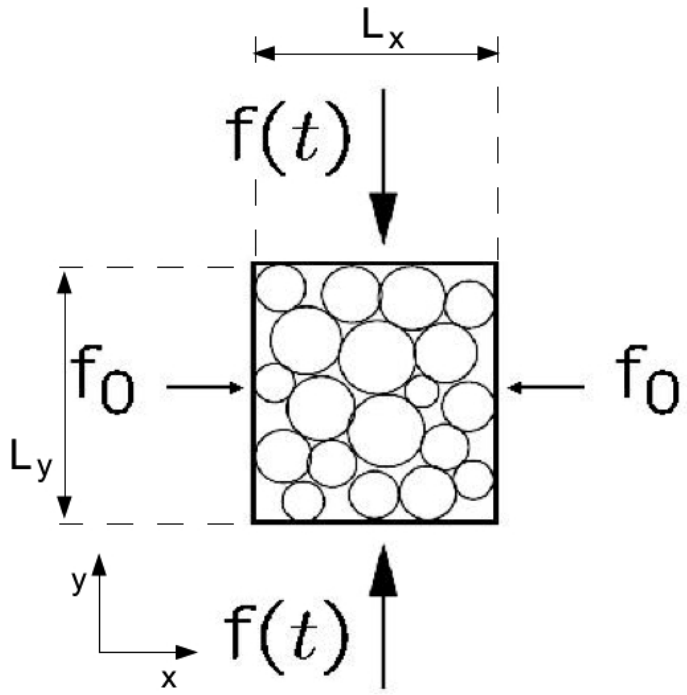

Figure 2.6: Rigid wall boundary conditions. The walls are smooth and can move normal to their surface. The coordinate system is defined in the bottom left corner.

To obtain a pressure $p = f_0/L_x$ that is approximately unity, the force is set to $f_0 = 0.8\hat{f}$. The prefactor α determines the value of the very small force increment per timestep. The aim is to study failure in the quasi-static limit, meaning that force f_{fail} at which failure happens is independent of load velocity α. Performing runs with different α, We checked that the simulations are quasi-static for $\alpha = 1.28 \times 10^{-3}\hat{f}\hat{t}^{-1}$. This is the value chosen for the small systems that are investigated in Chap. 3. For the larger systems investigated in Chapters 4 - 10, α was chosen one order of magnitude larger, $\alpha = 1.28 \times 10^{-2}\hat{f}\hat{t}^{-1}$. The reason for that adjustment is that the simulation time increases approximately linearly with the number of particles, thus the large simulations would take much longer than a month. The force at the failure f_{fail} just slightly increases with increasing rate α. Thus the simulations can still be considered quasi-static. At the beginning of the simulation, a parabolic matching is applied to obtain a continuous differentiable force curve.

The systems with membrane boundary conditions are loaded in the same way in the y-direction, but the sidewalls are replaced by the membranes. Similar to the forces exerted on the rigid sidewalls, here forces are exerted on the grains of the membrane. The strength of the forces depends on the membrane stiffness. It is $k_{\text{mem}} = 0.67$. This value gives a packing dimension L_y that is similar to that of the rigid walls system in Fig. 2.6.

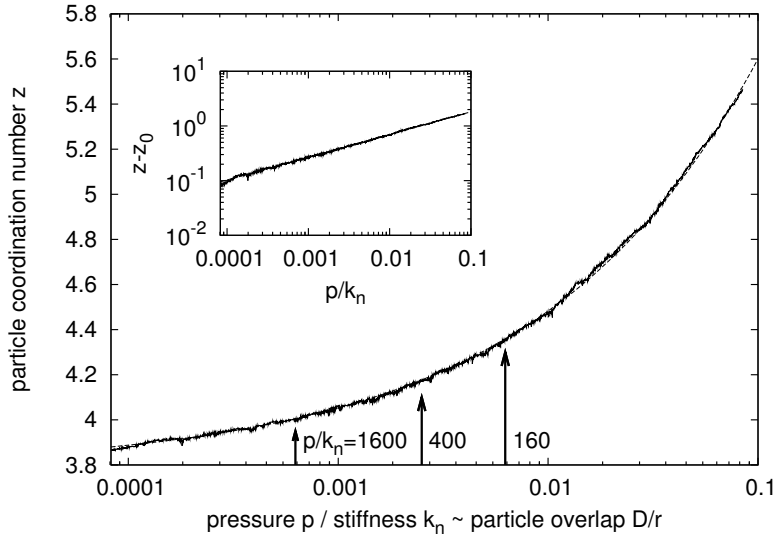

Figure 2.7: Particle coordination number z as a function of the external pressure p (average over 20 systems with 100 particles) in a lin-log plot. The inset shows the graph in a log-log plot. In both plots the power law, which is fitted to the curve, is also displayed. In the inset, the value $z_0 = 3.785$ in the label of the y-axis is the coordination number obtained when one extrapolates the fit to zero pressure ($p = 0$). During the simulations, the friction coefficients in Eqs. 2.1, 2.3 are zero, preventing possible friction dependencies of z. The three arrows in the figure correspond, from left to right, to the particle stiffnesses $k_n = 1600, 400, 160$ at pressure $p = 1$. This pressure is applied during the preparation of all systems in this thesis.

2.12 Investigation of the quasi-rigid limit with simulations

In the derivation of the stiffness matrix from the equations of motion in Sec. 2.8.2, the quasi-rigid limit has been defined as the limit where the average particle overlap D is much smaller than the average particle radius r: $D \ll r$. Here, the quasi-rigid limit is related to a certain number of particle contacts. Central to this idea is the observation that the number of contacts depends on the deformation of the particles. The deformation in turn depends on the particle stiffness. When the particles are soft, the overlaps at the contact points of the particles are large, thus the voids between particles are small. When voids disappear, additional contacts are created. Thus the number of contacts increases. When, on the other hand, the stiffness of the particles is infinite, the number of contacts attains a minimum. This minimum puts a lower bound on the number of contacts in stable systems. Without friction ($\mu = 0$), and in two dimensions, the number of contacts of a particle, called coordination number, is four [38, 52]. Now, when the particles have a finite stiffness, the number of contacts is larger. In this context, the quasi-rigid assumption says that the number of additionally created contacts is small. Thus, relative to hard particles, the excess number is a vanishing additional fraction of all contacts.

The deformations of the particles depend on the one hand on the stiffness of the particles, but on the other hand they also depend on the pressure exerted on the system. To be precise, the ratio between pressure and particle stiffness governs the particle deformations. The average deformation

is[4]

$$\text{particle deformation } D \approx \frac{\text{pressure } p \cdot \text{particle radius } r}{\text{particle stiffness normal to surface } k_n}. \tag{2.72}$$

Now the question is: how does the number of contacts depend on the deformation? Fig. 2.7 shows this dependence. The curve shows the average of 20 systems with 100 particles. Rigid wall boundaries are applied, and the friction coefficient μ is zero. The samples are prepared with the preparation procedure described in Sec. 2.10. The curve in the figure is produced by setting the particle stiffness to a constant value while slowly increasing the pressure at the boundaries at constant rate.

We first investigate the minimum number of contacts at the left side of Fig. 2.7. In the literature, one finds that when $D/r \ll 1$ in Eq. 2.72, the contact network is *isostatic*, i.e. the coordination number z is four [4, 21, 23]. This result for quasi-static particles matches observations in hard disk models [52], where the stiffness is infinite. In Fig. 2.7 the coordination number z is below four for low pressure values. One explanation for this observation is the large effect of the boundaries in the small systems with 100 particles. At the walls, voids smaller than a particle diameter form, therefore the particles in proximity have fewer neighbors. The effect of the boundaries could be tested by applying periodic boundary conditions, or by comparing the results with larger systems. This is not done here, because we are just interested in additionally created contacts due to finite stiffness and nonzero pressure.

In [38] a power law dependence is experimentally observed for low pressure. When we do a log-log plot of the data, shown in the inset of Fig. 2.7, the power law is confirmed. When we fit the values with the function

$$z = z_0 + A\left(\frac{p}{k_n}\right)^B, \tag{2.73}$$

the curve can be well reproduced. We obtain the exponent $B = 0.4156 \pm 0.0007$ and the prefactor $A = 4.7272 \pm 0.0268$. The best fit is obtained when the number of contacts at zero pressure is adjusted to $z_0 = 3.785$.

For $p/k_n \leq 10^{-3}$, the relative number of excess contacts in Fig. 2.7 is below 10%. In the samples investigated in this thesis, the initial pressure to stiffness ratio p/k_n is chosen in this region: in a system with $N = 16384$ particles, it is $p/k_n = 5 \times 10^{-4}$ at the beginning of the loading procedure, described in Sec. 2.11, and it increases to $p/k_n = 8 \times 10^{-4}$ at failure. The failure is characterized by a sudden macroscopic deformation. The increase in p/k_n leads to an increase in the average particle overlap by 77%. The stiffness $k_n = 1600$ is constant.

The number of contacts during the loading evolves differently than expected from the increasing overlaps. Since friction is turned on at the beginning of the loading process ($\mu \neq 0$), the average coordination number *decreases*. In a system with $N = 16384$ particles, the initial coordination number is $z = 4.004$ (prepared without friction), and it decreases to $z = 3.372$ at failure. The underlying reason is that the isostatic limit for *frictionless* systems is $z = 4$, while it is $z = 3$ for *frictional* systems. The evolution of the contact number is discussed in more detail in Sec. 4.1.

Note that the amount of contacts is very important for the stability of the system. This has various reasons. For instance, the number of contacts affects macroscopic quantities such as bulk and shear

[4]Note that it is assumed there are only normal forces ($\mu = 0$) excerted at the particle contacts. For $\mu \neq 0$, tangential forces arise at the contacts. In that case there are two independent stiffnesses k_n, k_t at one contact, one in normal and one in tangent direction. Then the normal stiffness might be not a good parameter any more. Thus it should be replaced by some average stiffness depending on k_n and k_t. This could be the system's stiffness, $\frac{\mathbf{vkv}}{\mathbf{vv}}$, where $\mathbf{k}$ is the stiffness matrix and $\mathbf{v}$ is a vector containing the particle velocities.

modulus [53]. As we have seen, the number of contacts is governed by the pressure, which affects both geometric and mechanical properties of granular packings [54].

2.13 Conclusion

This chapter contains the theoretical material necessary to understand the simulation results in the following chapters. The chapter contains three parts. The first part explains the macroscopic model (Secs. 2.1 – 2.5). The second part concerns the analytical solution of that model (Secs. 2.6 – 2.8). Finally the simulation procedure for solving the model numerically is explained in the third part (Secs. 2.9 – 2.11).

The model of the system has four parts: a model of the particles, a model for the particle interactions, a set of boundary conditions of the system, and a specific set of parameters. This defines the model system which is investigated in detail in the next chapters.

The model can be investigated analytically. One can inspect the number of grains without any contacts (rattlers), and one can define a global hyperstatic number $\mathcal{H}$ which tries to identify failure with a specific value of $\mathcal{H}$. A deeper understanding of weakening and failure provides the stiffness matrix description. In quasi-static simulations of stiff particle systems, it relates the change in external forces to the occurring particle velocities.

Another possibility of solving the model is conducting numerical simulations. In this thesis the *molecular dynamics method* is used for integrating the equations of motion. In the sample preparation, a granular gas is compressed to form a solid. This solid is called *granular packing*. The packing is then submitted to an uniaxially increasing external force, while the forces on the other sides are constant. Since the particles are quasi-rigid, the number of particle contacts is close to the minimum value required for stability.

Failure of a granular system is identified with a change in the system dimensions. This change appears at a certain value of the increasing external force. The failure is inspected numerically in small systems in Chap. 3.

Chapter 3

What triggers failure in small granular assemblies?

3.1 Introduction

This chapter constitutes the first step towards understanding the failure of granular assemblies. The investigation herein considers packings of 16 particles in two dimensions. The reader might think that 16 particles is quite a small system to investigate. This is of course true. But small systems have a very limited complexity, and it is easy to relate the system's failure to a single change of a contact. Therefore one can investigate which kind of contact changes can lead to failure, and if there is always such a change that triggers the failure. The trigger of failure are investigated in this chapter.

Before proceeding with the subject matter, this section presents the most important parameters and indicates some important points. The setup and the load procedure are as described in Secs. 2.10, 2.11, and the systems limits are rigid wall boundaries (see Sec. 2.3 for details). During the simulations, the external force on top and bottom wall is increased at rate $\alpha = 1.28 \times 10^{-3} \hat{f}/\hat{t}$. Because the systems are very small, every system fails at a different external force f_{ext}. To match the point of failure of the different realizations, the interval between simulation beginning and the failure is rescaled so that the resulting scale is universal for all systems. In practice, this is done by rescaling the axis of force or, equivalently, time. Naming the time when the trigger of failure appears t_{trigger}, the rescaled time is

$$\tau(t) = (t - t_{\mathrm{trigger}})/t_{\mathrm{trigger}}. \tag{3.1}$$

On the rescaled axis, $\tau = -1$ corresponds to the simulation beginning at $t = 0$, and $\tau = 0$ marks the failure at t_{trigger}. These τ-values are the same for all systems. In that way, curves obtained for different systems can be compared, and ensemble averages of a given number of systems can be calculated for specific values of τ. When t approaches t_{trigger}, the time scale on which property changes occur is much finer. Then again the smaller simulation time units of $t - t_{\mathrm{trigger}}$ will appear in the figures instead of τ. Both time scales are centered around the time t_{trigger} where the trigger mechanism occurs. Its average is $t_{\mathrm{trigger}} = 734 \pm 436\hat{t}$. The time axis might be replaced by the axis of external force, because the force increases linearly with time. Due to the high stiffness of the particles, which is $k_n = 1600$, the deformations of the particles are always small. Thus the dimensions of the system do change by less than 1% until the failure. Therefore the stress, which is force per unit of length, changes in the same way as the external force on the walls. Thus one might replace time by

stress. The deviator stress, defined in Eq. 1.1 and explained in the introduction, is

$$\sigma_d = \frac{f(t)}{L_x} - \frac{f_0}{L_y}. \tag{3.2}$$

Here, f_0 and $f(t)$ are the horizontal and vertical external forces on the boundaries and L_x, L_y are the horizontal and vertical dimensions of the system. Unlike τ, the maximum deviator stress, occurring at the trigger, varies from one system to another one. Its average for the 16 particles systems is $\sigma_d = 1.20 \pm 0.83$. The large variance indicates that the trigger of failure appears at quite different levels of stress.

The heart of this chapter are the solutions to the equations of motion, which have been given in Eq. 2.42 in Sec. 2.8.2. However, the considerations in this chapter are limited to the quasi-static and quasi-rigid approximation of these equations. In this approximation the stiffness matrix $\mathbf{k}$ plays the central role. This matrix, first introduced in Sec. 2.8.1, is the subject of many details of failure which are discussed in several sections within this chapter.

The structure of the chapter is as follows. First, Sec. 3.2 is concerned with principal quantities of a granular packing describing its state on the way to failure. The section contains a subsection on the evolution of the number of sliding contacts, and another subsection dealing with the stiffness of the system, determined from both the macroscopic system dimensions and the microscopic values of the motions and forces of the particles. The Section thereafter (Sec. 3.3) examines one example of a modification of the system's stiffness in detail. This modification is associated with the change of a contact. The section can be considered an introduction to the following sections, which feature the trigger mechanisms of failure, appearing in the 16 particle systems. After the discussion of the three different triggers of failure in Sec. 3.4, Sec. 3.5 shows that even in 16 particle systems there can be more than one contact change involved in the failure. Of course, due to the limited size of a system, the trigger data have to be evaluated on a statistical basis. For the statistical analysis, 26 systems with $N = 16$ particles are investigated in detail in Sec. 3.6. Another important point is the generalization of the small system results to larger systems. Thus one has to compare data from different system sizes. In Sec. 3.7 assemblies with up to 100 particles are considered, showing that the relative occurrence of the trigger of the failure depends on system size. The comparison of different system sizes helps us to understand how the results on small packings translate to even larger systems.

When failure happens, the kinetic energy rises very quickly. One important question is the source of this energy. Is it the external forcing? Or is the potential energy stored in the particle contacts converted to kinetic energy of the particles? This question is investigated in Sec. 3.9. Section 3.9.2 considers the dependence of the rise in kinetic energy on the parameters density and particle stiffness. Section 3.11 considers the possibility of a succession of failure events in granular systems, and underlines that this possibility is also considered in the literature. Section 3.12 summarizes the results and illustrates how the conjectures about larger systems are substantiated in the following chapters. Most of this chapter's material is published in [55]. The investigation of the failure of small systems starts in the next section by considering the softening with increasing external force.

3.2 Leading up to failure

In this section, we determine principal quantities of the granular packing. These quantities describe the state of the system on the way to the macroscopic deformations at the failure. One important

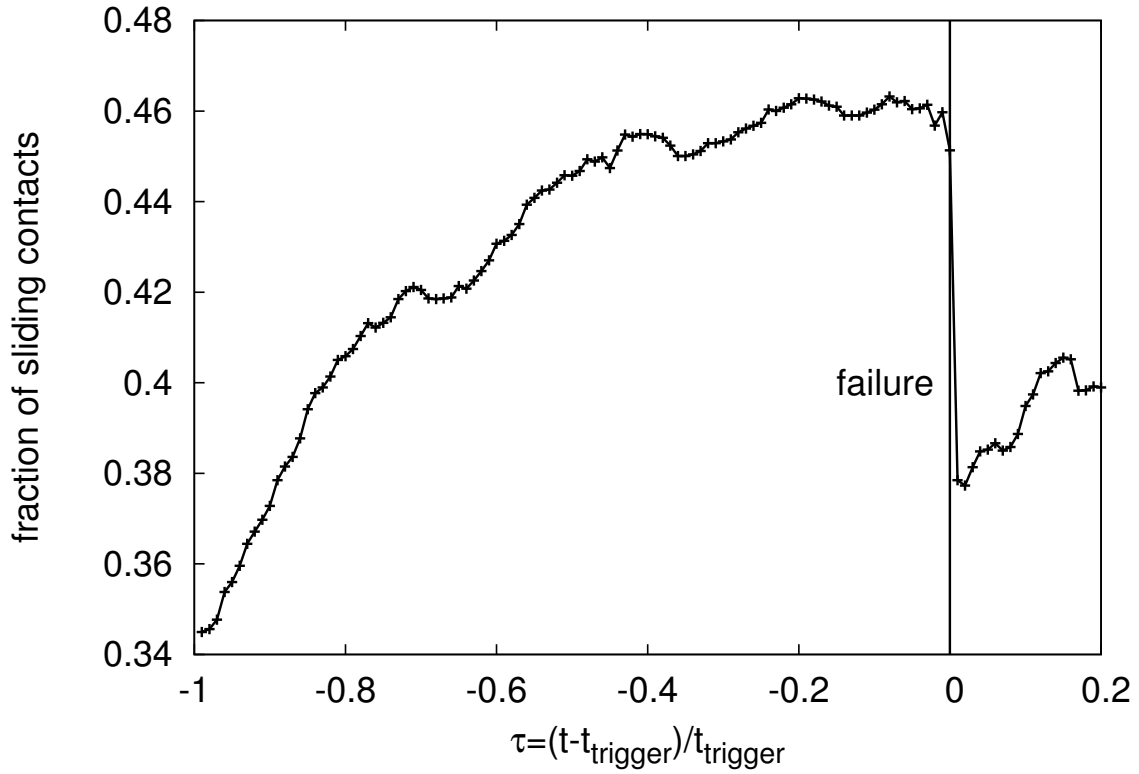

Figure 3.1: Fraction of sliding contacts, averaged over 26 different seeds. The fraction increases until the time when the assembly fails. During the deformation process, the fraction drops abruptly, and the intergranular contacts stop sliding when the assembly attains a new stable state. The remaining fraction are the contacts with the smooth walls.

quantity is the number of sliding contacts. Another quantity is the stiffness of the packing, which decreases with increasing external force $f_y = f(t)$.

3.2.1 Sliding contacts

When one linearly increases the force $f(t)$ on the packing, the number of sliding contacts rises [44, 56], as shown in Fig. 3.1. The number of sliding contacts increases linearly for $\tau < -0.8$, but then this increase slows. From $\tau > -0.1$ until the time of failure, the number of sliding contacts is approximately constant.

When the granular assembly fails, many contact rearrangements occur, leading to fluctuations in the number of sliding contacts that are not resolved in the above figure. After failure, all grain-grain contacts will become nonsliding again, and only the contacts with the smooth walls contribute to the value in Fig. 3.1. When the external force is increased further, the number of sliding contacts rises again.

3.2.2 Measuring the softening on the macroscopic and the microscopic scale

In Sec. 2.8 a matrix was introduced which allows for the calculation of the systems' stiffness from the knowledge of the microscopic structure. It takes into account the positions of all particles and the location of the contacts between them. In the same section, a criterion for the stability of a system, based on the analysis of this matrix, was explained. Here we evaluate this concept by comparing the microscopic stiffness, based on the stiffness matrix approach, with a stiffness expression derived from macroscopic quantities. Before presenting the results, the expressions for microscopic and macroscopic stiffness are given.

On the macroscopic scale the stiffness can be measured from the response of the walls to the force increment. When one increases the forces, the deviatoric stress also increases at the rate

$$\dot{\sigma}_D = \frac{\alpha}{L_x}\,. \tag{3.3}$$

α is the rate at which the external forces are increased according to Eq. 2.71. The deviatoric strain is

$$\epsilon_D = \frac{\Delta L_y}{L_y} - \frac{\Delta L_x}{L_x}\,. \tag{3.4}$$

One measure of the stiffness is thus

$$k_{\mathrm{macro}} = \frac{\dot{\sigma}_D}{\dot{\epsilon}_D}\,. \tag{3.5}$$

On the other hand, one can estimate the stiffness on the microscopic scale:

$$k_{\mathrm{micro}} = \frac{|\dot{\mathbf{f}}_{\mathrm{ext}}|}{|\mathbf{v}|}. \tag{3.6}$$

The numerator contains the derivative of the external force vector, and the denominator contains the vector of particle velocities. Only the norm of the vectors enter in the equation. That microscopic and macroscopic stiffness yield the same results is not obvious, because microscopic motions do not necessarily imply macroscopic changes. In the literature, several articles on the relation of microscopic to macroscopic variables exist, trying to establish a one-to-one correspondence [57–59]. An expression for k_{micro}, based on the stiffness matrix, can be established by first defining the normalized vectors $\mathbf{n}_{\dot{f}_{\mathrm{ext}}} = \dot{\mathbf{f}}_{\mathrm{ext}}/|\dot{\mathbf{f}}_{\mathrm{ext}}|$, and $\mathbf{n}_v = \mathbf{v}/|\mathbf{v}|$, and then multiplying Eq. 2.43 from the left by $\mathbf{v}/\mathbf{vv}$. Note that $\mathbf{vv}$ is scalar. One thus obtains

$$k_{\mathrm{micro}} = \mathbf{n}_{\dot{f}_{\mathrm{ext}}}\mathbf{k}\mathbf{n}_v \approx \left(\frac{\mathbf{vkv}}{\mathbf{vv}}\right)\frac{1}{\mathbf{n}_{\dot{f}_{\mathrm{ext}}}\mathbf{n}_v}. \tag{3.7}$$

The quadratic form $\mathbf{vkv}$ that appears in the microscopic stiffness is the essential term in the stability criteria presented in Sec. 2.8.3, and a negative or vanishing stiffness leads to failure. The mean value of $\mathbf{n}_{\dot{f}_{\mathrm{ext}}}\mathbf{n}_v$ in the 16 particles packings investigated in this chapter is 0.09, showing that the part of $\mathbf{v}$ parallel to $\dot{\mathbf{f}}_{\mathrm{ext}}$ is small. Note that Eq. 3.6 and Eq. 3.7 are furthermore not identical because Eq. 3.7 assumes the validity of $\dot{\mathbf{f}}_{\mathrm{ext}} = \mathbf{kv}$ (Eq. 2.43), whereas Eq. 3.6 does not.

Fig. 3.2 shows stiffness values calculated from different definitions. They exhibit the same qualitative time dependence: When we approach the onset of failure, the granular assembly will get much softer and attain its minimum value around $\tau = 0$. As we will see in the next section, the stiffness drops sharply at the time of failure, but the time scale in Fig. 3.2 is too coarse to reveal this. After the failure, stability is soon fully recovered.

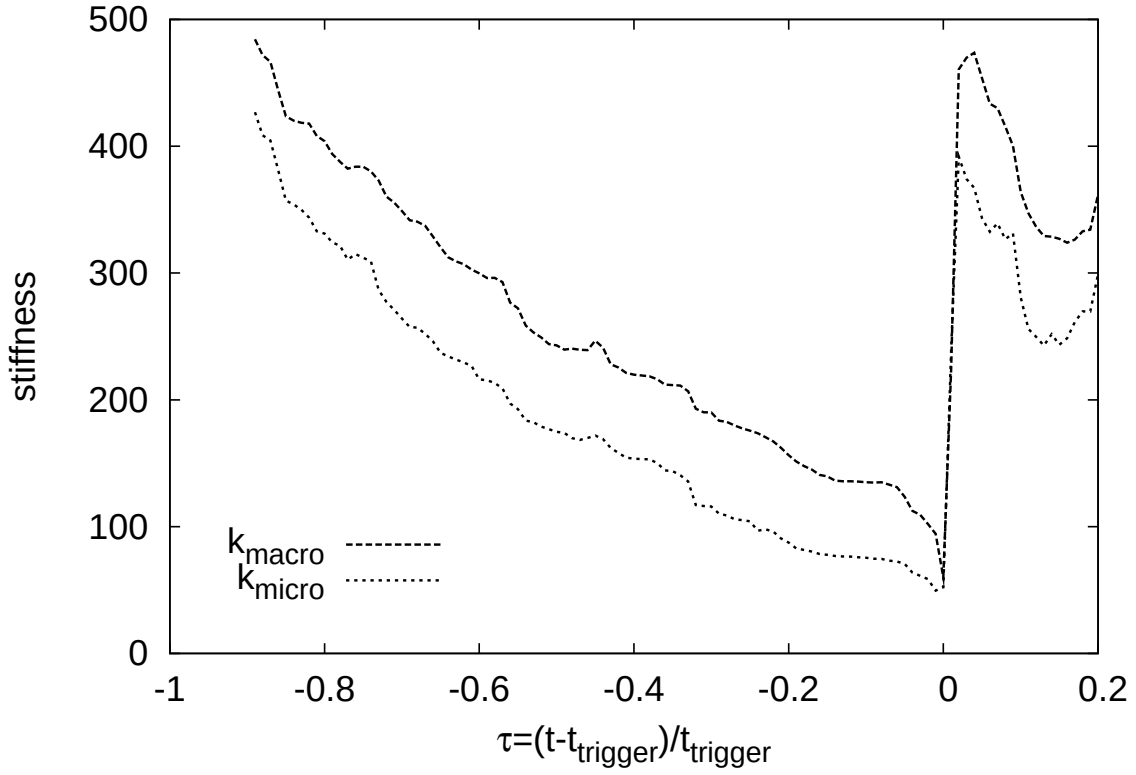

Figure 3.2: Comparison of the macroscopic and microscopic stiffnesses. The macroscopic stiffness is calculated from the response of the confining walls, according to Eq. 3.5. The microscopic stiffness is calculated using $\dot{\mathbf{f}}_{\text{ext}}$ and $\mathbf{v}$ according to Eq. 3.6.

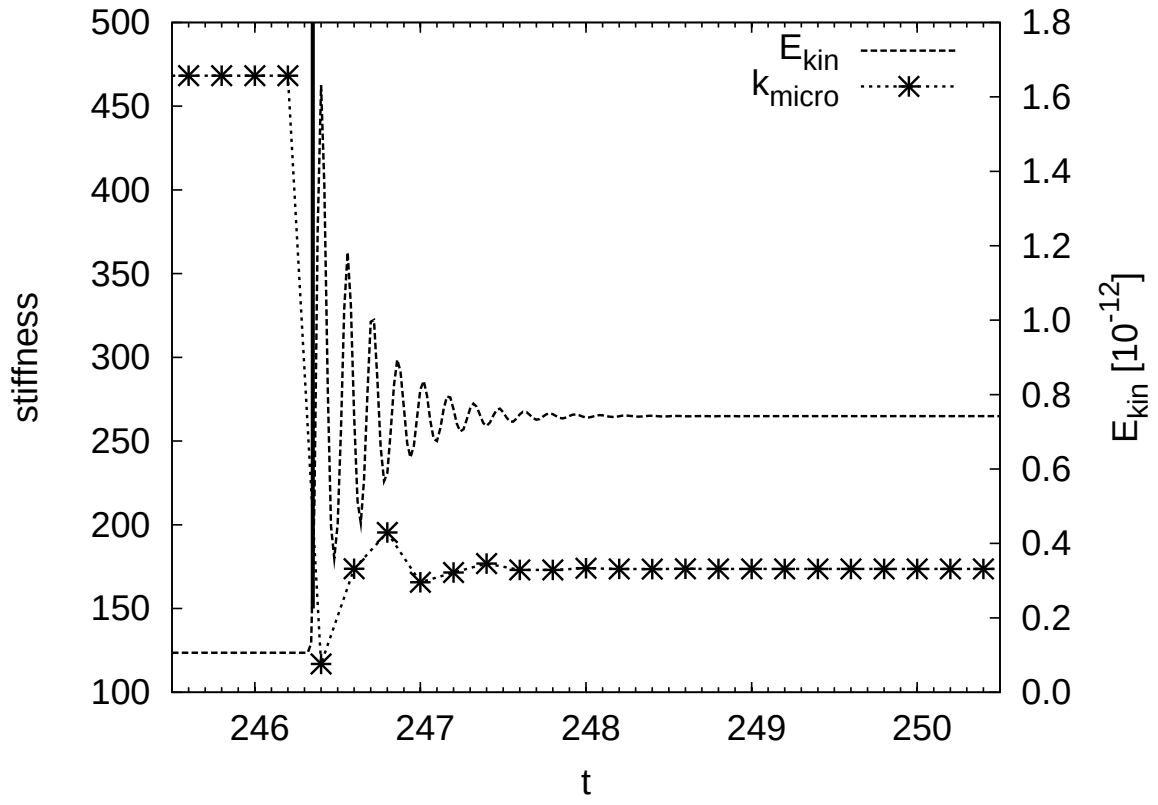

Figure 3.3: A close view of a status change. At $t \approx 246.35$, a contact becomes sliding. This means that a stiffness transition takes place. When this happens, the stiffness of the system k_{micro} and the total kinetic energy E_{kin} make a step like change. Due to particle inertia, the stiffness transition is accompanied by damped oscillations in E_{kin}.

3.3 Example of a stiffness transition

Fig. 3.2 is an average over 26 simulations, and should not lull one into thinking that the stiffness decreases smoothly and continuously in the individual simulations. In fact, the stiffness increases and decreases stepwise, and the steps in the stiffness correspond to contact status changes. Obviously the structure of the contact network is related to a specific value of the system's stiffness. So when one contact changes its status, e.g. it disappears, then the stiffness suddenly changes by a certain amount.

There are six different contact status changes possible between three different contact states. The first contact status is *closed*. This is the initial state of all contacts. One could also call it nonsliding state, in contrast to the *sliding* status, which is defined by $|F_t| = \mu F_n$ in Eq. 2.6. The third state appears when a contact is lost. All lost contacts are marked *open*, which is the third status possible. If $\mu = 0$, all contacts would be sliding, and transitions can occur only between the states sliding and open. Friction ($\mu \neq 0$) makes possible four additional contact transitions, two from closed to sliding and open, and two vice versa.

The steps in the system's stiffness correspond to contact status changes. Figure 3.3 shows one such event, where a contact becomes sliding at $t \approx 246.35\hat{t}$. Both before and after this event, the stiffness and the kinetic energy are constant, and the status change causes the stiffness to drop to

a new level, while the kinetic energy rises. If the system were perfectly quasi-static, the transition would be instantaneous and without oscillation. To understand these oscillations in detail, let us use the stiffness matrix theory. When the contact becomes sliding, there is an abrupt change in certain elements of the stiffness matrix, i.e., one has $\mathbf{k} = \mathbf{k}_1$ for $t < 246.35\hat{t}$, and $\mathbf{k} = \mathbf{k}_2$ for $t > 246.35\hat{t}$. Applying Eq. 2.43 gives $\dot{\mathbf{f}}_{\text{ext}} = \mathbf{k}_1\mathbf{v}_1 = \mathbf{k}_2\mathbf{v}_2$, for $\dot{\mathbf{f}}_{\text{ext}}$ is constant. At $t = 246.35\hat{t}$, therefore, Eq. 2.43 predicts an instantaneous change in the velocities. But the particles have a finite inertia and cannot change their velocities instantaneously. The status change in Fig. 3.3 is thus accompanied by a disturbance that is damped out after roughly 10 oscillations or $1.5\hat{t}$. The disturbance is accounted for by the inertia term $\mathbf{m}\ddot{\mathbf{v}}$ and the damping term $\mathbf{c}\boldsymbol{\Gamma}\mathbf{c}^T\dot{\mathbf{v}}$ in Eq. 2.42. If these terms are included, the equation of motion thus becomes

$$\mathbf{m}\ddot{\mathbf{v}} = \dot{\mathbf{f}}_{\text{ext}} - \mathbf{c}\boldsymbol{\Gamma}\mathbf{c}^T\dot{\mathbf{v}} - \mathbf{k}\mathbf{v}, \tag{3.8}$$

which is a vectorized version of a damped harmonic oscillator. This explains the damped oscillations present in Fig. 3.3.

The detailed discussion of an example of a stiffness transition in this section shows that vibrations are always involved in such transitions. Vibrations at stiffness transitions will become important again in Sec.3.4.4. We will now turn our attention to the appearance of failure.

3.4 The three triggers of failure

Before the grains velocities start to rise at the failure, there is always a contact status change that leads to a change of the stiffness matrix $\mathbf{k}$. This change provokes the collapse of the assembly. Three different trigger mechanisms can occur: First, a contact status change can lead to a *negative stiffness* of the contact network, i.e. $\mathbf{vkv} < 0$. Second, a null-mode can cause the violation of Eq. 2.43 due to the loss of mechanical stability. Finally, there is a third possibility: the packing can become unstable as it makes a transition between two stable states. The first two possibilities have been investigated analytically in Ref. [60], but the third possibility was not foreseen there. We investigate the three triggers of failure numerically in the following subsections.

3.4.1 Mechanical instability ($\mathbf{vkv} < 0$)

When the quadratic form $\mathbf{vkv}$, introduced in Sec. 2.8.3, becomes negative, the assembly becomes unstable for the reasons discussed in Sec. 2.8.3. Figure 3.4 shows the data from one simulation where this happens. There is a contact status change at $t = t_{\text{trigger}}$, which provokes a drop in $\mathbf{vkv}$. But, as can be seen in the figure, it takes a finite time for $\mathbf{vkv}$ to become negative and for the kinetic energy to start to rise exponentially.

One can show that the drop in $\mathbf{vkv}$ is caused by the contact status change by calculating $\mathbf{v}_{\text{th}}\mathbf{k}\mathbf{v}_{\text{th}}$, where $\mathbf{v}_{\text{th}}$ is a theoretical value which corresponds to the stiffness after the contact status change. It is calculated from $\dot{\mathbf{f}}_{\text{ext}}$ by constructing a pseudo-inverse of matrix $\mathbf{k}$ (details are given in Sec. 2.8.5). This quantity reveals the correspondence of contact status change and velocity adjustment, because it instantaneously changes (see Sec. 2.8.5). On the other hand $\mathbf{vkv}$ is calculated using the velocities $\mathbf{v}$ from the simulation. The particle masses $\mathbf{m}$ in Eq. 2.42 define the timescale needed for $\mathbf{v}$ to change. Also, $\mathbf{v}$ oscillates before failure, indicating the presence of vibrations. In any case, however, it is clear that the contact status change provokes an instability in the packing, causing it to fail.

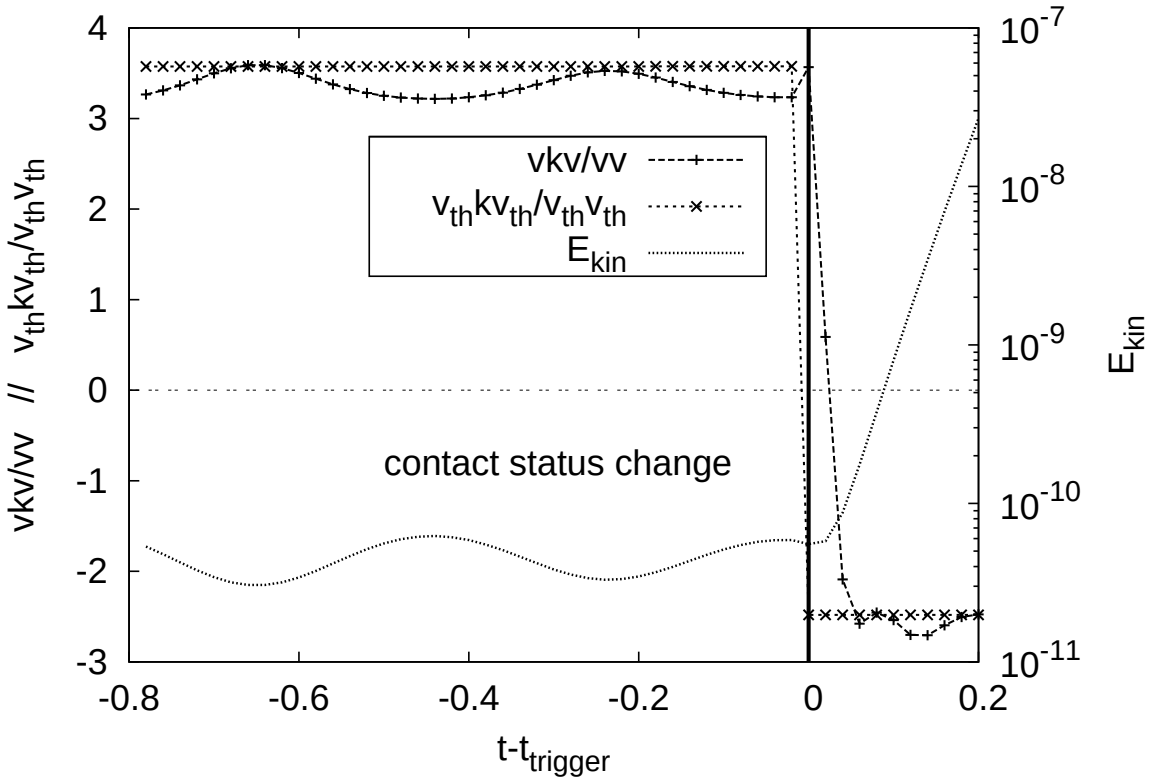

Figure 3.4: Mechanical instability at the origin of failure: When the contact status change occurs, the stiffness, represented by $\mathbf{vkv}/\mathbf{vv}$, decreases rapidly and finally attains negative values. The purely structure dependent quantity $\mathbf{v_{th}kv_{th}}$ changes instantaneously and hence shows the effect of the contact status change at the vertical line, whereas the simulation velocities $\mathbf{v}$ change on a time scale related to the particle inertia.

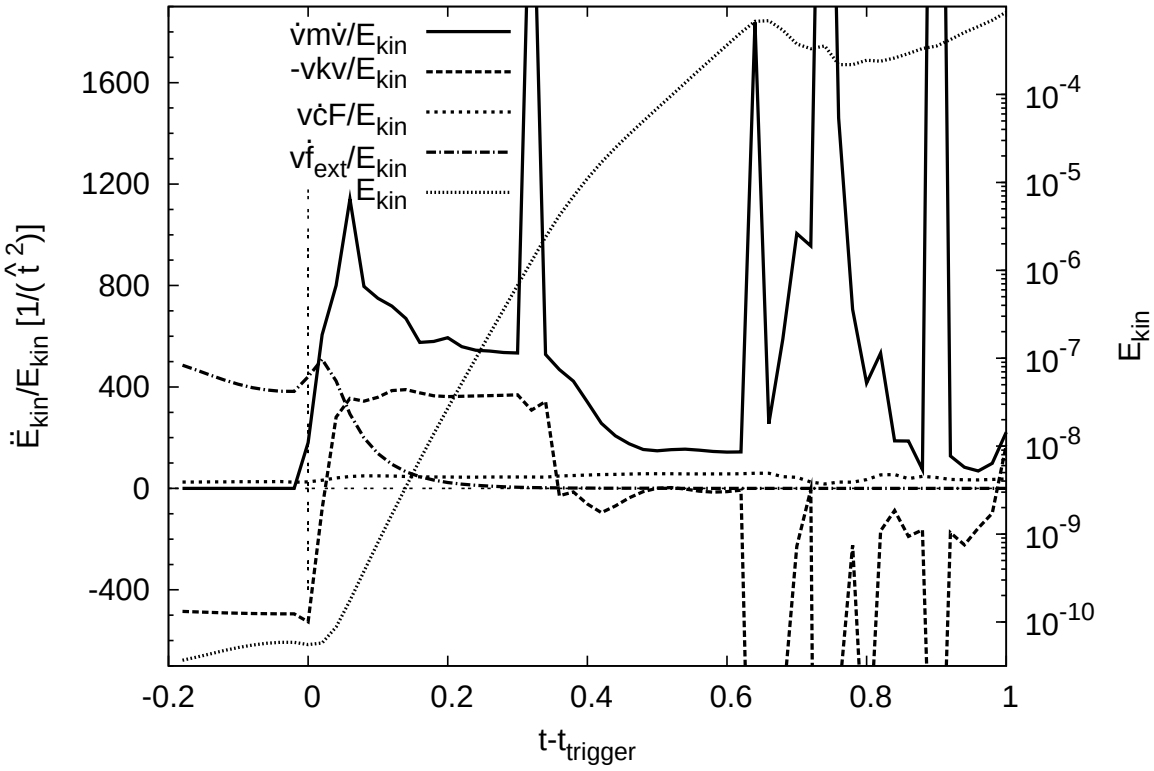

Figure 3.5: Contributions to $\ddot{E}_{\rm kin}$, and $E_{\rm kin}$, for the simulation shown in Fig. 3.4, where an instability triggers failure. The contributions to $\ddot{E}_{\rm kin}$ are plotted on a linear scale, indicated on the left, while $E_{\rm kin}$ is plotted on a logarithmic scale shown on the right. $\dot{\mathbf{v}}\mathbf{m}\dot{\mathbf{v}}$ is the contribution from the force imbalance. The force imbalance term is a measure for the difference between current configuration and static equilibrium. Assuming the equilibrium at the given configuration is close, the force imbalance term is small. Once instability appears, it increases quickly, because the equilibrium forces are very different from the current ones, and the particle velocities increase quickly due to the imbalance.

To understand more fully the mechanism of failure, let us examine the various contributions to the second derivative of the kinetic energy, which have been explained in Sec. 2.8.6. Fig. 3.5 shows these contributions. Before failure occurs, there is an equilibrium between three terms. The energy injected by the external forcing ($\mathbf{v}\dot{\mathbf{f}}_{\mathrm{ext}}$) and the geometric stiffness ($\mathbf{v}\dot{\mathbf{c}}\mathbf{F}$) contribute to the kinetic energy. This energy is removed by the mechanical stiffness ($\mathbf{vkv}$).

At $t = t_{\mathrm{trigger}}$, a contact status change occurs, and $\mathbf{vkv}$ begins to decrease toward 0. It can no longer absorb the energy injected by the other two terms, and the kinetic energy starts to rise. A short time later, the force imbalance ($\dot{\mathbf{v}}\mathbf{m}\dot{\mathbf{v}}$) rises, and becomes the dominant contribution to the kinetic energy throughout the rest of the failure. At $t = t_{\mathrm{trigger}} + 0.7$, the kinetic energy reaches a maximum, more than four orders of magnitude above its initial value. The system then starts to search for a new equilibrium configuration.

3.4.2 The null-mode trigger

The second failure mechanism that can occur is the disappearance of mechanical rigidity. This means that a motion $\mathbf{v}_0$ appears to which the packing opposes no resistance. This occurs when the dimension of the kernel of $\mathbf{k}$ increases due to a contact status change, and $\mathbf{v}_0$ is the dimension that has been added to the kernel. If $\mathbf{v}_0$ is compatible with the boundary conditions, then its amplitude will grow rapidly

Fig. 3.6 shows the data from a simulation where failure is triggered by the appearance of a null mode. At $t = t_{\mathrm{trigger}}$, there is a contact status change that causes the kernel of $\mathbf{k}$ to increase by one dimension. This was determined by constructing $\mathbf{k}$ both for and after the contact status change, and then carrying out a singular value decomposition. The result confirmed that the number of zero singular values increases by one. Note that the behavior of $\mathbf{vkv}$ is similar to Fig 3.4: it drops sharply at $t = t_{\mathrm{trigger}}$. On the other hand, $\mathbf{v}_{\mathrm{th}}\mathbf{k}\mathbf{v}_{\mathrm{th}}$ behaves quite differently, because these two quantities diverge at $t = t_{\mathrm{trigger}}$. The reason for this will be discussed below.

Figure 3.7 displays the new null mode that appears at the contact status change. The null mode is associated with the additional zero singular value at the contact change. As one can see, it corresponds to a crushing of the granular assembly between the upper and lower walls, which is exactly the kind of motion expected at failure. In the figure, the top row is moving to the right, and the second row to the left, meaning that the top row will slip down into valleys formed by the 2nd row, so that the packing will go roughly from square to triangular. The sliding contacts are marked by gray or black circles, with the black circle indicating the contact that becomes sliding when the null mode appears.

Further evidence of the null-mode failure is shown in Fig. 3.8, where the fraction of the velocity attributed to the null-mode is plotted. It rises rapidly at the contact status change, and quickly dominates the motion. This figure also explains the divergence of $\mathbf{vkv}$ and $\mathbf{v}_{\mathrm{th}}\mathbf{k}\mathbf{v}_{\mathrm{th}}$ in Fig. 3.7. After failure, we have $\mathbf{v} \approx \mathbf{v}_0$, so that $\mathbf{kv} \approx 0$. On the other hand, $\mathbf{v}_{\mathrm{th}}$ is orthogonal to $\mathbf{v}_0$ by construction. Thus calculating $\mathbf{v}_{\mathrm{th}}$ misses failure completely. This should be kept in mind whenever the stiffness matrix is used to calculate the motion of the packing.

Another subtlety is that the presence of a null mode is not sufficient to cause failure. Fig. 3.9 shows an example of a null-mode that does not cause failure. It is a global rotation mechanism, in which the assembly consists of loops comprising four grains. In these loops, the grains in contact rotate opposite to each other, and the absolute value of angular rotation times the grains radius is a constant for all the grains. No friction opposes this movement, and hence the energy stored in the rotation remains unchanged until it will be converted back to potential energy at the time when this null-mode disappears due to an opening or closing contact.

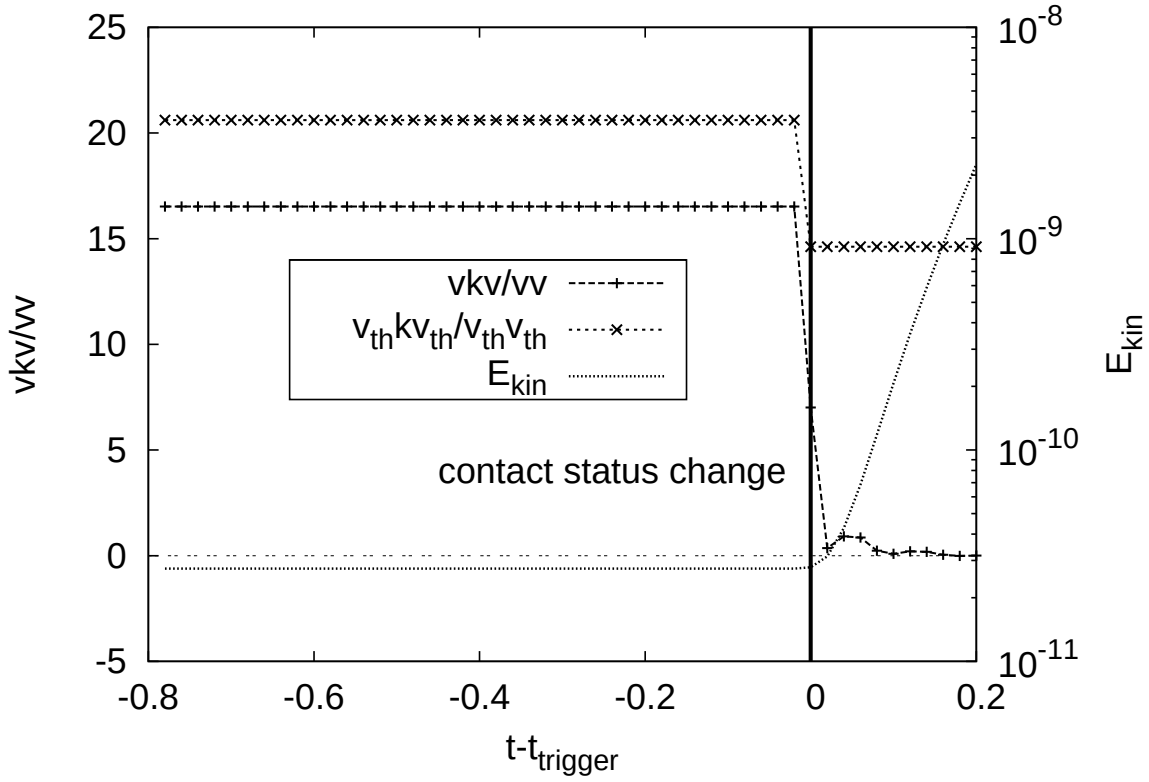

Figure 3.6: Stiffness of the granular assembly ($\mathbf{vkv}/\mathbf{vv}$) at failure, caused by the appearance of a null-mode. The thick vertical line at $t = t_{\mathrm{trigger}}$ shows the time when the null-mode appears due to a contact status change.

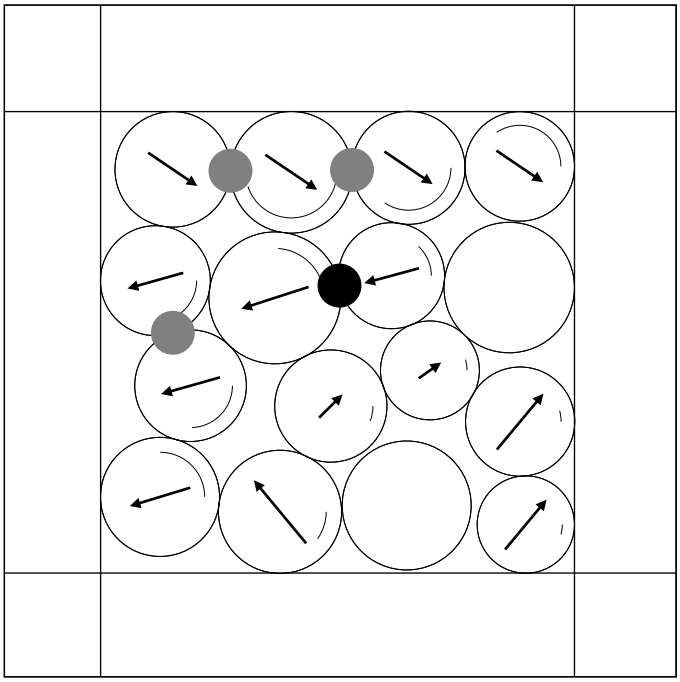

Figure 3.7: The particle motions associated with the null-mode. These motions trigger failure in Fig. 3.6. Velocities are indicated by arrows and angular velocities are represented by a circle segment starting at 3 o'clock inside the corresponding grain. Grains for which no velocity is shown are rattlers. When the null-mode occurs, the contact marked by the black circle starts to slide. The other sliding contacts are indicated by grey circles.

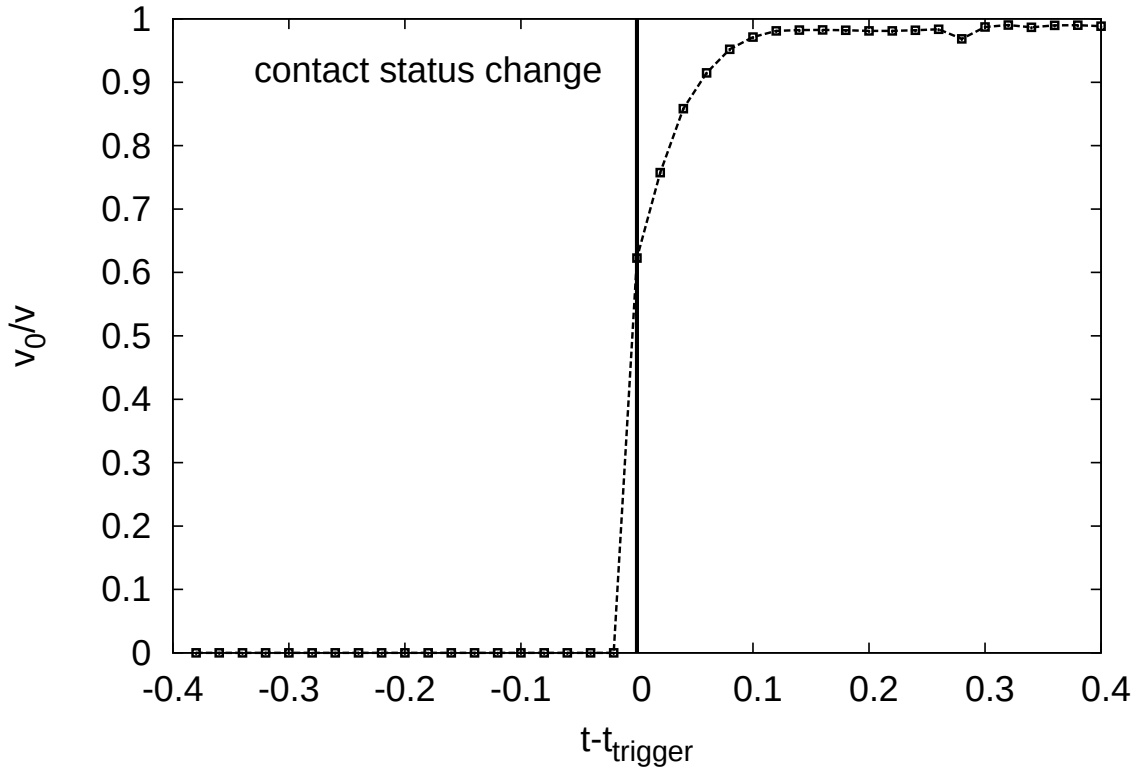

Figure 3.8: Fraction of the particle velocity $\mathbf{v}$ associated with the null-mode $\mathbf{v}_0$ at failure for the simulation shown in Fig. 3.6. Shortly after the contact status changes, the velocity vector points in the direction of the null-mode movement, i.e. $\mathbf{vv_0}/|\mathbf{v}||\mathbf{v}_0| \approx 1$.

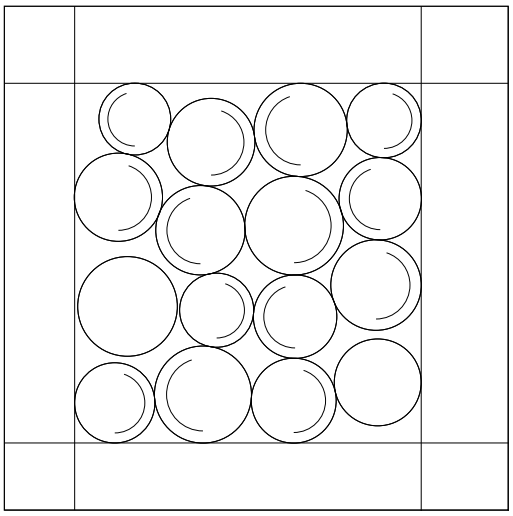

Figure 3.9: Rotation mode with zero stiffness that does not lead to the failure of the system: whenever four grains form a square and touch each other, they rotate at the same speed but in opposite directions at their points of contact (The rotations are indicated by the segment of a circle inside each grain; The segments start at the rightmost position and point in the direction of rotation. Their lengths indicate the speed). Grains without indicated rotation are rattlers.

Another issue is the increase in kinetic energy after failure. As shown in Fig. 3.10, the kinetic energy rises exponentially, but it is not clear why this should happen. If one assumes that the null-mode is independent of the other motions, the kinetic energy should rise with the fourth power of time [60]. For certain examples of null mode failure, it is possible to fit the beginning of the curves of kinetic energy to polynomials of the form $At^4 + Bt^2 + C$. The coefficients obey the scaling predicted below in Sec. 3.4.3. However, the kinetic energy then soon rises exponentially. The reason for this can be seen in Fig. 3.10: the force imbalance becomes large. Why this would happen is puzzling at first sight, because the null mode should not change the forces by definition. However, all these considerations neglect the geometric stiffness, which is always destabilizing. Hence, $\ddot{E}_{\mathrm{kin}}$ contains only positive contributions. Therefore, the kinetic energy injected by geometric stiffness ($\mathbf{v}\dot{\mathbf{c}}\mathbf{F}$) and external forcing ($\mathbf{v}\dot{\mathbf{f}}_{\mathrm{ext}}$) generates the force disequilibrium, which in turn generates the exponential growth of kinetic energy.

We will now inspect the coefficients of the polynomial $At^4 + Bt^2 + C$. The reader not interested in the scaling of the coefficients might skip Sec. 3.4.3 and continue with Sec. 3.4.4.

3.4.3 Excursion: Fit of the kinetic energy at null modes

Section 2.8.2 showed that a vanishing mechanical stiffness associated with the occurrence of a null-mode can trigger the onset of failure. In this section a very simplified model will give more insight into the contribution of the null-mode to the kinetic energy. The assumption $\mathbf{kv} = \mathbf{0}$ means that larger external forces will not be balanced by the contact forces any more, because the stiffness is zero. Then, a force imbalance will arise that makes the particle velocities increase. This increase is

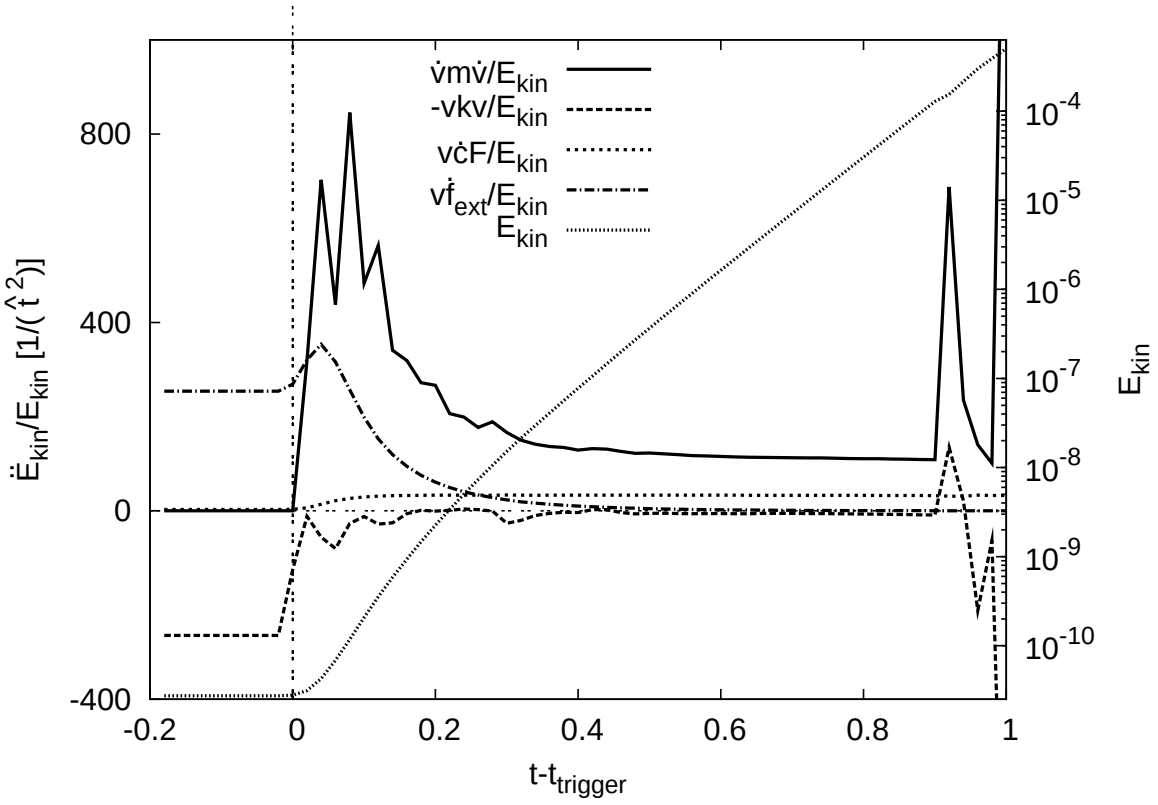

Figure 3.10: Contributions to $\ddot{E}_{\rm kin}$ and $E_{\rm kin}$, for the simulation shown in Fig. 3.6, where a null-mode triggers failure. The contributions to $\ddot{E}_{\rm kin}$ are plotted on a linear scale, indicated on the left, while $E_{\rm kin}$ is plotted on a logarithmic scale shown on the right.

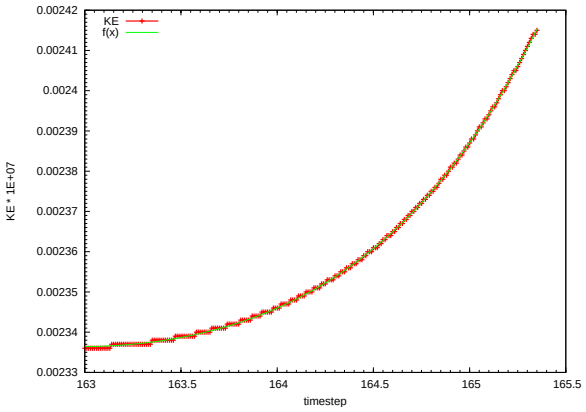

Figure 3.11: Fit to the algebraic increase in kinetic energy. Note the small range on the y-axis.

induced by the change in the external forces (see Eq. 2.42):

$$m\ddot{v} = \dot{f}_{\text{ext}} \,. \tag{3.9}$$

Here, the mass of the granular assembly and the external force acting on it are considered to be scalar quantities, because the latter will set the forces acting on the particles. Presuming that the right side is constant, integrating twice leads to

$$mv = \frac{1}{2}\dot{f}_{\text{ext}}t^2 + m\dot{v}_0 t + mv_0 \,. \tag{3.10}$$

Here, v_0 and $\dot{v}_0$ are velocity and acceleration at $t_0 := 0$. Just before the null-mode occurs, $\dot{v}$ will be small, so we can neglect the contribution of the second term. With this simplification the kinetic energy writes

$$\begin{aligned} E_{kin} &= \tfrac{1}{2}mv^2 \\ &= \tfrac{1}{8}t^4\frac{\dot{f}_{\text{ext}}^2}{m} + \tfrac{1}{2}t^2\dot{f}_{\text{ext}}v_0 + E_{kin,0} \,. \end{aligned} \tag{3.11}$$

Note that v is proportional to $\dot{f}_{\text{ext}}$, so E_{kin} is proportional to $\dot{f}_{\text{ext}}^2 + \mathcal{O}(\dot{f}_{\text{ext}})$. We checked this time dependence in one simulation and found the scaling with $\dot{f}_{ext}$ and m predicted by Eq. 3.11. This example is investigated below. The principal problem is that the algebraic growth soon is overlaid with the exponential growth coming from the negative geometric stiffness contribution $\mathbf{v}\dot{\mathbf{c}}\mathbf{F}$. Thus frequently the algebraic growth is too short for a fit.

We now want to investigate the rise in kinetic energy for one example of a null-mode failure in more detail. The parameters of the simulation are $\frac{df_{ext}}{dt} = 1.28 \times 10^{-3}$ and $m = 0.36$. The packing contains 16 particles. Denoting the prefactors in Eq. 3.11 by A, B, C, we have

$$E_{kin} = At^4 + Bt^2 + C \,. \tag{3.12}$$

Here, B and C depend on the initial velocity $v_0 = 3.60 \times 10^{-05}$. As C is given by the initial kinetic energy, only the values of A and B are of interest. The fit results for these parameters are given in Tab. 3.1. Whereas the fit value for A is close to the theoretical value, the one for the quadratic term differs by one order of magnitude. The main source of error is the very small interval of time during

	theory	fit
A	5.69×10^{-7}	6.61×10^{-7}
B	2.31×10^{-8}	2.03×10^{-9}

Table 3.1: Values for the prefactors in Eq. 3.12. The theoretical values (theory) come from comparing Eq. 3.11 and 3.12. The simulation result (fit) is obtained from a fit to the kinetic energy in the simulation.

$\dot{f}_{\mathrm{ext}}/1.28$	10^{-2}	10^{-3}	10^{-4}
$\mathrm{A_{fit}}/\dot{f}_{\mathrm{ext}}^2$	0.646	0.661	0.885
$\mathrm{B_{fit}}/\dot{f}_{\mathrm{ext}}^2$ $[10^{-3}]$	2.06	2.03	2.07

Table 3.2: Values for different load rates $\dot{f}_{\mathrm{ext}}$.

which the quadratic term dominates in Eq. 3.12. To check that the proximity of theoretical and fit values is systematic and not by chance, the model is now evaluated for different load rates $\dot{f}_{\mathrm{ext}}$ and different particle densities ρ.

Scaling of the fit values with density and load rate

Dependence on the load rate $\dot{f}_{\mathrm{ext}}$
According to Eq. 3.12, the prefactors A and B scale with $\dot{f}_{ext}^2$. This dependence is verified within three decades of values of $\dot{f}_{\mathrm{ext}}$ in Tab. 3.2. The values show the scaling expected by the theory: when A and B are divided by $\dot{f}_{\mathrm{ext}}$, the values are close to each other for all $\dot{f}_{\mathrm{ext}}$. Hence the assumption of the packing behaving like a solid of mass m is accurate enough to capture the essence of the null-mode failure.

Density dependence
Eq. 3.12 also depends on the mass m and thus on the particle density. While constant A should be inverse proportional to ρ, constant B should not depend on the density. This dependence is observed for $\rho = 1, 10$ in Tab. 3.3. Thus Eq. 3.11 is valid.

3.4.4 Ambushed transitions

In four out of the 26 simulations, failure seems to begin before an instability has appeared. One example is shown in Fig. 3.12. There is a contact status change at $t = t_{\mathrm{trigger}}$, and the energy begins to rise. The packing, however, is stable. As one can see, $\mathbf{vkv} > 0$, and it is large enough to dominate the geometric stiffness. Furthermore, no null-modes are present. Note however, that the increase of

ρ	1	10
$\mathrm{A_{fit}}$	6.61×10^{-7}	6.73×10^{-8}
$\mathrm{B_{fit}}$	2.03×10^{9}	1.81×10^{-9}

Table 3.3: Values for different particle densities ρ. Eq. 3.11 predicts $A_{\mathrm{fit}} \propto 1/\rho$ and $B_{\mathrm{fit}} \propto 1$. The fit values confirm this dependence on ρ.

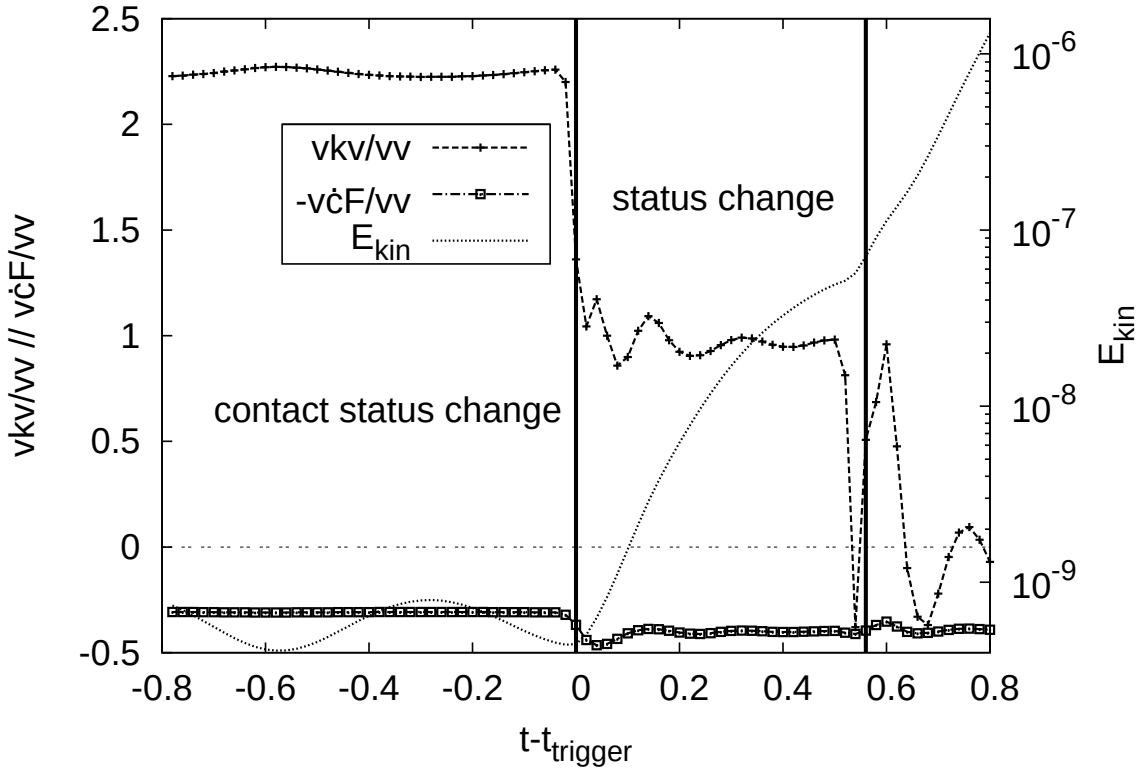

Figure 3.12: An example of an "ambushed transition": the kinetic energy starts to rise at $t = t_{\mathrm{trigger}}$, even though the packing is stable.

kinetic energy is slower than exponential for $t - t_{\text{trigger}} < 0.5$. At around $t - t_{\text{trigger}} = 0.5$, a second status change occurs, and the energy then rises exponentially.

It is believed that the initial increase of the kinetic energy is due to an oscillation associated with a stiffness transition, very similar to the one shown in Fig. 3.3. At $t - t_{\text{trigger}} = 0.5$, an instability appears, and it is this instability that causes failure. This phenomenon is called "ambushed transition", because there is first a transition from one stable state to another one. But during the very short transition period, an instability occurs. Thus, the initial rise in kinetic energy is due to a transition, but it is the instability that finally causes it to become very large.

When the stiffness is very low, vibrations of very low frequency often occur. These are damped insufficiently, and are therefore long-lasting. Note that the stiffness for $0 < t - t_{\text{trigger}} < 0.5$ is extremely low: $\mathbf{v}\mathbf{k}_{\text{tot}}\mathbf{v} \approx 0.5$. Two of the other three simulations displaying ambushed transitions also exhibit a very low stiffness, with $(\mathbf{v}_{\text{th}}\mathbf{k}\mathbf{v}_{\text{th}})/(\mathbf{v}_{\text{th}}\mathbf{v}_{\text{th}}) < 1$. This is smaller than the stiffness observed in all the other stable configurations.

However, one case did not fit this pattern. It is shown in Fig. 3.13. The kinetic energy begins to grow rapidly, even though the packing is still stable. Note that $(\mathbf{v}_{\text{th}}\mathbf{k}\mathbf{v}_{\text{th}})/(\mathbf{v}_{\text{th}}\mathbf{v}_{\text{th}}) \approx 4$ just after t_{trigger}, a value observed in other stable packings as well. One example can be seen in Fig. 3.4, where $(\mathbf{v}_{\text{th}}\mathbf{k}\mathbf{v}_{\text{th}})/(\mathbf{v}_{\text{th}}\mathbf{v}_{\text{th}}) \approx 4$ *before* failure. We therefore checked if the initial energy rise was part of an oscillation by running the same simulation with $\dot{\mathbf{f}}_{\text{ext}}$ reduced by a factor of 10. When this is done, the status change at $t - t_{\text{trigger}} \approx 0.1$ is postponed until $t - t_{\text{trigger}} \approx 0.5$. Shortly before the second status change, the kinetic energy starts to decrease, showing that the first rise in energy is part of an interrupted oscillation.

Changing $\dot{f}_{\text{ext}}$ also allows us to see that this failure mechanism is not purely quasi-static, for if it were, the instability would arise always at the same value of f_{ext}. But when $\dot{f}_{\text{ext}}$ is reduced, failure occurs at a smaller value of f_{ext}. Thus the oscillation plays an essential role in failure. On the other hand, if the appearance of the instability depended only on the oscillation, the separation in time between the two status changes would not change. But one observes that this time does indeed change. Thus both the oscillation and the value of f_{ext} have a role.

Another question is the curious nature of some of the transitions in Fig. 3.13. For example, just before failure, the curve $\mathbf{v}_{\text{th}}\mathbf{k}\mathbf{v}_{\text{th}}$ shoots up to about 30, off the scale of the graph, and then suddenly drops down to about 5. This is not an error but a sign of a null-mode that appears rapidly, and then disappears. Such compound transitions are discussed in the next section.

3.5 Compound Status changes

Fig. 3.13 illustrates another phenomena that is sometimes observed: a sequence of status changes. Apart from the contact status change at $t = t_{\text{trigger}}$, several other events are indicated by short vertical arrows at the bottom of the figure. These events can also be seen from $(\mathbf{v}_{\text{th}}\mathbf{k}\mathbf{v}_{\text{th}})/(\mathbf{v}_{\text{th}}\mathbf{v}_{\text{th}})$: when this quantity jumps upwards to a value above the top of the graph, a null-mode has appeared, and when it returns to a lower value, that null-mode disappears. Each appearance and disappearance is associated with a contact status change.

To understand what is happening, Fig. 3.14 shows the sequence of contact status changes until $t = t_{\text{trigger}}$ in Fig. 3.13. The transition as a whole involves a shift in the location of a single sliding contact. The system passes between these two states via a third state in the middle panel, where both contacts are sliding. Each of the three states corresponds to a different stiffness: the left hand state is relatively stiff, and corresponds to $\mathbf{v}\mathbf{k}\mathbf{v} \approx 17$ ($t - t_{\text{trigger}} < -0.02$ in Fig. 3.13), the middle to the

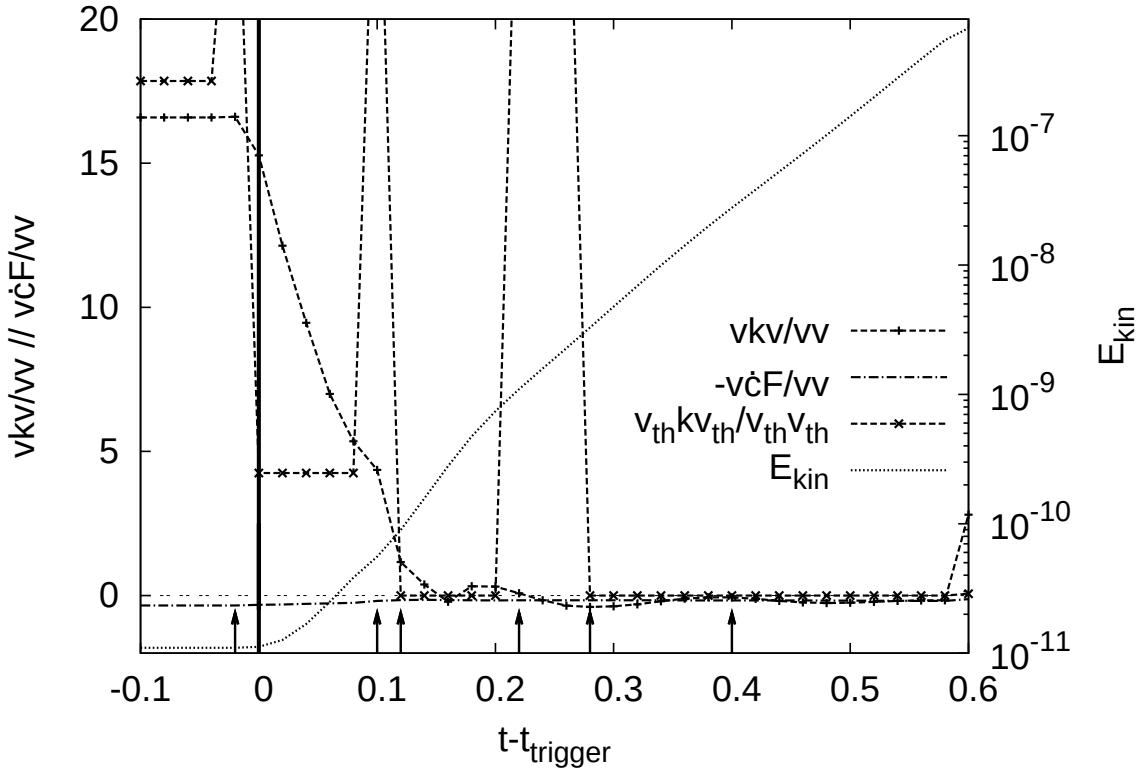

Figure 3.13: The most difficult example of failure to classify. The triggering event is shown by a heavy vertical line. Other contact status changes are shown by the short vertical arrows at the bottom of the graph. At certain short periods of time, a null-mode exists. When this occurs, $(\mathbf{v}_{\rm th}\mathbf{k}\mathbf{v}_{\rm th})/(\mathbf{v}_{\rm th}\mathbf{v}_{\rm th})$ jumps to a value near 30.

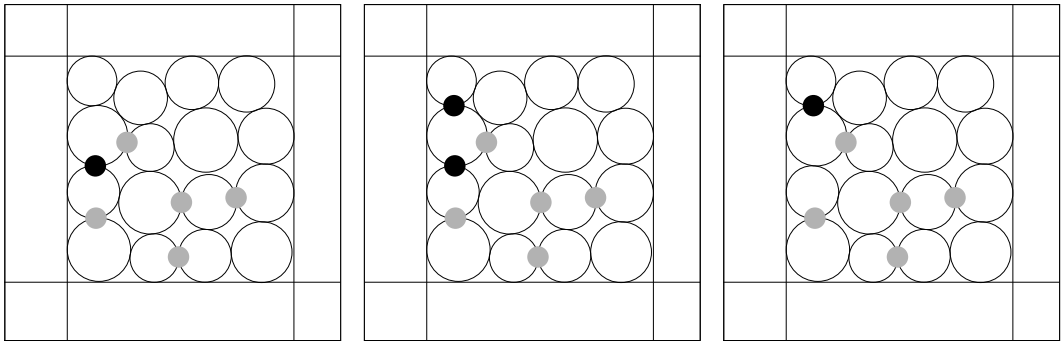

Figure 3.14: Compound status change. The compound status change involves the two contacts in the upper left corner, marked with the black circles when they are sliding. The other sliding contacts are marked with gray circles. The pictures are taken at $t - t_{\rm trigger} = -0.04, -0.02, 0$ (from left to right).

existence of a null mode ($t - t_{\mathrm{trigger}} = -0.02$), and the last state to a reduced stiffness of $\mathbf{vkv} \approx 4$ ($t = t_{\mathrm{trigger}}$).

Such "compound contact status changes" are observed several other times in Fig. 3.13, and occasionally in other systems. In Fig. 3.13, a compound contact status change is involved in an ambushed transition, but no such general relation exists: ambushed transitions and compound status changes occur independently of each other.

3.6 Relative occurrence of the trigger mechanisms

Each of the 26 assemblies has been examined to determine the trigger type. The first step is the identification of the contact status change that triggers failure by examining the simulation data at the point where the energy starts to grow. Then the trigger mechanism must be identified. This is done by a three step process:

1. First, one inspects the change in $\mathbf{vkv}$ and $\mathbf{v}_{\mathrm{th}}\mathbf{kv}_{\mathrm{th}}$ at the trigger event. If $\mathbf{v}_{\mathrm{th}}\mathbf{kv}_{\mathrm{th}}$ becomes negative at the trigger event, and $\mathbf{vkv}$ converges to $\mathbf{v}_{\mathrm{th}}\mathbf{kv}_{\mathrm{th}}$ after a short time, then the trigger is classified as an instability. An example is shown in Fig. 3.4. Simulations where $\mathbf{v\dot{c}F} > \mathbf{vkv} > 0$ are also classified as an instability, because the total stiffness is negative.

2. Next the possibility of null-mode failure must be considered. This is done by performing a singular value decomposition on $\mathbf{k}$ and checking if the number of null modes increases at t_{trigger}. Then the null mode must be consistent with boundary and load conditions. If $(\mathbf{vkv})/(\mathbf{vv})$ and $(\mathbf{v}_{\mathrm{th}}\mathbf{kv}_{\mathrm{th}})/(\mathbf{v}_{\mathrm{th}}\mathbf{v}_{\mathrm{th}})$ diverge from one another, the null-mode will trigger failure. Alternatively, one can check if $\mathbf{v_0 v}/(|\mathbf{v_0}||\mathbf{v}|) = 1$.

3. There are four simulations that could not be classified in this way. These systems display "ambushed transitions", and were discussed in Sec. 3.4.4.

It should be remarked that it was not clear how to classify some of the simulations. In three of them, first a null mode is present, then a weak instability appears. These three simulations where all classified as null mode, because the kinetic energy increases significantly before the instability appeared.

In the 26 assemblies, an ambushed transition occurs four times, whereas the null-mode trigger was observed 14 times. Instability is at the origin of failure in 8 assemblies. This results suggest that ambushed transitions are rather rare, whereas the null-mode trigger frequently occurs in the small systems.

One can also ask what kind of contact status changes causes failure. In 13 of 26 assemblies, a contact begins to slide (in one case two contacts become sliding). In 8 other assemblies one or more contacts opens when the trigger occurs, and in another three assemblies one contact closes at that time. In the two remaining assemblies two different contact status changes happen at the same time: In one assembly a sliding contact became nonsliding and another sliding contact opened, and in the other assembly one open contact became sliding while a different sliding contact opened. The statistics suggest that at the origin of the trigger usually at least one contact opens or starts to slide.

The trigger mechanisms can be related to one another as shown in Fig. 3.15. All systems begin in the box labeled "stability", and finish in the ovals "null-mode" or "instability" when they fail. Most systems make the transition directly, but a few pass by the box labeled "ambushed transition". In this case, the initial rise in kinetic energy is caused by an oscillation provoked by a transition between two

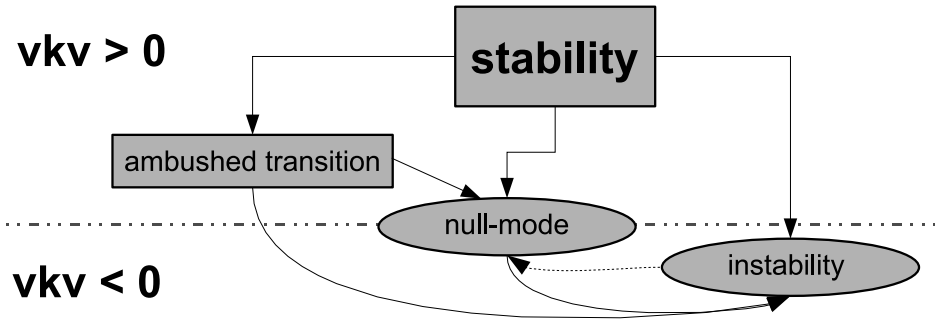

Figure 3.15: Relation of trigger mechanisms. All systems begin in the box marked "Stability". Then they can fail through three different ways, indicated by the three arrows emerging from this box. The remaining arrows indicate that transitions are sometimes possible between different mechanisms. Though no transition from the box "instability" to the "null-mode" oval appeared in any system, it might still be possible. The dotted horizontal line indicates $\mathbf{vkv} = 0$.

stable states, as discussed in Sec. 3.3. During the oscillation, a null mode or instability appears which then causes the system to fail. During the course of failure, null-modes can appear or disappear. The same figure also ranks the different trigger mechanisms by their stability. The lower they appear, the more unstable they are. Thus the upper region of the figure is labeled $\mathbf{vkv} > 0$, and includes "stability" and "ambushed transition", for the packing is stable in these states. The lower part of the figure is labeled $\mathbf{vkv} < 0$, and contains the oval "instability". The two parts of the figure are separated by a horizontal, dotted line, representing the condition $\mathbf{vkv} = 0$ which is met in the oval "null-mode".

3.7 Triggers in larger systems

This investigation so far considered trigger mechanisms in small packings with 16 particles, where the influence of the boundary conditions is quite pronounced. In larger larger systems, the relative occurrence of the trigger mechanisms might be different. This section tackles this question and provides statistics of the trigger mechanisms as a function of system size.

In Tab. 3.4 the number of systems that fail through the different trigger mechanisms are listed for systems with $N = 16, 32$, and 64 particles. First, the number of instabilities slightly decreases with increasing system size. This means that the system passes through one of the other trigger mechanisms before instability appears (see Fig. 3.15). Second one notes that a lot of small systems with $N = 16$ particles fail through the null-mode trigger, but only one system with 32 particles shows this trigger mechanism. No larger system was found to fail through the occurrence of a null-mode. On the other hand, the more complex trigger 'ambushed transition' becomes more frequent when the system size is increased. For $N = 32$ particles systems, this is already the most common trigger of failure. An argument for this turnaround is that each contact has a smaller effect on the stiffness. Thus the stiffness will not directly jump to a negative value through a single contact status change. Instead, the stiffness will decrease by small steps, and often arrive in the "soft" region, where deformations are large. Another argument for the rising number of ambushed transitions is the

	$N = 16$	$N = 32$	$N = 64$
ambushed	4	10	12
$\mathbf{vkv}$=0	14	1	0
instability ($\mathbf{vkv} < \lvert\mathbf{v\dot{c}F}\rvert$)	8	8	5
total	26	19	17

Table 3.4: Number of systems that fail through the different trigger mechanisms for different numbers of particles.

circuit	N=16	N=32
3	1.58	5.37
4	3.62	8.58
5	1.65	4.58
6	0.15	1.11
7	0.12	0.42
8	0	0.16
9	0	0.05

Table 3.5: Average number of circuits per system for systems with $N = 16$ and $N = 32$ particles.

increase in vibrations. This increase has several origins. First we have more vibration modes, as their number linearly increases with system size. Second, the longer the wavelength (measured in grains) of such a vibration, the less it is damped, and the longest wavelength is comparable to the size of the system. Third we have much more contact changes in the same time interval, so the time for one vibration to be damped is much shorter, before the next status change appears.

The striking number of null-mode triggers in the small systems is worth some closer examination. Figure 3.9 showed that, occasionally, a granular assembly can form a square structure. This square structure has only circuits with four grains, which explains why the rotation movement is possible: in even circuits, all the grains can rotate in opposite direction at their points of contact. If there is an uneven circuit, then at least one contact has to be sliding in order to allow for this movement. This is because in odd circuits there is at least one contact at which the grains have to move in the *same* direction. This is only possible if it is a sliding contact.

In Tab. 3.5 the number of circuits for systems with $N = 16, 32$ particles are compared. Because there is only one null-mode trigger for $N = 32$, it is favorable to average over all trigger mechanisms that can appear. The average number of even circuits in $N = 32$ particle systems is 9.85, slightly lower than the number of odd circuits 10.42. This is opposite to the $N = 16$ particles systems, where the number of even circuits 3.77 is higher than the number of odd circuits 3.35. The main difference between these two systems is not the system size, but the tendency to form a square structure. While 4 by 4 ($N = 16$) is innately square, $4\sqrt{2}$ by $4\sqrt{2}$ ($N = 32$) is incompatible with a square structure. This preference also explains, at least partially, the high number of null-mode triggers in the $N = 16$ particles systems.

On the other hand, 64 particles assemblies can form a square structure, but the probability of it being disrupted by "defects" due to polydispersity is much higher. More precisely, the appearance of

	nontrivial null-mode movements		
N	before	at t_{trigger}	during failure
16	0.19	0.69	0.62
32	0.00	0.11	0.32
64	0.00	0.00	0.21

Table 3.6: Average number of nontrivial null-mode movements per system for different system sizes at the times t=t_{trigger}-0.2 (before), t=t_{trigger}, and t=t_{trigger}+0.2 (during the failure).

an odd circuit can block the entire packing, and it's more difficult to avoid all odd circuits in a large packing than in a small one. Accordingly, one does not observe any null-mode failure for this system size. Therefore boundary effects seem to be very important in the $N = 16$ particles assemblies.

A more thorough investigation of null-mode motions is shown in Tab. 3.6, where the number of null-modes are listed as a function of system size, before, at, and after the time when the trigger appears. The result shows a clear tendency: the larger the system the less number of null modes appear. Before failure, there are already no more null-modes for $N = 32$, while at t_{trigger} one has to take systems with at least $N = 64$ particles to get rid of them. During the failure, the number of null modes does not vanish for any of the system sizes, but the trend toward fewer null modes in large systems remains.

A further test considered a possible dependence of the number of null-modes on the wall friction. This test was carried out for the smallest systems. When rerunning the $N = 16$ simulations with friction at the walls, one finds that failure is almost always accompanied by the appearance of a null-mode. Therefore the observed null-modes seem to be a proper feature of the failure process and not due to the absence of wall friction. However, those systems were not subjected to the lengthy process of a detailed analysis of the trigger mechanisms.

3.8 Testing the accuracy of the stiffness matrix description

In the last sections we have seen that the three triggers of failure correspond to a negative, a positive or a zero value of the quadratic form $\mathbf{vkv}$. This quadratic form is constructed from the stiffness matrix $\mathbf{k}$ and the particle velocities $\mathbf{v}$. Knowing the change in external force $\dot{\mathbf{f}}_{\mathrm{ext}}$, one can try to calculate the particle velocities theoretically. The procedure has been described in Sec. 2.8.5. The resulting velocity vector $\mathbf{v}_{\mathrm{th}}$ contains the velocities observed in the quasi-static and quasi-rigid limits. These limits have been described at the end of Sec. 2.8.2. One can check if the limits are fulfilled by comparing the theoretical velocities $\mathbf{v}_{\mathrm{th}}$ with the velocities $\mathbf{v}$ of the simulation. Or, equivalently, one can evaluate the difference between $\dot{\mathbf{f}}_{\mathrm{ext}} = \mathbf{kv}_{\mathrm{th}}$ and $\mathbf{kv}$. Thus we can check the validity of the assumptions leading to Eq. 2.43 by calculating

$$\Delta = \frac{|\dot{\mathbf{f}}_{\mathrm{ext}} - \mathbf{kv}|}{|\dot{\mathbf{f}}_{\mathrm{ext}}|} \,. \tag{3.13}$$

We will evaluate this equation for different system sizes, and for different particles stiffnesses. Let us begin with the examination of the particles stiffness, testing the assumption of quasi-rigidity. In the foregoing section of this chapter, the 16 particle packings have the stiffness $k_n = 1600$. The mean error arising in the 26 systems is shown in Fig. 3.16(b). In comparison, in Fig. 3.16(a) the error is

shown for the same packings, but at a stiffness that is ten times smaller: $k_n = 160$. The graphs show the evolution of the mean and maximum error observed in the simulations.

The values in Fig. 3.16(a) indicate that a stiffness value of $k_n = 160$ results in large errors long before failure appears. In the beginning of the simulation, the mean error is about 3.0%, but it increases to 28.9% at the failure. The maximum error increases off the scale in the figure at $\tau = -0.4$, i.e. long before failure, and exceeds 100% at $\tau \geq -0.2$. These values show that this particle stiffness is not sufficient for simulating quasi-rigid granular systems.

Let us now inspect the values for the higher stiffness value $k_n = 1600$. The mean error in Fig. 3.16(b) is around 1% in the simulation beginning and increases to only 5% just before failure. The maximum error is about 5% above this value. Close to the failure at $\tau = 0$, the maximum error rises sharply and attains 28% at $\tau = 0$. During failure, which lasts until about $\tau = 0.01$, the maximum error is much higher. It remains large after the failure, because vibrations arise that lead to large discrepancies from assumed the quasi-static behavior. In conclusion a stiffness of $k_n = 1600$ is sufficient to simulate quasi-rigid granular systems until failure. The systems studied in this thesis have this stiffness.

Another important point is the generalization of Eq. 3.13 to systems with larger numbers of particles N. For larger N, only systems with the stiffness $k_n = 1600$ are inspected. Figure 3.17 compares the errorbars for $N = 16, 32, 64, 256$ and 1024 particles systems. For all N, the average error is small in the simulation beginning and increases until failure.

In Fig. 3.17(b), for the $N = 32$ particles systems, two unexpected peaks appear between $\tau = -0.3$ and $\tau = -0.2$. These peaks are correlated with a sudden increase in the kinetic energy of an individual assembly. This increase does not lead to a significant deformation of the packing, and therefore it cannot be considered failure. We will see in Sec. 6 that such events are precursors of the failure, and they have specific characteristics.

While the error for $N = 16$ and 64 are comparable and small, the one for $N = 32$ is much higher. Probably part of this discrepancy arises from the compatibility of 16 and 64 particles with the square size of the system. $N = 32$ is incompatible with a square structure. The compatibility might lead to $N = 16, 64$ systems being rather stable over a long interval of time, because large forces should be necessary to break up the square structure. This means that contact changes will occur preferably close to the failure, and therefore the error related to contact changes will be smaller at foregoing time steps.

Comparing figures for small and large N, one observes a stronger increase of the error with time τ for the larger systems. Particularly close to the failure the average error increases much more in large systems. On the other hand the maximum errors are similar. This shows that deviations from the mean behavior are smaller in large system

In systems with $N = 16, 64, 256$ and 1024 particles, the error increases quickly only close to failure. The increase begins sooner and is smoother in the larger systems. But there are also many other things involved in the scaling behavior, such as the boundary conditions. In this chapter we have investigated only rigid wall boundary conditions. But other boundary conditions might lead to another scaling behavior with N. In conclusion, one can control the error of the stiffness matrix approximation not only in small, but also in large systems.

At the failure, the assumptions leading to the approximations are violated, and the error becomes always very large. The kinetic energy rises quickly, and the simulations are not quasi-static any more. The contributions to this energy rise are investigated in the next section.

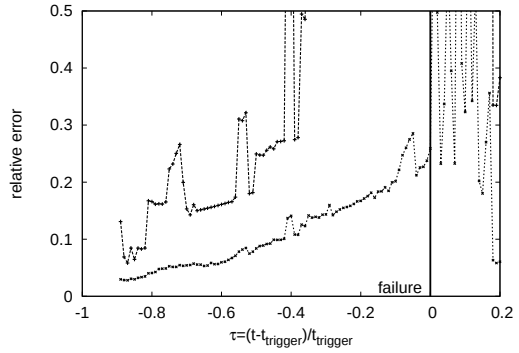

(a) Average and maximum error of the stiffness matrix approach (Eq. 3.13) at $k_n = 160$. The comparatively low stiffness k_n results in large average errors. The maximum error even exceeds 100% after $\tau = -0.2$. This shows that the quasi-rigid assumption, required for the stiffness matrix ansatz in Eq. 2.43, is not exactly valid.

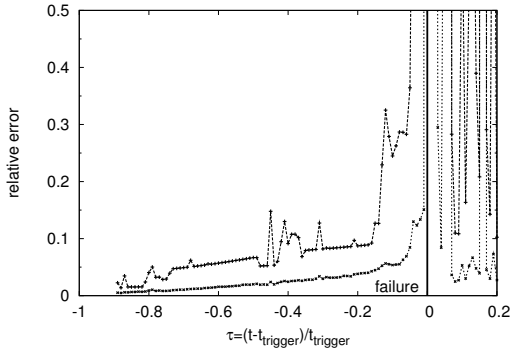

(b) Average and maximum error of the stiffness matrix approach (Eq. 3.13) at $k_n = 1600$. Both errors are small but increase quickly close to the failure. Failure lasts from $\tau = 0$ to about $\tau = 0.01$. One source of error are vibrations, they are especially important after failure has happened.

Figure 3.16: Error of the stiffness matrix approach for the two particle stiffnesses $k_n = 160, 1600$ at the system size $N = 16$. The maximum error and the mean error of 26 assemblies from the beginning of the simulation at $\tau = -1$, through the failure at $\tau = 0$, and after failure is shown. When k_n is small (Fig. 3.16(a)) the error is high. It reduces when k_n is increased by one order of magnitude (Fig. 3.16(b)).

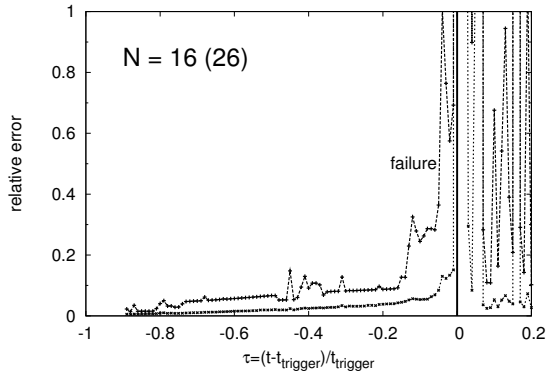

(a) $N = 16$ particles (average over 26 systems).

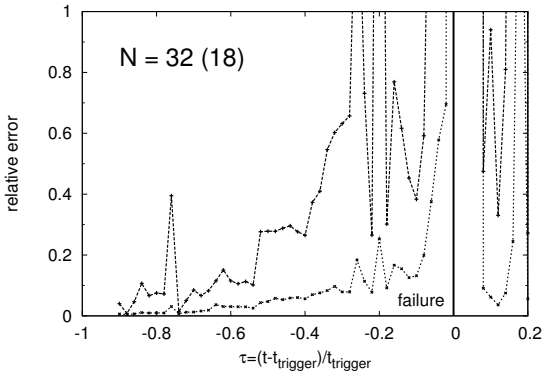

(b) Average and maximum error for $N = 32$ (average over 18 systems). The two sharp maxima around $\tau = -0.2$ are due to two precursors, each one appearing in a different system. Precursors of failure will be investigated in Sec. 6.

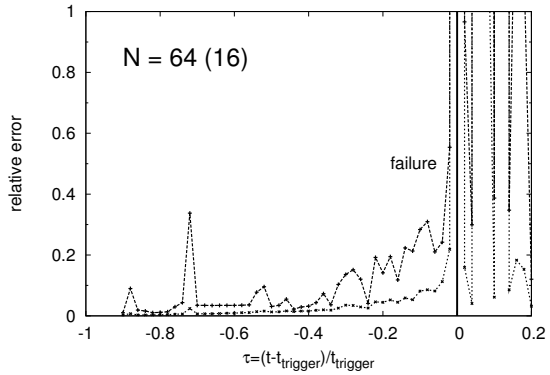

(c) $N = 64$ particles (average over 16 systems).

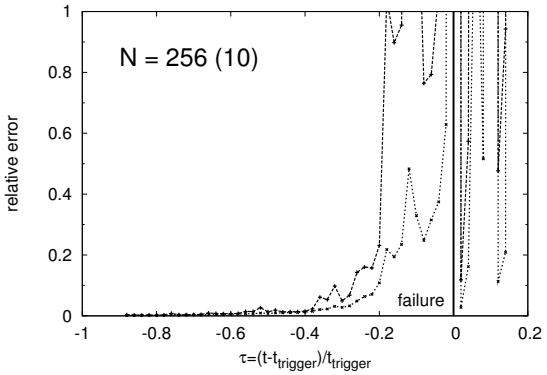

(d) $N = 256$ particles (average over 10 systems).

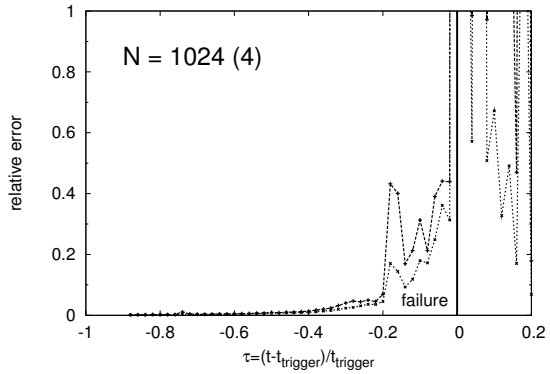

(e) $N = 1024$ particles (average over 4 systems).

Figure 3.17: Error of the stiffness matrix approach (Eq. 3.13) for different system sizes N ($k_n = 1600$). The figures show the maximum error and the mean error from the beginning of the simulation at $\tau = -1$, through the failure at $\tau = 0$, and after failure. For each figure, the number of systems studied is indicated in brackets.

3.9 What drives failure?

The failure leads to the kinetic energy rising very quickly. But is this rise always the same? If not, on which parameters does it depend? A first glimpse on the answer has been given in Sec. 2.8.6. In that section, the energy contributions to the kinetic and the potential energy have been discussed. When at failure the kinetic energy rises exponentially, there are three possible sources of energy: the mechanical stiffness $-\mathbf{vkv}$, the geometric stiffness $\mathbf{v\dot{c}F}$, and the force imbalance $\dot{\mathbf{v}}\mathbf{m}\dot{\mathbf{v}}$. Note that the latter contains the particles' masses, thus it is the contribution of inertia to the rising motions.

In this section the simulation results are evaluated. Once again, 26 systems with 16 particles are investigated. From this ensemble, average and standard deviation for the rise in kinetic energy are discussed in Sec. 3.9.1. Thereafter in Sec. 3.9.2 the different energy contributions are explained.

3.9.1 The exponential rise of the kinetic energy

During failure, the kinetic energy rises exponentially; $E_{\mathrm{kin}} \propto e^{\beta t}$. To determine β, we take the data points starting from the time when $E_{\mathrm{kin}} = 10E_{\mathrm{kin}}(t_{\mathrm{trigger}})$ until $t = t_{\mathrm{trigger}} + 1$ or the time when E_{kin} starts to decrease, which ever comes first. This *total fit* covers the whole exponential region. First we determine the exponent β directly from the kinetic energy observed in the simulations, and obtain $\beta = 0.32 \pm 0.07\, 1/\hat{t}$ after averaging over all 26 seeds. Second, a prediction of β can be obtained from the calculation of the second derivative of E_{kin}, given in Eq. 2.66, from the simulation data. This equation yields a very similar value of $\beta = 0.33 \pm 0.09\, \hat{f}/\hat{t}$.

Towards the end of failure, the increase in kinetic energy is much more regular. This can be seen in Figs. 3.5, 3.10. A second, *best fit* calculation of the exponent β in this region leads to the result $\beta = 0.34 \pm 0.10\, 1/\hat{t}$, which is very close to the value found by fitting the whole curve.

3.9.2 Contributions to the kinetic energy

The mechanism that drives failure can be uncovered by comparing the various terms in Eq. 2.66. As noted above, there are three contributions to $\ddot{E}_{\mathrm{kin}}$ that can dominate: the force imbalance, the mechanical stiffness, or the geometric stiffness. The contribution $\mathbf{v}\dot{\mathbf{f}}_{\mathrm{ext}}$ to $\ddot{E}_{\mathrm{kin}}$ is negligible in the exponential region of $E_{\mathrm{kin}} \propto \mathbf{vv}$, because $\mathbf{v}\dot{\mathbf{f}}_{\mathrm{ext}} \propto \mathbf{v}$, so its contribution evolves like $|\mathbf{v}|/E_{\mathrm{kin}} \propto |\mathbf{v}|/\mathbf{vv} \to 0$. The term $\mathbf{v}\dot{\mathbf{f}}_{\mathrm{ext}}$ does have a very special role at the onset of failure, however. In all 26 cases that have been examined, it is the main source of energy at t_{trigger}, but is then quickly replaced by the force imbalance. The damping, omitted from Eq. 2.66, cannot drive failure, since it always opposes motion.

The relative contributions to $\ddot{E}_{\mathrm{kin}}$ averaged over all assemblies are given in Tab. 3.7. The two rows correspond to the two different methods of averaging discussed in the previous subsection: the first row covers the whole exponential region, whereas the second row applies to the latter part. The variance of each contribution is much larger in the first row than in the second, which is a consequence of the fluctuations in Figs. 3.5 and 3.10 at the onset of failure. On the contrary, the latter, "best fit" part of the curve is very regular. This is a general feature of all the simulations.

The table also shows that the force imbalance contributes the largest part to $\ddot{E}_{kin}$, followed by the contribution of the geometric stiffness. The mechanical stiffness contribution is small, on average. It can indeed, depending on the system, be either positive or negative, driving or opposing failure. Thus the two stiffnesses do not directly drive failure; instead, they generate the force imbalance at the beginning of failure. Recall that a negative stiffness drives the system away from its equilibrium

		Contributions to $\ddot{E}_{kin}$ in [%]			
	β	$\dot{\mathbf{v}}\mathbf{m}\dot{\mathbf{v}}$	$\mathbf{vkv}$	$\mathbf{v}\dot{\mathbf{c}}\mathbf{F}$	Sum
Total fit	0.33 ± 0.09	93 ± 89	-25 ± 98	27 ± 19	95
Best fit	0.34 ± 0.10	72 ± 09	00 ± 18	25 ± 13	97

Table 3.7: Average exponential slope β and principal contributions to the second derivative of E_{kin} during failure, calculated from the simulation data. The average has been carried out over 26 systems. The upper values are obtained by fitting the whole exponential region (total fit) while the bottom values stem from a fit to 15 consecutive points of almost constant contributions (best fit). Note that $\mathbf{m}\dot{\mathbf{v}} = \mathbf{f_{ext}} + \mathbf{cF}$ is the force imbalance.

position, the force imbalance will become larger the more the system departs from its initial configuration. This evolution will eventually come to an end when a new stable state is experienced. This can be seen most clearly in Fig. 3.5, where the exponential rise of the kinetic energy is broken at $t - t_{\text{trigger}} \approx 0.7$, and the mechanical stiffness begins to fluctuate wildly, presumably due to vibrations. This process is not related to the onset of failure, and it has therefore not been investigated in detail.

3.10 Scaling of the rise in kinetic energy at failure

The rise of the kinetic energy is given by the change of the particle velocities. These can be calculated from the equations of motion, Eq. 2.42: when E_{kin} rises exponentially, all relevant terms on the right side of the equation are proportional to the velocity vector $\mathbf{v}$, while the left side is proportional to the second derivative of the velocities:

$$m\ddot{v} = Cv. \tag{3.14}$$

We make the ansatz

$$v = Ae^{\sqrt{\frac{C}{m}}t} + Be^{-\sqrt{\frac{C}{m}}t}. \tag{3.15}$$

The second term is negligible, because the velocity is quickly increasing. The ansatz depends on the system's mass m which depends on the particle mass density ρ. To evaluate the validity of Eq. 3.14, one system with 16 particles is investigated at five different densities. The results are rescaled, aiming to collapse the data on a single curve. The time is rescaled by $1/\sqrt{\rho}$ and E_{kin} is divided by ρ where $\rho = 0.01, 0.1, 1, 10, 100$. The resulting curves for $E_{kin} = \frac{1}{2}mv^2$ are shown in Fig. 3.18. The data collapse very well, except for the extremely light-weight sample ($\rho = 0.01$), where the walls carry almost all the mass of the system. This is because their masses $m_{\text{wall}} = 0.01$ are set independent of the density and are constant for all ρ.

While the increase depends on the particle density ρ, it should not depend much on the stiffness of the particles, because the main contribution to the rise in kinetic energy is coming from the force imbalance, which is independent of stiffness. The mechanical stiffness contribution to $\ddot{E}_{\text{kin}}$ depends on the particle stiffness, but, at least for a stiffness value $k_n = 1600$, it is canceled by the geometric stiffness. This is obvious from the average contribution (Total fit) to $\ddot{E}_{\text{kin}}$, shown in Tab. 3.7. In Fig. 3.19 the kinetic energy at the failure is plotted for the three stiffnesses $k_n = 400, 1600, 4000$. Although the beginning of failure seems slightly depending on the particle stiffness, the gradient of

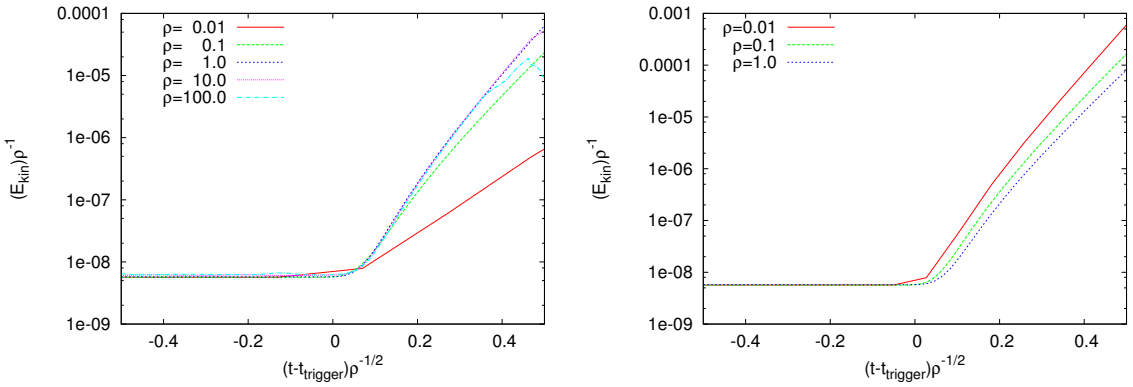

Figure 3.18: Left: fit for different mass densities ρ. Right: if the mass of the walls is taken into account in Eq. 3.14, the results for low densities ρ are in much better agreement.

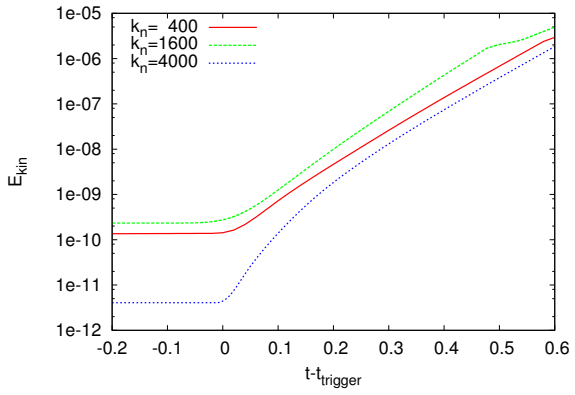

Figure 3.19: Increase of E_{kin} at failure for different particle stiffnesses k_n. As expected, the increase is independent of the particle stiffness.

E_{kin} is almost independent of the stiffness. This result suggests that the force imbalance is always responsible for the rise of E_{kin}, independent of the stiffness of the particles.

3.11 The failure staircase

In the small number of particle systems, failure occurs at the first abrupt change in the deviatoric strain. However, this event may be simply the first of a series. This possibility is suggested by the observation made at the end of the previous section: the system finds a new stable state when the exponential rise in kinetic energy is broken. The experiment could be continued until the second stable state collapses, leading to a third stable state, and so on. At each step, the sidewalls will move outward by a certain unit, and finally the grains will form a monolayer, and no further failure events are possible. Thus the strain as a function of time will be a staircase, with the steps corresponding to the events studied in this paper. This is reminiscent of the devil's staircase, observed in packings of perfectly rigid, frictionless grains [61].

In the small packings considered here, the number of steps in the staircase must be small, but in larger systems, there could be many more, and the size of the steps could become small. Strain-controlled simulations[1] of rigid frictional particles [62] suggest there are many stable states that the system passes through as it deforms. If this were true, what is called failure in large systems must be characterized by something in addition to an instability: the next stable state must be far away, so that a large change in the strain occurs. In the geomechanics community, failure is often considered to happen at the maximum deviator stress, i.e., at the maximum difference between vertical and horizontal external pressure. This definition does not only consider the strain, but instead also takes into account the external forces. Thus the failure is better defined in terms of maximum stress instead of a very fast change in strain. In small systems the two definitions are equivalent, because the change in strain is discrete, taking only a few values. But in large systems with many particles the strain changes almost continuously so that stress becomes a better tool for identifying the failure.

3.12 Conclusion

This chapter is concerned with failure in numerical simulations of small granular assemblies composed of sixteen particles subjected to a slowly increasing deviatoric stress under rigid wall boundary conditions. This system size is small enough to allow for a detailed analysis of failure, but large enough to exhibit complex behavior. Twenty-six different configurations are studied, and the stiffness matrix theory is the means for understanding the results.

The first part of this chapter studies the assemblies as the load is increased. As in previous works [63–65], one finds a reduction in stiffness, together with an increasing number of sliding contacts. The stiffness occasionally increases, but usually declines, always in a step-wise fashion, with sudden drops coinciding with contact status changes. These status changes are accompanied by damped oscillations.

The initial expectation for the cause of failure was based on Ref. [60]: failure would be triggered by a contact status change that leads to a negative stiffness or a null-mode. Negative stiffness means

[1] In strain controlled simulations one manipulates the velocities of the walls, while in stress controlled simulations one sets the external forces on the walls.

that an increment of force pushes the system away from its equilibrium, and a null-mode is a motion that does not change the contact forces at all. This expectation is to a large degree confirmed. Failure can always be associated with a contact status change that initiates the "trigger" of failure. Furthermore, twenty-two out of the twenty-six assemblies fail through a null-mode or instability. The remaining four assemblies fail through a process that is called "ambushed transition": The initial rise in kinetic energy is caused by oscillations provoked by a transition between two stable states. During these oscillations, a second status change occurs, that leads to a null-mode or to an instability, and thus to failure.

To assess the significance of ambushed transitions, one would have to study carefully the oscillations and their dependence on numerous parameters: the rate of loading, the stiffness of the particles, the damping, the size of the system, the boundary conditions, and dimensionality (2 or 3 dimensions) all affect the vibrations and must be considered. At present, little has been done to answer the question of whether the vibrations in the ambushed transitions are a serious issue in real systems.

The intent of this chapter is to show that the stiffness matrix can describe the quasi-static behavior of granular material on the way to failure. The results show that in the limit of sufficiently stiff particles, inertia and dissipation become irrelevant. Furthermore the study shows that the stiffness matrix can explain to a large extent the mechanisms leading to the collapse of granular assemblies.

In addition to the trigger of failure, we also examined the process of failure itself, by determining the various contributions to the kinetic energy. Before failure, energy is injected by the external load, and stored as potential energy in the contacts by the mechanical stiffness. Just at failure, the mechanical stiffness is reduced, and can no longer compensate for the energy injected by the load. Thus the kinetic energy begins to rise. Shortly thereafter, however, the dominate contribution to the kinetic energy is the force disequilibrium.

The kinetic energy always rises exponentially during failure. Ref. [60] expected that this would be so only when failure was triggered by an instability. For a null-mode, the energy was expected to rise algebraically. A detailed analysis shows that the geometric stiffness, which has not been anticipated by Ref. [60], then becomes significant at failure, leading to the exponential rise of the energy. In agreement with Ref. [66], the findings show that the geometric stiffness is always destabilizing. Hence failure involves always an exponentially rising kinetic energy.

What happens in large systems? It is certainly more difficult to identify the cause of failure: while in small systems the contact status changes can be well-separated in time and thus the effect of each one can be ascertained, in large systems the changes are more frequent, and also each one has a smaller effect. Thus the steps with which the stiffness declines decreases with system size, and finally, the stiffness can be approximated by a continuous function. This means that the mechanical stiffness cannot suddenly become negative, or zero, as in many examples in this chapter. It must therefore decline until it is eventually canceled out by the geometric stiffness, and failure occurs. Just before this happens, however, the packing will be very soft, and "ambushed transitions" will occur frequently. The observations of larger systems containing 64 particles confirm these trends. Certainly, compound status changes become more frequent in large systems. Therefore they are more often involved in the occurrence of failure.

The small systems do not display any precursors of failure. This is an expected behavior, because the number of possible contact status changes is limited, and every modification results in a large change in stiffness. In many particle systems, however, precursors are frequently encountered, which we will see in Chap. 5. The next chapter shows how general properties of the failure, such as the external force at failure, generalize to much larger systems.

Chapter 4

Properties of failure for different system sizes

In the introduction, failure has been defined as the instant when suddenly the boundary walls of the system start to move: top and bottom walls move towards the center of the system, while the sidewalls move outwards. At the same time, the grains' kinetic energy rises very quickly. An example of such a behavior is shown in Fig. 4.1. The figure shows a time series of snapshots of the granular system at equidistant points in the control parameter *external force* f/f_0, which is linearly increased with time, starting from $f/f_0 = 1$ (see Sec. 2.11 for details). The black grains have a kinetic energy above the average, while the kinetic energy of the other grains is below the average. When failure occurs between Fig. 4.1(d) and Fig. 4.1(e), the particles in the upper right corner of the system move to the right side, while the grains in the lower left corner move to the left. After failure, in Fig. 4.1(e), the system is wider, but smaller in height.

The foregoing chapter was concerned about the triggers which cause the failure in granular systems. But what does failure look like? Some fundamental properties of the failure are investigated in this chapter. All results in this section are discussed particularly with respect to their system size dependence. First, the number of constraints on the particle motions is compared to the number of internal degrees of freedom in the system in Sec. 4.1. This concept has been explained in detail in Sec. 2.7. One expects that at the failure the number of constraints is smaller than the number of degrees of freedom, giving rise to particle displacements. Then, in Sec. 4.2, the external force at which the failure happens is calculated for different system sizes. After that, Sec. 4.3 shows the change in the number of rattlers, i.e. of grains not contributing to the system's stability, during the failure. The results are summarized in Sec. 4.4.

4.1 Is failure an isostatic transition?

A system is isostatic when the global hyperstatic number $\mathcal{H}$, introduced in Sec. 2.7, is zero. The number $\mathcal{H}$ compares the number of forces transmitted between the particles (contact forces) to the number of degrees of freedom of the particles. The latter is equal to the number of particle forces: for each particle in equilibrium, the two linear forces and the torque of the particle must vanish. When the number of contact forces is larger than the number of particle forces, $\mathcal{H} > 0$, meaning that the system is hyperstatic. When the two mumbers are equal, $\mathcal{H} = 0$, and the system is isostatic. In this particular case, there is only one set of contact forces possible in a stable system. The hypothesis

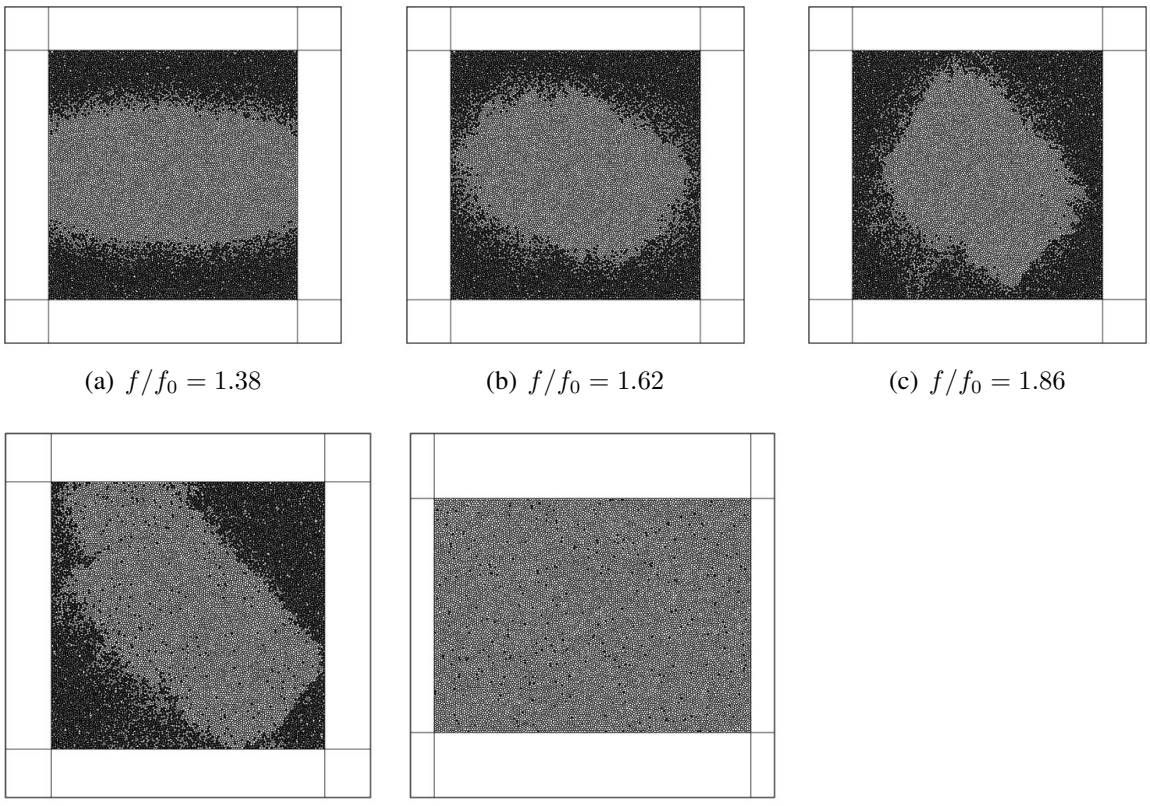

(a) $f/f_0 = 1.38$ (b) $f/f_0 = 1.62$ (c) $f/f_0 = 1.86$

(d) $f/f_0 = 2.10$ (e) $f/f_0 = 2.34$

Figure 4.1: Example of an assembly on the way to the failure. The force on the top and bottom wall f/f_0 is linearly increased, while the force on the sidewalls f_0 is constant. Particles with above average kinetic energy are colored black. The figures are taken at equal intervals of the linearly increasing force f/f_0. The series starts at the top left position. In the first figure, high energy particles appear close to upper and lower boundary on which the external force increases. A transition in the positions of high energy particles is visible from Fig. 4.1(a) to Fig. 4.1(d): close to the failure, which happens between Fig. 4.1(d) and Fig. 4.1(e), the particle motions are highest in two opposite corners of the system, separated by a band in which the energy is lower. This region divides the two regions where particles move to the left (lower left corner in each figure) from the particles that move to the right (upper right corner) at the failure. In the last figure (Fig. 4.1(e)), which is taken after the failure, the high energy grains are not concentrated anywhere.

$\mathcal{H}$		
before t_{trigger}	after t_{trigger}	% of assemblies
> 0	$= 0$	27
> 0	> 1	8
$= 0$	< 0	50
< 0	< 0	8
< 0	$= 0$	8

Table 4.1: Changes of $\mathcal{H}$ that have been observed in 26 different 16 particles systems.

inspected here is whether or not the system crosses the barrier from $\mathcal{H} > 0$ to $\mathcal{H} < 0$ at failure. For a more detailed definition of $\mathcal{H}$, the reader is encouraded to read Sec. 2.7.

It is well known that systems of frictionless grains ($\mu = 0$ in Eq. 2.6) are isostatic at the jamming transition [22, 67, 68], i.e. at the point when the grains come so close to each other that the pressure p in the system becomes nonzero. Are frictional systems ($\mu \neq 0$) also isostatic at the jamming transition? The failure, which is investigated in this thesis, corresponds to the inverse transition (the unjamming), meaning that the kinetic energy rises and particles start moving. The next two subsection contain results on $\mathcal{H}$ at the failure transition in small and large systems.

4.1.1 Small systems

The degree of hyperstaticity $\mathcal{H}$ is investigated in systems of 16 particles with rigid wall boundaries. The graph of $\mathcal{H}$, averaged over 26 granular assemblies, is shown in Fig. 4.2. At the beginning of the simulation, the granular assemblies are hyperstatic with $\mathcal{H} = 6.3$ on average. When the external force is increased as shown in Fig. 2.6, the value decreases rather quickly in the beginning, but this change slows significantly when approaching the time when failure occurs. The data plotted in the graph is too coarse to show what happens at the time of failure.

The lower graph in Fig. 4.2 shows the degree of hyperstaticity close to the trigger mechanism. Before the trigger occurs, the granular systems are on average hyperstatic. Through the trigger at $t = t_{\text{trigger}}$, the average $\mathcal{H}$ falls by 0.7 units, crosses the isostatic line towards hypostaticity and immediately attains its minimum value. Shortly afterwards it increases slightly. This indicates that the trigger event is the essential mechanism that renders the granular system unstable. In the interval after t_{trigger}, which constitutes the region when the kinetic energy of the grains increases quickly, the average of $\mathcal{H}$ does not change significantly.

The crossing of the isostatic line at the trigger event is however not necessary. In fact, before the trigger event, the individual assembly can exhibit $\mathcal{H}$ of any sign: positive, negative, or zero. Tab. 4.1 shows that only 35% of them are hyperstatic ($\mathcal{H} > 0$) before failure. These assemblies mostly become isostatic through the trigger (27% w.r.t. all assemblies), or they remain hyperstatic (8%). Half of all the assemblies turn out to be isostatic before failure, but become hypostatic afterwards. Furthermore, four assemblies (15%) have already been hypostatic before failure, half of which become isostatic through the trigger mechanism (8%), whereas the others remain, with changed or unchanged degree, hypostatic.

Based on the diversity of individual behavior, we conclude that the concept of isostaticity does not allow for the characterization of failure in small frictional granular assemblies.

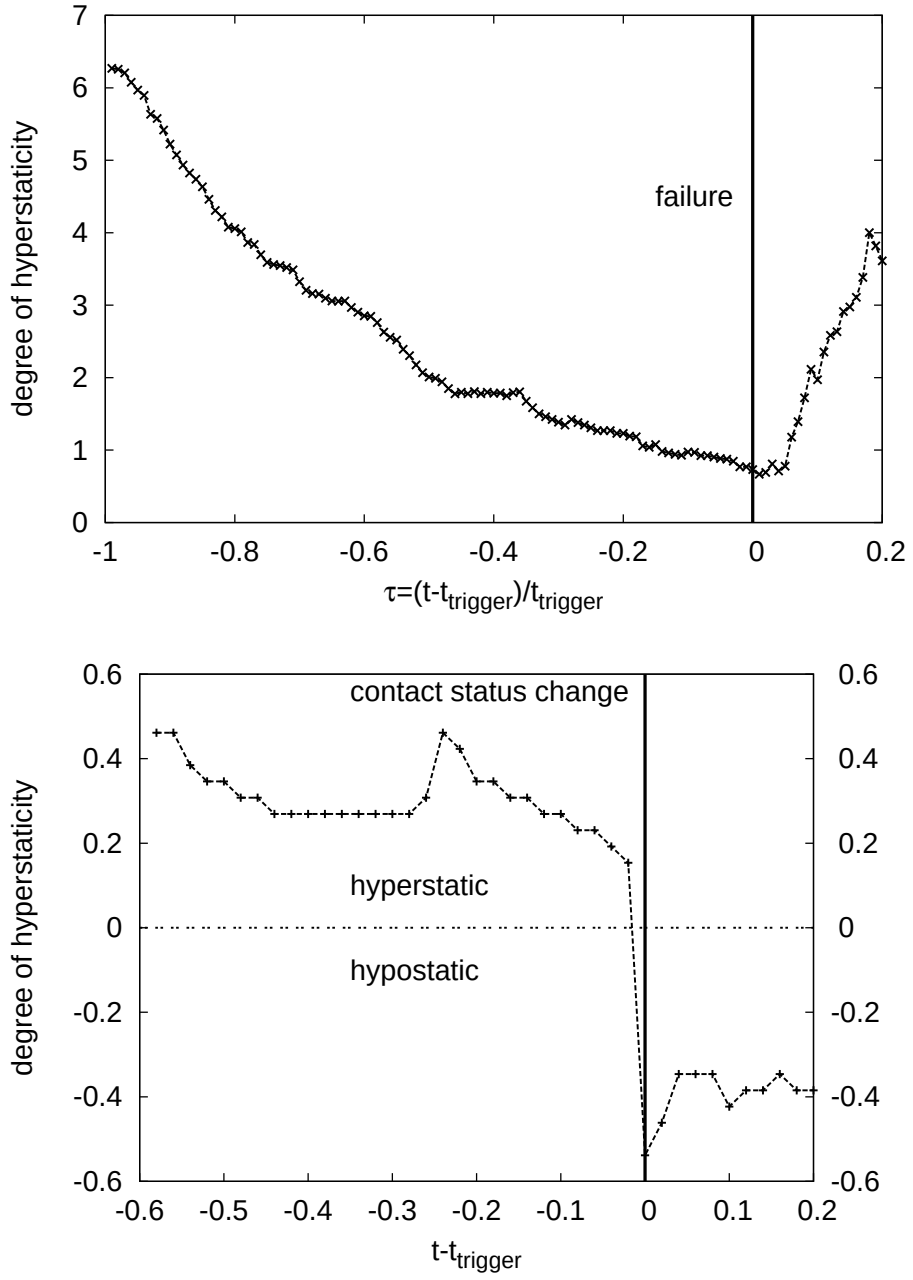

Figure 4.2: Degree of hyperstaticity, averaged over 26 different seeds. Top: Values from the beginning of the simulation until after failure. Bottom: Values for a small time interval around the trigger event. When a contact status change triggers the collapse, this leads on average to a decrease in the degree of hyperstaticity. Note that one time unit in the second figure is on average $1/500$ of a unit in the first figure, hence the period covered by the entire second figure corresponds to less than the thickness of the vertical line in the first figure.

$N_{particles}$	($N_{systems}$)	$\mathcal{H}_{min} < 0$ [%]	$\mathcal{H}_{min} = 0$ [%]	$\mathcal{H}_{min} > 0$ [%]
16	(28)	100	0	0
100	(20)	30	0	70
1936	(5)	0	0	100
20164	(1)	0	0	100

Table 4.2: Minimum hyperstatic number for different system sizes ($k_n = 1600$). For each system size 60 equidistant points are taken in an interval of external force $\Delta f/f_0 \approx 10^{-3}$ for $N < 10^4$ and $\Delta f/f_0 \approx 10^{-2}$ for $N > 10^4$.

4.1.2 Larger systems

In the last subsection, it has been shown that small packings are close to isostaticity, but the individual global hyperstatic number depends on the contact structure of a given assembly. Is this also true for large systems? Because boundary conditions are less important in larger systems, and the scatter in the individual values decreases with system size, the behavior of large systems can be very different.

Instead of determining whether the assembly is isostatic *at the appearance of failure*, we will detect if the system is isostatic somewhere *close to failure*. The advantage is that one does not need to know the precise time when the trigger event appears. This time is difficult to determine in large systems. Finding out which contact change triggers the collapse of a large system would be very difficult, because individual changes cannot be separated in time any more. Instead $\mathcal{H}$ is evaluated at 60 equidistant points in a small interval of external force $\Delta f/f_0 \approx 10^{-3}$ for $N < 10^4$ and $\Delta f/f_0 \approx 10^{-2}$ for $N > 10^4$. This is less than 1% of the change of f/f_0 from the simulation beginning until failure. Table 4.2 shows the values of $\mathcal{H}$ obtained for the different system sizes. The smallest systems with $N = 16$ particles are always hypostatic somewhere in this small interval, while only 30% of the $N = 100$ systems exhibit a negative $\mathcal{H}$ in this range. In larger systems the minimum $\mathcal{H}$ is always positive. This shows that the failure in frictional granular systems is not an isostatic ($\mathcal{H} = 0$) transition.

4.1.3 Conclusion

The average minimum hyperstatic number changes from negative in small systems to positive in large systems. Most probably this change is because of the decreasing influence of boundary conditions. However, other reasons are also possible. One possibility is failure being rather localized. This is at least what Fig. 4.1(d) suggests: two regions of collective motions are separated by a diagonal band. Therefore $\mathcal{H} < 0$ might occur only within the diagonal band. This possibility seems to be a realistic scenario. Organization processes appearing close to the failure show indeed that sliding contacts are concentrated in specific regions. The organization of sliding contacts will be discussed in Sec. 5.5. Further aspects of organization will be discussed in Chap. 7.

While negative $\mathcal{H}$ in small systems indicate that motions are possible, the situation is more complicated in large systems, because $\mathcal{H}_{\min} > 0$. In conclusion, on the basis of a global number of constraints, reflected by $\mathcal{H}$, it is not possible to judge stability. It seems that failure depends on the details of microscopic organization processes, which are not captured by the global hyperstatic number $\mathcal{H}$.

4.2 External force at failure for different system sizes and particle stiffnesses

How does the critical force at failure depend on the particle stiffness and the size of the system in question? Does this force converge to a specific value in the large particle number limit? Is there a large dependence on particle stiffness, so that convergence in the quasi-rigid limit is difficult to achieve? Answering these questions demands an investigation of the time at which failure appears in granular systems.

The time of failure is defined as the instant at which the dimensions of the system change abruptly. At this time, the deviatoric stress $\sigma_d = \frac{1}{2}(\sigma_y - \sigma_x)$, introduced in the introduction of the thesis in Eq. 1.1, decreases abruptly. It does so because the stress in y-direction $\sigma_y = f/L_x$ decreases when L_x increases, while $\sigma_x = f_0/L_y$ increases when L_y decreases at the failure. To monitor the time of this happening one can monitor the stress, or one can check for changes in L_x and L_y. The latter is done here. When the rate of change $\dot{L}_y$ exceeds a predefined threshold, which is only surpassed at the failure, the system deforms and thus fails. One is usually not interested in the change of L_x and L_y but in the critical value of the force f. This value is investigated in this section. First, we will discuss the dependence of the critical force on stiffness in Sec. 4.2.1. Then the critical force for different system sizes is compared in Sec. 4.2.2.

4.2.1 Dependence of failure on the particle stiffness

First of all, the time of failure depends on the stiffness of the particles. This is clear as the number of contacts decreases when the particles become stiffer (see Sec. 2.12). Therefore the time of failure decreases with increasing stiffness. This is shown in Fig. 4.3. The value of the critical force decreases by roughly 10% when the stiffness is increased by one order of magnitude from $k_n = 160$ to $k_n = 1600$. This decrease is accompanied by a small but significant decrease of the standard deviation from $\sigma_f = 0.32$ ($k_n = 160$) to $\sigma_f = 0.27$ ($k_n = 1600$). It can therefore be concluded that the stiffness of the particles does to some extend matter for the prediction of the time or critical force when the failure appears, but the dependence on stiffness is rather weak.

4.2.2 Dependence of failure on the system size

This investigation was done using a program intended for studying granular behavior under cyclic loading. During one cycle, a sinusoidal change in the applied load with a tunable amplitude is applied:

$$f(t) = f_0 + 2\left(1 - \cos\left(2\pi\frac{t}{T}\right)\right). \tag{4.1}$$

Here, $f_0 = 1$ is the initial force and the period is $T = 500$, except for the largest systems with 20164 particles, where it is 200. Failure always appears at $t \approx 0.2T$. The particle stiffness is $k_n = 160$.

Table 4.3 shows the system size dependence of the external force at failure for assemblies with rigid wall boundary conditions. The first column shows the number of particles and the number of systems over which the average is taken (in brackets). The second column shows the average external force at which the packings fail, followed by the standard deviation in the third column. The numbers show that failure happens on average always at the same force, independent of the size of the packing. The scatter in the force just falls short of the average value for systems with $N < 10^2$

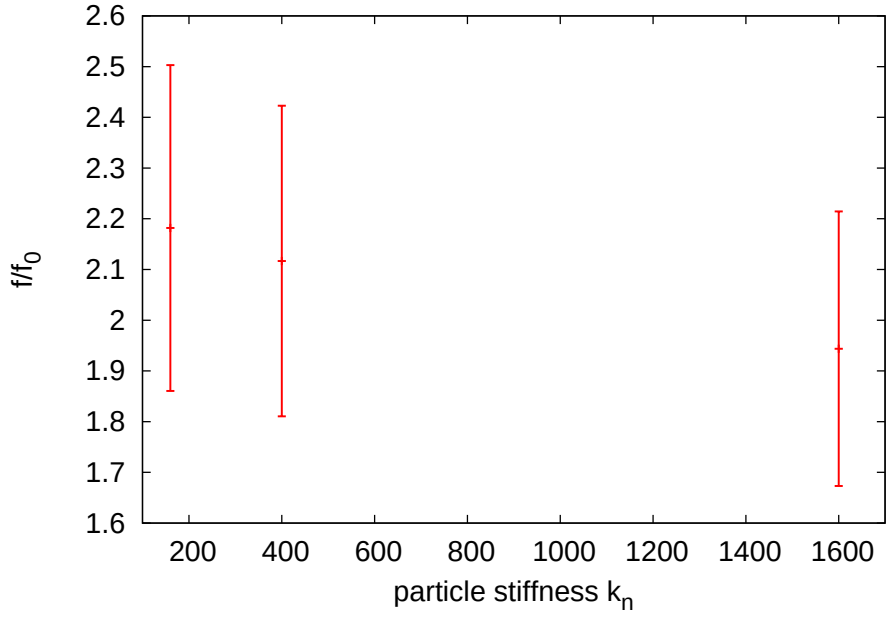

Figure 4.3: Average vertical external force at the failure of granular systems with $N = 100$ particles for different particle stiffnesses (averages over 20 Systems).

particles, but quickly decreases for larger systems. For $N > 10^3$, the scatter is already one order of magnitude smaller than the mean. Finally, the force at failure in systems with $N > 10^4$ particles shows variations below 2% of the mean.

The average force at failure is 2.2 times the initial force at the simulation beginning. Although this value certainly depends on the chosen friction coefficient (here $\mu = 0.25$), it shows that the systems can bear forces much higher than the initial forces.

The convergence behavior of the external force at failure with increasing system size seems to be barely influenced by the applied boundary conditions. This can be seen by comparing Tabs. 4.3 and 4.4. Table 4.4 shows the force at failure for membrane boundary conditions. The force at failure depends on the boundary conditions (here $f_{\text{fail}}/f_0 \approx 2.5$ for membrane boundaries), but the convergence of the average with increasing system size is similar. The standard deviation of the individual force values decreases also in the same way as it does when rigid wall boundary conditions are applied: for the membrane simulations it decreases from $\sigma_f = 0.69$ for $N = 16$ particles packings to $\sigma_f = 0.09$ for $N = 8100$ particles systems. For systems with rigid wall boundaries it decreases from $\sigma_f = 0.85$ for $N = 16$ to $\sigma_f = 0.03$ for $N = 8100$.

$N_{particles}$	($N_{systems}$)	f_{fail}/f_0	σ_f
16	(91)	2.40	0.85
225	(20)	2.32	0.23
4096	(3)	2.20	<0.01
8100	(3)	2.20	0.03
20164	(1)	2.19	-

Table 4.3: External force at failure in packings with rigid wall boundary conditions. Systems with $> 10^3$ grains fail at very similar values f_{fail} of the external force. The columns contain the following data (from left to right): grains per system (number of systems), average external force at the failure of the systems, standard deviation of the external forces.

$N_{particles}$	($N_{systems}$)	f_{fail}/f_0	σ_f
16	(100)	2.50	0.69
225	(20)	2.18	0.52
4096	(3)	2.62	0.06
8100	(3)	2.49	0.09
20164	(1)	2.48	-

Table 4.4: External force at failure in packings with membrane like boundary conditions. Assemblies with $> 10^3$ grains fail at almost the same time, although the standard deviations are slightly larger than with rigid wall boundary conditions (Tab. 4.3). The columns contain the following data (from left to right): grains per system (number of systems), average external force at the failure of the systems, standard deviation of the external forces.

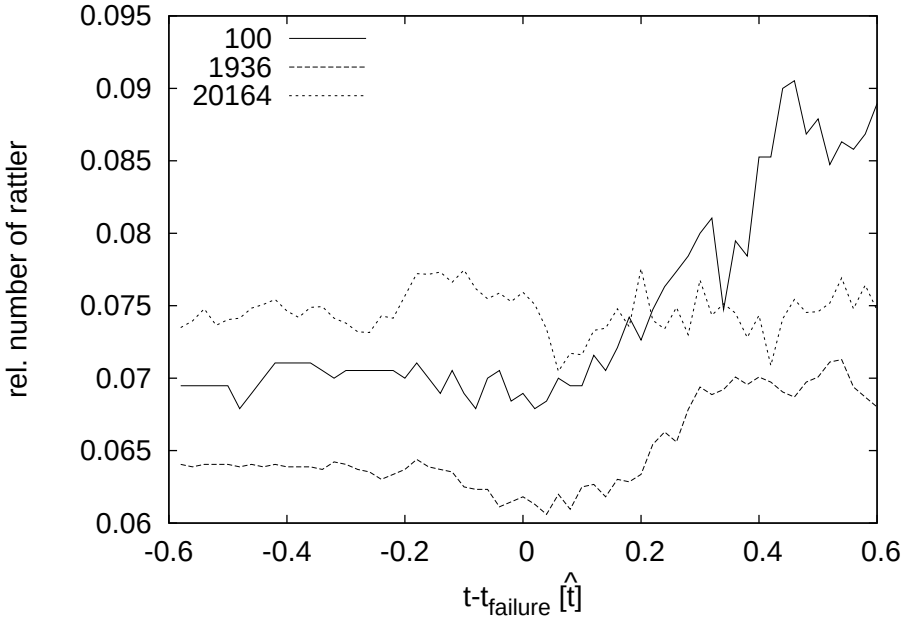

Figure 4.4: Average fraction of grains that are rattlers for systems with 100 (3), 1936 (3) and 20164 (1) particles around the time when failure happens. The number of systems is indicated in brackets.

4.3 Does the number of rattlers change at failure?

Grains that are not part of the force carrying structure of the system have usually no contacts (but might occasionally have one) and can move freely in voids bounded by neighboring particles. The grains that are free to move are called rattlers. We want to investigate if they are involved in the failure process. Does their number change during the failure? If this was true, then we might need to inspect the rattlers in more detail.

Figure 4.4 shows the fraction of rattlers in systems with $N = 100, 1936$ and 20164 particles for a small interval of time around the appearance of failure. The interval of time shown, $\Delta t = 1.2$, corresponds to a range in external force which depends on the system size. For systems with $N = 100, 1936$ and 20164 it is $\Delta f = 9.6 \times 10^{-5}, 9.6\times, 10^{-4}$ and 4.8×10^{-2}. The size dependence of Δf arises because the external force in Eq. 2.71 on the larger systems is increased at a higher rate α. However, in comparison to the total simulation time ($t_{\rm sim} > 100$) these intervals of time are always very small. Thus the figure shows a very small period around the appearance of the failure. The time axis is centered around the time of failure $t_{\rm failure}$. This time coincides with $t_{\rm trigger}$, the time at which a trigger of failure appears in the small systems in Chap. 3.

Fig. 4.4 shows that at the happening of failure, in the smallest systems with 100 particles, the number of rattlers increases towards the end of the plot. It is then slightly larger than in bigger systems. The intermediate systems with 1936 particles have a smaller number of rattlers, and their number shows smaller variation. A small minimum in the number of rattlers at about $t = t_{\rm trigger}$ is visible in the figure. Towards the end of the scale, the number of rattlers increases slightly, similar to the increase in the smaller systems. The large packings with 20164 particles have an almost constant number of rattlers throughout the range of Fig. 4.4. Their number is slightly above the number of

rattler in smaller systems in the beginning, and lies between the $N = 100$ and the $N = 1936$ particles systems' number of rattlers at the end of the plot in Fig.4.4.

From the small number of rattlers and the negligible fluctuation in their number in large systems it can be concluded that, although rattlers are obviously related to the internal structure of the system, their number is not much affected by the failure process. Hence the failure of granular systems does not create many additional rattlers.

4.4 Conclusion

In this chapter some interesting properties of the failure of granular systems have been investigated for different numbers of particles. Section 4.1 showed that failure is not an isostatic transition. We will see in the next chapter that failure in large systems is concentrated in specific regions inside the system. Thus the idea of failure being an isostatic transition might still be valid locally. Section 4.2 showed that the time or force at which the failure happens is almost independent of the system size N, and the scatter in force decreases with increasing N. The grains' stiffness does not affect much the force at which the failure happens. This suggests that compounds of very different stiffness are similar in terms of their structural stability. The last section, Sec. 4.3, is concerned with the relative number of grains which are not part of the load carrying structure of the system. The data shows little change in their number during the failure, suggesting instability is not connected to the creation of rattlers.

The results in this section show that it is necessary to investigate systems larger than the ones in Sec. 3, because the large systems behave differently from small ones. The next sections consider the properties of such large systems in more detail.

Chapter 5

Weakening process in large two-dimensional systems

In the last chapter, the concern was the generalization of failure properties to much larger systems than in Chap. 3. In this chapter the details of the softening process, prior to the appearance of the failure, is examined in detail for one example of a large system with $N = 16384$ particles. For this system size, all quantities investigated in Chap. 3 vary only little from one system to another one. Hence averaging over many systems, like it was done in the $N = 16$ particles analysis in Chap. 3, is not needed, and one example of a system is enough to understand the physical attributes in large systems.

To begin with, in the first section the stress, i.e., the external force exerted onto the system, is compared to the resulting strain, i.e., the macroscopic deformation. The stress-strain curve is a common means for investigating mechanical stability in solids. The increasing deformation leads to an increase in the kinetic energy of the particles of the system. This energy is examined in Sec. 5.2. Deformation and increasing particle motions are related to a changing volume, and a varying number of contacts. These are considered in Sec. 5.3. Besides these changes, some contacts eventually become sliding, and this process contributes to the softening of the system. Section 5.4 examines the evolution of the number of sliding contacts, and shows that the strength of these contacts is increasing. The sliding contacts are not always random distributed in the system. Section 5.5 examines their ordering tendency as a function of increasing external force. The section thereafter, Sec. 5.6, puts the results together by revealing that the way to the failure can be divided into two periods. In these two period, the granular system shows two qualitatively different behavior. Many quantities investigated in this chapter change their behavior from the first region to the second. And although the precise transition region might depend on the quantity in question, the results suggest this transition is happening at roughly the same time for all quantities. Sec. 5.7 is concerned with the most stable structures one can find in a two dimensional solid. It turns out that these structures, composed of three grains and connected by three contacts (*triangles*) are very important for the stability of the system. Sec. 5.8 closes the chapter with concluding remarks.

5.1 Stress-strain curve

Fig. 5.1 shows a typical stress-strain curve for one simulation. Here, the deviatoric strain is defined as

$$\epsilon = \epsilon_x - \epsilon_y = \frac{L_x - L_{x0}}{L_{x0}} - \frac{L_y - L_{y0}}{L_{y0}}\,, \tag{5.1}$$

Where L_x, L_y are the horizontal and vertical length of the system, sketched in Fig. 2.6, and L_{x0}, L_{y0} are their initial values. The quantities ϵ_x, ϵ_y are the relative deformations along x and y-direction. Similarly, the deviatoric stress is

$$\sigma_d = \sigma_y - \sigma_x = \frac{f(t)}{L_x} - \frac{f_0}{L_y}\,. \tag{5.2}$$

σ_x, σ_y are the stresses in x and y-direction. With these two definitions one can construct the stress-strain curve. We will refer to the slope of this curve in Fig. 5.1 as the *stiffness of the assembly*. At the beginning of the simulation, the assembly's stiffness is about equal to the stiffness of an individual grain, which is $k_n = 1600$. As the stress increases, the assembly becomes softer. The thin arrows indicate two "precursors" or small rearrangement events preceding failure. These events leave no clear sign on the stress-strain graph, but appear clearly when other quantities are plotted. We will examine the precursors in detail in Sec. 6. Finally, the slope of the curve becomes nearly flat, and the assembly is very weak. Then little horizontal jumps appear that are associated with rearrangement processes. These are events where the walls move rapidly. The heavy arrow indicates the beginning of failure, which is defined as the event where the strain crosses a threshold of 5%. This value is more than twice the strain just before failure, but much lower than the strain directly after failure.

Note that failure could have equivalently been defined as the point of maximum stress in Fig 5.1. The sudden deformation leads to L_y decreasing, while L_x increases in Eq. 5.2. Thus σ decreases through the failure. When this happens, the grains' kinetic energy increases strongly.

5.2 Kinetic energy and vibrations

During the simulations, the kinetic energy E_{kin} rises as the packing becomes softer due to some contacts becoming sliding and some contacts disappearing. This behavior is shown in Fig. 5.2. For instance, a two-decade increase of E_{kin} is accompanied by a one-decade decrease of stiffness. When the system becomes very soft, vibrations become much larger in amplitude. The first pronounced vibrations appear at the two precursors from Fig. 5.1. They are also indicated in Fig. 5.2 but not visible on the scale of the figure, for their short duration is comparable to the distance between two consecutive data points. On the other hand they provoke slowly damped long range vibrations, visible in Fig. 5.2. The typical oscillation period observed is $T = 2 \times 10^{-3}\hat{t}$. The interval from the beginning of the simulation until the failure corresponds to $\sim 4\,10^4$ oscillation periods. This might seem a very long interval of time. Yet it is much shorter than realistic time scales, for instance those inspected in experiments. On the way to the failure, several more precursors appear, increasing the vibrations further. Finally failure shows up as a pronounced maximum of kinetic energy at about $f/f_0 = 2.15$.

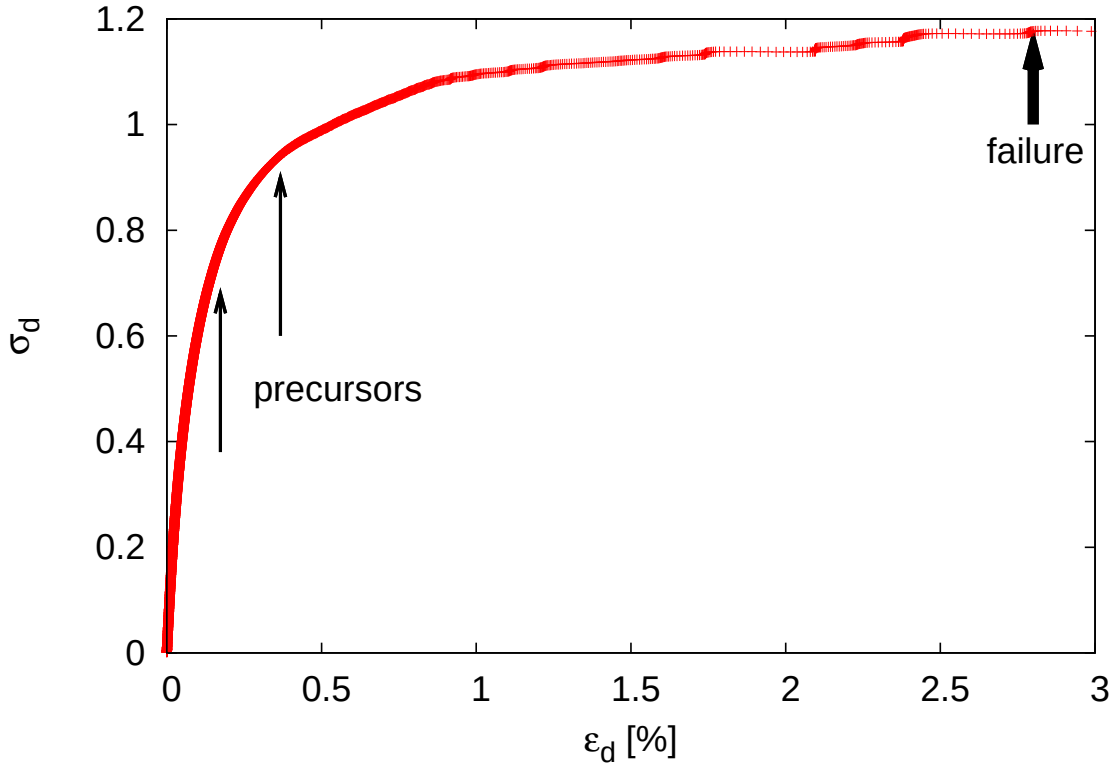

Figure 5.1: Deviatoric stress versus deviatoric strain for a typical quasi-static simulation with a large number of particles (parameters defined in Secs. 2.5, 2.11 and discussed in Secs. 2.11, 5.1). The two slim arrows indicate two precursors which are also indicated in Figs. 5.2, 5.5, 5.6 and 5.7. The heavy arrow indicates the beginning of the failure. When failure happens, the strain jumps to a value close to 22%.

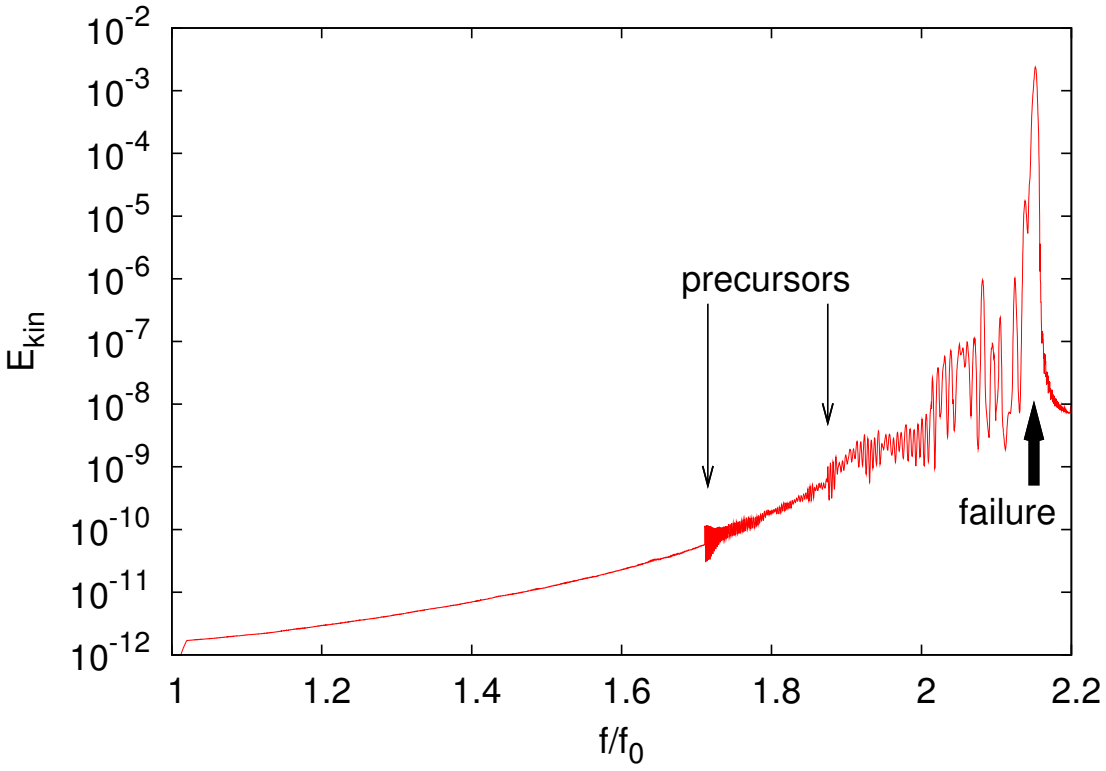

Figure 5.2: Kinetic energy for one simulation at $\alpha = 1.28\ 10^{-2}\hat{f}/\hat{t}$. At the failure, $E_{\rm kin}$ rises by many orders of magnitude (heavy arrow). Prior to the failure, precursors appear, which can be considered localized failures. We will examine their properties in Chap. 6.

5.3 Volume, injected power and number of contacts

One expects the volume of the packing to decrease with the increase of f_{ext} (Fig. 5.3), because the particles are deformable. However, this decrease is very small for the stiff particles system: its maximum is $\Delta V_{\max}/V_0 = -0.05\%$ at $\epsilon = 0.25\%$. With the decrease of V, one expects the number of contacts M to rise due to the particles getting closer to each other. But one observes a *decrease* in M during this interval of increasing strain ϵ. The decrease implies that the particles try avoiding each other. But what is the reason for this behavior? Solving this riddle needs first of all recalling that friction is disabled in the preparation of the system. Thus the system's density is close to densest packing in the beginning. Turning on friction after the preparation will block certain types of particle motion, providing a possible reason for the decrease of M, although the density increases. Remember that contacts put constraints on the particles motions, a decreasing number M allows for more motions.

In the second period, after $\epsilon = 0.25\%$, the volume starts to increase again, while M still decreases, but at a lower rate. Note that the continuing increase in V is almost linear in ϵ, while the rate of the decrease in M slows further down with ϵ increasing and vanishes at the failure.

Therefore we have two periods in Fig. 5.3: a decrease in volume until $\epsilon = 0.25\%$, and thereafter an increase in V until the failure. From the perspective of thermodynamics, an increasing volume under increasing pressure indicates a *negative compressibility*, and a thermodynamically unstable system: the system is expected to explode. The simulation results show however that the system is stable, and it takes some more force to make it fail. The key to resolving this paradox is that the stress is strongly anisotropic: $f_y \sim 2f_0 = 2f_x$ in Eq. 5.2. If the stress was increased by the same amount from all sides, V would decrease, or otherwise the system would indeed explode. But the strong anisotropy causes the average stress in the system to increase, while along one direction the external stress on the boundaries is constant ($\sigma_x = f_0/L_y \approx const$). Thus the higher stress inside the system pushes the sidewalls outwards (L_x increases) while in the direction of increasing external stress the dimension decreases as expected ($L_y \searrow$).

An increase in volume usually means that the system is loosing energy, because the inverse process of decreasing the volume needs the injection of power. However, when calculating the power injected at the walls (Fig. 5.4) one sees that it is always *positive*: the energy of the system always rises.

A loss in contacts M also always implies a loss of additional possibilities to stabilize the packing: when fewer contacts are present, it is more difficult for the system to balance a higher load. Figure 5.1 shows that the higher the actual load, the more the system deforms with a further increase. This evidences that a lower number of contacts correlates with a higher deformation. Besides the number of contacts, sliding contacts require special care. These are detailed in the next section.

5.4 Sliding contacts

5.4.1 Number of sliding contacts

The number of sliding contacts rises as the deviatoric part of the external stress on the packing is increased (Fig. 5.5). Previous works [55, 56, 69, 70] lead one to suppose that the number of sliding contacts finally attain a maximum at failure. However, this is not true, as the maximum is attained well before failure (Fig. 5.5). This maximum coincides with the minimum in volume, shown in the

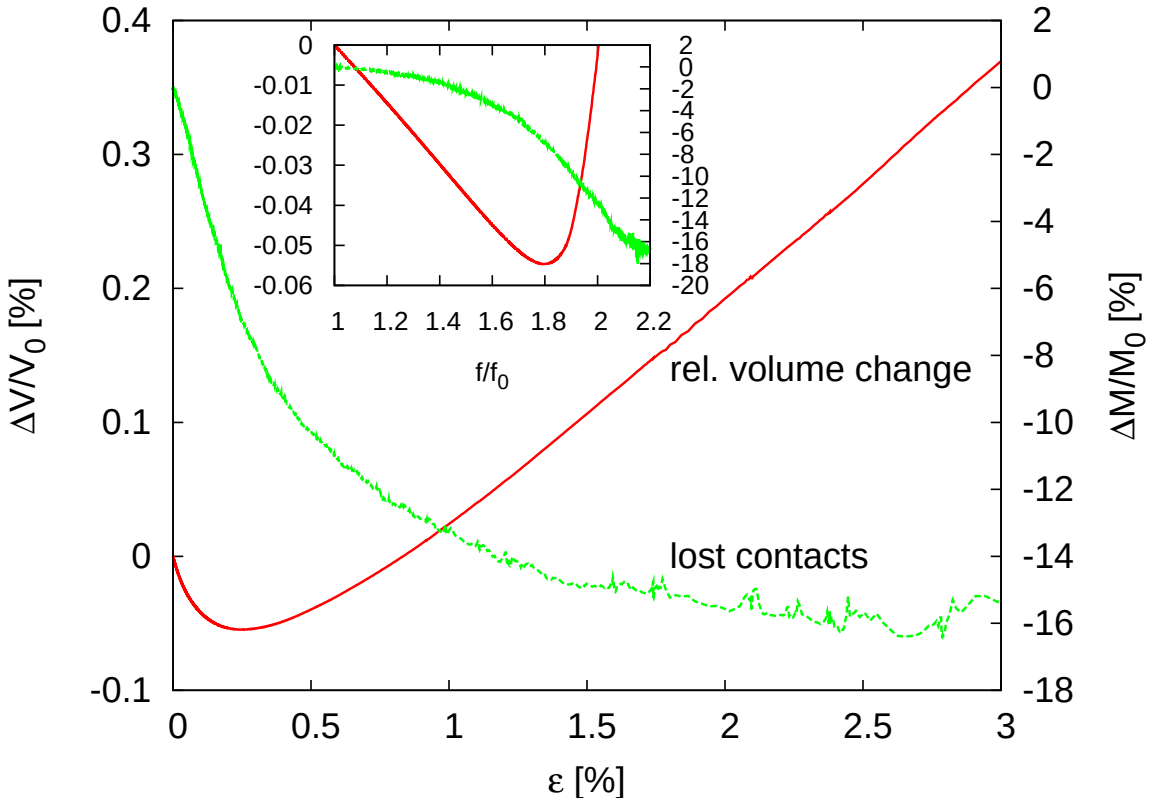

Figure 5.3: Relative change of the volume (left scale) and relative change of the number of contacts (right scale) as a function of deviatoric strain. The inlay shows the same quantities as a function of external force. The initial number of contacts is $M_0 = 32798$.

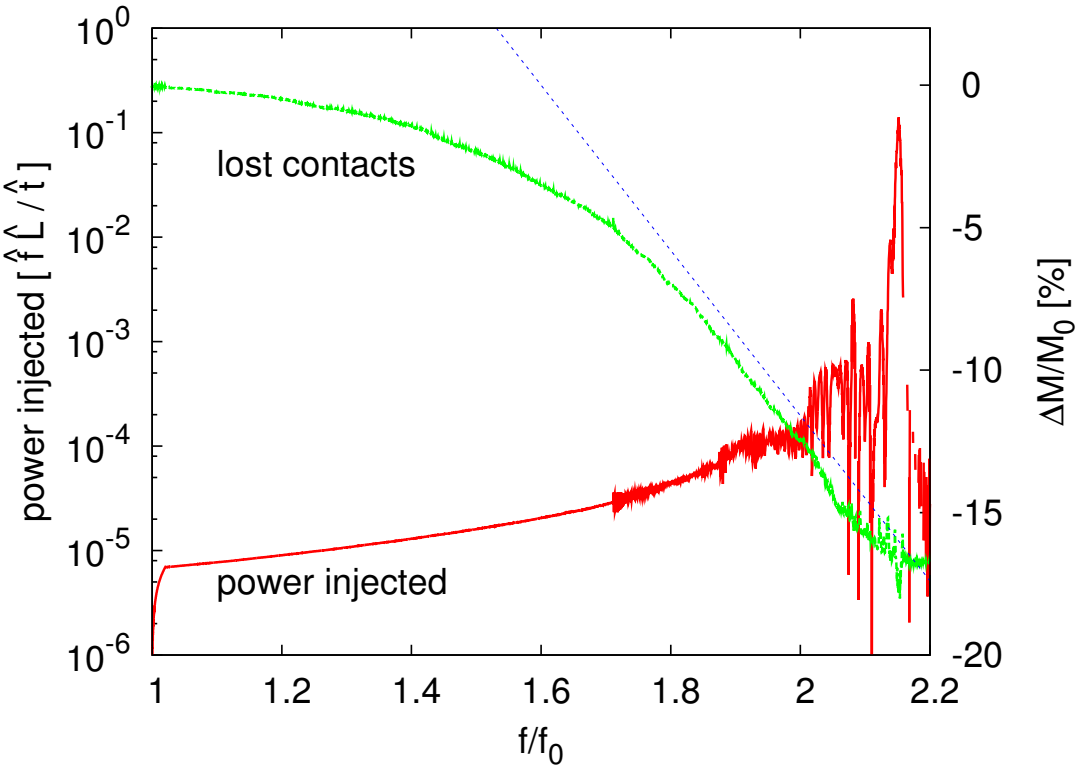

Figure 5.4: Power injected into the system (left scale) and relative change of the number of contacts (right scale) as a function of external force. The power injected per unit of time increases quickly after $f/f_0 = 1.8$. Simultaneously, the number of contacts decreases linearly (the dashed line is a guide to the eye).

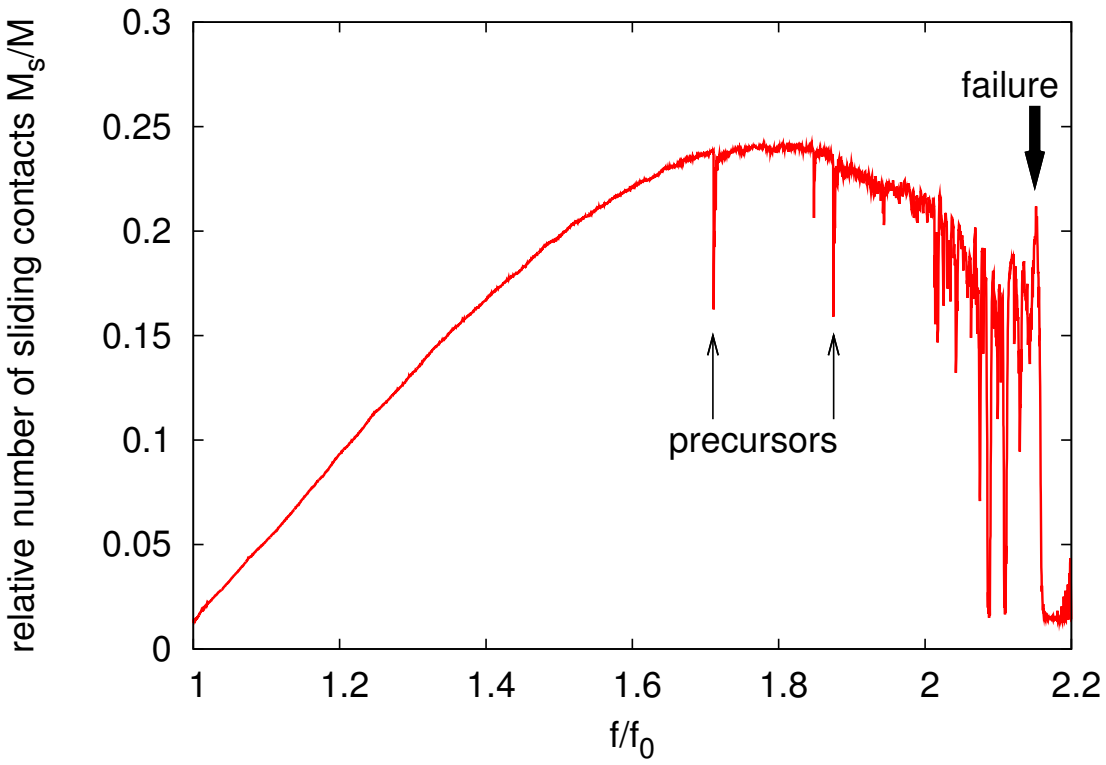

Figure 5.5: The number of sliding contacts M_s, normalized by the total number of contacts M. There is always a decrease of M_s/M before failure, followed by an increase at the failure. Right after the failure M_s/M is close to zero, as only the contacts with the walls remain sliding ($\mu_{\text{wall}} = 0$).

inlay of Fig.5.3. In small packings the existence of a maximum before the failure is not observed, probably because of the limited number of contacts. This small number allows only for few contact status changes at a time, and every change results in large changes in the stability of the granular assembly. Therefore very few changes can already lead to instability and cause failure [55].

One observes that when the increase in M_s becomes slower, the number of sliding contacts plunges at certain positions and then quickly recovers. The sudden plunges in the number of sliding contacts are the signature of precursors. In much faster simulations ($\alpha \gg 10^{-2}$ in Eq. 2.71), they are not observable. This was carefully checked on the basis of an equal number of data points for many simulation speeds.

During failure, large rearrangements occur, and almost all sliding contacts between particles disappear or close.

5.4.2 Strength of Sliding Contacts

Fig. 5.6 shows the average normal force $\langle F_n \rangle$ at a contact and compares its value to the average normal force at a sliding contact $\langle F_n \rangle_{\text{sliding}}$. $\langle F_n \rangle_{\text{sliding}}$ is always much smaller than $\langle F_n \rangle$, in accord with the findings of Ref. [71]: most sliding contacts transmit less than average forces. Both $\langle F_n \rangle$ and $\langle F_n \rangle_{\text{sliding}}$ increase about linearly in the first half of the simulation. However, the average force at sliding contacts increases much faster than the average force for all contacts. Then, later in the simulation, $\langle F_n \rangle$ increases faster than before, whereas the increase in $\langle F_n \rangle_{\text{sliding}}$ slows until a plateau is reached close to the failure.

Note that in the beginning of the simulation the average force at sliding contacts is very small. Therefore the first appearing sliding contacts are very weak contacts. As the deviatoric stress is increased, new sliding contacts appear that carry larger forces. When the maximum in M_s is reached, the increase in $\langle F_n \rangle_{\text{sliding}}$ becomes slower. Finally $\langle F_n \rangle_{\text{sliding}}$ attains a maximum when M_s starts to decrease again. This leads to the conclusion that while sliding contacts constantly disappear, this does not change the average force at sliding contacts. This finding implies that sliding contacts are not part of the force chains carrying the external load. On the other hand the global mean $\langle F_n \rangle$ increases strongly close to the failure. We will see in the next subsection that this behavior is linked to the disappearance of contacts, so every remaining contact has to carry a higher fraction of the load, on average.

5.4.3 Understanding the evolution of sliding contacts

We will now examine in detail the variation in M_s. We will see that both the increase and the following decrease can be understood in terms of the frequency of transitions between the three contact statuses that have been introduced in Sec. 2.1: closed, sliding, and open.

In Fig. 5.7 the most important contact status changes are shown. In the beginning the most frequent transitions are from closed to sliding $C \to S$. But the number of inverse transitions $S \to C$ increases exponentially, and becomes approximately equal to the frequency $C \to S$ at about $f/f_0 = 1.7$, i.e., near the maximum of M_s. From then on, the two transitions cancel each other, i.e. their difference fluctuates around zero. The third most important transition is $S \to O$. Once $S \to C$ and $C \to S$ cancel each other, $S \to O$ leads to the decrease in M_s that is observed in Fig. 5.5 before the failure. The other possible contact status changes (not shown in the figure) are much less frequent. At the failure itself at $f/f_0 \approx 2.15$, all sorts of contact changes become very important, even those

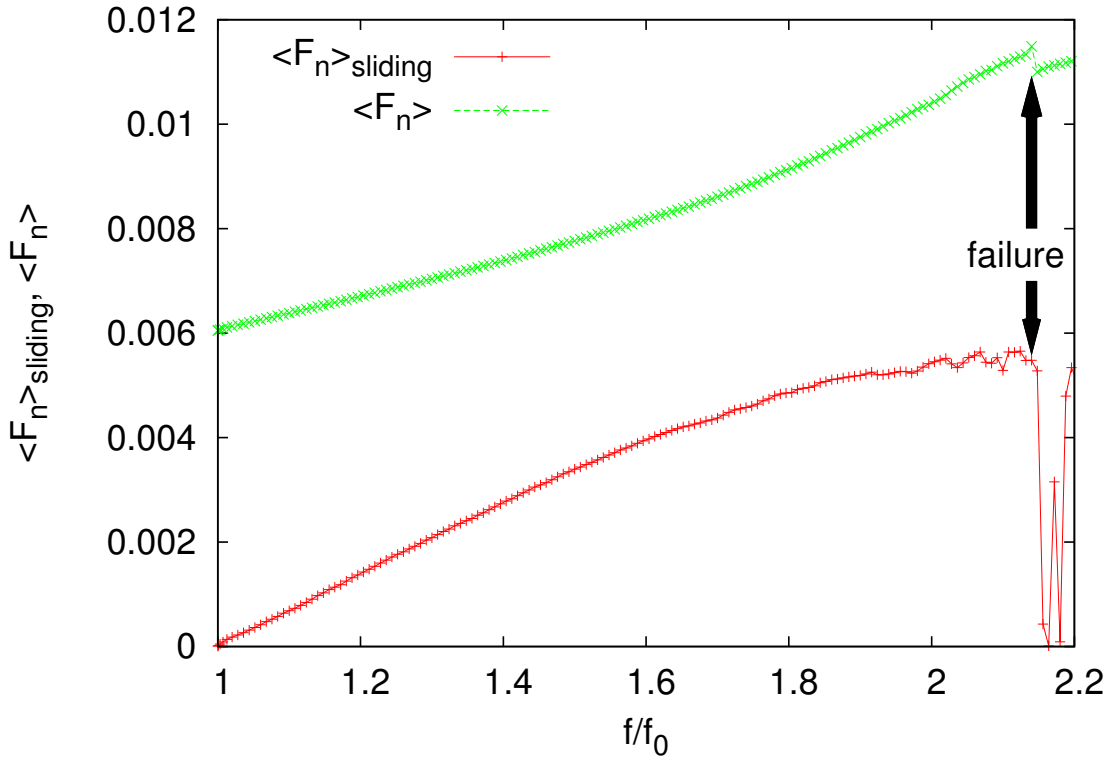

Figure 5.6: Average normal force transmitted at a contact, and average normal force transmitted at sliding contacts. For details see Sec. 5.4.2.

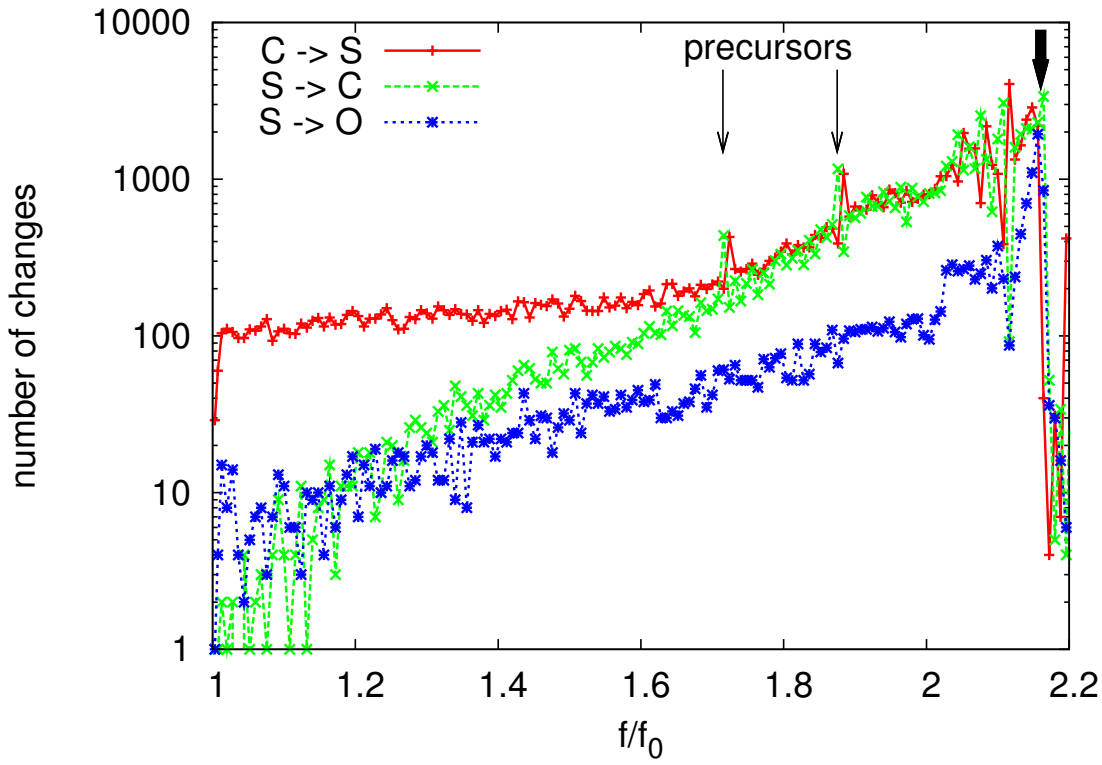

Figure 5.7: Rate of the contact status transitions which involve sliding contacts (S). The figure shows the number of transitions occurring in intervals of external force $\Delta f/f_0 = 8 \times 10^{-3}$. The initial number of contacts is $M_0 = 32798$. The heavy arrow indicates the failure. See Sec. 5.4.3 for details.

that are not displayed. The signature of two precursors can also be seen in the figure: sharp peaks in $C \to S$ and $S \to C$ at $f/f_0 \approx 1.75$ and 1.9 (See the next section for details on precursors).

Another important question is the spatial organization of sliding contacts, which will be investigated in the following.

5.5 Local number of sliding contacts

5.5.1 Definition of boxes

There are quantities one wishes to evaluate for both the whole system (global characteristic) or just for small parts of the system (variations, fluctuations). The latter allows for statistical evaluation of the values. In this section the number of sliding contacts is such a quantity which is analyzed in small regions or boxes that first have to be defined. We choose the length of a quadratic box to be $l = 8r_{av}$, where r_{av} is the average particle radius. This choice gives boxes containing about 16 particles with roughly 24 contacts. In this counting, only contacts between the particles in a box are considered, and contacts between adjacent boxes are disregarded. The resulting boxes are shown in Fig. 5.8.

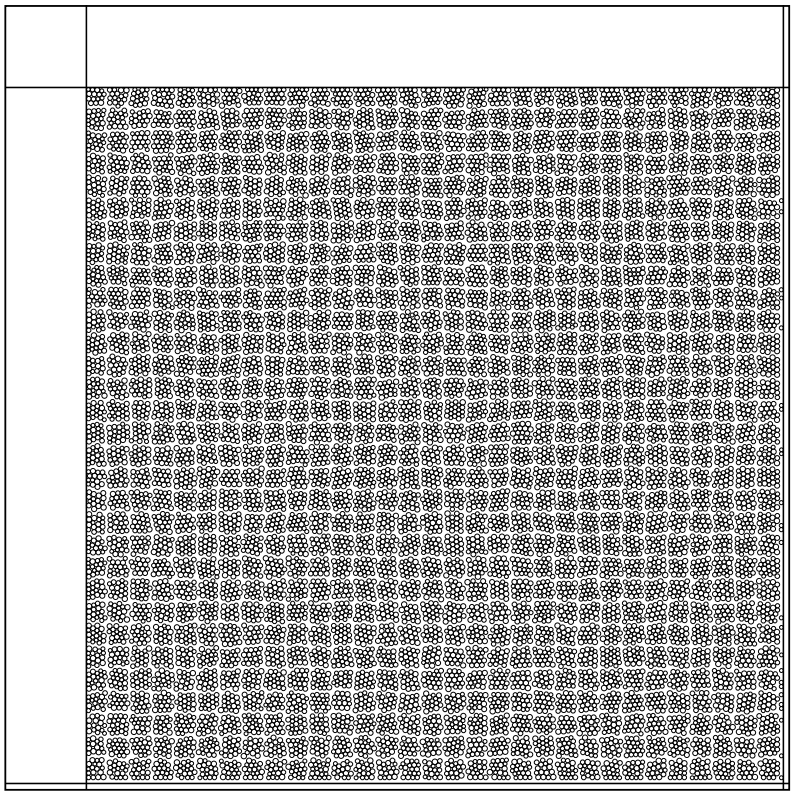

Figure 5.8: Sketch of the boxes with length $l = 8r_{\mathrm{av}}$. Small spacings distinguish the boxes.

Small velocities might occasionally lead to a particle changing the box. This is unfortunate, because it changes the configuration of the box it comes from, and also that of the box it goes to, leading to time dependent results. The workaround is to assign the particle only once to a box at the simulation beginning, and consider it always belonging to that box. Although only about 1% of the grains change the box number until the failure, with this procedure we are on the safe side.

When calculating the number of grains in a box, one observes that it contains on average 17.4±1.5 particles. Because 17 or 18 grains can be connected in many more ways than 16 particles, this number results in a significantly higher number of contacts than in the small systems of Sec. 3 with $N = 16$ particles. While in Sec. 3 we have on average 19.3±1.8 contacts between the grains, here one region contains on average 25.4±5.3 contacts.[1] This is an increase of 31%.

The boundary conditions of the boxes are naturally different from that of the small systems in Chap. 3. While grains at the boundary of a box touch particles in surrounding boxes, the small systems have rigid walls at the boundaries. Despite this difference, the behavior of the two might in some respect be similar.

Only contacts between two particles of the same box are taken into account, and contacts between particles in different boxes are ignored. These boundary conditions for the boxes are also applied in [72]. To include all contacts at least once, the boxes are therefore offset by $0.5l$ against each other, in both x and y-direction independently. The overlap of adjacent boxes by half of their size assures that we incorporate every contact in at least one box. In an assembly with N=16384 particles, we have about 20 boxes in each direction, giving a total of 400 boxes. This number provides good statistics. Particle-wall contacts are not taken into account, because they might have very different properties. For instance, they are always sliding.

5.5.2 Number of sliding contacts in boxes

In Fig. 5.9 the probability distribution of the number of sliding contacts M_s in one box is shown. This number is called the *local number of sliding contacts*. Initially, most regions have no sliding contacts. As the external force is increased, the mean number of sliding contacts in a box $\bar{M}_s$ and the width of the distribution both increase monotonically. Then there is a maximum in $\bar{M}_s$, attained at $f/f_0 = 1.80$ in Fig. 5.9. The duration of this maximum is similar to the one in Fig. 5.5, where the fraction of sliding contacts in the system is shown. The distribution is about symmetric at that time. A further increase of the external force results in $\bar{M}_s$ decreasing again, while the width of the distribution remains about constant. Close to the failure of the system, the distribution shifts to lower values of M_s, while the shape of the distribution is similar. Finally, the failure at $f/f_0 \approx 2.16$ results in almost all sliding contacts disappearing. The probability distribution thereafter is a virtual clone of the one at the simulation beginning: the process of weakening and failure starts from the beginning.

5.5.3 Local change and disappearance of sliding contacts

The average number of sliding contacts in a box changes continuously with the external force f until the failure, as shown in the last subsection. But how does this number evolve in the individual box? To investigate if fluctuations are large, One possible approach is to look at the change ΔM_s of this number, and calculate its norm. Taking the average over the individual values, one can see how much the number of sliding contacts changes on average in a box in an interval $\Delta f/f_0 = 6.4 \times 10^{-3}$.

[1] Contacts with walls are not considered in both of the cases.

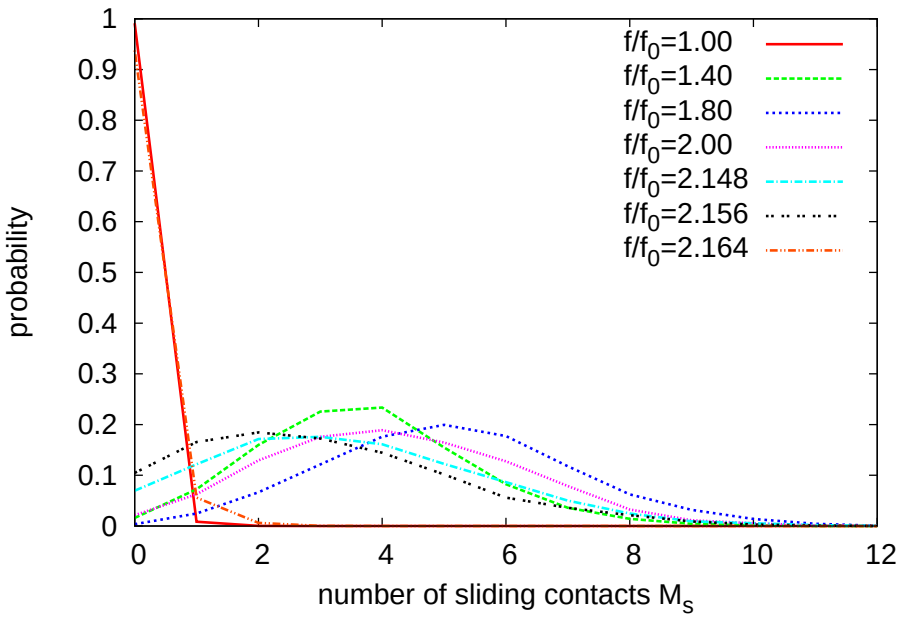

Figure 5.9: Probability distribution function of the number of sliding contacts in local regions ($l_{loc} = 8\bar{r}$). At the beginning of the simulation, only a few regions contain sliding contacts, and there at most two sliding contacts in a region. The average number increases with f until $f/f_0 \approx 1.8$. Afterwards it decreases again and becomes broader until the failure. After the failure at $f/f_0 = 2.16$, the distribution recovers its initial shape.

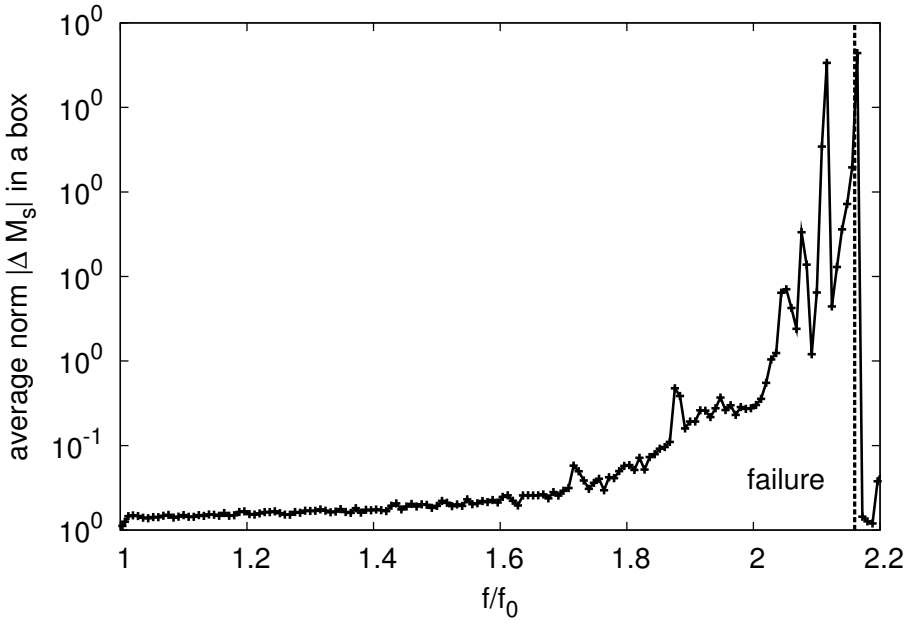

Figure 5.10: Mean norm of change ΔM_s in a box in an interval $\Delta f/f_0 = 6.4 \times 10^{-3}$. Failure is marked by a vertical line.

This number is shown in Fig. 5.10 for different f. At small f, in the beginning of the simulation, the number of sliding contacts changes only slightly with f, although the total number of sliding contacts increases quickly (see Fig. 5.5). This behavior is observed until the end of the first period at $f/f_0 = 1.8$, when the total number of sliding contacts is maximal. In the second period until the failure, the norm of the changes increases very quickly with f, and attains an absolute maximum at the failure. Note that during the second period, the number of sliding contacts is decreasing (see Fig. 5.5. This decrease happens at a lower rate than the increase in the beginning, but on the other hand, the average change in sliding contacts in a box is much larger in this second period than in the first one.

We have seen in Fig. 5.5 that failure means all sliding contacts in the system become nonsliding. If something like a localized failure exists, one should be able to observe the same behavior on the local scale. It is therefore appealing to calculate the number of boxes in which first some contacts are sliding, and no more sliding contacts exist at the next step. The number of such boxes is shown in Fig. 5.11. In the first half of the simulation until $f/f_0 = 1.8$, only occasionally one finds such a box. But in the second half this number increases about exponentially until the failure, where it attains its maximum value.

Figs. 5.10, 5.11 both show that once again we observe two periods of different granular behavior. While in the first period the *local number* of sliding contacts changes only slowly, in the second period many *changes in the positions* of the sliding contacts occur, suggesting an increasing length scale on which these changes take place. Although the total number of sliding contacts changes in the second period far less than in the first, local changes are much more important. Thus it seems in the first period the *change in number* is the dominating process, while in the second period the *position changes* are dominating. These position changes are investigated further in the next subsection.

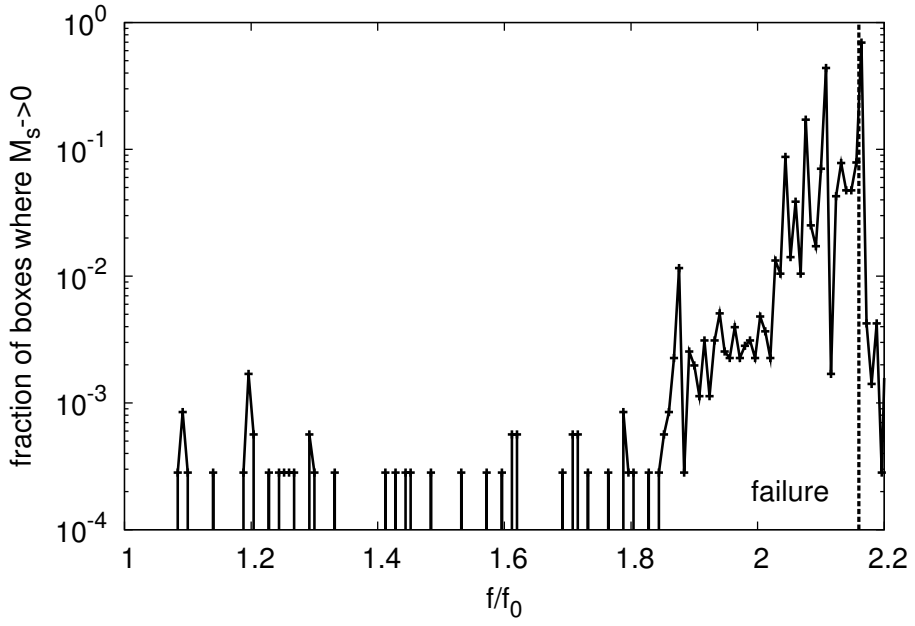

Figure 5.11: Fraction of boxes where the number of sliding contacts first is $M_s \geq 2$ and then decreases to zero in an interval $\Delta f/f_0 = 6.4 \times 10^{-3}$. The values directly at failure, which is indicated by a vertical line at $f/f_0 = 2.16$, are not very precise, because the grains' velocities are high, and they might change their position rather quickly. Thus the time independence of the boxes is not valid any more, because either the particles are fixed to certain boxes, then the shape of the boxes changes with changing particle positions. Or the shape of the boxes is fixed. But then a significant fraction of the particles will change the box they belong to during failure.

5.5.4 Spatial distribution of sliding contacts

To assess the spatial organization of sliding contacts, one can investigate whether a Poisson process [73] could generate their observed spatial distribution. Recall that a Poisson process is one where a fixed number of points in a region are selected, with each point having an equal probability of being chosen. Furthermore, each point is chosen independently of the others: the choice of point A has no influence on the probability of choosing point B. If the region is subdivided into boxes of equal size, the probability of observing x points in a box is

$$P(x;\lambda) = \frac{e^{-\lambda}\lambda^x}{x!}, \quad x = 0, 1, 2, \ldots \tag{5.3}$$

Here, λ is the average number of points expected in one box. Note that the variance of the Poisson distribution is equal to its mean. We will make use of this later.

To check if the sliding contacts are distributed according to a Poisson process, we divide the packing into equally-sized square boxes of length $l = 4d$ (d is the average particle diameter), and count the number of sliding contacts in each box. One can then compare the observed frequencies with the prediction in Eq. 5.3. One convenient way to do this is the so-called "t-test".

The t-test compares the variance σ^2 of the distribution to the mean $\bar{M}_{s,box}$ [73]:

$$t = \frac{(\sigma^2 - \bar{M}_{s,box})}{\sqrt{2/(N-1)}} \tag{5.4}$$

Negative t-values indicate low variance or evenness of the distribution while positive t-values indicate a departure in the direction of high variance or clumping (clustering). The values in Fig. 5.12 show that in the beginning of the simulation the sliding contacts tend to be distributed randomly over the packing ($t \approx 0$). However, the very initial values might not be significant as the number of sliding contacts is small. As more sliding contacts appear, the t-value decreases and becomes negative, indicating a sharply peaked distribution (low variance), meaning that the sliding contacts repel each other: the presence of one sliding contact reduces the probability that a neighboring contact will become sliding. Later, close to the failure, the t-values become positive and increase strongly. This indicates that at the failure the sliding contacts strongly tend to cluster.

Fig. 5.13 shows the positions of the sliding contacts at $f/f_0 = 2.15$, shortly before the failure at $f/f_0 = 2.16$. One discerns a diffuse diagonal band that crosses the sample from lower left to upper right. At failure, a shear band forms in this region. The other sliding contacts are concentrated at some distance in another band that is parallel to the shear band. The formation of the shear band will finally lead to the failure of the assembly.

5.6 Two qualitatively different periods

As discussed in Sec. 5.3, one can identify two periods of loading with different behavior. Table 5.1 shows the behavior during the two periods. Most quantities in the table depend on the contact status changes. In the first period ($f/f_0 < 1.8$) the most frequent contact transition is from closed to sliding. Therefore the number of sliding contacts M_s increases with the load, while their spatial distribution is quite uniform ($t < 0$). Also the volume decreases during this period. In the second period, the dominant contact status transition is from sliding to open (disappearing of formerly sliding contacts). This entails a decrease in M_s, and a clustering tendency ($t > 0$). This clustering is connected to

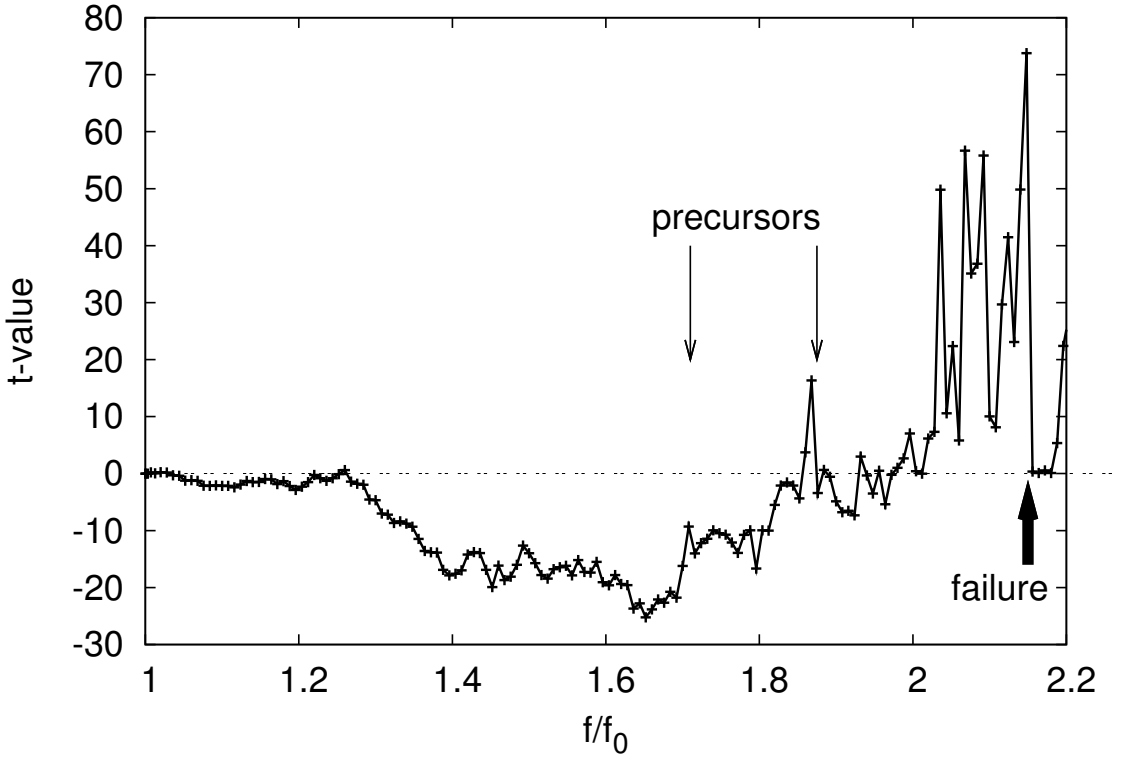

Figure 5.12: Values from the t-test (Eq. 5.4). This test checks the spatial distribution of sliding contacts: $t < 0$: contacts are more uniform than random, $t > 0$: contacts cluster.

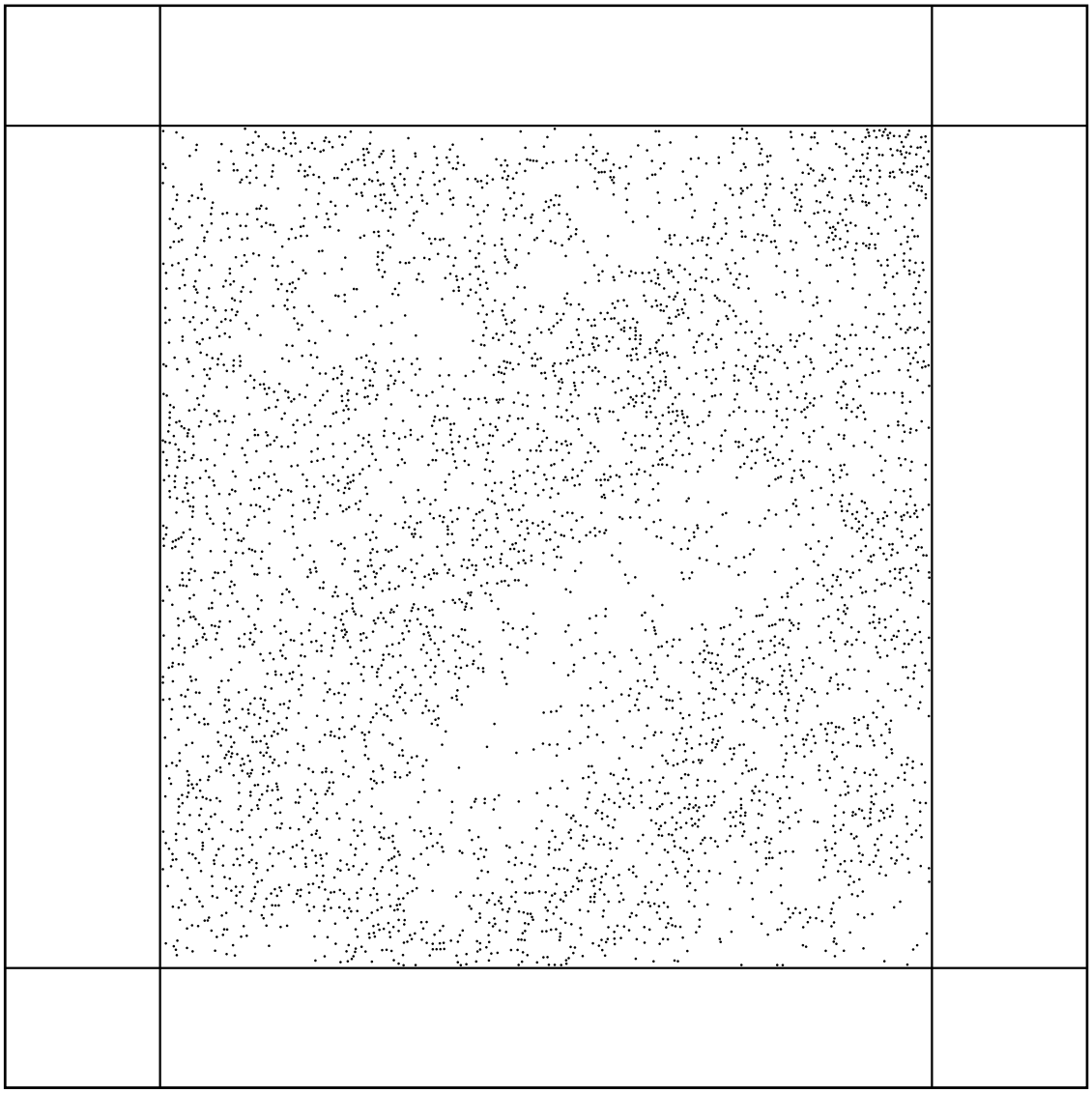

Figure 5.13: Positions of the sliding contacts for $f/f_0 = 2.15$, i.e., at failure. At this time, the t-test yields $t = 50$.

	$f/f_0 < 1.8$	$f/f_0 > 1.8$
dominant status change	C→S	S→O
sliding contacts M_s	$\nearrow$	$\searrow$
local M_s in box	little changes	large changes
t-test (M_s)	ordering ($t < 0$)	clustering ($t > 0$)
$\langle F_n \rangle_{\text{sliding}}$	$\nearrow$	$=$
volume V	$\searrow$	$\nearrow$
precursors	few	many

Table 5.1: Time behavior of characteristic quantities during the two periods. The arrows indicate the evolution with increasing load (rising $\nearrow$ or falling $\searrow$). The few precursors observed in the first period preferably appear towards the end of that period.

increasing changes in the number of sliding contacts in small boxes. During this period, the average normal force transmitted at sliding contacts does not increase any more. Last but not least, the change in volume is reversed: V increases, while the power injected stays positive (see Fig. 5.4 in Sec. 5.3).

Towards the beginning of the second period, precursors of failure appear that become more frequent with increasing f. Their appearance has been outlined in Sec. 5.4.1 and indicated in Fig. 5.5. They will be discussed in detail in the next section.

5.7 Triangular figures: importance for stability

In the foregoing sections the evolution of the number of contacts and sliding contacts has been investigated in detail. But in fact it is the structure of the contacts, i.e. the network of contacts of the granular system that has to withstand the external forces. Thus the mere number of contacts is not a precise measure for stability, but the structure of the network of contacts has to be investigated instead. This structure can be decomposed into many small structures, called geometric figures. The most important geometric figures are triangles, and their number is investigated in this section. But why are triangles so important, and which other figures occur?

Carrying out a structure decomposition into the smallest geometric figures that contribute to the system's stability, one finds that three contacts connecting three grains is the minimum size of such a figure. When all contacts of this triangle are nonsliding, it is rigid in the sense that it cannot be deformed without effort, unless one removes a grain or a contact. On the other hand, when a contact of the triangle becomes sliding, the grains in touch start to slide relative to each other. Thus the triangle is not stable any more. The next bigger geometric figure contains four grains, connected by four contacts. If it had five contacts, one could decompose it into two triangles, and it wouldn't be a new sort of figure. The four particle figure can never be stable, because the grains can always rotate in opposite direction at the contacts. This motion is called a null-mode, because it correspond to zero stiffness. Such motions have been investigated in the $N = 16$ particle packing in Chap. 3. They appear in structures with an even number of particles. Next comes a figure with five particles and five contacts. Once again, if there were more contacts, one could decompose the figure in smaller parts. Five particles is such a large number that the structure can be deformed without much effort. Thus this structure cannot be considered rigid. Figures with an even larger number of particles N are still more fragile, because the number of kinetic degrees of freedom increases with N. Hence triangles are

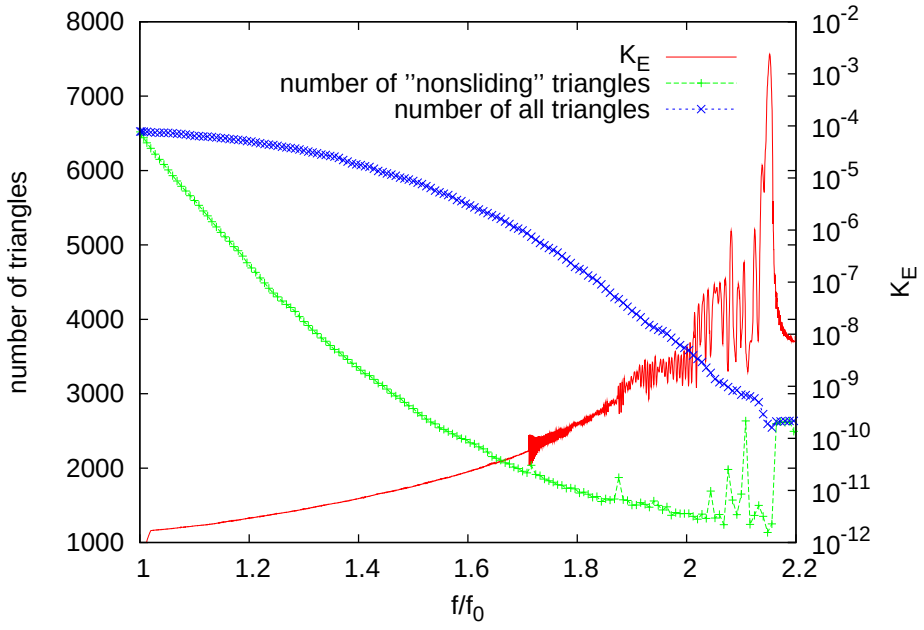

Figure 5.14: Evolution of the number of triangles from the beginning of the simulation until the failure. Triangles are figures with three particles connected by three contacts. In *nonsliding* triangles, none of the contacts has the status *sliding*. See Sec. 5.7 for details.

the most rigid figures in two dimensional granular systems. We will see that their number is closely related to the system's stability.

We examine the number of triangles during one simulation. First we discuss the process of weakening. Then we focus on a small period before the failure. The inspected example system has rigid wall boundary conditions, while results with membrane boundaries are discussed in Sec. 8.5.

On the way to failure

Figure 5.14 shows the number of triangles, i.e. the figures with three particles connected by three contacts, in an example of an assembly. It is the same system as investigated in the other sections in this chapter. On the way to failure, the number of triangles decreases continuously. In the beginning, the decrease is slow, but it is accelerating until about $f/f_0 = 1.7$. Afterwards the number of triangles decreases linearly until the failure. During the failure, when the kinetic energy rises exponentially, the number of triangles sharply decreases. It slightly increases again right after the failure.

The number of triangles that have only nonsliding contacts changes however in a different way. At the beginning of the simulation, it decreases strongly. But then the decrease slows, and the nonsliding triangles attain a minimum number at the failure. Close to the failure spikes appear in the number of nonsliding triangles. These spikes coincide with the increase in the vibrations in the kinetic energy. This means that they are related to the appearance of precursors of failure. Note that a similar increase in the number of nonsliding triangles appears after the failure. This time, however, the number remains constant.

One could also raise the question if the decrease in triangles is caused by a decrease in the num-

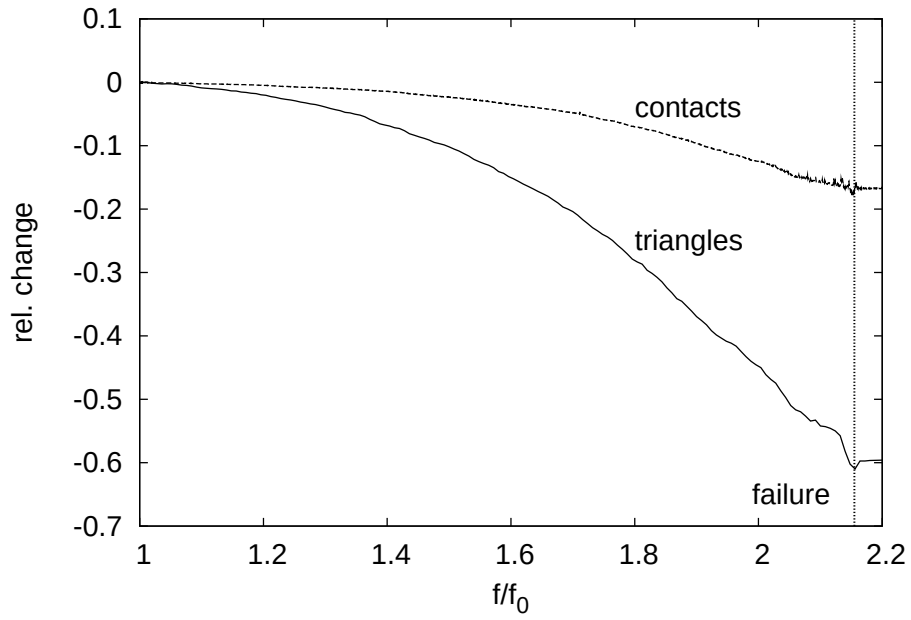

Figure 5.15: Comparison of the relative change in the number of triangles $M_{\rm tr}$ to the relative change in the number of contacts M. The fraction of disappearing triangles $\Delta M_{\rm tr}/M_{\rm tr}$ is much larger than the fraction of lost contacts $\Delta M/M$: at the failure about 60% of all triangles are lost, while the number of contacts is 18% smaller.

ber of contacts. Fig. 5.15 shows the relative number of lost triangles $\Delta M_{\rm tr}/M_{\rm tr}$ and lost contacts $\Delta M/M$. While about 60% of the triangles are lost until the failure, the number of contacts decreases only by 18%. Thus the decrease in triangles must at least partially be attributed to the loss of contacts in the system.

Let us now inspect the change in the number of triangles at the appearance of failure.

Close to the failure

When the system comes close to the failure, the sliding contacts concentrate in a diagonal band going through the center of the packing. This band of sliding contacts has been shown in Fig. 5.13. In this region a shear band develops at failure, which is a band where adjacent particles move in opposite directions. In the region of the shear band, the number of triangles can evolve quite differently from the regions outside, because in this region the density of structural rearrangements will be higher than outside. To investigate the differences, the system is divided into one region in which the shear band forms and in another region with the remaining parts of the system. The thickness of the shear band region was set to $d = 0.1\hat{L}$, where $\hat{L}$ is the length of the simulation box. The results do not depend qualitatively on d.

In Fig. 5.16, the number of triangles inside and outside such a shear band region is shown. Of particular importance is the behavior around the force value $f/f_0 = 2.15$. At this moment, the system is failing, and the kinetic energy is very high (right axis in the figure). During the failure from $f/f_0 \approx 2.145$ to $f/f_0 = 2.16$, the number of triangles in the shear band region decreases. Almost

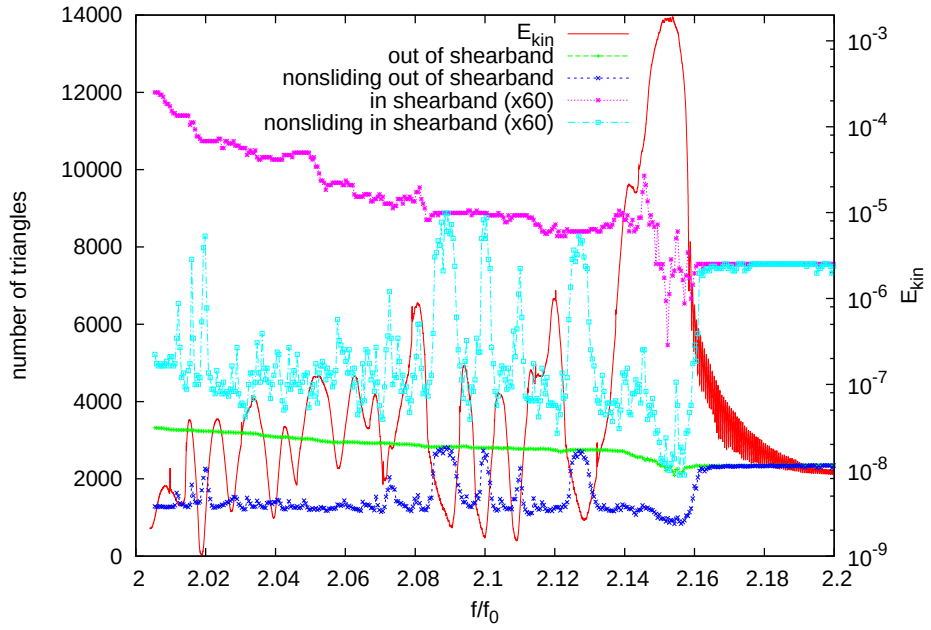

Figure 5.16: Number of triangles close to the failure. The figure shows the total number of triangles outside and inside the region where the shear band forms. At failure both of them decrease. When the shear band forms, the number of nonsliding triangles in the shear band region strongly decreases, whereas the relative decrease is much smaller outside of this region.

only nonsliding triangles are lost, i.e. such triangles that are devoid of sliding contacts. During the same interval, the decrease in triangles outside the shear band region is only moderate.

When the packing becomes stable again, the shear band disappears and the number of triangles rises again. When the grains come to rest, all contacts between the grains are nonsliding, hence the number of nonsliding triangles is equal to the total number of triangles. Note that the total number of triangles decreases through the failure process, while the number of contacts does not change much. This shows that a change in triangles is not necessarily connected to a change in the number of contacts. Furthermore the lower number of triangles after the failure evidences that one cannot compare stiffness and number of triangles one-to-one.

In conclusion, the number of contacts and the number of triangles both decrease until the failure. Both numbers are related to the stability of the system. At the failure, the decrease in the number of triangles is more pronounced in the region of the shear band.

5.8 Conclusion

This chapter discussed the behavior of granular packings with $N = 16384$ particles in two dimensions. At the rigid wall boundaries, the external force f is slowly increasing along one direction, while it is constant in the other direction. This *biaxial test* is performed under quasi-static conditions, and f is increased up to a critical value. This critical force leads to a large deformation of the packing.

The force increase up to failure can be divided into two roughly equal periods. Many variables show a qualitatively different behavior in these two periods. First of all, the volume decreases in the first period, but increases in the second. Then there is the number of sliding contacts M_s which increases linearly in the first period, and then decreases in the second. During the transition between these two behaviors, M_s attains its global maximum. Thus the number of sliding contacts is not unequivocally related to the stiffness or the stability of the packing. Furthermore the spatial organization of sliding contacts also changes during the simulation. Before the maximum, in the first period, sliding contacts are more uniformly distributed in the packing than afterwards. Comparison with a Poisson process shows that sliding contacts initially repel each other: the presence of a sliding contact reduces the probability that a neighboring contact will become sliding. After the maximum, in the second period, the situation is reversed: sliding contacts are concentrated in specific regions. Near failure, the formation of the shear band is foreshadowed by a concentration of sliding contacts. These contacts cluster preferably to form diagonal bands, suggesting that the localization of deformation begins long before any shear band is visible.

The changes in the number of sliding contacts are caused by the different frequencies of contact statuses transitions; in the first period, the main transition is from closed to sliding, leading to an increase in M_s. In the second period, the transition sliding to open is dominating, decreasing M_s.

The number of triangles decreases with increasing load. In the first period, the decrease is accelerating, while it is constant in the second period.

Towards the end of the first period, the first precursors of the failure appear, becoming more frequent in the second period. These precursors have been spared from this chapter. But they are an important feature of granular behavior, so the next chapter is concerned with their properties.

Chapter 6

Precursors of failure

During a simulation, where the external force is slowly increased in one direction, the number of sliding contacts M_s first increases linearly, and then decreases again for a shorter period before the failure. Towards the end of the increase, one observes the first of a series of sudden plunges of M_s that last only for a very short time. These plunges are associated with the appearance of precursors of failure. These precursors do always precede the failure, unless the system is so small that very few contact changes lead to the failure.

Some properties of precursor are similar to the behavior at failure, but the precursor particularly changes the system's behavior only in a localized region. In some respect a precursor can therefore be considered to be a local failure. But there are also differences. Both are investigated in this description of precursors.

The structure of the chapter is as follows. First of all, Sec. 6.1 presents the definition of what is considered a precursor. Then the sections thereafter present a typical example of a precursor. While every precursor is unique, there are common properties of all precursors that are discussed each in a separate section. In Sec. 6.2 the evolution of the number of sliding contacts during a precursor is investigated. The stability of the system at the appearance of a precursor is examined in Sec. 6.3. In Sec. 6.4 the localization of the kinetic energy at the precursor is discussed. The precursor is connected to a decrease in the number of sliding contacts. This number is investigated in Sec. 6.5. There is also a change in the number of contacts at a precursor. This is examined in Sec. 6.6. Sec. 6.7 considers the possibility of detecting precursors in experiments. At the end of the chapter, Sec. 6.8 summarizes the main results.

6.1 Definition of precursors

Prior to the collapse of the packing, several precursors occur where M_s plunges and then quickly recovers. In this work, a precursor is defined as an event where M_s plunges by at least 10% of its maximum value before the failure and quickly recovers again. The drop in $\mathrm{M_s}$ at a precursor varies from one to another, but the qualitative behavior at the precursors is always the same. Precursors are initiated by a localized instability that gives rise to a local increase in the kinetic energy. The decrease in the number of sliding contacts is then just a consequence of the release of potential energy.

Precursors of failure have been observed by other authors for other system geometries. Most frequently the authors consider granular avalanches. Such an avalanche happens when the underlying surface of a granular bed is tilted up to a critical angle at which the kinetic energy of the particles

suddenly increases quickly, and global rearrangements occur. The inclined surface boundary condition has been defined in Sec. 2.3 and sketched in Fig. 2.2. Several different definitions of precursors exist, but they are all connected to increasing motions. Quite a few authors have identified precursors with clusters of grains at the surface of such a granular system which are set in motion in experiments [30, 31, 33, 74–76]. On the other hand, Staron et al. [28, 77] identify precursors as a mixture of reorganization of the internal network of contacts, governed through loss and creation of contacts, and sliding motions appearing at sliding contacts. They conclude that the frequency of precursors rises with the rising probability of appearing rearrangements close to the stability limit.

Figure 5.5 tells us that in the geometry defined by the boundary conditions of type biaxial, the precursors become also more frequent as the failure is approached. Therefore they might play an important role for the appearance of failure. In this chapter we will see what happens at one such precursor. This information will provide first hints on their meaning for failure.

6.2 Number of sliding contacts at precursors

To better understand the precursors, we examine in detail the first precursor indicated by the first arrow in Figs. 5.1, 5.2, 5.5, 5.7 and 5.12 at $f/f_0 \approx 1.71$. Figure 6.1 shows M_s around this precursor. At its appearance, the drop in M_s is very sharp, while the recovery afterwards is slower and represents the relaxation to a new (force) equilibrium. Figure 6.1 also shows the kinetic energy at that precursor. When M_s starts to decrease, $E_{\rm kin}$ increases quickly. However, the kinetic energy very soon decreases again. This happens *before* M_s reaches the minimum value. The maximum of $E_{\rm kin}$ can vary from one precursor to another one, but it is always much smaller than the maximum at failure. This is due to the limited time in which the energy rises [55].

6.3 Appearance of an instability

Fig. 6.2 shows another measure of the stiffness of the assembly. This stiffness is calculated by reducing the stiffness matrix $\mathbf{k}$, introduced in Sec 2.8, which contains the stiffnesses of all the contacts, to a scalar stiffness by multiplication with the particle velocities $\mathbf{v}$:

$$k = \mathbf{vkv}/\mathbf{vv}\,. \tag{6.1}$$

Note that k contains the velocities of all the particles, whereas the stiffness defined in Sec. 5.1 concerns only the walls. The advantage of k is that it can detect localized instabilities [55]. Specifically, $k < 0$ means that the packing is (at least locally) unstable, whereas $k > 0$ indicates that it is stable. This stability criterion has been discussed in Sec. 2.8.3. Furthermore, k is correlated to the stiffness defined in Sec. 5.1: large positive k correspond to stiff assemblies. In Fig. 6.2 we see the stiffness k of the assembly at the time when the precursor appears. At $f/f_0 \approx 1.711$, the stiffness k becomes negative and the kinetic energy rises rapidly. But at $f/f_0 = 1.7111$, k suddenly jumps to a positive value, and $E_{\rm kin}$ starts a rapid decline. This shows that the $\mathrm{E_{kin}}$ is controlled by k. We showed this dependence in an earlier paper on failure in small packings [55].

After the precursor, large vibrations appear that last for a long time compared to the intervals shown in Figs. 6.2, 6.1 and 6.5. These vibrations can be observed in Fig. 5.2. It has been anticipated in [55] that vibrations will become important in large packings around failure. The vibrations triggered by the precursor studied here do not cause failure, but Fig. 5.2 shows that vibrations grow as failure

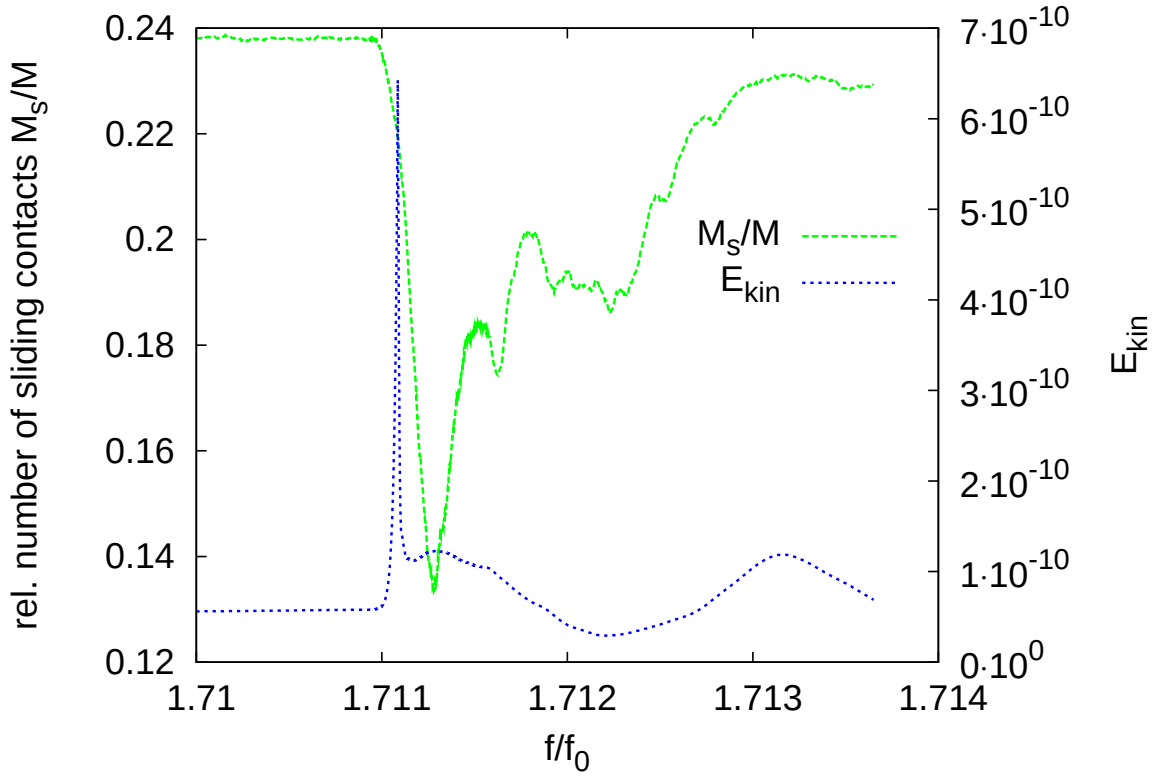

Figure 6.1: Kinetic energy E_{kin} (right scale) at the first precursors indicated in Figs. 5.1, 5.2, 5.5, 5.7 and 5.12. The energy E_{kin} increases quickly, and then decreases again. Shortly before, the number of sliding contacts M_s (left scale) starts to decrease. This decrease last until after E_{kin} decreased again. Thereafter M_s recovers slowly.

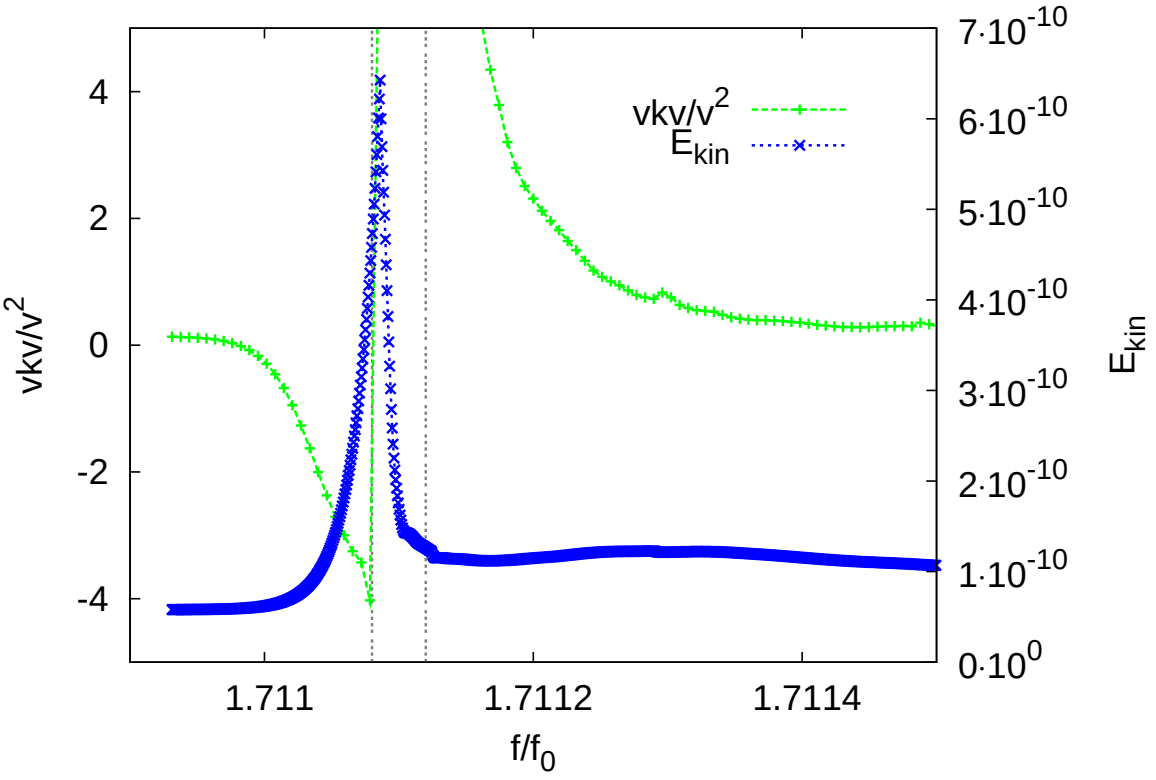

Figure 6.2: Stiffness of the assembly (left scale) at the occurrence of the precursor. When the instability appears, E_{kin} rises quickly (right scale). The dotted horizontal line separates the two regions *stability* and *instability*. The two vertical lines indicate the positions of Figs. 6.3, 6.4.

is approached. These vibrations may play an essential role in causing the collapse of the assembly. Therefore failure might finally be initiated by the vibration generated by the precursors immediately preceding failure.

6.4 Localization of the kinetic energy

When E_{kin} starts to rise at the beginning of the precursor, the velocities in a small region rise and become significantly larger than everywhere else. Figure 6.3 shows the grains of the packing that carry most of the kinetic energy near the peak of E_{kin}. But the instability at the precursor lasts only for a short while, and the velocities in this region decrease again very soon. However, there is a wave of large movements spreading from this small region across the packing. Figure 6.4 shows the grains with large kinetic energy shortly thereafter, when the energy is propagated through the system. In this energy spreading many different orientations are involved, and the propagated waves will move across the entire packing. Looking at Figs. 6.2, 6.3, and Fig. 6.4, we see that the width of the spike in $\mathrm{E_{kin}}$ in Fig. 6.2 is much smaller than the time it takes for the disturbance to cross the sample. That means that the "high" energies ($> 10^{-10}$) occur only in a very localized region. This in turn shows that precursors are indeed "localized failure".

6.5 Where does the number of sliding contacts decrease?

Figure 6.5 shows M_s and the t-test at the precursor. Before the precursor, the values are negative and do not change with increasing external force. When the precursor appears, the t-values increase strongly and become positive. Note that the maximum positive value is much larger than the negative value before the precursor. It is reached at the time of minimum M_s. Fig. 6.6 shows the spatial distribution of the sliding contacts at the maximum t-value. The sliding contacts disappear in some regions around the precursor, while the number of sliding contacts looks much more uniform far away from the precursor. After the precursor, the t-values decrease again and become close to the values before the precursor. This indicates that ordering effects appear at the precursor, and disappear again after the precursor. Comparing Fig. 6.4 and Fig. 6.6, we see that sliding contacts disappear in regions of elevated kinetic energy. Thus we conclude that the drop and subsequent recovery of M_s are due to wave radiating outwards from the local failure. After the wave passes, the sliding contacts reappear, explaining why both M_s and the t-test return to their initial values.

In Sec. 3 it has been anticipated that *local failures* will occur. One of the findings in that section, which was also published in [55], is that the number of sliding contacts vanishes at the failure. This statement is now extended to precursors, therefore these can indeed be called local failures.

6.6 Change in the number of contacts

Another feature of the precursor event is a transitional change in the total number of contacts. Fig. 6.7 shows the total number of contacts M as well as the number of sliding contacts M_s during the precursor. Surprisingly, these quantities are anti-correlated: The sudden drop in the number of sliding contacts coincides with a peak in the number of contacts. The contacts that are created are concentrated in the high kinetic energy regions of Figs. 6.3, 6.4. Therefore they are probably another effect

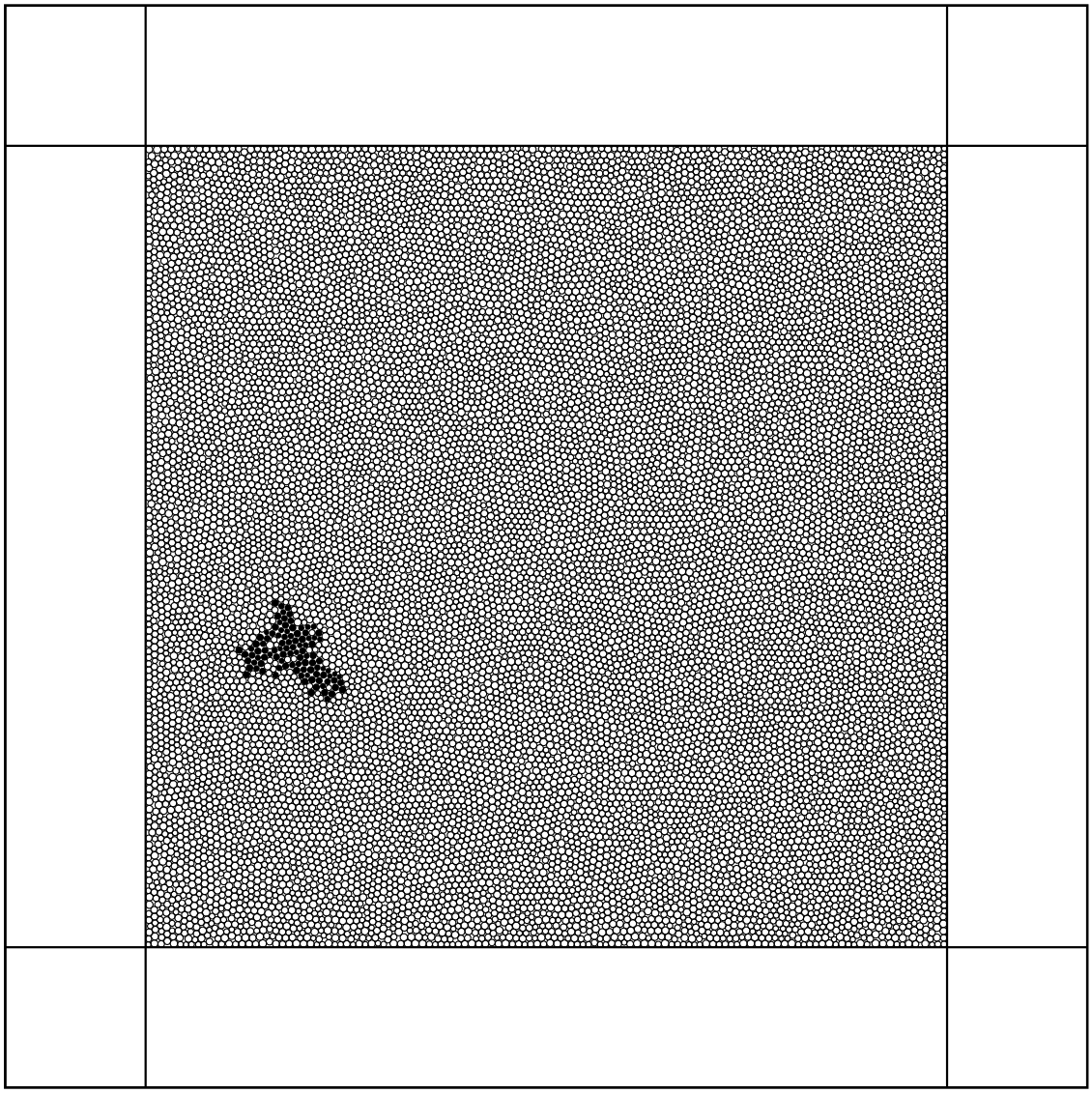

Figure 6.3: Velocities in the assembly near the peak in E_{kin} (the last point of instability at $f/f_0 = 1.71108$ in Fig. 6.2). The black particles (0.63% of the total) have above average kinetic energy and carry 85% of the total energy.

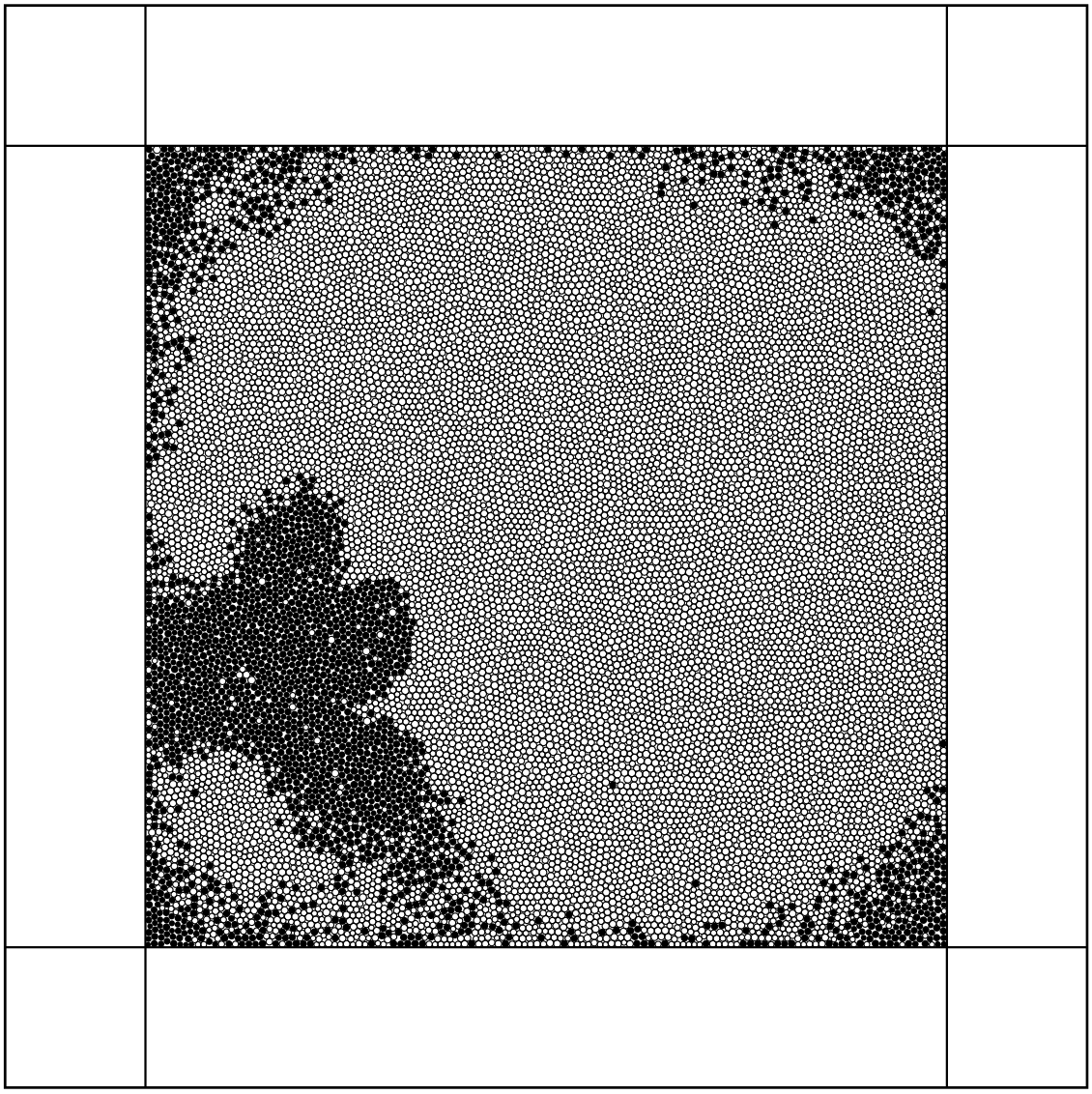

Figure 6.4: Velocities in the assembly at $f/f_0 = 1.71112$, shortly after the recovery of stability in Fig. 6.2. The black particles (16% of the total) have above average kinetic energy and carry 64% of the total energy.

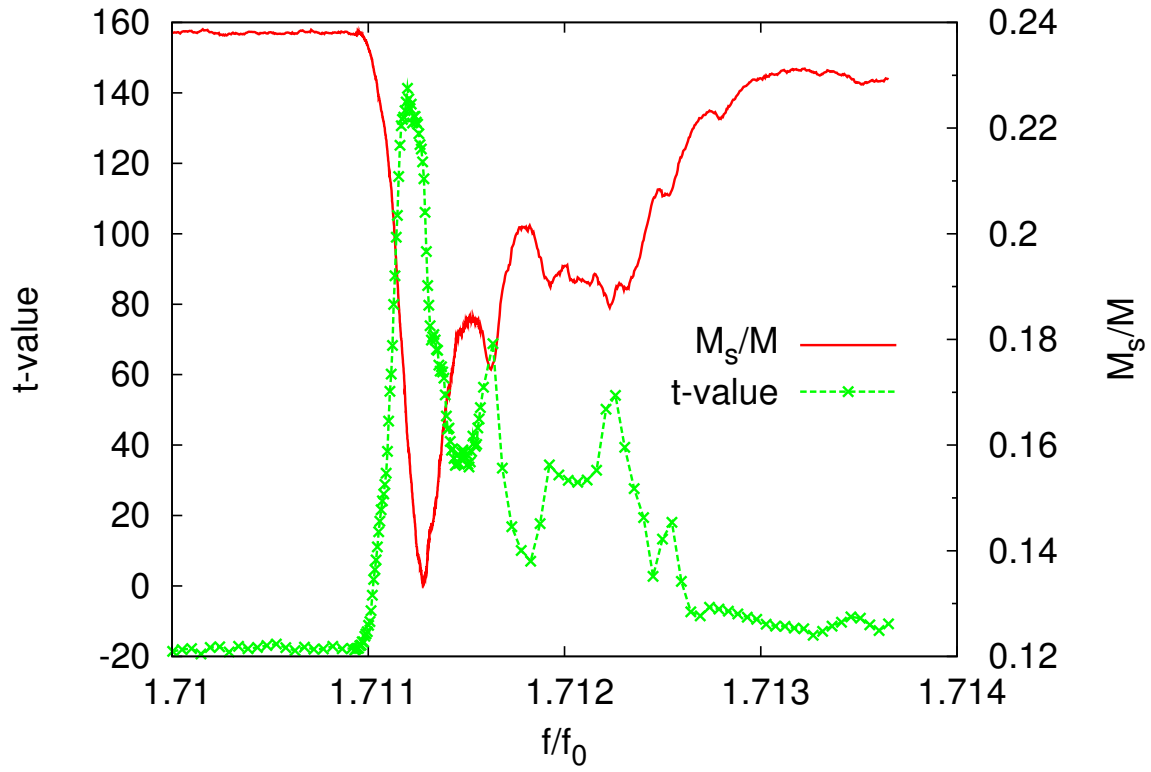

Figure 6.5: Values from the t-test (Eq. 5.4) and number of sliding contacts M_s, normalized by the total number of contacts M, during a precursor. The decrease in M_s corresponds to a clustering of sliding contacts ($t > 0$).

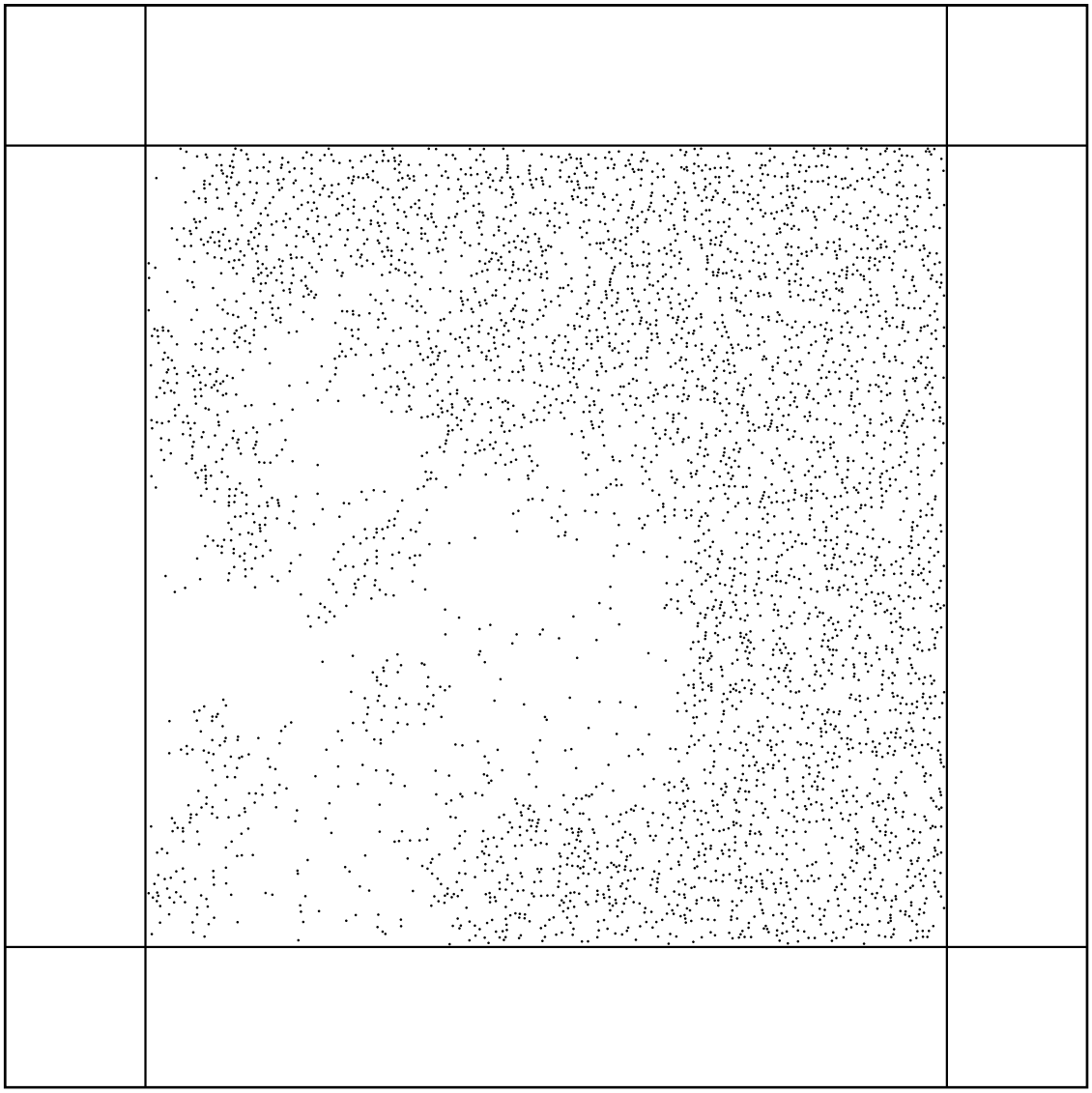

Figure 6.6: Distribution of the number of sliding contacts in the packing at the time of the highest t-value in Fig. 6.5. The external force f corresponding to this figure is just slightly higher than for Fig. 6.4. Comparing the two figures, one notices that the sliding contacts have been suppressed in the high E_{kin} regions in Fig. 6.4.

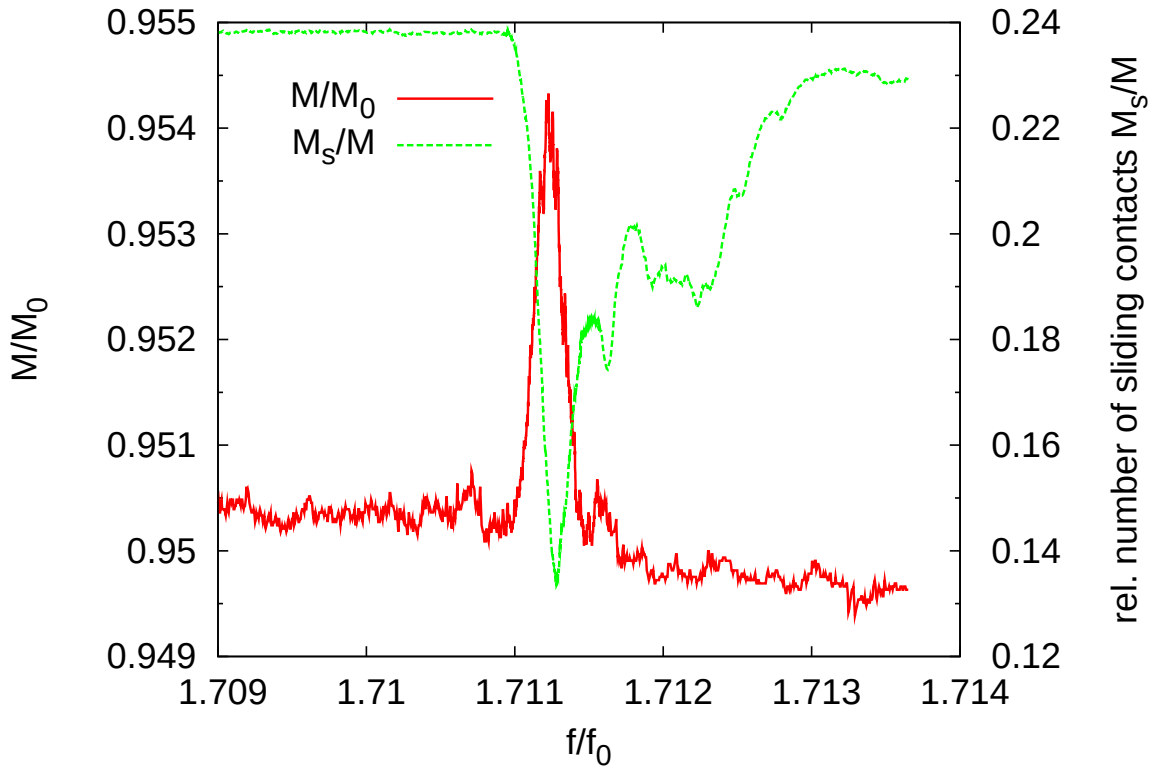

Figure 6.7: Change in the number of contacts M at one precursor. In the beginning of the simulation the number of contacts is $M_0 = 32798$. At the peak at $f/f_0 = 1.7112$, 130 additional contacts appear.

of the wave. When M_s rises again, the number of contacts reduces slowly and attains values lower than those before the precursor.

Another issue raised by Fig. 6.7 are the permanent changes induced in the contact network by the precursor. For example, M decreases by about 30 between $f/f_0 = 1.709$ and 1.713 – is the precursor responsible for this change? Plotting M and M_s over a long time (Fig. 6.9) shows that these changes are just part of a long term general trend. Furthermore, if one identifies the contacts that have disappeared, one finds that they are not concentrated anywhere in particular.

We therefore conclude that the precursor does not lead to a significant change in the number of contacts. Furthermore the geometric structure of the contact network remains almost unchanged. Temporary changes mainly originate from an increase of the normal force F_N at some contacts. This increase is generated by the compression wave radiated outward from the precursor.

6.7 Can precursors be observed experimentally?

While the stiffness of the assembly becomes negative and the kinetic energy rises, the stress-strain curve does not show a maximum at the time the precursor appears, but rather a dip (Fig. 6.8). Thus in the stress-strain curve in Fig. 5.1 it is hard to identify the precursors. Therefore it seems to be

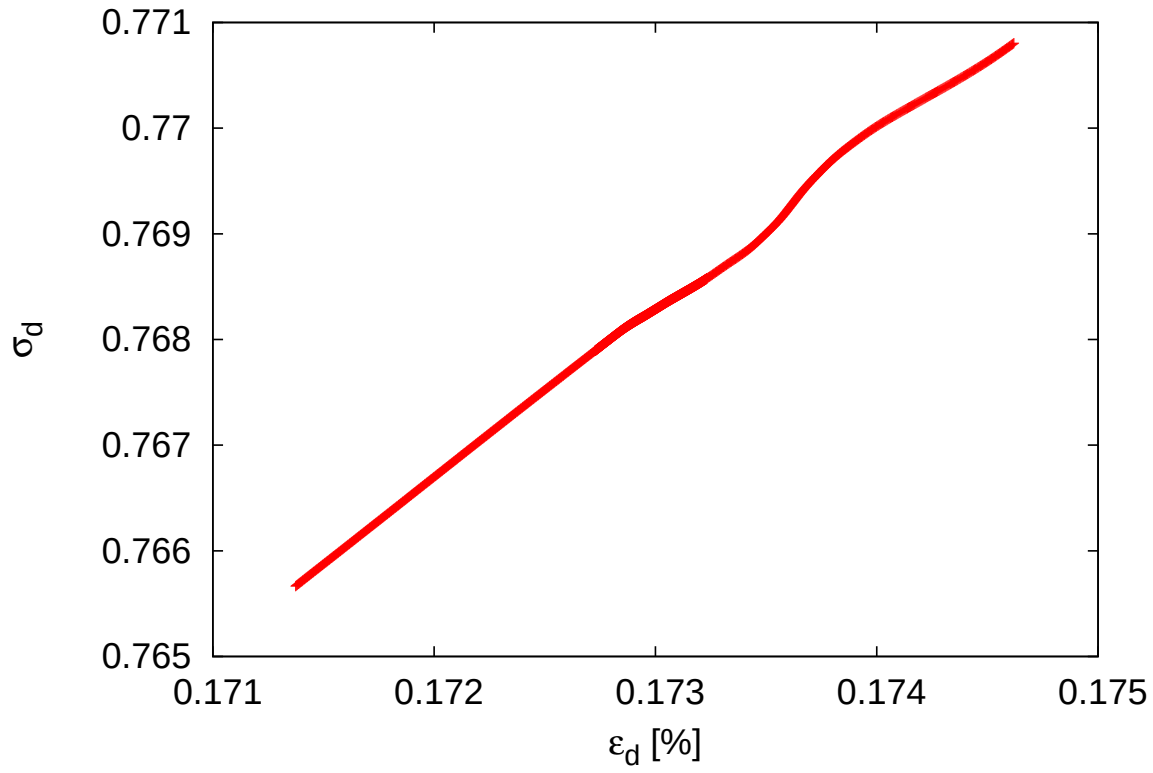

Figure 6.8: Stress-strain relation during a precursor. The range of the data corresponds to the range in Fig. 6.1. At the precursor the relation is not linear any more, but there is no visible peak at that time.

hard to even *notice* precursors in experimental tests, as it is difficult to detect small fluctuations of the stress-strain curve.

One possibility to detect precursors in experimental investigations is therefore to monitor the kinetic energy by detecting sound emissions from these regions. These sound emissions arise at the local grain displacements [78]. Sound waves of high frequency are quickly diffused [79], while low frequency waves can travel the assembly almost unchanged and can then be detected at the boundaries of the sample. By measuring the travel distance to different detectors, the spatial origin of the sound waves can be reconstructed [80]. However, one must take into account the dependence of the speed of sound on both the surface structure of the grains and the dimensionality (2D or 3D) [81]. Sound waves have been observed in triaxial tests but not analyzed so much.

6.8 Conclusion

Around the time of the maximum number of sliding contacts, precursors begin to appear, becoming more and more frequent as failure is approached. The definition of precursors is based on the observation that the number of sliding contacts decreases suddenly at certain values of the external force f. A closer inspection of one precursor shows that there is a multifaceted behavior at this time.

The precursors are triggered by localized instabilities that lead to a sudden rearrangement of a small, localized number of grains who carry most of the kinetic energy. Precursors involve also a strong decrease in the number of sliding contacts, and a temporary increase in the number of contacts. When stability is recovered, the packing relaxes to a new equilibrium with properties (M, M_s, E_{kin}, ...) close to the values before the precursor.

Precursors are initiated by instabilities, therefore inertia effects become important. Hence, when investigating the micro-macro transition, inertia cannot be neglected any more, complicating the establishment of a macroscopic theory based on microscopic, static quantities such as the fabric tensor or the number of sliding contacts.

The appearing instability during the precursor leads to large vibrations involving motions of all particles. These motions let the packing explore a larger part of the phase space. When approaching the critical external force, the packing becomes very soft, and the vibrations, triggered through the precursors, become larger. Therefore the precursors should be significantly involved in the processes leading to failure.

Precursors are not only observed in two dimensions, but appear in three dimensions as well. In both cases, they have similar properties. Precursors in three dimensions will be investigated in Chap. 10. But before that, there still remain some observations in two dimensional systems that need to be discussed. One such observation is the presence of rolling motions, arising at the particle contacts and being present throughout the simulation. Besides the sliding motions, rolling motions are responsible for the softening and failure of granular systems. While the sliding motions have been discussed in detail on both global and local scale in several foregoing sections, rolling motions are the topic of the next chapter.

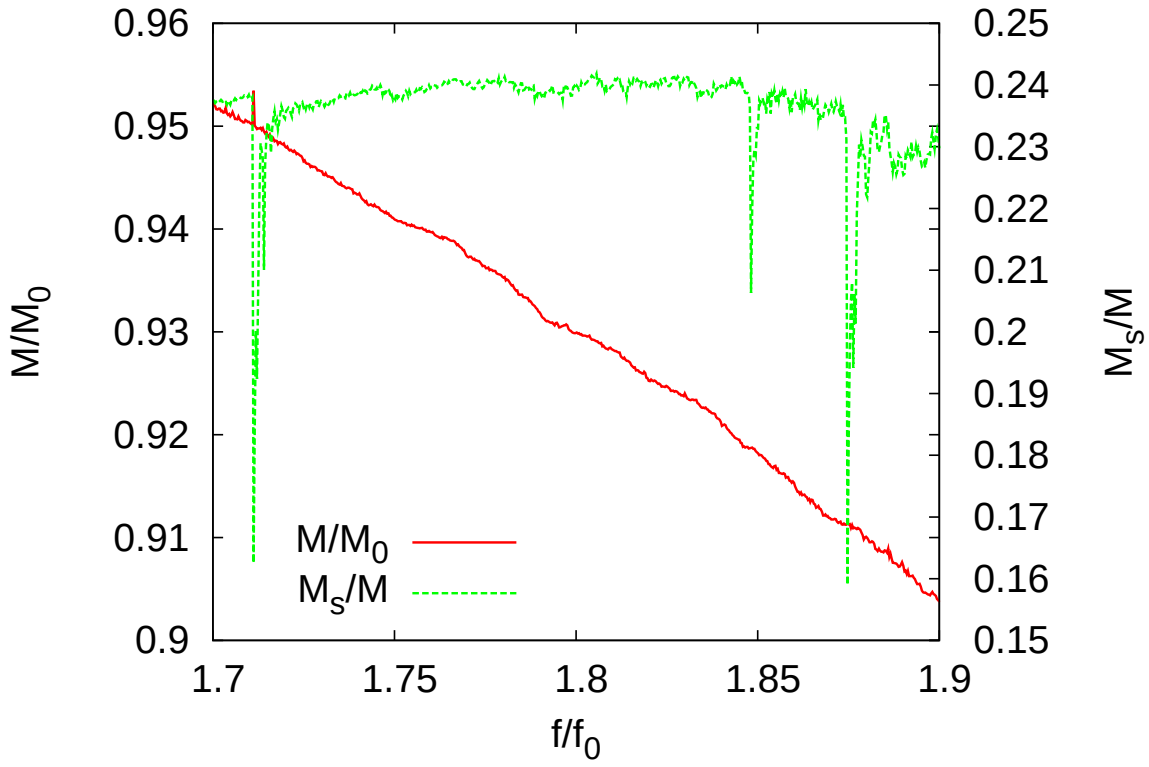

Figure 6.9: Number of contacts M in the assembly during a period where three precursors appear. The initial number of contacts is $M_0 = 32798$ The loss in the number of contacts is not connected to the appearance of precursors.

Chapter 7

Organization of rolling motions

Besides its great practical importance, yielding or failure of a granular material poses also several interesting, yet partially unsolved theoretical questions [1–8]. One of these questions concerns the geometric organization of particle motions [34, 82]. At the beginning of the loading process, the strain is approximately uniform: at the length scale of several grain diameters, the material behaves like a continuous medium with uniform properties. With increasing external force, the strain concentrates in specific regions. Therefore, one passes from a situation where the strain is uniform to one where it is strongly organized. Kuhn et al. [83], for instance, find that rotations organize in chains. This chapter aims at enlightening the details of this organization process.

So far many aspects of weakening and failure were connected to either contact status changes, or to the number of sliding contacts. Thus many details of material weakening depend on the contacts which put constraints on relative particle motions. While sliding contacts allow for relative displacements of touching particles tangent to their surfaces, closed contacts are devoid of this displacement mode. But rolling motions, which are also relative displacements of touching particles, can occur at closed contacts. Thus rolling motions do occur independent of the contact status closed or sliding, and it is possible that they are even more important for material weakening [84] than sliding contacts, which are only few in the simulation beginning. This chapter investigates the importance of rolling motions for weakening and failure and also addresses the organization of such rolling motions. We will see that the organization increases until the failure, and we will identify a growing length scale of organization.

The system has rigid wall boundaries as sketched in Fig. 2.6: a granular material is fixed between four movable frictionless walls that are perpendicular to each other. This biaxial box with $N = 16384$ particles has already been investigated in Chaps. 5 and 6 in much detail. When the system is modeled as a uniform continuous medium, the stress is spatially constant and diagonal in the coordinate system whose axes are parallel to the walls:

$$\sigma = \begin{pmatrix} \sigma_1 = f_0/L_y & 0 \\ 0 & \sigma_2 = f(t)/L_x \end{pmatrix}. \tag{7.1}$$

In general the stress is space-dependent. But we can consider a small region of a continuous medium with a coordinate system in which σ is diagonal. The walls of our system are then simply the limits of this region. Thus the biaxial box is relevant in all situations of slowly varying stress.

The strain can be measured by tracking the positions of the walls. At the scale of a particle radius, however, the strain is nonuniform, even at small loads, and this can have a significant effect on the stiffness of the packing [85]. The local strain can be monitored by calculating the rolling

velocity at the particle contacts. The definition of the rolling velocity is presented in Sec. 7.1. In Section 7.2 the concentration of rolling contacts in specific directions is discussed. Thereafter Sec. 7.3 addresses the organization of rolling contacts. A length scale of organization, defined in Sec. 7.4, shows the increasing size of organized regions. As both rolling and sliding contacts are responsible for weakening in granular systems, Sec. 7.5 investigates their correlations during the simulation. Sec. 7.6 summarizes the main results. Most of the results presented in this chapter will be published in [86].

7.1 Definition of the rolling velocity

While grains with many contacts cannot move independent of other grains, they might be able to rotate relative to each other. When two grains are in contact, they might rotate in opposite direction with similar absolute rotation velocity. Thus one way to define rolling is adding up the rotation velocities of the two grains in touch.

To monitor the local strain caused by the rolling of the particles, we calculate the rolling velocity at the particle contacts. For two touching particles i and j with radii r_i and r_j and angular velocities ω_i and ω_j, the rolling velocity is defined as

$$v_r = \frac{r_i r_j}{r_i + r_j} \left| \omega_i - \omega_j \right| . \tag{7.2}$$

This quantity is objective [87], that is, it vanishes for a pair of particles undergoing solid-body rotation or translation. v_r measures the bearing-like relative motions of particles i and j at their point of contact. This type of motion has previously been implicated in failure and deformation [88]. A similar expression for rolling has been investigated in [83], where the authors found that rolling of particles organizes in chains. These chains seem to occur along specific directions, although in [83] this is not investigated in detail. We take the finding of the organization in chains as starting point for this investigation. Before describing the procedure for accessing the direction of rolling chains, two examples, shown in Fig. 7.1, should motivate this investigation. In the figure, all contacts with a rolling velocity above the average are indicated by black dots. The figure illustrates the observation of chains of rolling contacts for two different values of the external force f. The direction of the chains is not arbitrary, but it depends on the interparticle friction coefficient μ. While f is different in the two snapshots, the direction of the chains is very similar, although the number of chains is different. The left panel corresponds to roughly $3/4$ of the peak stress, whereas the right panel was taken just before the peak stress at the failure. The figures in [83] resemble very much the right panel in Fig. 7.1. However, they are constructed in a different way, namely by highlighting particles with large angular velocity. The chains of rolling can be identified as bands going across the entire system. Such bands are always present, but they are submitted to frequent changes in position until the failure.

The direction of the rolling bands in Fig. 7.1 is close to the Mohr-Coulomb direction. At this direction a shear band is expected at failure. The Mohr-Coulomb angle is defined later and compared to the direction of rolling in this chapter.

7.2 Organization of rolling in specific directions

We now want to present the method to access the rolling band directions. The scheme is sketched in Fig. 7.2. The large square stands for the system of grains. The center of a circle is adjusted to coincide

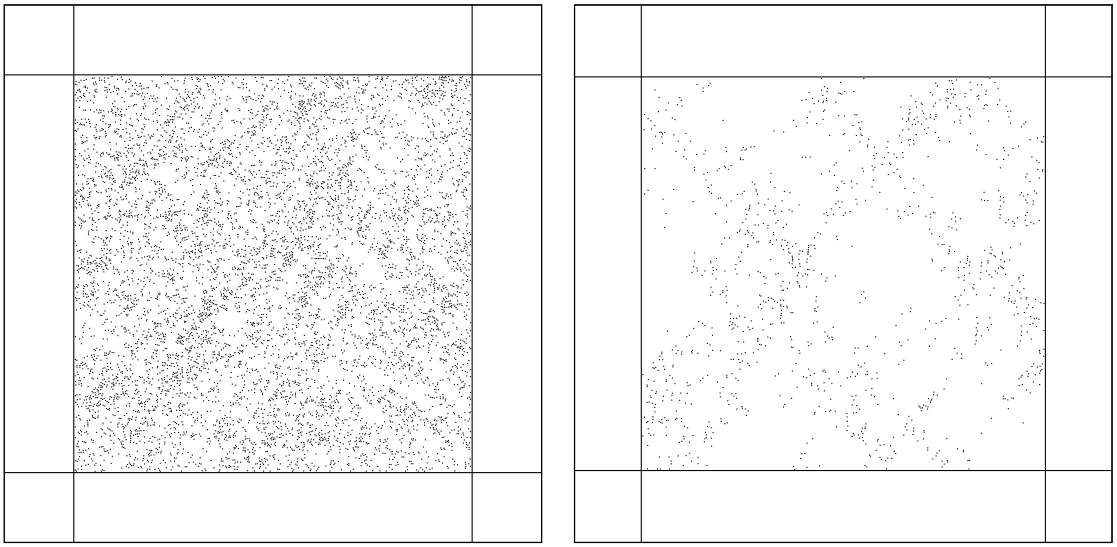

Figure 7.1: Snapshots of the system showing the contacts at which $v_r > \bar{v}_r$ at two different external forces; left: at $f/f_0 = 1.84$; right: at $f/f_0 = 2.13$, shortly before failure. The value $\bar{v}_r$ is the average rolling velocity.

with the center of the system. The circle's radius is such that a layer of at least two particles remains between the circle's surface and the boundaries, represented by the square. Only grains inside the circle are further processed. Through the center of the circle, a line is oriented at an angle Θ relative to the horizontal axis. A coordinate $S \in [0, 2R]$ measures the position on this line as shown in Fig. 7.2. The line is divided into about 140 bins of equal length, and all contacts are projected onto a bin on the line. Finally, we calculate the average of v_r at the contacts in a bin. This provides $\overline{v}_r(S)$.

Two example curves are shown in Fig. 7.3. One shows $\overline{v}_r(S)$ at $\Theta = 0°$ and one at $\Theta = 45°$. The curve for $\Theta = 45°$ displays a sharp maximum near $S \approx 0.7R$. This maximum indicates that $\overline{v}_r$ is elevated in a band oriented perpendicular to the direction of the bins, i.e. at $\Theta \approx 135°$. It intersects the line of the bins at $S \approx 0.7R$. The curve for $\Theta = 0°$ is relatively flat, indicating the absence of vertical bands.

As Θ changes, the total average rolling velocity $\overline{v}_r(\Theta) := \overline{\overline{v}_r(S)}$ is about constant. On the other hand, the variance $\sigma_r(\Theta) := \sum_{i=1}^{N} \left[v_r \left(i \frac{2R}{N} \right) - \overline{v}_r \right]$ of the values $v_r(S)$ strongly depends on Θ. N is the number of bins along S in direction Θ, and $\overline{v}_r$ is the mean of $v_r(S)$. When one evaluates $\sigma_r(\Theta)$ for all Θ, one obtains a graph as shown in Fig. 7.4(a). The graph illustrates the dependence of $\sigma_r(\Theta)$ on Θ at $f/f_0 = 2.13$, shortly before the failure. While $\sigma_r(0°) = 0.01$, the variance along the diagonal is $\sigma_r(45°) \approx 0.02$, i.e. about twice as large, reflecting the peak at $S \approx 0.7R$ along $\Theta = 45°$ in Fig. 7.3. A plot of σ_r against Θ therefore shows the preferred orientation of rolling bands. Note that the maximum variance does not appear at exactly $45°$ in Fig. 7.4(a), but at a slightly lower angle. To calculate the direction of the two peaks in the curve, both peaks were fitted with Gaussian curves, which are also shown in Fig. 7.4(a). The fit shows the left peak is located at $\Theta = 36.5° \pm 0.3°$, and the right peak appears at $\Theta = 141.5° \pm 0.7°$.

Examining the evolution of the peaks shown in Fig. 7.4(a), we observe in Fig. 7.4(b) that these peaks always appear at about the same directions during the simulation. The width of the peaks

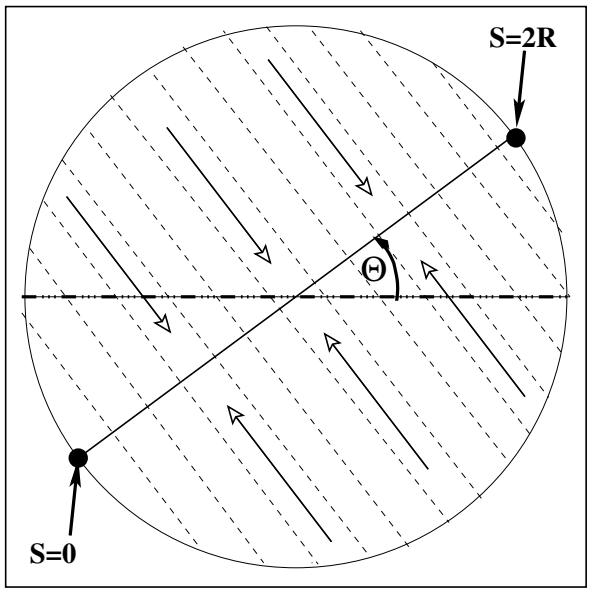

Figure 7.2: Mapping of the rolling velocities onto a line at angle Θ. The line along Θ is divided into steps that each contain the average of the mapped velocities v_r. The granular system is represented by the square.

decreases in the first half of the simulation, and it seems about constant afterwards.

What is the meaning of the peak directions? Considering failure, rolling motions are expected to concentrate in the shear band that forms, because within a shear band the relative motions are much higher than anywhere else. The direction of the shear band can for example be estimated by the Mohr-Coulomb theory [89]. It defines an angle $\pm\alpha_{MC}$ relative to the direction of increasing force f at which the shear band at failure is expected to appear in a continuous medium. It is [89]

$$\alpha_{MC} = 45^\circ - \frac{\phi}{2}, \tag{7.3}$$

$$\phi = \frac{\arctan\left(\sqrt{\frac{\sigma_2}{\sigma_1}} - \sqrt{\frac{\sigma_1}{\sigma_2}}\right)}{2}. \tag{7.4}$$

In this equation, $\sigma_1 < \sigma_2$ are the two principal stresses from Eq. 7.1, and ϕ is the internal friction angle. It is related to the interparticle friction angle $\phi_p = \tan(\mu)$ [90–92]. In our case $\sigma_2/\sigma_1 \approx f/f_0 = 2.15$ at failure and hence $\phi = 21.4^\circ$. Thus the shear band is expected to appear at $\alpha_{MC} = 34.3^\circ$ or, symmetry equivalent, at $180^\circ - \alpha_{MC} = 145.7^\circ$. These angles are very close to the values in Fig. 7.4(b).

Kuhn and Bagi [83] state that "after the appearance of a shear band, the rotation chains are obscured by the more intense rotations within the shear band". In this chapter, we see that rotations are not obscured but *concentrated* within the shear band. Indeed the direction of the shear band at failure seems identic to the direction of maximum rolling. We therefore call the rolling bands *proto shear bands*, i.e. bands which might become a shear band at the peak stress.

These proto shear bands in Fig. 7.1 resemble the shear band patterns observed by Török et al. [93]. Török explains the formation of shear band patterns in one specific direction by the principle of least dissipation rate. The authors of that paper explain that the shear bands will always develop in the direction for which dissipation is minimal. Their theory predicts the same shear band angle as

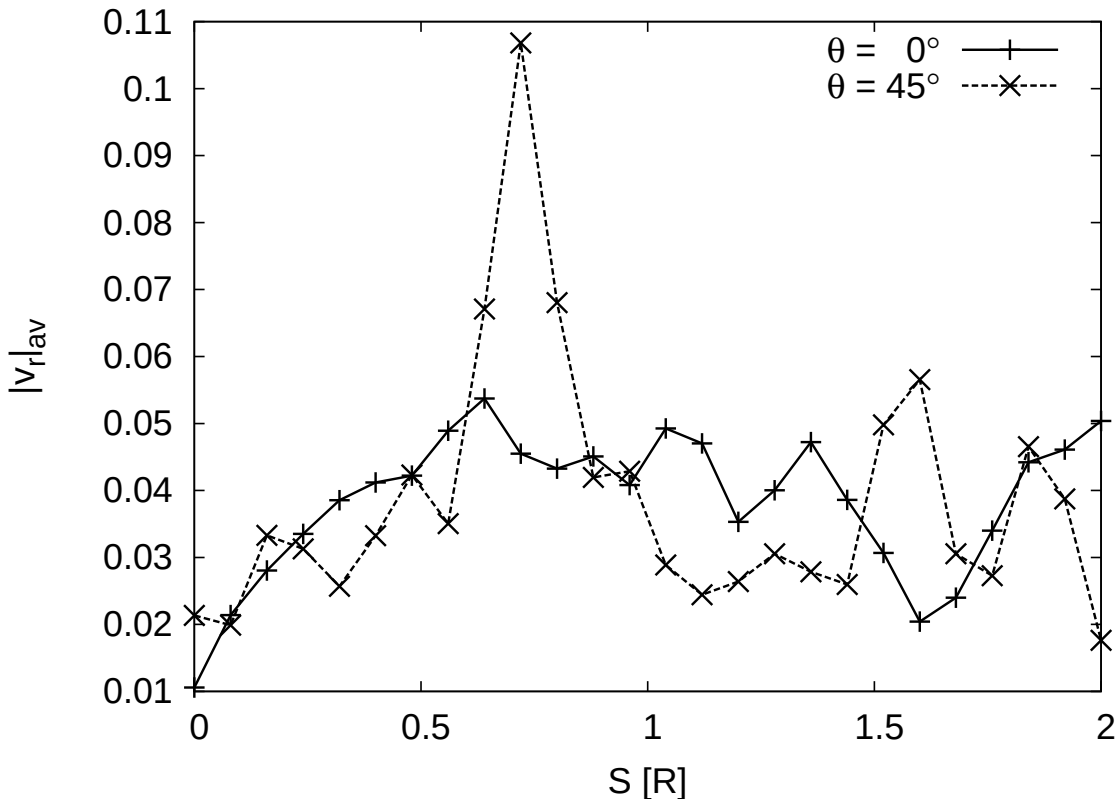

Figure 7.3: The average rolling velocity $\overline{v}_r(S)$ as a function of S for the two angles $\Theta = 0°$ and $\Theta = 45°$. The large peak for $\Theta = 45°$ indicates a diagonal band of rolling contacts.

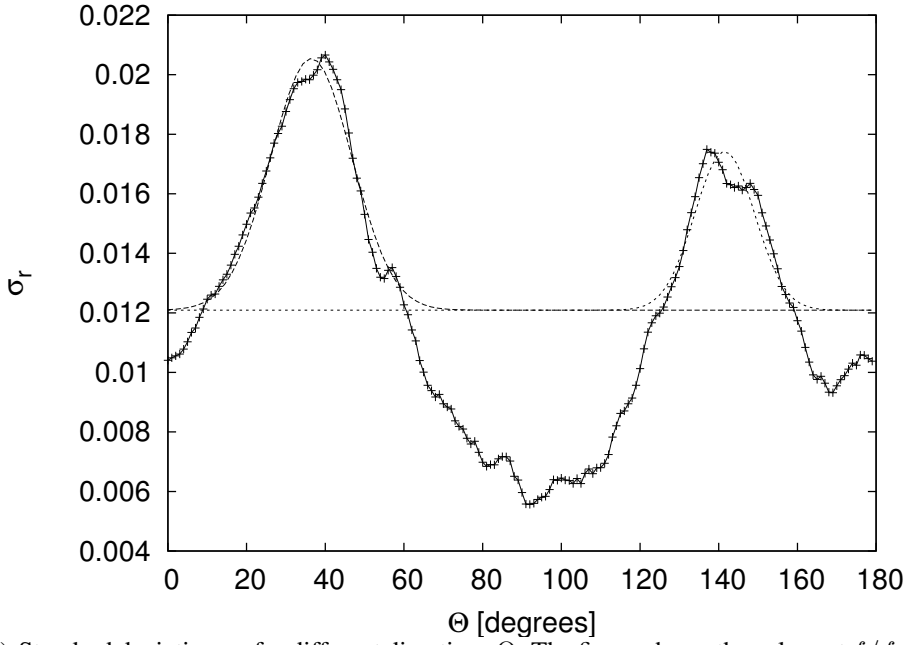

(a) Standard deviation σ_r for different directions Θ. The figure shows the values at $f/f_0 = 2.13$, shortly before the failure. Each peak is fitted with a Gaussian curve. The peak positions in the fits are $\Theta = 36.5(3)$ and $\Theta = 141.5(7)$ (numbers in brackets are the errors). The horizontal line marks the average value, while the other dashed lines are Gaussian fits of the maxima.

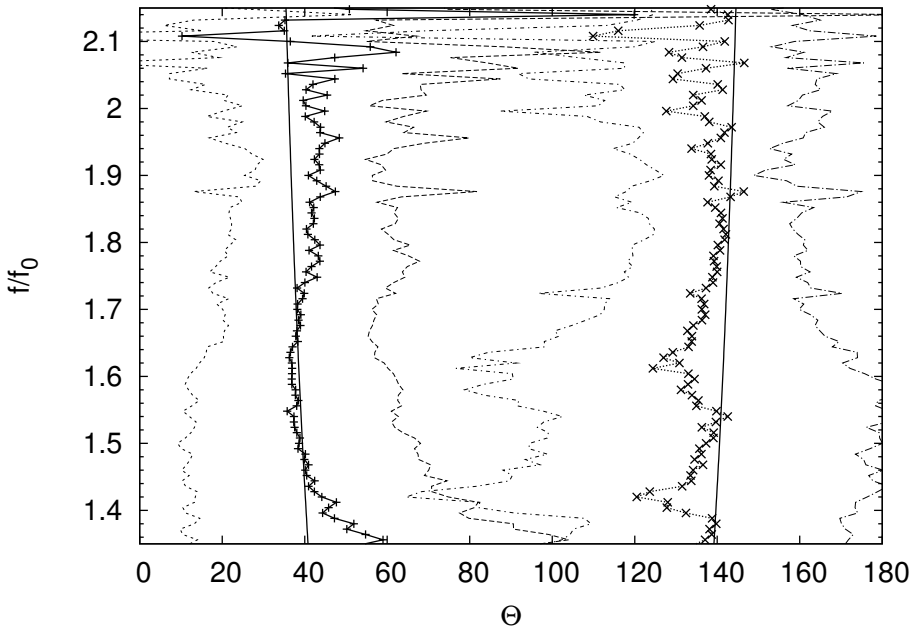

(b) Evolution of the position of the two peaks in Fig. 7.4(a) until the failure at $f/f_0 = 2.15$. Values for $f/f_0 < 1.35$ are omitted because the peak size is similar to local fluctuations, resulting in large errors. The heavier lines are accompanied by smaller lines on each side, indicating the width of the peaks. The almost vertical lines indicate the positions of the peaks predicted by Mohr-Coulomb.

Figure 7.4: Peaks of $\sigma_r(\Theta)$ at $f/f_0 = 2.13$, shortly before failure, (top figure), and during the simulation (bottom figure).

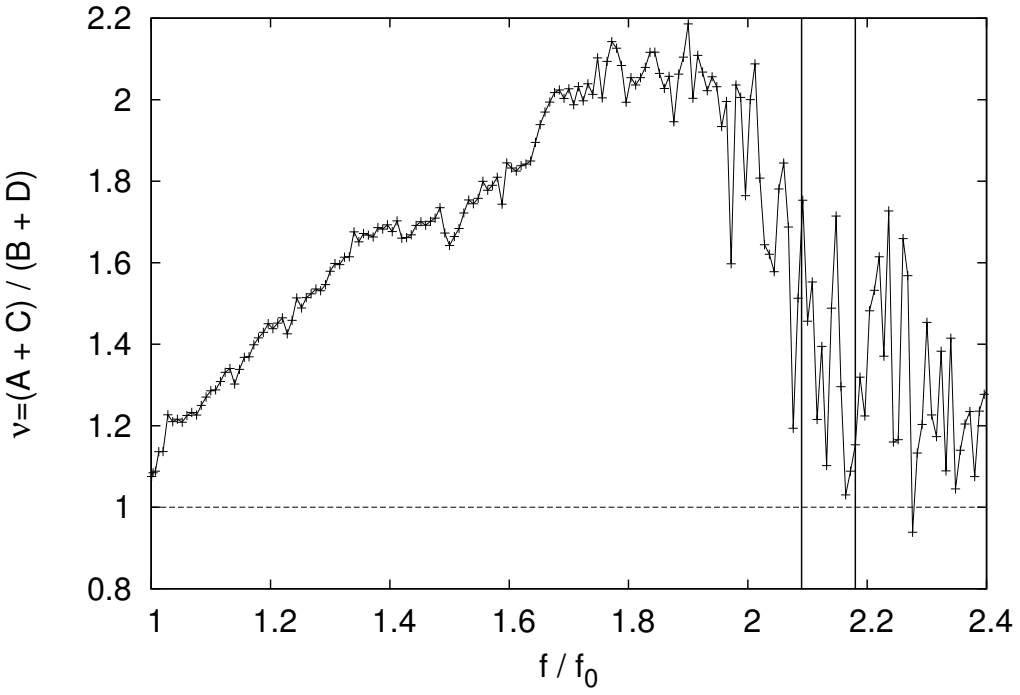

Figure 7.5: Ratio $\nu = (A + C)/(B + D)$, averaged over four different systems. The values A, B, C, D are the sum $\Sigma_r(\Gamma)$ for the four directions $\Gamma = 0°(A)$, $45°(B)$, $90°(C)$ and $135°(D)$. This sum is defined in Eq. 7.5. Failure occurs, depending on the system, between $f/f_0 = 2.09$ and $f/f_0 = 2.18$. The two values are indicated by vertical lines.

the Mohr-Coulomb condition in Eq. 7.3. While the predicted angle is unique, the number of shear bands cannot be calculated from the theory of least dissipation: indeed the number of shear bands is undefined. A later section in this chapter will investigate the number of the proto shear bands. We will see that their number decreases until the failure. The decrease is related to an increasing length scale of organization.

To condense the observation of preferred directions of rolling to one number, we calculate the sum of $\sigma_r(\Theta)$ over adjacent directions $\Theta \in [\Gamma - 15°, \ldots, \Gamma + 15°]$ and compare the outcome in the direction of the rolling bands with other directions. This sum is:

$$\Sigma_r(\Gamma) = \sum_{\Theta=\Gamma-15}^{\Gamma+15} \sigma_r(\Theta) \tag{7.5}$$

$\Sigma_r(\Gamma)$ is calculated for the directions $\Gamma = 0°(A)$, $45°(B)$, $90°(C)$ and $135°(D)$. We denote the four values of Γ by A, B, C and D. Plotting $\nu = (B + D)/(A + C)$ against the external force f in Fig. 7.5, one observes that $\nu > 1$ soon after the simulation beginning. ν increases continuously until about $f/f_0 = 1.8$. This value coincides with an important change in the dominant contact transition; until this time, the system's most frequent contact transition is a contact becoming sliding. After $f/f_0 = 1.8$, the rate of lost sliding contacts exceeds in any time interval until the failure the rate of other contact status transitions. This is the two stage weakening process investigated in detail in

Sec. 5.6. Finally, after $f/f_0 = 2$, the ratio ν decreases again until the failure at $f/f_0 = 2.15$, where it suddenly increases again (probably due to the formation of a single shear band).

7.3 Evolution of the organization of rolling

We now want to investigate the number of rolling bands (the proto shear bands) as a function of increasing external force. Specifically, we calculate the distribution of the values $\overline{v}_r(S)$ in the line steps in Fig. 7.2 for direction $\Theta = 140^\circ \approx 180^\circ - \alpha_{MC}$. This is the direction of the shear band which appears at the failure. We evaluate the distribution of rolling motions for about 150 different values of f/f_0 until failure. The result is shown in Figure 7.6. The gray-scale is adjusted to fit the largest average rolling velocity (black regions) and the lowest average rolling velocity (bright regions). The simulation starts at the bottom of the figure ($f/f_0 = 1$), and goes until shortly after failure. The failure is indicated by a black vertical line close to the upper limit. The left side corresponds to position $S = 0$ in Fig. 7.2 and the right side to position $S = 2R$. The width of the figure covers about 140 different values.

At the bottom of the figure, where the simulation begins, the distribution of rolling is quite uniform, although some irregularities show up as small peaks. These irregularities remain present for a long time. This reveals that the rolling motions are not arbitrary, but they are determined by the granular structure. This structure changes only slightly with increasing $f(t)$.

As the simulation proceeds and f rises linearly, some peaks increase while others decrease. The most pronounced peak is located close to the center of the figure. It appears early in the simulation, increases with f for quite a while, and after some fluctuations disappears shortly before the failure. This disappearance nourishes two other peaks: one is located at a rightward position and one at a leftward position. They both constantly increase until the failure. At the failure, both peaks disappear, and a broader, unique dark area appears close to the center of the distribution. This spot is the signature of the single shear band that governs the particle motions. Note that the dark spot shows that rolling motions are concentrated within a small region in the direction $\Theta \approx 40^\circ$. The width of the shear band can be estimated by the width of the spot, which is about 1/10th of the total width of the figure, corresponding to 10-15 particles. This finding is in agreement with the literature [94, 95].

7.4 Length scale of the organization

Figure 7.6 showed that one finds a decreasing number of rolling bands with increasing f. Finally this section provides a measure for their number. One possibility to extract a length scale is to evaluate the Fourier coefficients of a function. We approximate $\overline{v}_r(S)$ by a truncated Fourier series:

$$\overline{v}_r(S) \approx A_0 + \sum_{k=1}^{n} A_k \cos\frac{k\pi S}{R} + B_k \cos\frac{k\pi S}{R}, \tag{7.6}$$

where n is the number of Fourier coefficients. The Fourier coefficients are

$$\begin{aligned} A_k &= \frac{1}{N}\sum_{j=1}^{N} \cos\left(\frac{2j\pi}{N}\right)\overline{v}_r(2Rj/N), \\ B_k &= \frac{1}{N}\sum_{j=1}^{N} \sin\left(\frac{2j\pi}{N}\right)\overline{v}_r(2Rj/N), \end{aligned} \tag{7.7}$$

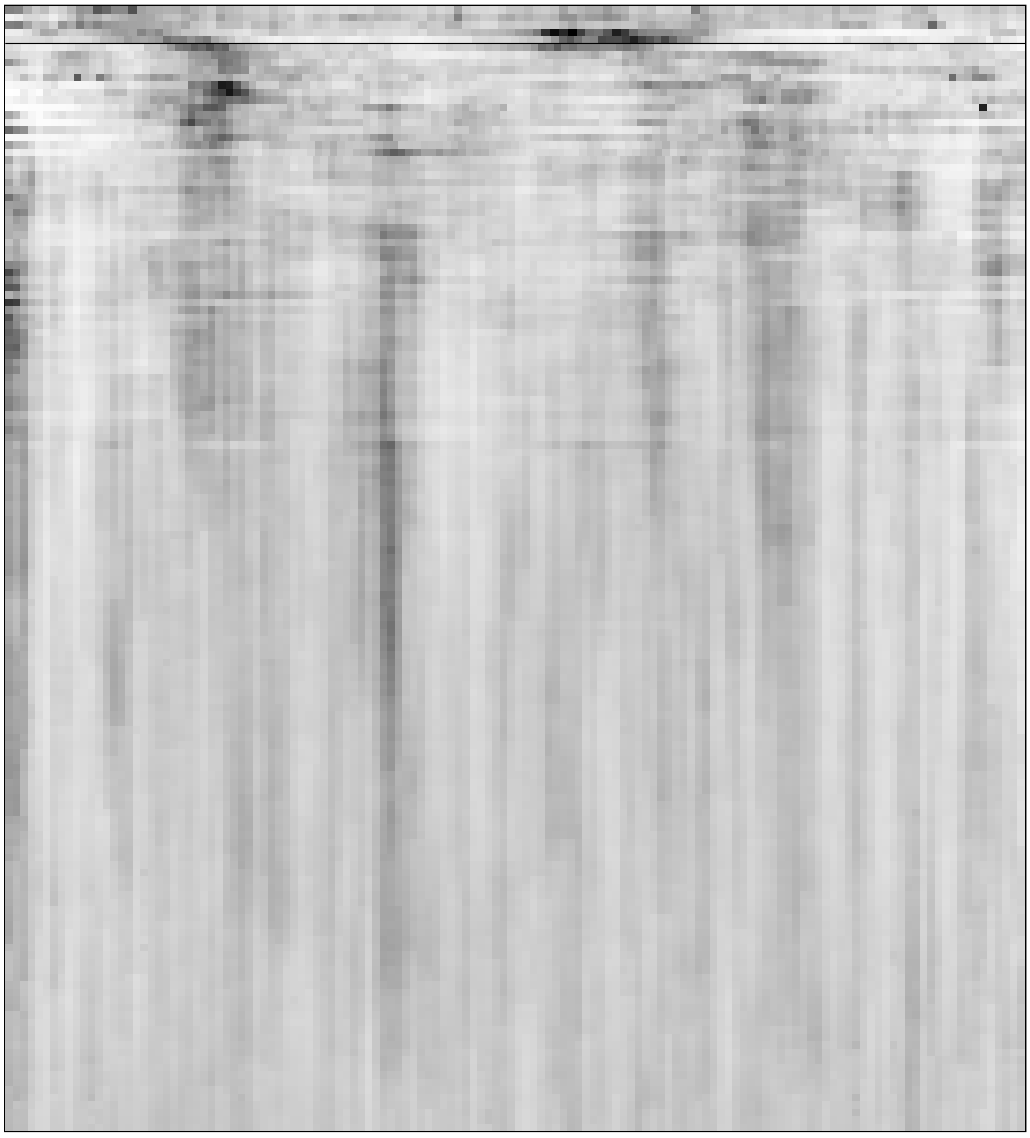

Figure 7.6: $\overline{v}_r(S)$ at $\Theta = 140°$. In horizontal direction, the coordinate S, taking about 140 different values, increases from left to right, while from bottom to top f/f_0 increases. The horizontal line close to the top marks the failure.

with N being the number of steps or bins in Fig. 7.2. If n is small, we obtain a very smooth curve, but risk to smear out the bands, and therefore not resolve them. On the other hand, if n is too large, we will not be able to distinguish between statistical fluctuations and the bands themselves. The resolution is also limited to the number of steps in Fig. 7.6, which is about 140. We will therefore truncate the number of coefficients to $n = 5, 10, 20, 30, 40$ and compare results for different n.

For each n, we obtain an approximation of $\overline{v}_r(S)$. We then estimate the number of bands by counting the number of zero-crossings of $\overline{v}_r(S) - \overline{\overline{v}_r(S)}$, where $\overline{\overline{v}_r(S)}$ is the average of $\overline{v}_r(S)$. We assume each band generates two zero-crossings, and plot in Fig. 7.7 the number of bands detected. Naturally, the number of bands depends on the value of n, but a clear downward trend is visible for $n \geq 10$ when f increases. This trend starts at the simulation beginning and continues until the failure, which appears between $f/f_0 = 2.09$ and 2.18, depending on the system. In the beginning, we observe in the individual simulations 18-20 peaks. The length of one system is about 128 particle diameters, so the distance between two peaks is roughly six particles. Although no clear plateau is visible in the simulation beginning, the observation of even smaller length scales most probably requires much larger systems. At the failure, the number of peaks drops to 2-3. Thus it decreases by almost one order of magnitude, meaning that the correlation length increases in the same way. For example, for the values in Fig. 7.6, we find that for all $n \geq 2$ exactly the two peaks shortly before the failure at $f/f_0 = 2.15$ are detected, meaning that the length of organization close to the failure is half the system size.

Fig. 7.7 shows that the number of bands becomes almost independent of n close to the failure at $f/f_0 = 2.15$. This is not an averaging effect, but applies to the individual simulation. The higher order Fourier components are therefore suppressed with increasing external force f and the lowest Fourier components dominate. Figure 7.7 is an average over four systems, but if one plots the values for a single system the number of peaks decreases to two to three at the failure. Two is the number of rolling bands observed in Fig. 7.1 in the right side figure, taken just before failure. The increasing characteristic ordering length scale is most probably connected to the increase in the number of low frequency vibrational modes, observed close to the stability limit by Wyart and coworkers [8, 41]. One important source of such vibrations are precursors of failure, investigated in Chap. 6.

In Sec. 5.5.4 it was shown that similar to the organization of rolling contacts in bands, sliding contacts tend to organize close to failure. This organization was shown in Fig. 5.13 to correspond to the clustering of sliding contacts in diagonal bands. Although the direction of these bands has not been investigated in detail, it is clearly similar to the direction of the rolling motions. This suggests that sliding and rolling motions are correlated. The next section investigates these correlations.

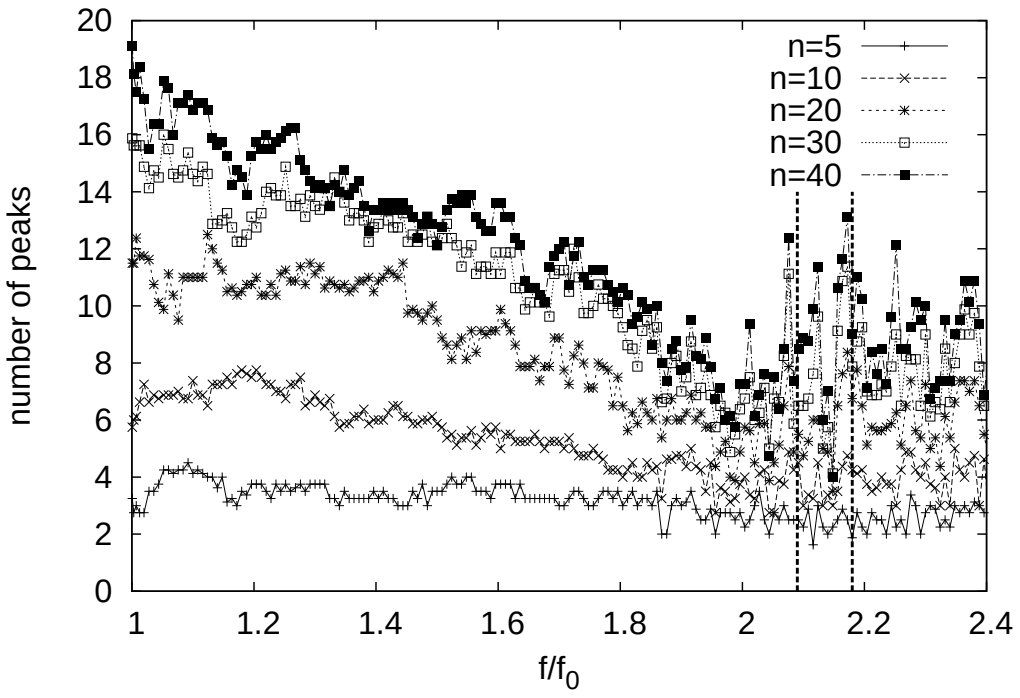

Figure 7.7: Number of peaks at $\Theta = 140$ for different cutoffs n in the Fourier series. The values are averages over four systems with $N = 16384$ particles. The failure of the systems appear in the range marked by two vertical arrows at $f/f_0 = 2.09$ and $f/f_0 = 2.18$.

7.5 Correlation of sliding and rolling motions

When looking at the positions of sliding contacts or the concentration of rolling, one finds that the positions of sliding contacts are not concentrated anywhere in the system at the simulation beginning, whereas the rolling motions are always correlated. As the simulation continues and the external force increases, sliding contacts anticorrelate while rolling motions correlate stronger. This very different behavior indicates a quite different functional dependence on the external force f of sliding and rolling contacts. Close to the failure, however, both sliding contacts and rolling motions do correlate strongly, and both of these quantities are concentrated in the same regions in the system. This observation suggests there is an increasing correlation between the positions of sliding contacts and large rolling motions. To reveal if correlations between sliding and rolling motions are indeed increasing, the local values of the number of sliding contacts and the rolling motions are correlated. This is done for each region. These square regions have been defined in Sec. 5.5.1. Their length is four particle diameter. Carrying out the sum over all N_{regions} regions, one obtains the correlation coefficient:

$$Corr = \frac{1}{N_{regions}} \sum_{i=1}^{N_{regions}} \frac{\left(M_{s,i} - \overline{M}_s\right)}{\sigma_{M_s}} \frac{\left(M_{r,i} - \overline{M}_r\right)}{\sigma_{M_r}} . \tag{7.8}$$

Here $\overline{M}_s$ and $\overline{M}_r$ are the average number of sliding contacts and the average rolling velocity as defined in Eq. 7.2. The standard deviations of sliding and rolling are σ_{M_s} and σ_{M_r}. The coefficient $Corr$ can take values between -1, indicating perfect anticorrelation, and +1, showing perfect correlation. Fig. 7.8 shows the value of the correlation coefficient as a function of the external force f/f_0. The standard deviation of the quantity of which $Corr$ is the average is not shown in the figure. It is always close to unity, indicating rather large scatter in the individual contribution to the sum in Eq. 7.8. In the figure one nicely sees that at the simulation beginning the correlations are very low. In a short period of time they increase until $f/f_0 = 1.1$. Then the correlation decreases again until $f/f_0 = 1.8$. This external force separates two periods of different granular behavior. The two periods have been introduced in Sec. 5.6: the number of sliding contacts increases during the first period, and decreases again in the second period. Also the organization of sliding contacts changes from ordering in the first period to clustering in the second period. This suggests that the correlation between sliding and rolling also changes. Figure 7.8 shows that indeed the correlation increases again after $f/f_0 = 1.8$. The increase becomes more pronounced close to failure, where also some sharp maxima appear. These maxima coincide with the positions at which precursors have been observed in many figures in Chaps. 5, 6. Thus the appearance of precursors is related to an increase in the correlations of sliding and rolling. However, only some of the precursors show up. Most probably there are too few data points in Fig. 7.8 to resolve all of them. Finally, when failure happens at $f/f_0 = 2.15$, the correlation quickly decreases, but increases again after a short period. Most probably the decrease just after failure is due to the system returning to a state close to the one at the beginning of the simulation. This behavior was also observed for the total number of sliding contacts, which decreases almost to zero, and also for the rolling motions, which no longer show a preferred direction in Fig. 7.5.

7.6 Conclusion

We find that the rolling of particles is concentrated in diagonal bands across the system. These bands appear at the beginning of the simulation, but not at any orientation: they organize in specific

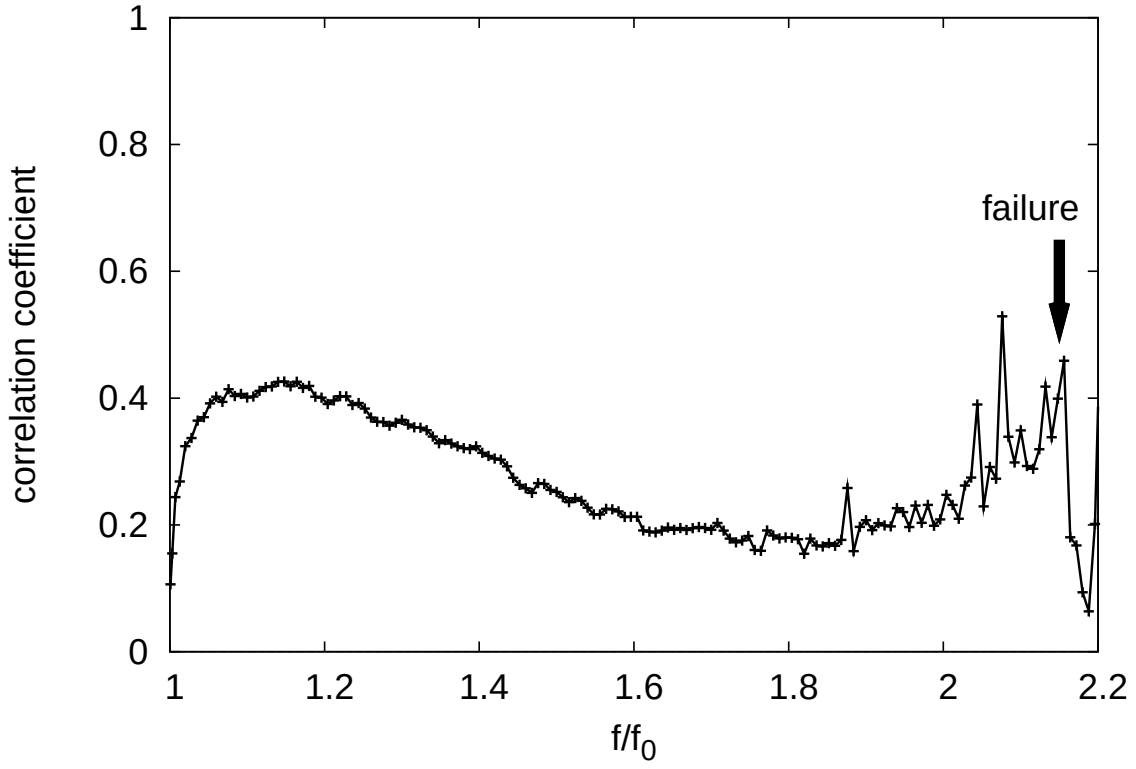

Figure 7.8: Correlation of the density of sliding contacts and the density of rolling motions in the local regions. The correlation is calculated through Eq. 7.8.

directions. The direction of the rolling bands is very similar to that of the shear band appearing at failure. This has been shown by comparing the direction predicted by the Mohr-Coulomb theory, and the resulting direction of the theory of least dissipation of Török et al., with the observed directions of rolling in the simulations.

The organization of rolling motions in bands increases with increasing external force until the failure. In the beginning of the simulation, the particular microscopic structure determines the local rolling. But with increasing f, rolling motions concentrate in two symmetry-equivalent directions which can be determined by the Mohr-Coulomb theory. The Fourier analysis evidenced increasing long range correlations of the rolling motions, with a length scale that increases by roughly one order of magnitude during the simulation and attains a value close to the size of the system shortly before the failure.

Rolling and sliding motions are correlated. This correlation is stronger just after the simulation beginning and at the failure, and weaker at the maximum number of sliding contacts. As sliding and rolling are two types of motion, correlations to other types of motions might also exist. For example rolling motions and the nonaffine part of deformations [34] might be correlated, because nonaffine motions are also involved in failure.

The results show that weakening and failure have many interesting aspects that need to be investigated. But do the results depend on the setup of the system, specifically on the boundary conditions? The next chapter investigates this possible dependence in detail.

Chapter 8

Comparison of rigid wall and membrane boundaries

The preceding chapters considered many different aspects of the the weakening and failure of small and large granular assemblies. One of the achievements was the observation of precursors of failure, appearing at specific values of f which depend on the contact structure of the system and the system size. Another aspect was the number of sliding contacts, which first rises, and then decreases again for a short period before the failure. We have also seen the spatial correlation of sliding contacts changing. In the beginning, sliding contacts are randomly distributed, but they cluster close to failure. Rolling motions also organize close to the failure, and concentrate in the same specific regions as the sliding contacts. All these results were obtained from simulations with rigid wall boundaries, introduced in Sec. 2.3.

Some of these results may, however, depend on the boundary conditions [36]. Therefore it is necessary to conduct the same experiment with different conditions and evaluate the outcome. In this chapter the sidewalls of the rigid wall system are replaced by membranes. These membrane boundary conditions have been explained in Sec. 2.3. The results presented in this chapter are obtained for systems with $N = 16384$ particles. This is the same size as the rigid wall systems investigated in the preceding chapters, and allows for a direct comparison of the results to the data in Chaps. 5, 6. Although only one example of a system is detailed here, the same results were observed in at least four membrane systems of the same size and are thus independent of the realization.

The membrane conditions applied here can be considered a two dimensional version of the three dimensional experimental *triaxial test*. In such experimental tests of granular assemblies, one often encloses the sample in a cylindrical membrane. Then sample and membrane are submerged in water, and the stress on the sides of the sample are controlled by water pressure. Although the properties of the membranes here might be different, the membrane boundary conditions are closer to the experimental conditions that the rigid wall boundaries in the chapters before.

As we have seen in Sec. 4.2, the external force f_{fail} at which the failure appears depends on the boundary conditions. Thus, when comparing the behavior of systems with different boundary conditions, it is helpful to define a parameter which matches failure to a unique, system independent value. One possible choice for this parameter is the simulation time, rescaled by the time it takes until the failure. This choice has been made for the investigation of the trigger mechanisms of failure in Chapter 3. But as the external force f increases linearly with time, one can also rescale the force by

the difference between simulation beginning (f_0) and failure (f_{fail}):

$$\tau_f = \frac{f - f_{\text{fail}}}{f_{\text{fail}} - f_0} \,. \tag{8.1}$$

The reason why instead the time is rescaled in Chapter 3 is that two different averaging procedures are involved in extracting the results in that chapter, and the averaging gets much simpler when done for a certain interval of time instead of an interval of force (for details see footnote[1]). The dimensionless parameter τ_f takes the value $\tau_f = -1$ at the beginning of a simulation, and $\tau_f = 0$ marks the appearance of failure. Failure happens for the rigid wall simulation at the external force $f_{\text{fail}}/f_0 = 2.15$, and the example system with membrane boundaries, which is investigated in more detail in the following, fails at $f_{\text{fail}}/f_0 = 2.38$. With the results plotted against parameter τ_f, it is simple to compare results for different boundary conditions.

The sections in this chapter investigate the most important aspects of weakening and failure. The first section, Sec. 8.1, examines the dependence of the kinetic energy on the boundary conditions. The next section, Sec. 8.2, investigates the number of sliding contacts M_s, and compares the results to the number M_s discussed in Sec. 5.4 for rigid wall boundaries. Next, Sec. 8.3, discusses the number of contacts changes. For rigid wall boundaries, they have been examined in Sec. 5.4.3. The next section, Sec. 8.4 considers the organization of sliding contacts, which have first been presented for rigid walls in Sec. 5.5.4. An important measure for stability is the number of triangular figures in the packing. These figures, introduced for the first time in Sec. 5.7, are examined in Sec. 8.5. Very important for the weakening process is also the appearance of precursors. These are investigated in more detail in Sec. 8.6, finally showing that many features do not depend on boundary conditions. Thereafter, Sec. 8.7 summarizes which features are related to the boundary conditions, and which properties of granular behavior are more general.

8.1 Kinetic energy and vibrations

The first question to answer is the possible boundary dependence of the evolution of the kinetic energy. Figure 8.1 shows the energy during a rigid wall simulation (figure on top), and also in a membrane boundary system (figure on bottom). The figure enables easy comparison between the different boundary conditions. The two systems behave very similar until the appearance of the first precursor, which is marked by arrows. For the membrane conditions, vibrations appearing after such a precursor are much larger than for the rigid walls. This behavior is expected, because the membrane boundaries are more flexible.

In the membrane simulation the difference in the peak height between the last precursor and the failure is just about one order of magnitude, while it is more than three orders of magnitude in the system with rigid walls. Comparing the maximum kinetic energy in the two systems, in the membrane simulation this maximum is about one order of magnitude lower than in the rigid walls system, and the peak is also much thinner.

[1] In the beginning of the simulation, a parabolic matching is applied to obtain a continuously differentiable force curve. Thus time and force are not linearly related during the first 2.5% of the simulation time. Due to the parabolic matching, the averaging over many systems in time is much easier than averaging in force, because the number of data steps per interval of time is always constant. Here, only one system is investigated, so there is no averaging.

In conclusion, the main difference between the two curves is the vibrations being much more pronounced in the membrane simulations. The general evolution of the kinetic energy until the failure is similar. The next sections are concerned about quantities related to the microscopic scale, in particular the number, distribution and organization of sliding contacts.

8.2 Number of sliding contacts

During the weakening of granular assemblies, the number of sliding contacts M_s increases as the external force f rises. Figure 8.2 shows the relative number $m_s = M_s/M$ of sliding contacts for two systems, one with rigid walls, and one with membrane boundary conditions. The general trend in the relative number of sliding contacts m_s is similar in the two cases. The simulations start with a linear increase in m_s, and a plateau follows at $\tau_f \approx -0.4$. The maximum of m_s is higher for rigid wall boundaries. Presumably this is due to the fact that the rigid walls stabilize the system, and a higher number of contacts being sliding is required to weaken the system and drive it to failure. During the plateau of m_s, the first precursors of failure appear for both boundary conditions. After the plateau a decrease follows, and failure appears during a sharp increase of m_s thereafter. This sharp increase at failure is for the membrane boundary conditions preceded by a very fast and deep decrease of m_s. This decrease might be a precursor, or it is due to a large vibration appearing after a precursor. In the two figures, the rise in m_s at the failure is similar, at least when one disregards the last precursors before the failure in the membrane boundaries simulation.

After the failure, all sliding contacts disappear, except for the contacts with the walls, which are by definition always sliding. Note that the membrane boundaries also contain two walls (at the top and the bottom of the system).

The signature of precursors is always a decrease of m_s. But this decrease in m_s is much stronger for membrane boundaries, meaning that precursors are more pronounced there. Furthermore the number of precursors observed in the figure is much larger for the membrane boundaries, and the frequency of their appearance becomes much larger close to the failure. A closer inspection of the number of precursors shows that in the rigid walls simulations there are less precursors just before failure than around $\tau = -0.1$. In the membrane simulation the frequency is higher at $\tau = -0.2$, then decreases, and increases again before failure.

Another important difference in the figures is m_s being more noisy after the first precursor in the membrane simulation, meaning that vibrations are more important for these conditions. Since the boundaries are less rigid than the straight walls, particles of the membrane can move independent of other particles of the membrane with which they are not in contact. This difference between rigid wall conditions and membrane boundaries has been explained in detail in Sec. 2.4, where the membranes were constructed.

In conclusion, in this section we have seen that the number of sliding contacts is lower for the membrane simulation, but the general evolution of this number is similar to the rigid walls conditions. The next section examines the contact status transitions which are responsible for the observed evolution of sliding contacts.

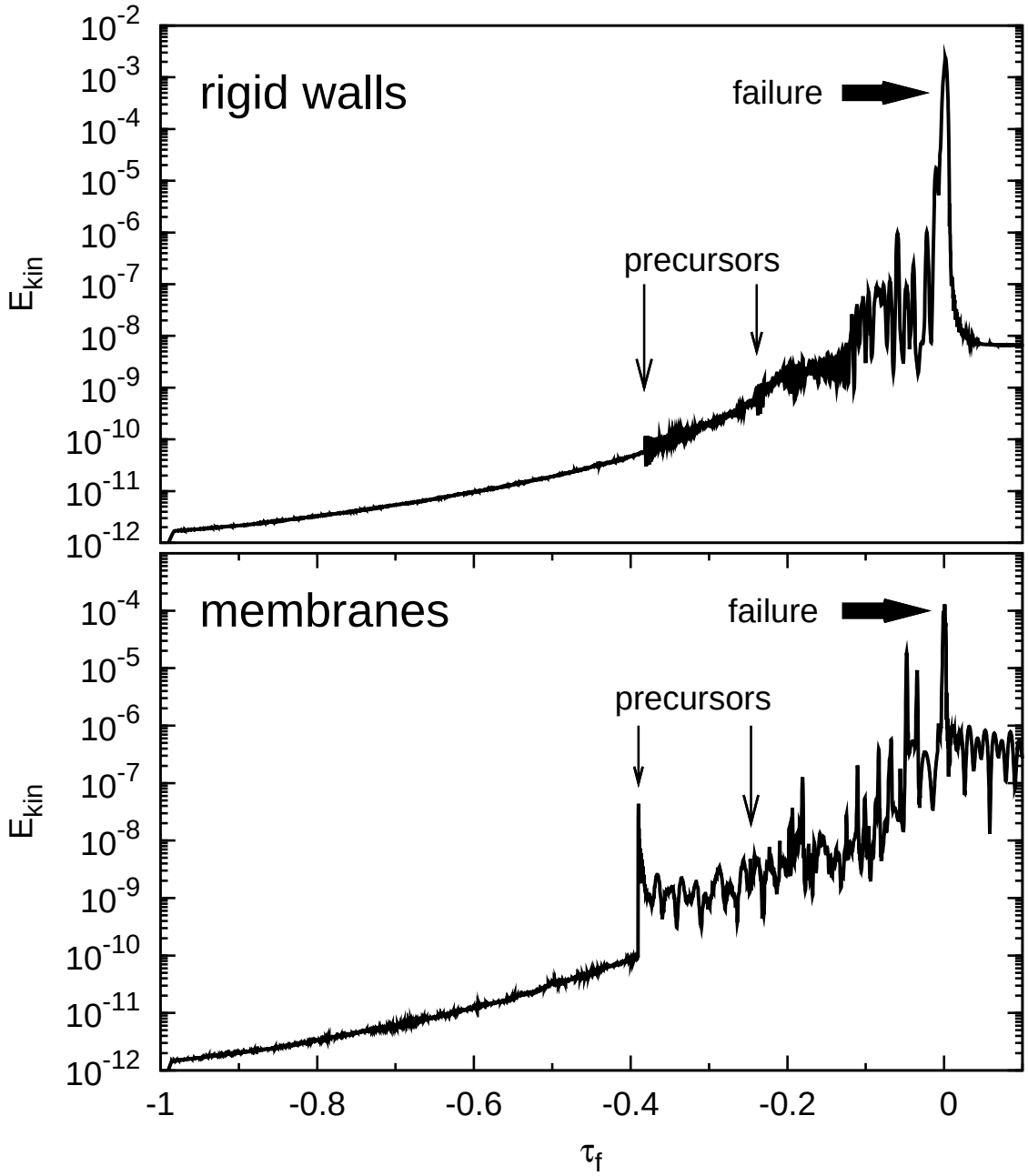

Figure 8.1: Kinetic energy for two systems with $N = 16384$ particles. Top: example of a system with rigid wall boundaries; Bottom: example of a system with membrane boundaries. For each curve, the first and one subsequent precursor are indicated by arrows.

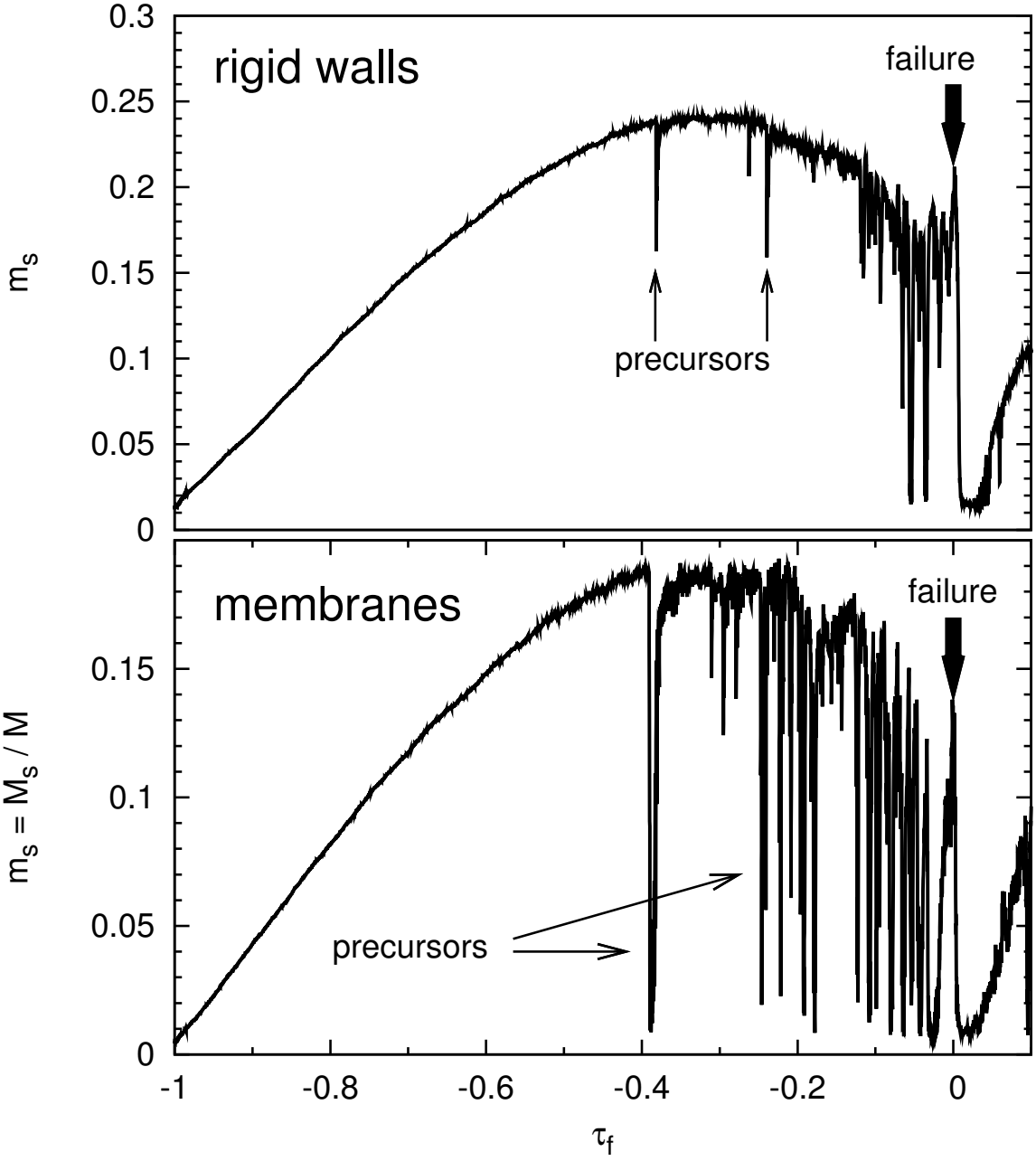

Figure 8.2: Number of sliding contacts for systems with $N = 16384$ particles. Top: system with rigid wall boundaries; Bottom: system with membrane boundary conditions.

8.3 Contact status transitions

In the beginning of the simulation, all particle-particle contacts are nonsliding. In fact these contacts are not only nonsliding, but the tangential forces are zero, because in the compression stage prior to the simulation, the particles' surfaces are assumed perfectly smooth, i.e. no friction is allowed. When the simulation starts, friction is turned on, and tangential forces arise when the external force f increases. The tangential force F_t at some contacts increases and eventually attains the threshold μF_n at which a transition occurs, and the contacts become sliding.

The evolution of the number of sliding contacts in Fig. 8.2 can be understood in terms of the different numbers of contact status transitions. These are shown in Fig. 8.3 for the straight walls boundaries (upper figure) and the membrane boundaries (bottom figure). The three most frequent transitions in the systems are exactly those that alter the number of sliding contacts. In both simulations, the number of contacts becoming sliding is about constant until $\tau_f = -0.4$. But as more and more contacts become sliding, the probability for the inverse transition rises, and an increasing number of contacts become nonsliding again. Thus there are two competing transitions, one from closed (or nonsliding) to sliding, $C \rightarrow S$, and one from sliding to closed, $S \rightarrow C$. These two transitions control the increase in sliding contacts until they balance each other at $\tau = -0.4$. Then a third transition becomes important, which is the disappearance of a sliding contact, $S \rightarrow O$ (the O means that the contact opens, and the forces transmitted vanish). The observed frequency of the status transitions for the membrane conditions is very similar to those for the rigid wall boundary conditions.

Another similarity is the number of transitions $S \rightarrow C$ and $C \rightarrow S$ changing quickly in Fig. 8.3 at the appearance of a precursor of failure. For both the rigid walls and the membrane boundaries, the first precursor appears when the curves $C \rightarrow S$ and $S \rightarrow C$ match each other. Close to the failure, the fluctuations in the curves are more pronounced in the membrane simulation, confirming the observation in Fig. 8.2 that the number of sliding contacts is fluctuating. After the failure, all kinds of status transitions decrease quickly by more than two orders of magnitude for the rigid wall condition, while in the membrane simulation the decrease is smaller but still of one order of magnitude. The force until the next failure happening is short in both simulations ($\Delta f / f_0 \approx 0.15$).

The observed behavior for the two boundary conditions shows that the number of contact status transitions, which is responsible for the evolution of the sliding contacts in Fig. 8.2, is almost independent of the type of boundary conditions.

8.4 Organization of sliding contacts

So far the number of sliding contacts has been the point of interest. But the sliding contacts are not randomly distributed; instead they show either clustering or ordering tendencies, depending on the value of the external force f and the boundary conditions. Thus we gain new insight into the system's behavior by investigating their distribution. In the same way as done for the rigid wall boundaries simulations in Sec. 5.5.4, the system is divided into small square boxes containing a small number of particles. The length of one square box $l = 8r_{\mathrm{av}}$ is the same as for the rigid wall systems, and the average number of particles in a box is also the same.

Some confusion might arise about how to define the position of the boxes, and how to find out which boxes are at the systems' boundaries and should thus be disregarded. Figure 8.4 shows the division for one simulation with $N = 16384$ particles. The figure does not show the boxes which are offset at half length of one box. Thus in each direction it shows only every second box. In each

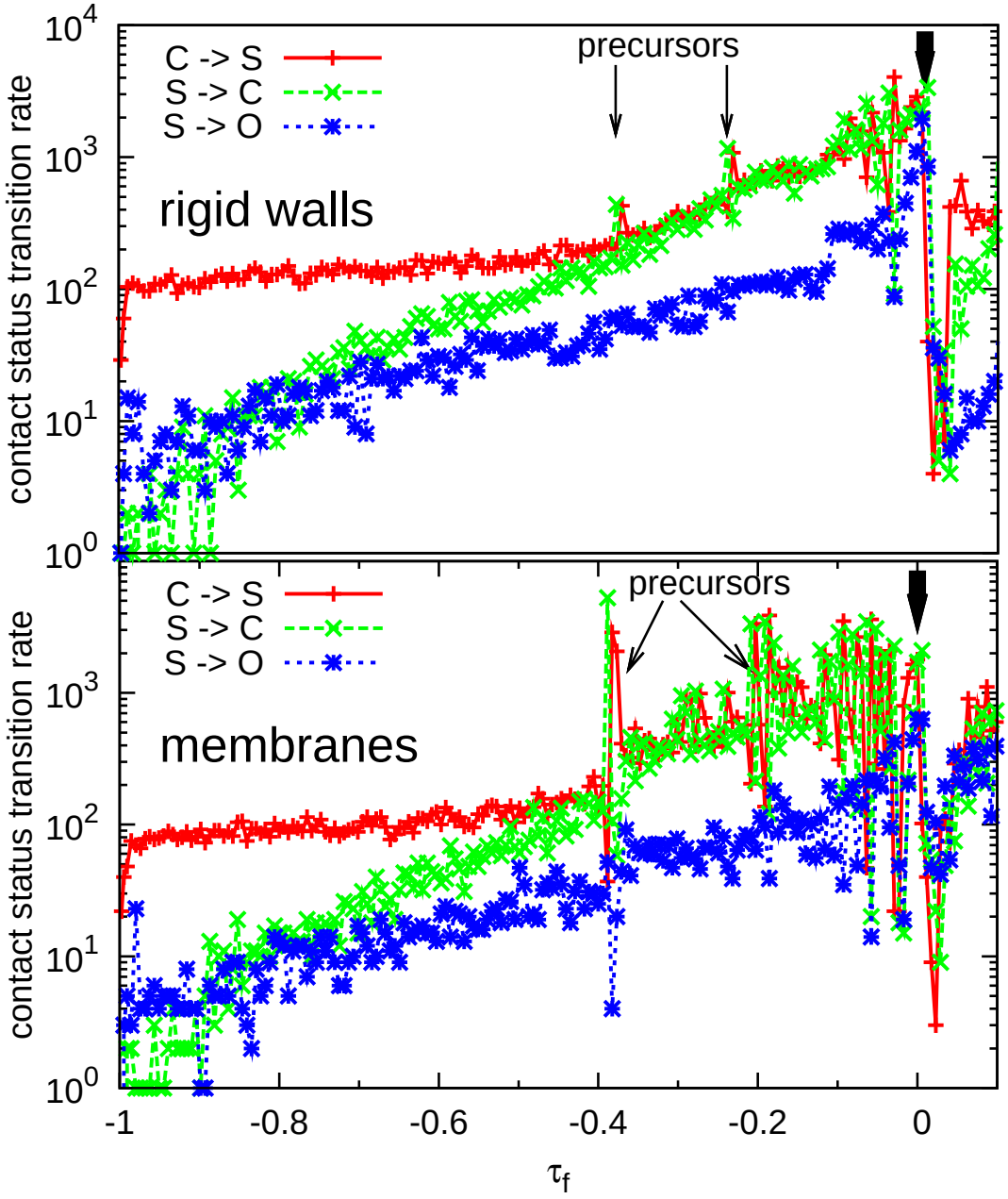

Figure 8.3: Rate of contact status transitions. Top figure: transitions in a system with rigid walls at the boundaries. Bottom figure: transitions in a system with membrane boundaries. The figures show the rate of transitions occurring in an interval of external force $\Delta f/f_0 = 8 \times 10^{-3}$. This corresponds to $\Delta\tau_f = 5.6 \times 10^{-3}$ in the upper figure and $\Delta\tau_f = 4.6 \times 10^{-3}$ in the lower figure. In both figures failure is marked by a heavy arrow.

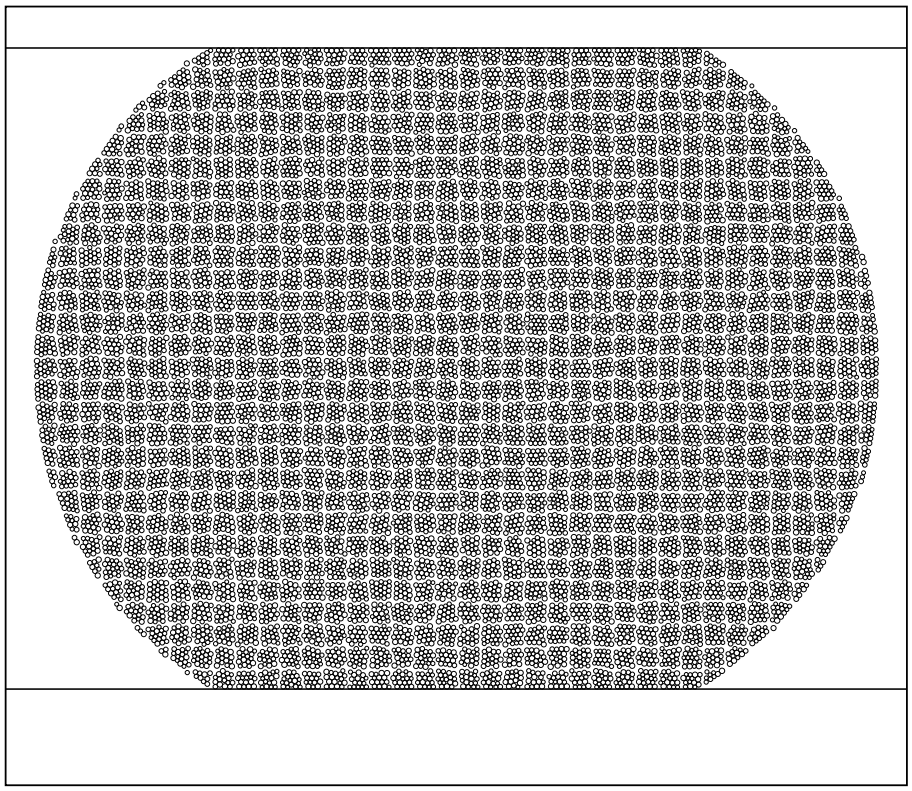

Figure 8.4: Division of a membrane system with $N = 16384$ particles into small square boxes. Small spacings distinguish the boxes.

row, the four boxes at both the left and right ends are not considered in the analysis because they may contain a portion of the space lying outside the membrane. This means that for each row, the two leftmost boxes and the two rightmost boxes in Fig. 8.4 are omitted. This procedure prevents boundary effects from dominating the calculated ordering behavior.

To investigate the ordering, the t-test, introduced in Sec. 5.5.4, is performed on the sliding contacts in the boxes. Figure 8.5 shows the t-values obtained. The figure compares the results from a system with rigid wall boundaries (upper figure) with one system with membrane boundaries (lower figure). The t-test indicates whether sliding contacts are randomly distributed ($t = 0$) and measures ordering ($t < 0$) or clustering ($t > 0$) tendencies for different values of external force f. At the very beginning of the simulation, the vanishing values show that the few sliding contacts in the systems are randomly distributed for both boundary conditions. At higher values of τ_f, the t-values are positive for membrane boundary conditions, but negative for rigid wall boundaries. This indicates a significant difference in the organization of sliding contacts.

Precursors of failure, which show up as narrow valleys in the number of sliding contacts, do lead to sharp maxima (spikes) of large, positive t-values for both types of boundaries. The number of these maxima is much larger in the membrane simulation. This corresponds to the larger number of precursors visible in Fig. 8.2. The second half of the membrane simulation before the failure is clearly dominated by the precursors: when the first precursor appears, the t-value suddenly jumps to 70, and only decreases back to about 20, remaining much larger than before. Through the subsequent

precursors, the minimum t-value increases further until the failure. Only just before the failure large fluctuations disturb this general trend. At the failure, the t-values shows a peak for both simulations, and the height of the peak is similar ($t \approx 73$ for rigid walls to $t \approx 80$ for membranes). This suggests precursors play a role in the ordering of deformation. After the failure, the t-values are close to zero in the two simulations.

The results presented in this section reveal that the distribution of sliding contacts strongly depends on the boundary conditions. Rigid boundaries lead to a more uniform distribution, while membrane boundaries enforce the clustering of sliding contacts. Only close to the failure sliding contacts in the rigid walls simulation do also start to cluster.

The difference between the first appearing failure and the next consecutive failure is about equal for both systems. And thus it seems that the different ordering tendencies in rigid wall and membrane systems, captured by the t-test method, are not connected to a change in stability persistent to after the first failure. The next section examines another measure for stability: the number of triangular structures in a system.

8.5 Number of triangular figures: importance for stability

In Sec. 5.7 the number of triangular figures has been investigated for the rigid wall boundary conditions. Their number has proven to be a good measure for the system's stability. In Fig. 8.6 the number of triangles is compared between the rigid wall conditions and the membrane boundaries. It shows that the evolution of the number of triangles is very similar in the two simulations. In the beginning, the number of triangles decreases slowly. But the decrease of triangles devoid of sliding contacts (nonsliding triangles) is more rapid, because many sliding contacts are created. In the second half until the failure at $\tau_f = 0$, the number of nonsliding triangles decreases only slowly, but the total number of triangles decreases quickly. In Sec. 5.7 this has been explained by the decreasing number of contacts in the system. It decreases also in the membrane system, which is captured by the number of transitions $S \rightarrow O$ in Fig. 8.3 in Sec. 8.3. At the precursors, the change in triangles without sliding contacts is much larger in the membrane system.

Right after the failure, all particle-particle contacts become nonsliding, and thus the number of sliding triangles is always zero after the failure. One can discern this feature of failure in both plots in Fig. 8.6, and thus it is a general feature which does not depend on the boundary conditions.

On the way to the failure, the sharp peaks in the two graphs indicate the appearance of precursors of failure. The precursors in the membrane simulations are inspected in the next section.

8.6 Precursors with membrane boundaries

Figure 8.7 shows the evolution of the kinetic energy and the number of sliding contacts at one example of a precursor with membrane boundary conditions. As found in Chap. 6 for precursors in rigid wall systems, the number of sliding contacts quickly decreases, and the kinetic energy rises. Both the example here and the one in Chap. 6 are the first appearing precursor in the corresponding system. They are indicated by arrows in Figs. 8.1, 8.2, 8.3, 8.5. These precursors can be easily discerned from the continuous evolution of kinetic energy and number of contacts, but have characteristics very similar to the the following precursors.

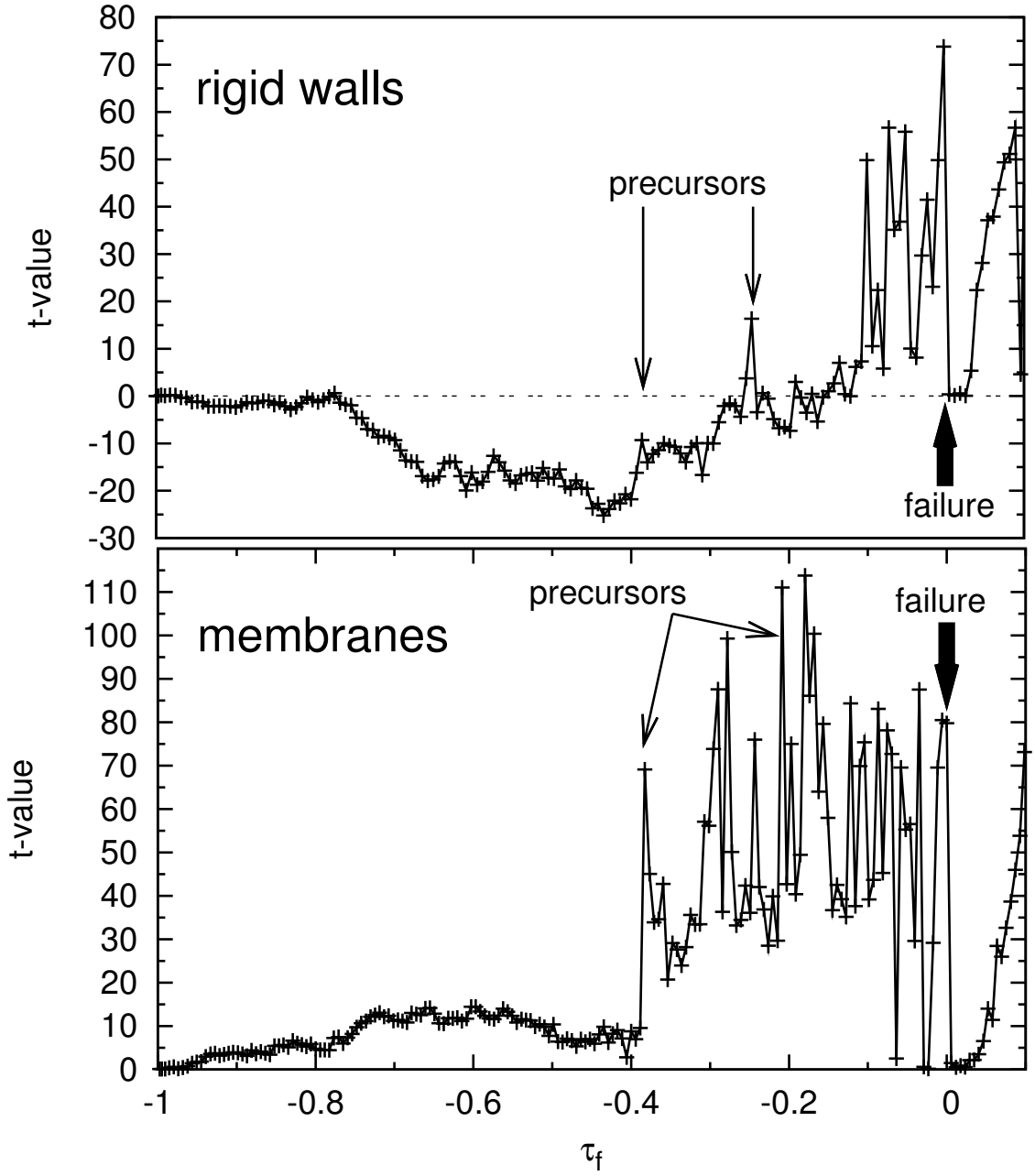

Figure 8.5: Organization of sliding contacts. Negative t-values indicate ordering while positive t-values indicate clustering. Upper figure: t-values for a system with rigid walls; Bottom figure: t-values for a system with membrane boundary conditions. Note the different scale of the y-axes in the two plots.

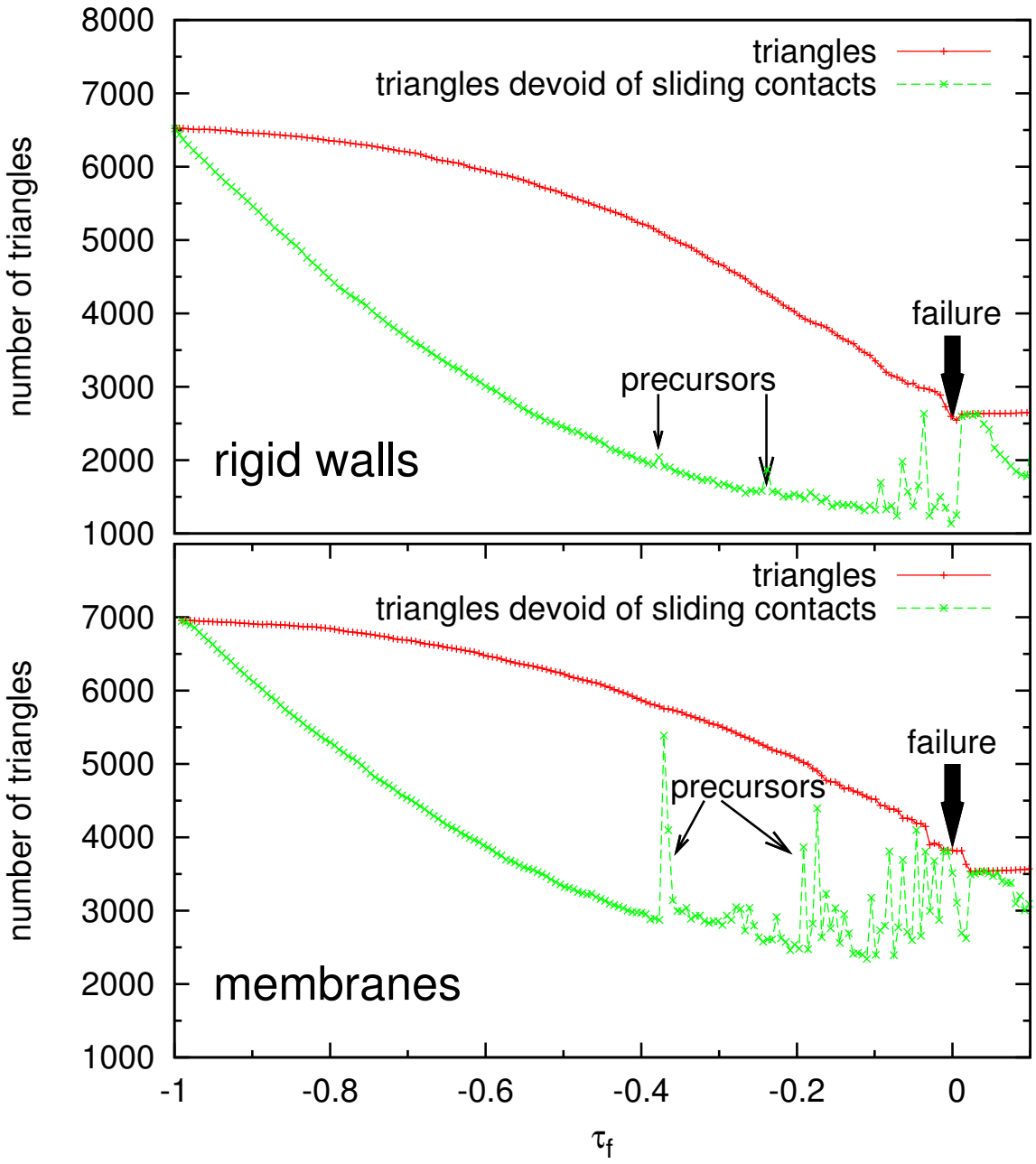

Figure 8.6: Comparison of the number of triangles in an assembly with membrane boundary conditions (lower figure) with an assembly with rigid wall boundary conditions (upper figure).

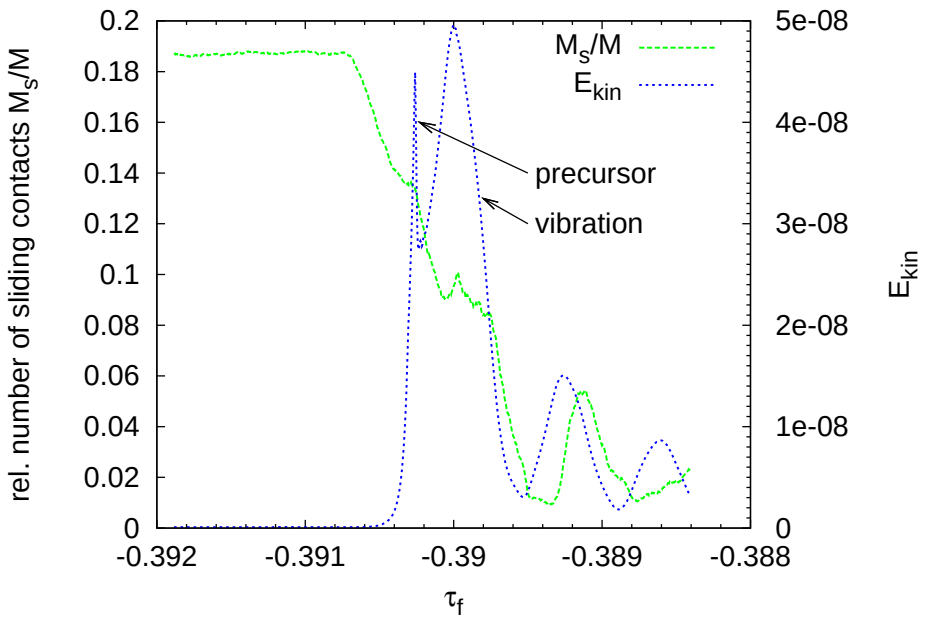

Figure 8.7: Kinetic energy and number of sliding contacts at an example of a precursor for the membrane boundary conditions. Note the large vibration wave generated by the precursor.

Figure 8.7 shows that the vibration that appears after the precursor is very pronounced, exceeding the peak in the kinetic energy at the precursor. This behavior is not observed in rigid wall systems, where vibrations after precursors are much smaller. The pronounced vibration lasts for a long time, and the recovery of the number of sliding contacts, which is related to the disappearance of the vibration, takes much longer than the small range shown in the figure. The recovery can be grasped from Fig. 8.2: it shows that the recovery takes roughly $\Delta\tau_f = 0.05$, while the recovery in the rigid wall system (upper curve) does not reveal such a long duration: it takes $\Delta\tau_f \approx 0.01$ (see Fig. 6.5).

Is the kinetic energy at precursors in membrane systems also concentrated, as observed in rigid wall systems? Figure 8.8 shows a snapshot of the kinetic energy distribution close to the maximum of kinetic energy at the precursor in Fig. 8.7. Opposite to Fig. 6.3 in Sec. 6.4, here the snapshot is in color, showing high energy grains in red. The colors facilitate discriminating the precursor grains from vibrations, which are already present before the first precursor. The precursor appears in the bottom right corner, i.e. at the position where the bottom wall and the right side membrane meet. This precursor's position is special, because subsequent precursors appear at very different positions inside the system. The kinetic energy rises at the appearance of the precursor by more than two orders of magnitude. This can be seen in Fig. 8.1 at $\tau_f \approx -0.4$. The concentration of the energy is less pronounced than at the precursor in the rigid walls system: here 18.8% of the grains have a kinetic energy above the average and carry 84% of the total kinetic energy, while at the precursor in Fig. 6.3 in Sec. 6 0.63% of the grains carry 85% of the total kinetic energy at the maximum of E_{kin}. Note that the rise in kinetic energy at the rigid wall precursor, which is the first precursor marked in the upper plot in Fig. 8.1, is much smaller than in the membrane system.

In conclusion, the characteristics of the precursors observed for the two boundary conditions are similar, while the vibrations appearing afterwards are much larger in membrane systems.

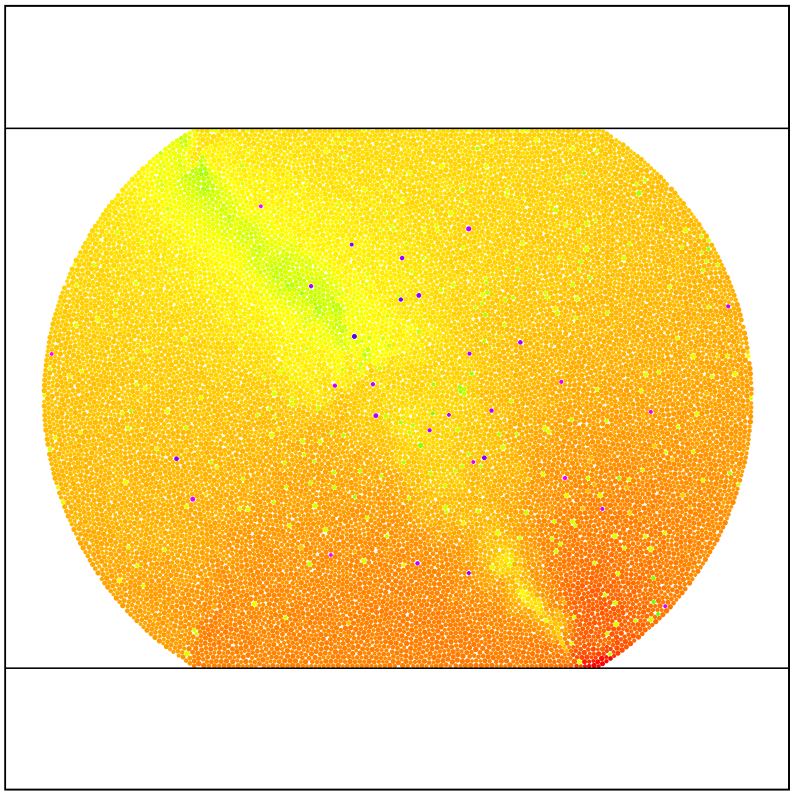

Figure 8.8: Snapshot of the kinetic energy at the appearance of the first precursor of failure in the membrane system in Figs. 8.1, 8.2, 8.3, 8.5. The colors in the figure are proportional to the logarithm of the kinetic energy. High kinetic energy (red) indicates the position of the precursor, which is in the bottom right corner, where the right side membrane and the bottom wall go together. The lowest kinetic energy (blue) is carried by rattlers, which are distributed over the packing. See Sec. 8.6 for details.

8.7 Conclusion

This chapter showed that it is indeed necessary to consider different types of boundary conditions when investigating weakening and failure in granular assemblies. In doing so, one can separate the general behavior from individual trends. We have seen that many features of the evolution towards the failure can be considered general, but some quantities also show a trend which strongly depends on the type of the boundary conditions.

First of all, the evolution of the kinetic energy is very similar before the first precursor. But afterwards, vibrations are much stronger with membrane boundary conditions. Second the number of sliding contacts m_s shows a general evolution with a linear increase in the beginning, and a decrease in the second period, before the failure. When failure happens, the number m_s increases quickly, but almost all sliding contacts disappear again shortly after failure. The rate of contact status transitions, responsible for the creation and annihilation of sliding contacts, also shows the same general dependence on external force f. However, fluctuations in the number of transitions are much more pronounced in the membrane systems.

The investigation of the spatial distribution of the sliding contacts showed that they first tend to distribute uniformly in rigid wall systems, and only cluster close to failure and at precursors. On the contrary, in the membrane systems, sliding contacts always cluster, with increasing clumping tendency until failure. Thus the distribution of sliding contacts depends on the boundary conditions. At the failure, the boundaries become irrelevant: the clustering tendency at this happening is very similar in the two systems.

The plunges in the number of sliding contacts, identified as precursors, are more frequent in the membrane systems. The reason might be the membranes not being as rigid as the walls, allowing for more local motions with low resistance. Eventually, a low resistance might become a localized instability, i.e. negative resistance, which would explain the appearance of the many precursors. Drawing a definite conclusion, however, needs much more investigation. An important result is the characteristics of the precursors of failure being independent of the boundary conditions, although the localization of the precursor is weaker for the membrane boundary conditions.

Besides the boundary conditions, the friction coefficient μ affects the number of sliding contacts in a system and hence stability. This influence is investigated in the next chapter.

Chapter 9

Does weakening and failure depend on particle roughness μ?

In the assembling process described in Sec. 2.10, the grains are isotropically compressed without friction, and afterwards friction is turned on. This process assures on the one hand that all contacts are nonsliding at the beginning of the loading procedure. On the other hand the density of the system is close the one believed to be the density of *random close packing* (see Tab. 2.2 for details). Rigid walls are at the boundaries of the systems in this chapter. These conditions are also applied in many other chapters (Chaps. 3 – 7).

When the external force is uniaxially increased, the forces transmitted at particle contacts change. Both the normal and the tangential forces can, depending on contact orientation and topology, increase or decrease, and contacts will eventually become sliding or open (disappear). At a sliding contact, the tangential force is $F_t = \mu F_n$, where F_n is the normal force. Thus modifying the particle roughness, given by μ, changes the time when contacts become sliding. For small μ, a small increase in F_t is sufficient to make the contact slide. As μ increases, the critical value of F_t also increases. Thus the number of sliding contacts M_s at a given external force f depends on μ. When the maximum of M_s is reached, sliding contacts become *open* contacts, i.e. these contacts disappear. The rate of disappearing sliding contacts depends on their number and thus on μ. Both the sliding contacts M_s and the total number of contacts M are important for weakening and failure. These numbers M_s, M are also involved in the degree of hyperstaticity $\mathcal{H}$, which is investigated in Sec. 9.1. The question answered in that section is if failure is occurring at a universal value of $\mathcal{H}$ which is independent of μ. The force at which the failure happens for the different μ is investigated in Sec. 9.2. In Sec. 9.3 the evolution of sliding contacts is investigated for different μ. Thereafter the number of contacts is inspected in Sec. 9.4. Sec. 9.5 discusses the different contact status transitions which are responsible for the evolution of M_s and M. The conclusion in Sec. 9.6 summarizes the most important results.

9.1 Is failure an isostatic transition for certain $\mu \neq 0$?

In Sec. 4.1 it has been shown that failure is not an isostatic transition at $\mu = 0.25$. But does isostaticity depend on μ? This question is answered here. Recall that a system is isostatic if the degree of hyperstaticity $\mathcal{H}$, introduced in Sec. 2.7, is zero. $\mathcal{H}$ compares the number of constraints, given by the number of independent contact forces, with the number of degrees of freedom of the particles. Figure 9.1 shows the degree of hyperstaticity $\mathcal{H}$ during the simulation for several μ. $\mathcal{H}$ decreases with

increasing external force f. For large μ, the decrease in $\mathcal{H}$ is slower.

There are two different types of the evolution of $\mathcal{H}$ in Fig. 9.1: when $\mu < 0.3$, the curve is convex, but it is concave for $\mu > 0.3$. Thus $\mu = 0.3$ is a particular value of the friction coefficient that separates two types of behavior. The fluctuations in the curves prior to failure come from the fluctuations in the number of sliding contacts. As we have seen in Chap. 6, these fluctuations are related to precursors of failure.

The minimum of $\mathcal{H}$ is always attained near the failure of the system. When one does not take into account the sudden drop of $\mathcal{H}$ at failure, $\underline{H} \approx 4000$ is some kind of "floor" for all μ: $\mathcal{H}$ descends below this value only during a very rapid decline at failure, and immediately recovers thereafter. Apart from this rapid decline, the minimum value of $\mathcal{H}$ is always above $\underline{H}$ and rather similar for all μ. Thus failure might have some μ-independent properties and therefore a universal character. For $\mu < 0.5$, the minimum $\mathcal{H}_{\min}$ is reached just *before* the failure, and $\mathcal{H}$ increases during failure. For $\mu > 0.5$, the minimum $\mathcal{H}_{\min}$ is attained directly *after* failure, when $\mathcal{H}$ just has dropped to a significantly smaller value.

We will see in Secs. 9.3, 9.4 that the change of $\mathcal{H}$ at failure depends very much on the number of contacts M and sliding contacts M_s: for small μ, M_s quickly decreases at failure, increasing $\mathcal{H}$. For large μ, M quickly decreases at failure, decreasing $\mathcal{H}$.

9.2 Critical force at failure for different μ

As we have seen in the foregoing section, the critical external force f_{fail} at the failure depends on the particle roughness μ. Because a higher roughness means higher tangential forces are required for contacts to become sliding, the force f_{fail} at which failure happens is expected to increase with increasing μ. In Fig. 9.2 f_{fail} is plotted against μ. f_{fail} increases with increasing μ less than linearly. At $\mu = 0$, we have $f_{\text{fail}}/f_0 = 1.23$. The reason why $f_{\text{fail}}/f_0 > 0$ at $\mu = 0$ is that the finite particle stiffness leads to additional contacts that stabilize the system. This means the system is not isostatic but hyperstatic: the degree of hyperstaticity, introduced in Sec. 2.7, is $\mathcal{H} = 1043$ at $\mu = 0$. Thus per particle there are $\mathcal{H}/\tilde{N} = 0.07$ additional contacts. Although this number is small, the effect is non-negligible. Note that if $\mu \neq 0$, the hyperstatic number in the simulation beginning is much higher: $\mathcal{H} = 17535$. When fitting the values $f_{\text{fail}}(\mu)$ in Fig. 9.2 with the function

$$f_{\text{fail}}(\mu) = 1.23 + C \cdot \log(1 + \beta\mu), \tag{9.1}$$

one obtains $C = 0.83 \pm 0.05$ and $\beta = 8.68 \pm 1.27$. An algebraic fit of the form $f_{\text{fail}} = 1.23 + C\mu^{\beta}$ would less accurately match the observed values. Fig. 9.2 shows that the data points are fairly well approximated by the fit equation 9.1. The measured values $f_{\text{fail}}(\mu)$ are used in Sec. 9.3 to rescale the simulations so that failure always occurs at the same position in the plot. This simplifies the comparison of the number of sliding contacts until the failure for the different μ.

9.3 Number of sliding contacts

Fig. 9.3 shows the relative number of contacts that slide as a function of external force for different values of μ. The force axis is rescaled such that the simulation beginning is always at $\tau_f = -1$ while the failure always happens at $\tau_f = 0$. The rescaling procedure is

$$\tau_f = \frac{f - f_{\text{fail}}}{f_{\text{fail}} - f_0}\,. \tag{9.2}$$

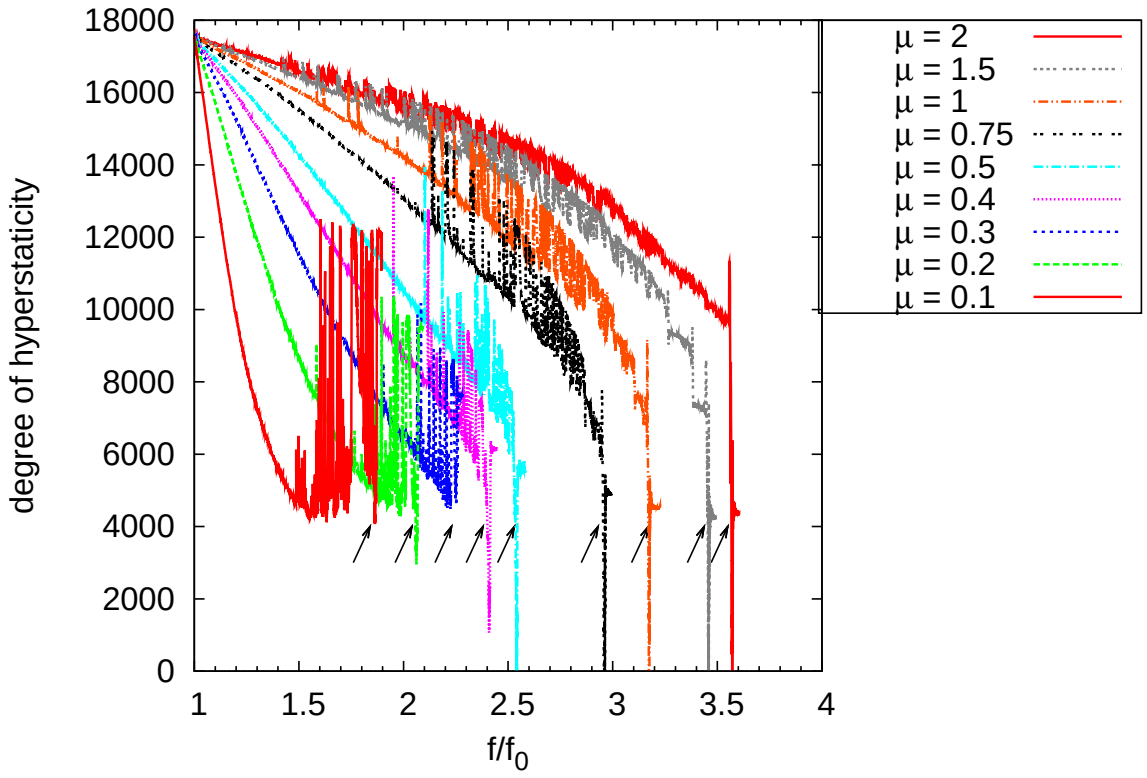

Figure 9.1: Degree of hyperstaticity $\mathcal{H}$ for simulations with different friction coefficients μ ($N = 16384$). For each μ, failure is indicated by an arrow. The minimum $\mathcal{H}_{\min}$ is attained near failure. For small μ, $\mathcal{H}$ increases during the failure, while for large μ, failure is accompanied by a sudden drop of $\mathcal{H}$.

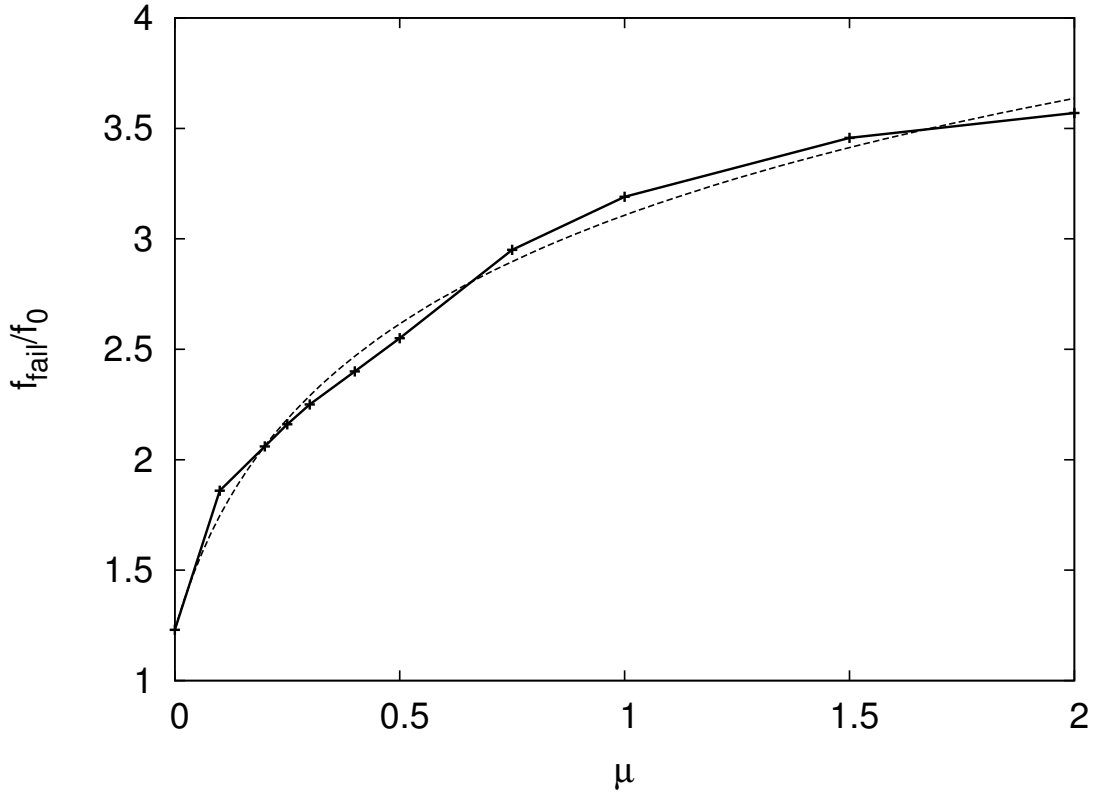

Figure 9.2: Critical external forces at which failure happens for different values μ.

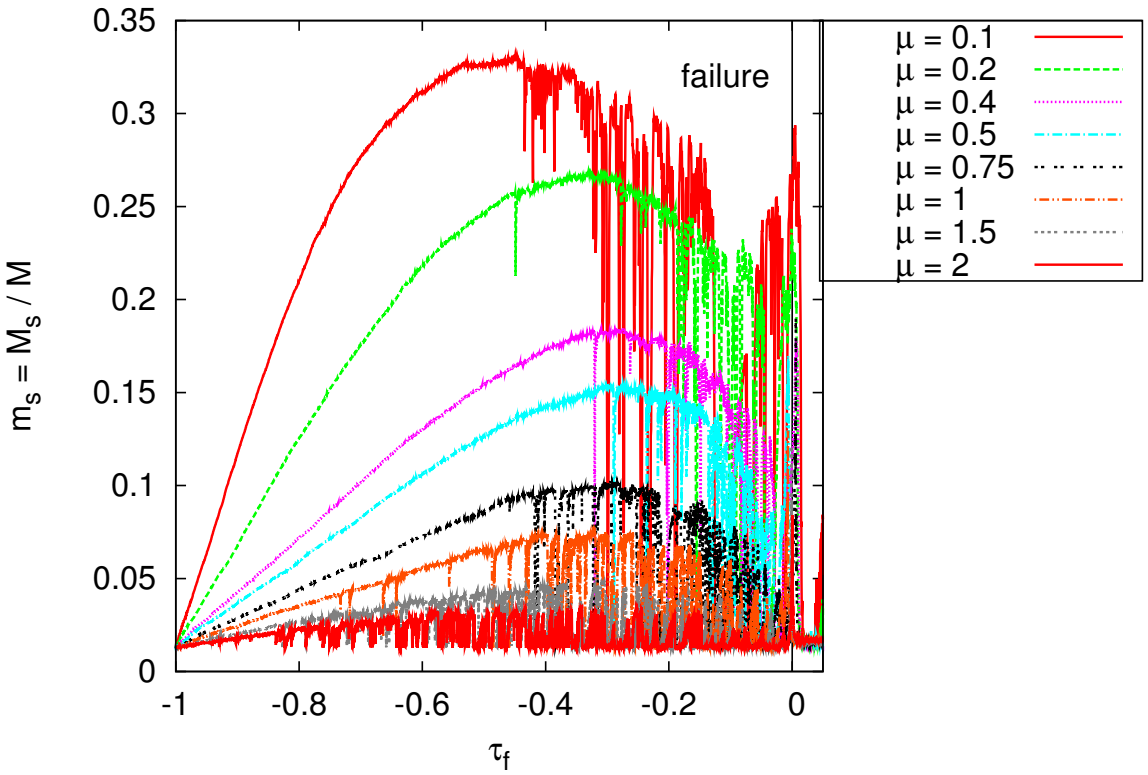

Figure 9.3: Relative number of sliding contacts for different values of μ as a function of external forcing ($N = 16384$ particles). The horizontal axis is rescaled by the external force at failure f_{fail}. Thus the simulation always starts at $\tau_f = -1$ and failure always happens at $\tau_f = 0$. See Eq. 8.1 for details on the rescaling of the force.

This relation has been introduced for the first time in Eq. 8.1 in Chap. 8. For smooth particles (low μ), the number of sliding contacts increases much faster with τ_f. Also the maximum in M_s occurs at a lower load and is much higher. This observation can be understood in terms of friction mobilization: for rough particles (large μ), a higher tangential force is required for a contact to become sliding. Therefore the probability for creating a new sliding contacts decreases with particle roughness.

When one rescales for each μ the two axes *force* and *number of sliding contacts* by the values at the maximum number of sliding contacts, the m_s-graphs can be superimposed. However, this only works for a limited range of μ-values. When $\mu = 0.1$, for instance, the maximum is much broader than for higher μ. And if $\mu \geq 1.5$, the number of sliding contacts does not decrease any more shortly before the failure. For $0.4 \leq \mu \leq 1.0$ we get the graphs in Fig. 9.4. Note that contacts with the walls, which are always sliding, are disregarded in the figure. The graphs in Fig. 9.4 show that until the maximum of m_s, the graphs fall on top of each other. Therefore the behavior in the beginning is similar for all μ shown. The evolution after the maximum is also similar, but the distance to the failure depends on μ. This might be a dynamic effect, because the simulations cannot be considered quasi-static any more close to the failure.

The values for rescaling Fig. 9.4 are plotted in Fig. 9.5. The figure shows two graphs. One is the maximum number $m_s(\mu)$ as a function of μ. The other graph is the external force f at the maximum

m_s for the different μ. The curve $m_{s,max}(\mu)$ starts at the value one for $\mu = 0$, and it tends to zero for $\mu \to \infty$. Fitting $m_{s,max}(\mu)$ with the function

$$m_{s,max}(\mu) = C/(\mu + 1)^{\alpha}, \tag{9.3}$$

one obtains $C = 0.426 \pm 0.004$ and $\alpha = 2.95 \pm 0.03$. Thus the decrease of $m_{s,max}$ is roughly inverse proportional to the third power of μ. The other curve, which shows the external force at which the maximum m_s appears, increases with μ. This behavior is expected, because the tangential force required for a contact to become sliding increases with μ, and therefore the maximum m_s also shifts to larger forces. The function to fit the curve in Fig. 9.5 is

$$f_{m_{s,max}}(\mu)/f_0 = C\mu^{\alpha}. \tag{9.4}$$

One obtains $C = 1.54 \pm 0.03$ and $\alpha = 0.49 \pm 0.03$. Thus the increase is proportional to the square root of μ.

While the general trend of m_s in Fig. 9.4 is similar for all μ, the number of sudden plunges in m_s, identified as precursors of failure in Chap. 6, increases with μ. Also the first precursors occur sooner, i.e. at smaller values of τ_f.

9.4 Number of contacts

As the number of sliding contacts is much lower for rough particles (large μ), there must be another mechanism involved in the softening of the assembly. One possibility is the disappearance of some contacts; instead of some contacts in the system becoming sliding, for rough particles it is more favorable to *give up* some contacts. Fig. 9.6 shows the remaining number of contacts M for different particles roughnesses. For a higher roughness, the decrease of M per load increment is smaller, whereas the maximum loss in M attained after failure is much larger. The minimum $M_{\min}$ coincides with the appearance of failure for all roughnesses. For rough particles, M quickly drops at failure to much lower values, while the evolution is smooth and continuous for low μ. This shows that the change of the behavior at failure with increasing μ, observed in Fig. 9.1, applies also to the number of contacts. Thus, while failure appears in all systems at $\tau_f = 0$, the system's property *number of contacts* evolves differently for different μ.

9.5 Contact status transitions

In the last two sections the number of sliding contacts M_s and the total number of contacts M have been shown to depend on μ. But why do M_s and M depend on μ, while the degree of hyperstaticity $\mathcal{H}$, shown in Fig. 9.1, is universal at failure? In this section we will see that the evolution of M and M_s is governed by the competition between two different weakening processes. Their relative contribution to the weakening of the assembly depends on μ.

The weakening of a granular assembly can be understood in terms of contact status transitions. Such transitions have been investigated for rigid walls boundary conditions in Sec. 5.4.3. But in that section only such contributions have been inspected which change the number of sliding contacts. For low particle roughnesses (low μ), sliding contacts are very important for the weakening process. Here we have to consider all possible contact status transitions, because their frequency will depend on μ, and transitions which are not important for low μ can be very important for large μ.

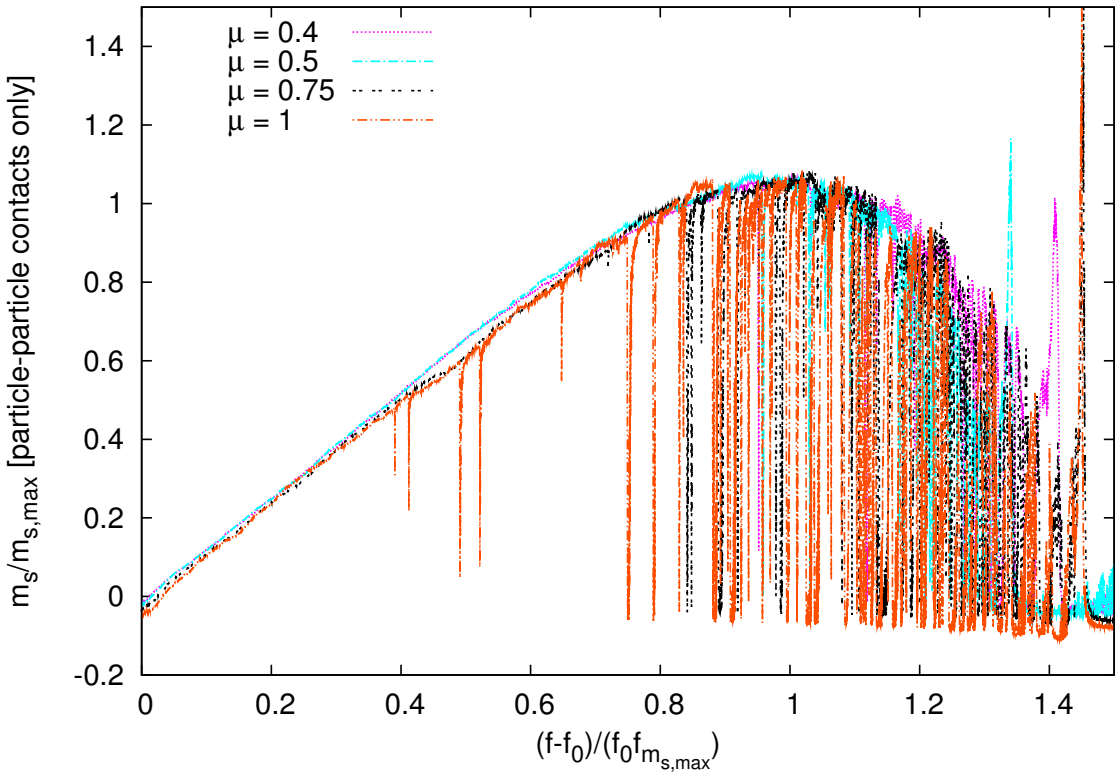

Figure 9.4: Curves showing the relative number of sliding contacts. Both m_s and f are rescaled by the values at the maximum in m_s, the curves therefore fall on top of each other at that value. One nicely sees that the linear increase in the beginning is similar for all μ displayed here.

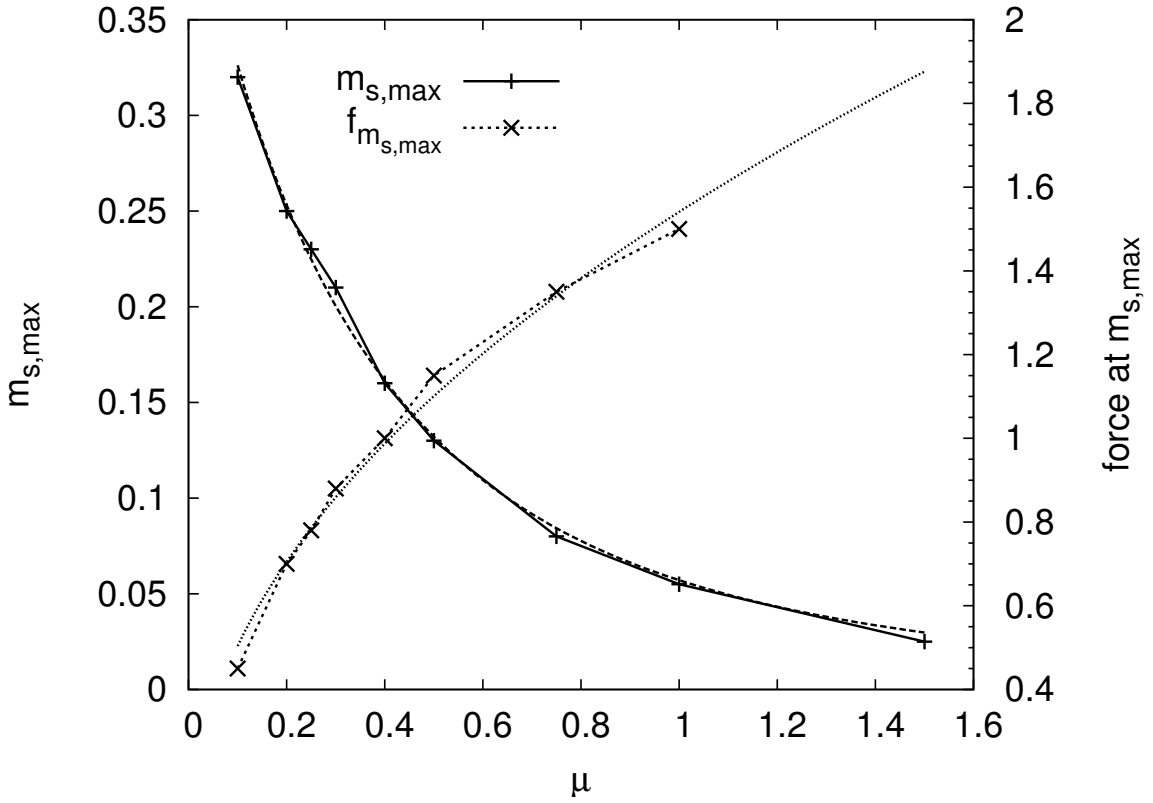

Figure 9.5: Maximum of m_s (left scale) and force at that maximum (right scale) for different values of μ. The fits of the two curves match the data fairly well. For details see Sec. 9.3.

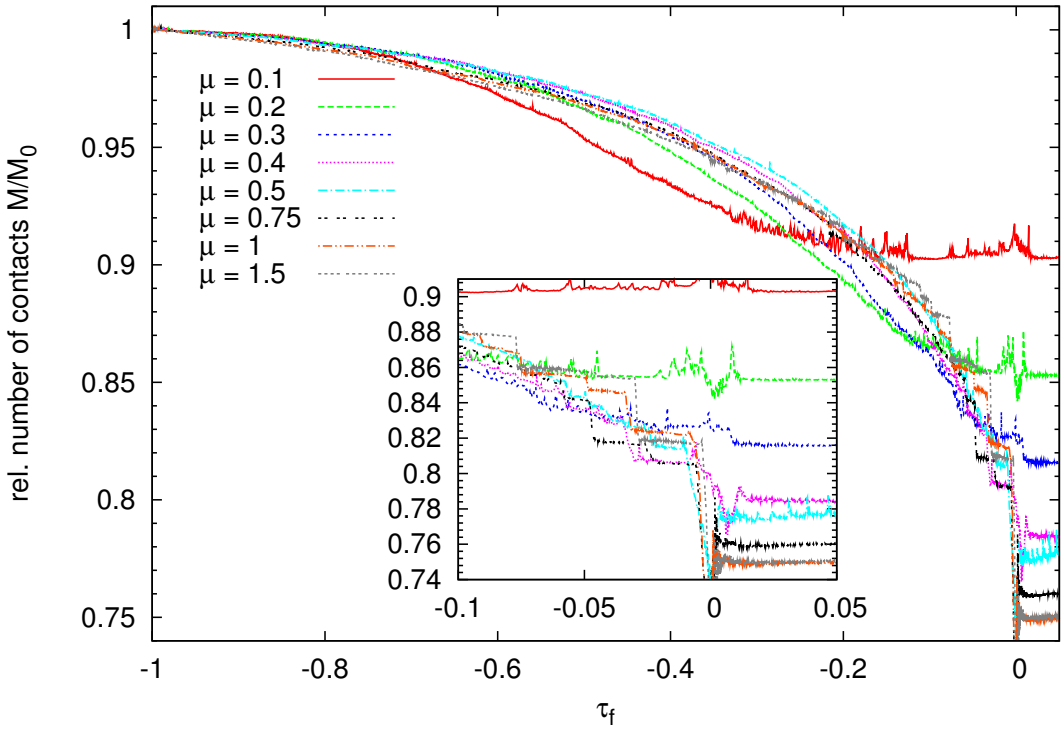

Figure 9.6: Number of contacts M for different values of the friction coefficient μ. The values are normalized by the initial number of contacts $M_0 = 32778$. The inset provides a closer view of the values around the failure at $\tau_f = 0$.

Before inspecting the different contact transitions that can occur, it should be noted that the evolution of each contact status transition is very similar for all μ. Thus we will not inspect the evolution in detail but only consider the total amount of changes from the simulation beginning until the failure. Figure 9.7 shows the transitions which can occur between the three contact states closed (C), sliding (S), and open (O). Each transition is marked by an arrow. Transitions leading on average to a decrease in the stiffness of the system are shown by heavy arrows, and the other transitions are represented by light arrows. In Fig. 9.7 there are three pairs of transitions:

$$\begin{aligned} C &\leftrightarrow S, \\ C &\leftrightarrow O, \\ S &\leftrightarrow O. \end{aligned} \tag{9.5}$$

Note that in each line of Eq. 9.5, both the transition from left to right and the inverse transition is possible. The difference between the two is the net number of transitions. If it is positive, then transitions from the left to the right side are more frequent. Such transitions contribute to the weakening of the system.

Now we will inspect the net number of the transitions in Eq. 9.5. First, the two limits $\mu = 0$ and $\mu \to \infty$ are inspected. In each limit one has only one sort of contacts: if $\mu = 0$ all contacts are sliding, while for $\mu \to \infty$ all contacts are closed, i.e. nonsliding. One can regard the limits as conditions on the tangential contact forces:

$$\begin{aligned} \mu = 0: &\quad F_t = 0 \quad \forall \text{ contacts}, \\ \mu \to \infty: &\quad F_t < \mu F_n \quad \forall \text{ contacts}. \end{aligned}$$

The first condition enforces all contacts to be sliding ($F_t = \mu F_n$) while the second prohibits contacts to become sliding. From another perspective, in the limit $\mu = 0$ only normal forces are exerted, while for $\mu \to \infty$ all particles are at their contacts *glued together* in the direction tangent to their surfaces. Because in each limit one contact status is excluded, the limiting cases allow only for these contact changes:

$$\mu = 0: \quad S \leftrightarrow O, \tag{9.6}$$

$$\mu \to \infty: \quad C \leftrightarrow O. \tag{9.7}$$

Every finite value of μ means both types of contact changes are relevant, and there is a competition between them.

Next we inspect two important values of μ at which one observes a change in the qualitative evolution of certain system properties. One change has been detected in Sec. 9.1 at $\mu = 0.3$. At this μ, the evolution of the degree of hyperstaticity $\mathcal{H}$ changes from a smooth decrease to a sudden plunge at the failure for larger μ. The frequency of the contact status changes is related to the evolution of $\mathcal{H}$, thus it also changes qualitatively at that value. The second important change occurs at $\mu = 1$. At this value the normal and tangential contact forces are identical at sliding contacts: $F_t = F_n$. We will now inspect these values of μ in detail. Table 9.1 shows the net number of transitions from the beginning of the simulation until $\tau_f = -0.05$, shortly before the failure, for the different μ. The values are the sum of transitions that occur in an interval of external force $\Delta f / f_0 = 8 \times 10^{-3}$ during the simulation. The table shows the values for the three transitions in Eq. 9.5. Between $\mu = 0.2$ and $\mu = 0.3$, the number of net transitions $C \leftrightarrow O$ changes sign. Thus this transition is not important at that μ, and the material weakening only happens through the process $C \to S \to O$. This means

μ	0.1	0.2	0.25	0.3	0.4	0.5	0.75	1	1.5	2
$C \leftrightarrow S$	12689	10208	10279	10271	8968	6561	5208	4054	3072	2042
$C \leftrightarrow O$	-2011	-1074	-599	455	972	934	1987	4162	5313	5516
$S \leftrightarrow O$	5100	5738	6146	5837	5931	6474	4453	4021	2655	1798

Table 9.1: Total number of contact status transitions from the simulation beginning until the failure for different values of μ. Positive values show that the transition from left to right (e.g. $C \rightarrow S$) is more frequent than the inverse transition ($C \leftarrow S$). The inverse transition is more frequent when the value is negative.

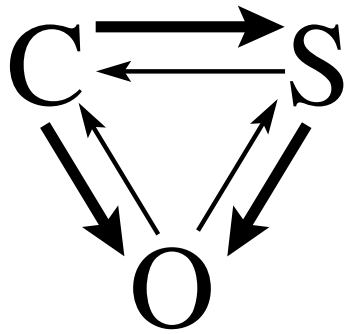

Figure 9.7: Transitions between the three contact states closed (C), sliding (S), and open (O). The contact status transitions contributing on average to the weakening of the system are represented by heavy arrows, while the other transitions are represented by light arrows. See Tab. 9.1 for the μ-dependent numbers of transitions until the failure.

that the weakening fully happens through a two step process, as observed in Sec. 5.6 for $\mu = 0.25$. Sliding contacts are very important in that two step weakening. At the other transition region at $\mu = 1$ another interesting behavior is observed: the number of transitions $C \leftrightarrow O$ equals the number of transitions $C \leftrightarrow S \leftrightarrow O$. Thus the material weakening happens through the two processes $C \rightarrow O$ and $C \rightarrow S \rightarrow O$. Note that at $\mu = 1$, these two processes are equally likely in Tab. 9.1. Thus this value of μ separates the domain $\mu < 1$, where the two step weakening is more important, from the domain $\mu > 1$, where the weakening is mainly a single step process. These observations underline the general trend, determined from the limiting cases in Eq. 9.6, 9.7, that with increasing μ the transition $S \rightarrow O$ becomes less important while the transition $C \rightarrow O$ is dominating.

9.6 Conclusion

In this chapter, the weakening and failure of granular systems is studied for different values of the friction coefficient μ. Failure is represented by a universal, μ-independent value of the degree of hyperstaticity $\mathcal{H}$, while the evolution of $\mathcal{H}$ until the failure depends on μ. Although $\mathcal{H}$ is universal, the failure of the granular system happens at a higher value of the external force f/f_0 when μ is larger. The number of contacts and sliding contacts also depend on μ. For small μ, the number of sliding contacts is higher than for large μ. Rescaling the simulations by the coordinates of the maximum number of sliding contacts, a similar behavior of all simulations until the maximum of

sliding contacts is observed. The total number of contacts M decreases more slowly for larger μ, but then suddenly drops to a very low value at failure. Thus the decrease of M is continuous for small μ, but discontinuous for large μ. The evolution of the contacts and the sliding contacts can be understood in terms of contact status transitions. For small μ, the dominating weakening process is $C \to S \to O$, while for $\mu > 1$ the weakening transition $C \to O$ is more frequent. Thus, with increasing μ the two step weakening process observed in Sec. 5.6 becomes a one step process.

Chapter 10

Failure in three dimensions

The weakening and failure of granular systems in two dimensions has been investigated in much detail in Chaps. 3-9. After the explanation of weakening, failure, and precursors in Chaps. 3 – 6, the organization of rolling motions has been examined in Chap. 7, and the dependence of structural changes on boundary conditions and friction coefficient has been examined in Chaps 8, 9. But do all the results for two dimensional systems generalize to real world systems? Is it sufficient to conduct investigations in two dimensions, although in the world around us granular systems are three dimensional? Or is granular behavior in three dimensions quite different from the observed two dimensional behavior? This chapter targets answering this fundamental question by comparing two and three dimensional granular behavior. In that way one can, similar to Chap. 8, distinguish a dimensionality dependence from the more general observations that always apply. From another point of view, comparing two and three dimensions puts one in the place to conduct less time consuming two dimensional investigations where granular behavior is general, and carry out three dimensional experiments only where necessary.

The three dimensional example system investigated in this chapter will be compared to a two dimensional system with rigid walls. The two dimensional system can be considered a cut through the three dimensional system with rigid boundaries. Thus one expects a similar behavior in two and three dimensions. However, we will see that this expectation is not always confirmed. Although this chapter shows the results only for one example system, it has been checked that the results apply also to three other systems of that size and that type of boundary conditions. Therefore the results presented are general.

The beginning of this chapter covers general aspects of dimensionality. Sec. 10.1 discusses why dimensionality must matter when investigating weakening and failure of granular systems. Sec 10.2 thereafter considers the number of degrees of freedom and compares it with the number of constraints. Both numbers increase with dimension. Sec. 10.3 introduces the reader to the boundary conditions in three dimensions and to important parameters. The sections thereafter examine aspects of weakening and failure in three dimensions in one example system. This system is compared to an example system in two dimensions. Sec. 10.4 examines the stress-strain curves of the two and three dimensional systems. Section 10.5 discusses the number of sliding contacts, the number of contact status changes, and the organization of sliding contacts. Thereafter Section 10.6 examines an example of a precursor in three dimensions. It shows that precursors appear independent of dimension, giving further evidence that precursors are a more general observation. The same section clarifies that the observation of precursors is not related to a specific feature of the simulation program: the same precursor is detected with two independently developed simulation programs. This shows that precursors are real

features of our model of granular matter. The observations on weakening, failure, and precursors of failure in three dimensions are summarized in Sec. 10.7.

10.1 Does dimensionality really matter?

Many details of particle motions depend on the dimension of space. First, the number of all degrees of freedom increases with dimension d. Second, the number of translational degrees of freedom increases differently than the rotational degrees of freedom. while the number of linear displacements is always equal to the dimension of space, in two dimensions there is one degree of rotational freedom per particle, but three rotations exist in three dimensions. Thus one expects the relative contribution of the two types of motion to the kinetic energy to change from two to three dimensions.

Another dimension dependent aspect is the number of contacts required for stability, which increases with d. Higher dimensions also lead to new possibilities for stable configurations of the arrangement of grains, and the number of ways of how to pack a given number of grains will increase strongly with dimension.

Failure of a granular systems is always connected to the appearance of a shear band. The direction of this band depends on the value of the friction coefficient μ and the applied boundary conditions, specifically the direction of the stresses applied and the geometry of the boundaries. The direction of the shear band can be calculated from the knowledge of these data. However, while the direction is unique, the position is frequently not [93, 96, 97]. The number of different, possibly degenerate directions increases with dimension. These considerations suggest that the failure of granular systems in three dimensions can be very different from failure in two dimensions.

10.2 Degrees of freedom and number of constraints

For the stability of a granular system the number of contacts is an important quantity. The larger their number the more possibilities to distribute the external load on the set of contacts in the system. In two dimensions, a closed contact contributes two constraints on the particle motions, and one constraint when it is sliding. The minimum number of constraints needed for stability has been explained in Sec. 2.7. It has also been compared to the number of linearly independent particle motions. Simulation results in two dimensions have been presented in Sec. 4.1. In this section we want to extend that investigation to a more general consideration of the number of constraints and the kinetic degrees of freedom in an arbitrary dimension of space.

10.2.1 Number of degrees of freedom

There are two types of kinetic degrees of freedom: linear particle motions and particle rotations. But what is the contribution of these two types to the total number of degrees of freedom? The first type of motions is driven by a force pushing the particle in a certain direction, and the number of such independent motions is equal to the dimension of space d. The second class of motions, particle rotations, is initiated by a torque on a particle, i.e. a force exerted in the tangential direction at the surface of the particle. The number of independent rotations is $\frac{d(d-1)}{2}$. Therefore in three dimensions three rotation modes appear, while one rotation is possible in two dimensions.

From this knowledge one can deduce the expected relative contribution of the motions to the system's kinetic energy. Depending on dimension d, the rotations contribute

$$N_{rot}/\left(N_{rot}+N_{lin}\right)=\frac{\frac{d(d-1)}{2}}{\frac{d(d-1)}{2}+d}=\frac{d-1}{d+1} \tag{10.1}$$

Thus the contribution from the rotations is expected to increase with d. Equivalently, the relative contribution from the linear displacements is expected to decrease with d, although the number of possible displacements increases. According to Eq. 10.1, in two dimensions the rotations should contribute $1/3$ to the kinetic energy, while in three dimension they should be responsible for half of the kinetic energy. Thus rotations are expected to be more important in three dimensions than in two. In a gedankenexperiment, if one increases d further, rotations will dominate over translations, and the process of failure will strongly depend on the rolling mechanisms. In the limit $d \to \infty$, linear displacements become a negligible contribution, suggesting that in this limit the number of sliding contacts, which is important for the weakening and the failure in two and three dimensional granular systems, loses its importance.

10.2.2 Number of constraints

Of particular importance for the observed motions in the system are the constraints on the particle motions. These constraints are given by the interparticle contacts at which the contact forces have to fulfill the equilibrium condition (i.e., zero resulting force on each particle).

As the force exerted at a contact is a vector, the number of constraints introduced by one contact is d. Therefore every non-sliding contact contributes d constraints on the particle motions, and every sliding contacts contributes $d-1$ constraints. The number of constraints is reduced by 1 because the absolute value of the tangential force is deduced from the normal force.

As the number of degrees of freedom increases with the dimension, the number of contacts must also increase. While the lower bound for stability is three contacts per particle in two dimensions, four contacts are needed in three dimensions to stabilize the particles at their positions. Let z be the coordination number, i.e. the number of contacts per particle, then the total number of constraints per particle is $dz/2$, assuming that all contacts are non-sliding. The factor 2 accounts for the fact that each contact is counted twice, because it belongs to two particles. The number of constraints must be equal to or larger than the number of degrees of freedom $N_{\mathrm{lin}}+N_{\mathrm{rot}}=(d+d^2)/2$. Thus one obtains the inequality for the coordination number

$$z \geq 1+d. \tag{10.2}$$

This equation defines the minimum number of contacts needed for stability in frictional systems. When the grains are frictionless, i.e. when friction coefficient μ is zero, then the number of constraints introduced by the contacts is $z/2$, and the number of degrees of freedom is $N_{\mathrm{lin}}=d$. In this case the inequality defining the stability limit is

$$z \geq 2d. \tag{10.3}$$

Thus z always increases linearly with d. In both two and three dimensions, the lower limit for frictionless systems is higher than for frictional systems. It is $z=4$ in two dimensions and $z=6$ in three dimensions, while frictional systems can be stable when $z=3$ in two dimensions and $z=4$ in three dimensions. Note that the minimum coordination number in frictional systems increases when some contacts become sliding.

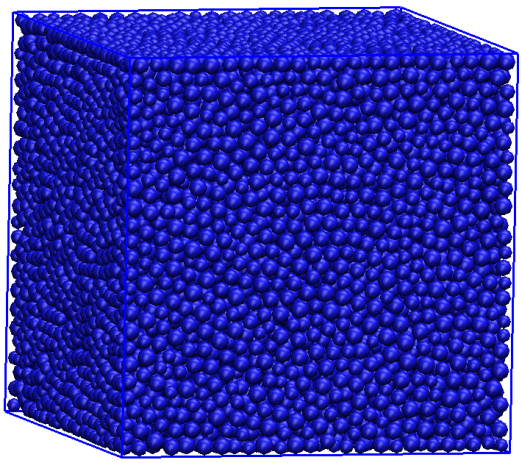

Figure 10.1: A three dimensional cubic system with planar walls at the boundaries. The walls are indicated by lines at the positions where they intersect. The walls are light-weight and movable. The system of particles is compressed during preparation by a force f_0 on each wall.

10.3 Definition of the system and parameters

The three dimensional system can be considered a larger, more realistic version of a two dimensional system with the rigid wall boundary conditions. Inversely, the two dimensional system can be considered a cut through a three dimensional system. Thus the four walls of the two dimensional systems are in three dimensions four planes. The three dimensional system is limited in the third dimension by two additional planes, which are perpendicular to the other four planes. In this system, the circular particles of the two dimensional system become spheres. Such a system shows Figure 10.1. The spheres are not identical, but each sphere i has its individual radius $r_i \in [0.7r_{\max}, r_{\max}]$. All particles have the same density $\rho = 1$ in the units introduced in Sec. 2.5.

Figure 10.1 shows a system with rigid wall boundary conditions. To make visible the particles inside the system, the walls are omitted in the figure. On the set of the six walls, a constant force f_0 is exerted that confines the particles to form a solid. The details of the preparation procedure are the same as in two dimensions, and have been explained in Sec. 2.10.

Due to the very slow, quasi-static simulations, the maximum system size one can simulate in reasonable time (2 – 3 weeks) is limited. Therefore the largest system size investigated in three dimensions has $N = 16875$ particles. If this is a large or a small system can be estimated from the number of particles in each direction. The cubic root of N tells us that the length of a system equals about 26 particle diameter. Thus a two dimensional cut through this system contains about $26^2 = 676$ particles. This is the size of a two dimensional system with which the three dimensional system should be compared, because the diameter of the particles will be similar. The performed two dimensional simulations which are closest to this value contain $N = 1024 = 32^2$ particles. This number is slightly larger than the 2D-cut of the 3D system, but the average particle size is similar: it is $r_{\mathrm{av,2D}} = 1.18 \times 10^{-2}$ in two dimensions and $r_{\mathrm{av,3D}} = 1.53 \times 10^{-2}$ in three dimensions.

One might object that, although the radii are similar, the masses of the particles are much different in two and three dimensions. This is of course true. But in the quasi-static limit, inertia effects are irrelevant. Therefore the particle masses are not a parameter that needs to be considered. At failure, the system is of course no longer quasi-static, because failure implies that rapid motions of particles and boundaries occur. But this study focuses on what is happening before the failure, and failure itself is not considered in detail. On the way to the failure, at certain values of the external force, precursors appear. These could be called localized failures, and thus they are also not quasi-static; at the appearance of such a precursor, the local kinetic energy rises quickly, and inertia will become relevant. But the time which a precursor lasts is extremely small (see e.g. Fig. 6.1), and during the precursor only few persistent changes in the geometrical structure appear. This means that the structure is hardly affected by the precursor. Thus the evolution of the contact structure is given by the continuous adaption of the system to the slowly increasing external force. The influence of the precursors on the system's structure and behavior is small.

Similarly to Chap. 8, where different boundary conditions lead to different forces f at the appearance of failure, different dimensionality also changes the external force at which failure appears. Therefore the same rescaling of the force as in Chap. 8 is applied here to compare results for two and three dimensions:

$$\tau_f = \frac{f - f_{\text{fail}}}{f_{\text{fail}} - f_0} \,. \tag{10.4}$$

The simulations start at $\tau_f = -1$, and failure happens at $\tau_f = 0$. For the two dimensional example system, failure appears at $f/f_0 = 2.22$, and in three dimensions the system fails at $f/f_0 = 2.40$. Note that, although the three dimensional system is very different from the two dimensional one, the difference in force is only about equal to the difference between membrane and rigid walls boundary conditions, investigated in Chap. 8. In that chapter, the difference was $\Delta f/f_0 = 0.23$. For each system, the value of the force at the failure f_{fail} can be extracted from the stress-strain curve, which is examined in the next section.

10.4 Stress-strain curve

In the introduction of this work, it has been pointed out that the stress can be represented by a matrix. In three dimensions this matrix is

$$\sigma = \begin{pmatrix} \sigma_{11} & \sigma_{12} & \sigma_{13} \\ \sigma_{21} & \sigma_{22} & \sigma_{23} \\ \sigma_{31} & \sigma_{32} & \sigma_{33} \end{pmatrix} . \tag{10.5}$$

It is called the Cauchy stress tensor [98] and contains the stresses acting on the system that lead to deformations. Matrix σ is symmetric. Similar to the example system in the introduction, the three dimensional systems have frictionless, smooth boundaries ($\mu_{\text{wall}} = 0$) that are perpendicular to each other and aligned in the direction of the coordinate axes. In this coordinate system, the stress tensor is diagonal with the three eigenvalues $\sigma_1, \sigma_2, \sigma_3$:

$$\sigma = \begin{pmatrix} \sigma_1 & 0 & 0 \\ 0 & \sigma_2 & 0 \\ 0 & 0 & \sigma_3 \end{pmatrix} \tag{10.6}$$

This tensor can be decomposed in two additive parts. One is the volumetric part $\sigma_{\rm vol}$, which contains the isotropic pressure on the system, and the other is the deviatoric stress tensor $\sigma_{\rm dev}$:

$$\sigma_{\rm vol} = \mathbb{1}\frac{Tr(\sigma)}{Tr(\mathbb{1})}, \tag{10.7}$$

$$\sigma_{\rm dev} = \sigma - \sigma_{\rm vol}. \tag{10.8}$$

The symbol $\mathbb{1}$ denotes the 3×3 identity matrix. Because the trace is independent of the coordinate system [99], $\sigma_{\rm vol}$ and $\sigma_{\rm dev}$ can also be directly calculated from Eq. 10.5. Important for the investigation of failure is $\sigma_{\rm dev}$, the deviatoric stress tensor, which controls all deformations not resulting from an isotropic pressure. In the simulations, the applied force increases in direction 3, while it is constant in the other two directions. Thus σ_1, σ_2 remain constant, while σ_3 increases. The deviatoric stress in this third direction is the 33-component of $\sigma_{\rm dev}$:

$$\sigma_d = \sigma_{\rm dev,33} = \frac{2}{3}\sigma_3 - \frac{1}{3}\left(\sigma_2 + \sigma_1\right). \tag{10.9}$$

Similar to the stress tensor σ, one can define a strain tensor ϵ:

$$\epsilon = \begin{pmatrix} \epsilon_{11} & \epsilon_{12} & \epsilon_{13} \\ \epsilon_{21} & \epsilon_{22} & \epsilon_{23} \\ \epsilon_{31} & \epsilon_{32} & \epsilon_{33} \end{pmatrix}. \tag{10.10}$$

This tensor contains the relative deformations of the system. It is also symmetric. Because the walls are frictionless ($\mu_{\rm wall} = 0$), and they move only normal to their surface, ϵ is even diagonal. One can decompose tensor ϵ in two parts, $\epsilon_{\rm vol}$ and $\epsilon_{\rm dev}$, in the same way as the stress tensor was decomposed above. From the two parts again the deviatoric part $\epsilon_{\rm dev}$ is important. It contains the deviatoric deformations of the system, given by the displacements of the boundary walls. Similar to Eq. 10.9, one can define the deviatoric strain, which is the third component on the diagonal of $\epsilon_{\rm dev}$:

$$\epsilon_d = \epsilon_{\rm dev,33} = -\frac{2}{3}\epsilon_3 + \frac{1}{3}\left(\epsilon_1 + \epsilon_2\right). \tag{10.11}$$

Similar expressions for σ_d and ϵ_d in two dimensions have been given in Eqs. 5.1, 5.2 in Sec. 5.1. With the definition of σ_d and ϵ_d, we can understand the graphs in Fig. 10.2. They show the stress-strain curve for one system with $N = 16875$ particles in three dimensions (lower figure), and one system with $N = 1024$ particles in two dimensions (upper figure). Both simulations are stress controlled, i.e. the external forces applied at the boundaries are controlled in the way described in Sec. 2.11. The general evolution of two and three dimensional system is similar. In the beginning, the rise of the stress σ_d does not cause much deformation. In three dimensions, the initial slope of the stress-strain curve is much steeper than in two dimensions. But at $\sigma_d = 0.88$, the slope suddenly decreases. This point separates two periods of different behavior. In two dimensions, the transition between the two different periods is smooth and happens between $\sigma_d = 0.6$ and 1.0. But in three dimensions, there is no smooth transition between the two periods. At about $\sigma_d = 0.9$, the further rise in stress leads to significant deformations in the three dimensional system. At certain positions the stress decreases again slightly. A similar behavior has been observed in two dimensions at the appearance of precursors, although the decrease was much less pronounced than in this example of a three dimensional system. One reason is the limited size of the three dimensional system. As the system size increases, the stress-strain curve is expected to become smoother, and the kinks at the precursors are expected

to be less pronounced. Comparing the two dimensional system in the upper part of Fig. 10.2 with the larger two dimensional system in Fig. 5.1, this trend is confirmed, at least for two dimensions. In the second half of the figure for three dimensions, three maxima appear in the curve at the strain values $\epsilon_d = 2.7, 3.5$, and 4.4. These three maxima correspond to the failure of the system. In the most common case, the failure or the stability limit of a system is defined as the point of maximum stress. Here, there are three such maxima, and each of them can be considered failure. However, as mentioned above, the limited size of the system is the reason for the appearance of three individual peaks instead of one broad maximum, which is expected in the large particle number limit. In two dimensions, this trend can be seen again by comparing the upper part of Fig. 10.2 to Fig. 5.1. Thus the three peaks in the three dimensional systems are a finite size effect.

Note that the values of external force f/f_0 at which the three maxima appear in the three dimensional system are close to each other: the first maximum appears at $f/f_0 = 2.35$, and the last maximum appears at $f/f_0 = 2.4$. Thus the difference in force is small, although the difference in strain ϵ_d is large. After the third peak, the strain increases by about 2%, which exceeds the scale in Fig. 10.2. For the comparison of two and three dimensions in the next sections, the external force at failure is set to $f_{\text{fail}}/f_0 = 2.4$. The two dimensional system in Fig. 10.2 fails at $f_{\text{fail}}/f_0 = 2.22$. The plots in the next sections are given in units of τ_f. This parameter has been defined in Eq. 10.4.

The comparison between two and three dimensions continues in the next section with the investigation of the number of sliding contacts.

10.5 Sliding contacts

This section has three parts. In the first part we compare the evolution of the number of sliding contacts in two and three dimensions. In the second part we investigate the differences between the two systems in detail, particularly the rate of contact status transitions as a function of the external forcing. In the third part the organization of the sliding contacts is inspected.

10.5.1 Number of sliding contacts

The evolution of the fraction of contacts that are sliding m_s in two and three dimensions is shown in Fig. 10.3. In both cases m_s increases about linearly in the beginning of the simulation. This increase is steeper in three dimensions, but the maximum is reached at the same value $\tau_f = -0.4$ (τ_f has been defined in Eq. 10.4).

In the two dimensional system the maximum fraction of sliding contacts is $m_{s,max} = 0.27$, while in three dimensions it is much higher: $m_{s,max} = 0.41$. This shows that a larger fraction of contacts become sliding during the weakening process in three dimensions. The maximum in m_s is followed by a decrease before the failure. In two dimensions, the decrease is smooth and continuous, while in three dimensions a fast decrease occurs which is immediately followed by the appearance of a precursor of failure. Many more precursors of failure follow thereafter, each leading to a large temporary decrease in m_s. The decrease after the maximum probably initiates the appearance of the many precursors, for only one precursor appears prior to the decrease. Also the sudden decrease of m_s coincides with the kink in the stress-strain curve in Fig. 10.2 at $\sigma_d = 0.88$. Thus the decrease of m_s marks the sudden softening of the system, when the deformation ϵ_d increases much faster with increasing stress σ_d in Fig. 10.2. In two dimensions, there are much fewer precursors, but they

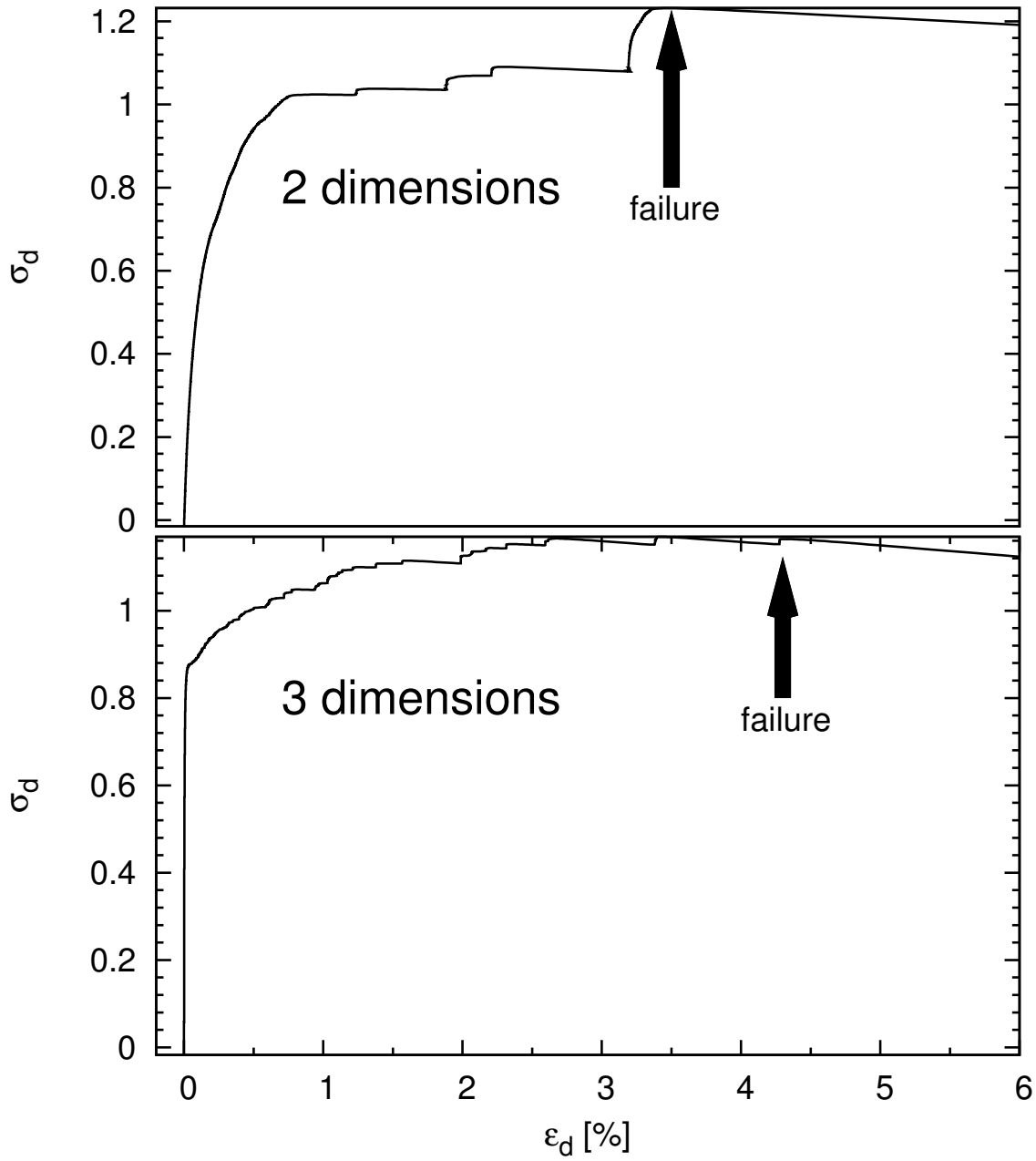

Figure 10.2: Stress-strain curve for one three dimensional system with $N = 16875$ particles and for one two dimensional system with $N = 1024$ particles. The fast initial rise in σ_d is much steeper in three dimensions. In both simulations, during this initial rise the number of sliding contacts increases, while it decreases again afterwards. For details see Sec. 10.4.

also appear during the decrease of m_s. At the failure, m_s increases quickly in both two and three dimensions.

One very important thing should be stressed at this point. Systems even larger than the three dimensional system with $N = 16875$ particles might behave differently than shown in Fig. 10.3. This is so because finite size effects alter the result. For instance, boundary effects reduce the fraction of space occupied by particles, which has been shown in Tab. 2.2. A size dependence of certain quantities has also been observed in two dimensions, and a similar size dependence is expected in three dimensions. For instance, the evolution of m_s might be different in larger systems. In two dimensions, larger systems showed a smoother evolution of m_s with many more precursors appearing before the failure (cf. Fig. 5.5 for 16384 particles with Fig. 10.3 for 1024 particles). Although many precursors appear in the three dimensional system investigated here, in larger systems the number of precursors might be even larger. Last but not least it would be interesting to know if the fast decrease of m_s at $\tau_f = -0.32$ appears in larger systems as well. This point marks the beginning of a series of many precursors, appearing one shortly after the other. The many precursors suggest the range from $\tau_f = -0.32$ until failure at $\tau_f = 0$ being a *critical interval*, because (local) instabilities always appear after a small force increment only. Further insight into the evolution of the sliding contacts can be gained from the rate of the contact status transitions which affect the number of sliding contacts. These are investigated in the next section.

10.5.2 Contact status transitions

Fig. 10.4 shows the frequency of the contact status transitions that change the number of sliding contacts in the three dimensional assembly in the lower half of Fig. 10.3. The contact status transitions in the two dimensional system are not shown, because the very limited number of contacts gives rise to few contact changes only. Their number in a larger two dimensional system has been shown in Fig. 5.7. In Fig. 10.4, the number of closed (C) contacts that become sliding (S) is almost independent of the external force until about $\tau_f = -0.4$. This is the time when the maximum number of sliding contacts is attained. At this value of τ_f, the number of inverse transitions is equally high, and the two curves cancel each other. The first precursor marked in Fig. 10.3 appears as a spike in Fig. 10.4 at $\tau_f = -0.38$.

The number of sliding contacts that disappear (O) in the three dimensional system increases quickly after $\tau_f = -0.4$, and forms a spike at $\tau_f = -0.32$. This very fast increase of the number of transitions $S \to O$ explains the fast decrease of m_s in Fig. 10.3. This fast change is surprising, because it did not occur in two dimensions. Here it happens at $\tau_f = -0.32$, significantly before the failure at $\tau_f = 0$. Right after the spike, the number of disappearing sliding contacts ($S \to O$) slowly increases in Fig. 10.4 until the failure at $\tau_f = 0$. The large fluctuations in the three curves are due to the many precursors of failure, although there are too few data points to resolve all precursors visible in Fig. 10.3.

After the failure at $\tau_f = 0$, the curves do not change much. This is also different to two dimensions, but might also be related to the limited number of data points: in Fig. 10.3, many precursors appear shortly after the failure, but they are not resolved by the limited number of points in Fig. 10.4.

This section showed the reasons for the time evolution of the number of sliding contacts in Fig. 10.3. In the next section the spatial organization of sliding contacts is investigated.

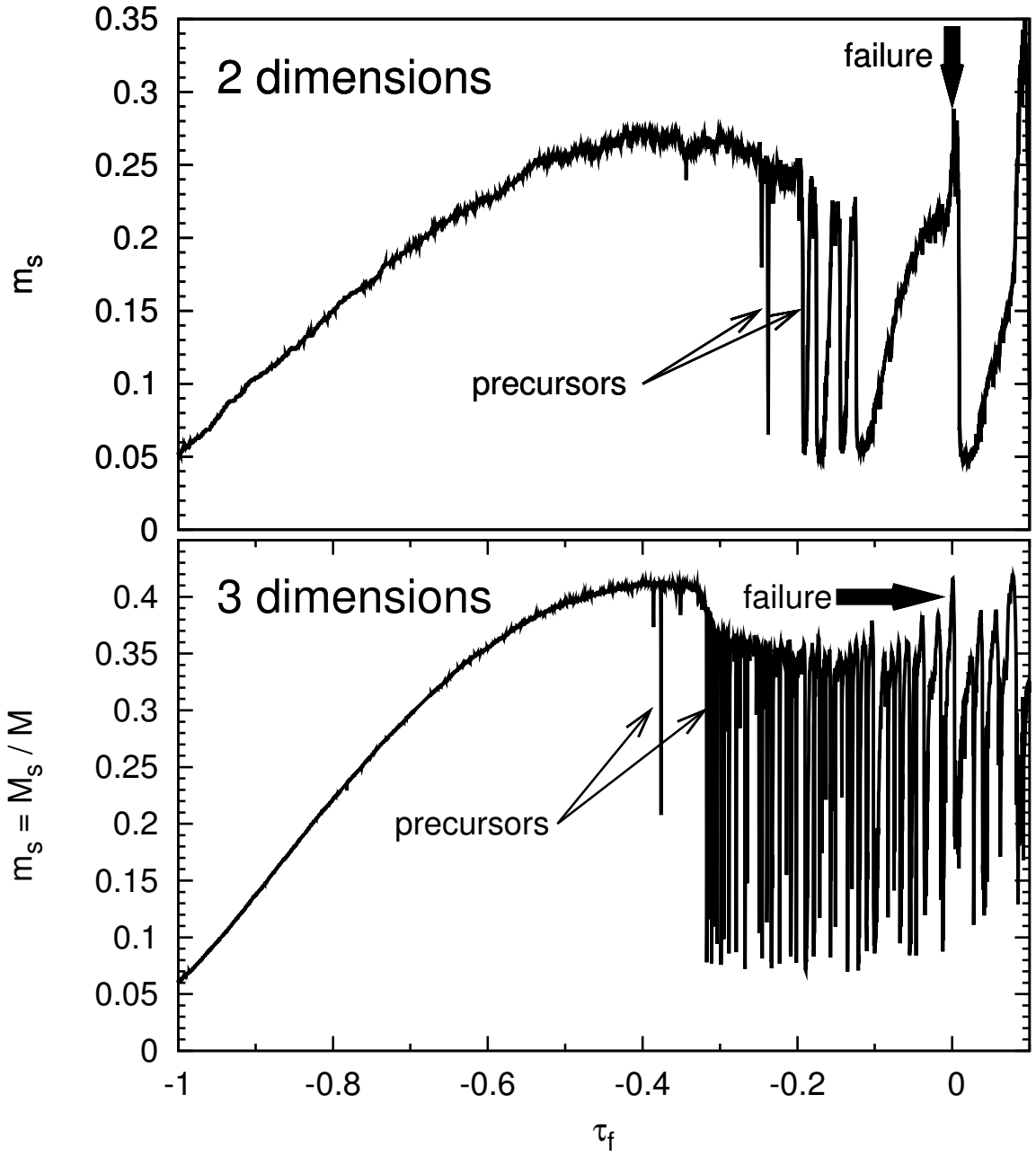

Figure 10.3: Number of sliding contacts in two and three dimensions. The quantity τ_f was defined in Eq. 10.4. It is constructed so that the simulation begins at $\tau_f = -1$ and failure occurs at $\tau_f = 0$.

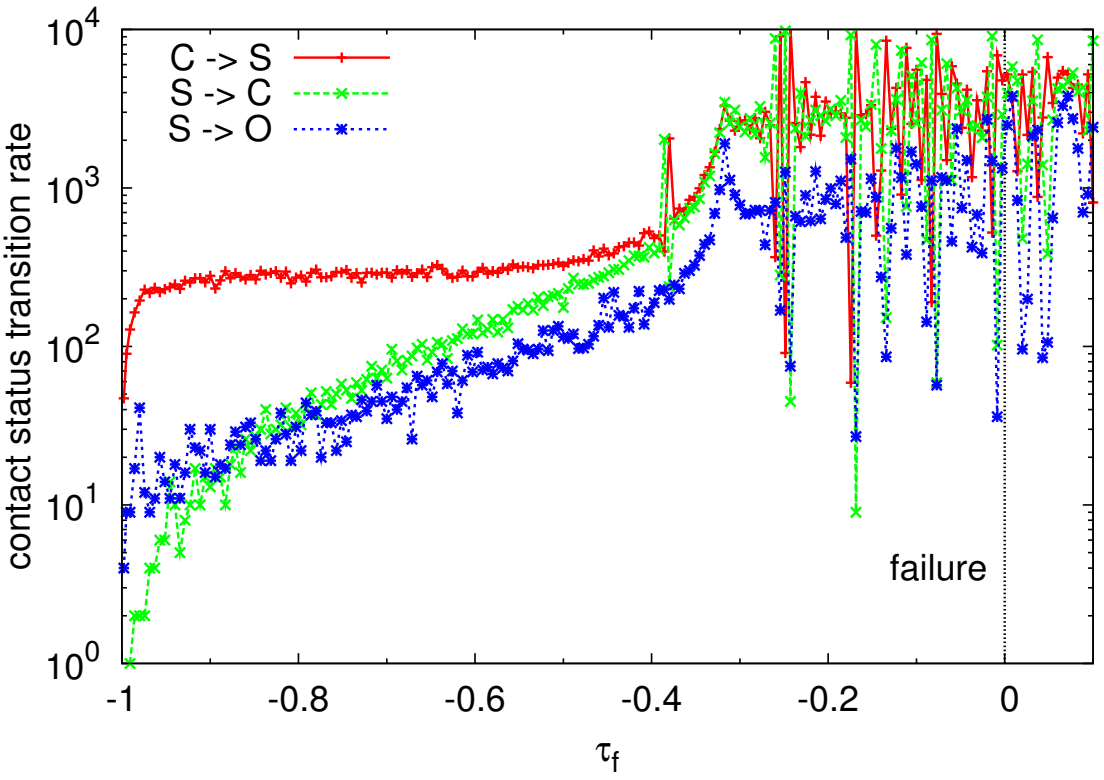

Figure 10.4: Frequencies of the different contact status transitions involved in the change of the number of sliding contacts that is shown in the lower part of Fig. 10.3. The above figure shows the rate of transitions occurring in an interval $\Delta\tau_f = 4.6 \times 10^{-3}$. The vertical dotted line indicates failure.

10.5.3 Organization of sliding contacts

In the same way as the sliding contacts organize in two dimensions, one expects increasing organization of sliding contacts in three dimensional systems when failure is approached. To access the organization, the number of sliding contacts in small test cubes, i.e. in small boxes in the system, is evaluated. Similarly to the boxes in two dimensions, the length of the cube is set to eight average particle radii, $l = 8r_{\mathrm{av}}$. Thus one cube roughly contains $4^3 = 64$ particles. In the same way as in two dimensions, only those contacts between grains inside the cube are counted. Thus contacts between particles of different cubes are never taken into account. To include these contacts in at least one cube, two adjacent cubes along one axis overlap by half of their length. This overlapping is done in all three directions of space independently. The number of boxes in each direction is 13, and the total number of boxes is $13^3 = 2197$. This number is sufficient for good statistics. Note that boxes at the boundaries are disregarded for the same reasons as explained in Secs. 5.5.1, 8.4. In the two dimensional system with 1024 particles, the number of boxes is higher in each direction, but the total number of boxes is much lower. In total, there are $17^2 = 289$ boxes.

In each box, the number of sliding contacts is calculated. The relative occurrence of each number is evaluated with the t-test method, introduced in Sec. 5.5.4. The lower plot in Fig. 10.5 shows the t-test values for the distribution of the sliding contacts in a three dimensional system with $N = 16875$ particles, while the upper plot shows the values for a system in two dimensions with $N = 1024$ particles.

First we discuss the general evolution of the distribution of sliding contacts without paying attention to the spikes that are visible in the graphs in Fig. 10.5. In both two and three dimensions, in the beginning of the simulation at $\tau_f \approx -1$, the first sliding contacts are randomly distributed ($t = 0$). In two dimensions, one then observes negative t-values until about $\tau_f = -0.2$, indicating a repelling of sliding contacts. The repelling leads to a more even distribution over the system. This observation applies also to the larger two dimensional system investigated in Sec. 5.5.4. After $\tau_f = -0.4$, the t-values increase again until failure. They become positive at $\tau_f \approx -0.2$, meaning that sliding contacts start to cluster. In three dimensions the evolution of the ordering behavior of sliding contacts is different: with increasing external force, the t-value rises roughly linearly from the beginning of the simulation until the appearance of the first precursor of failure at $\tau_f \approx -0.4$. The maximum of the t-values is attained at $\tau_f \approx -0.4$, shortly before the number of sliding contacts decreases quickly in Fig. 10.3. After $\tau_f = -0.4$, the t-value decreases until reaching a constant level at $\tau_f \approx -0.2$. The t-value is still positive and remains at that level until failure. Thus the sliding contacts always cluster ($t > 0$) in the three dimensional system. Note that when membrane boundaries are applied in two dimensions, the t-value is also always positive (see Fig. 8.5).

As in two dimensions, spikes in the evolution of the t-values correspond to precursors of failure that appear at certain values of the external force. However, there are too few data points to resolve all the precursors in the three dimensional system. As can be observed in Fig. 10.3, there are many precursors close to the failure of the system, but only few of them appear as spikes in Fig. 10.5 due to the limited resolution of Fig. 10.5. However, the large number of precursors can be noticed by the large fluctuations of the t-values in the second half of the figure until the failure. The failure in both two and three dimensions is visible as a spike in the t-values. After the failure, the t-values do not change much.

The next section investigates the system's properties at the spikes of the t-value before the failure: it examines the precursors of failure which occur at that positions.

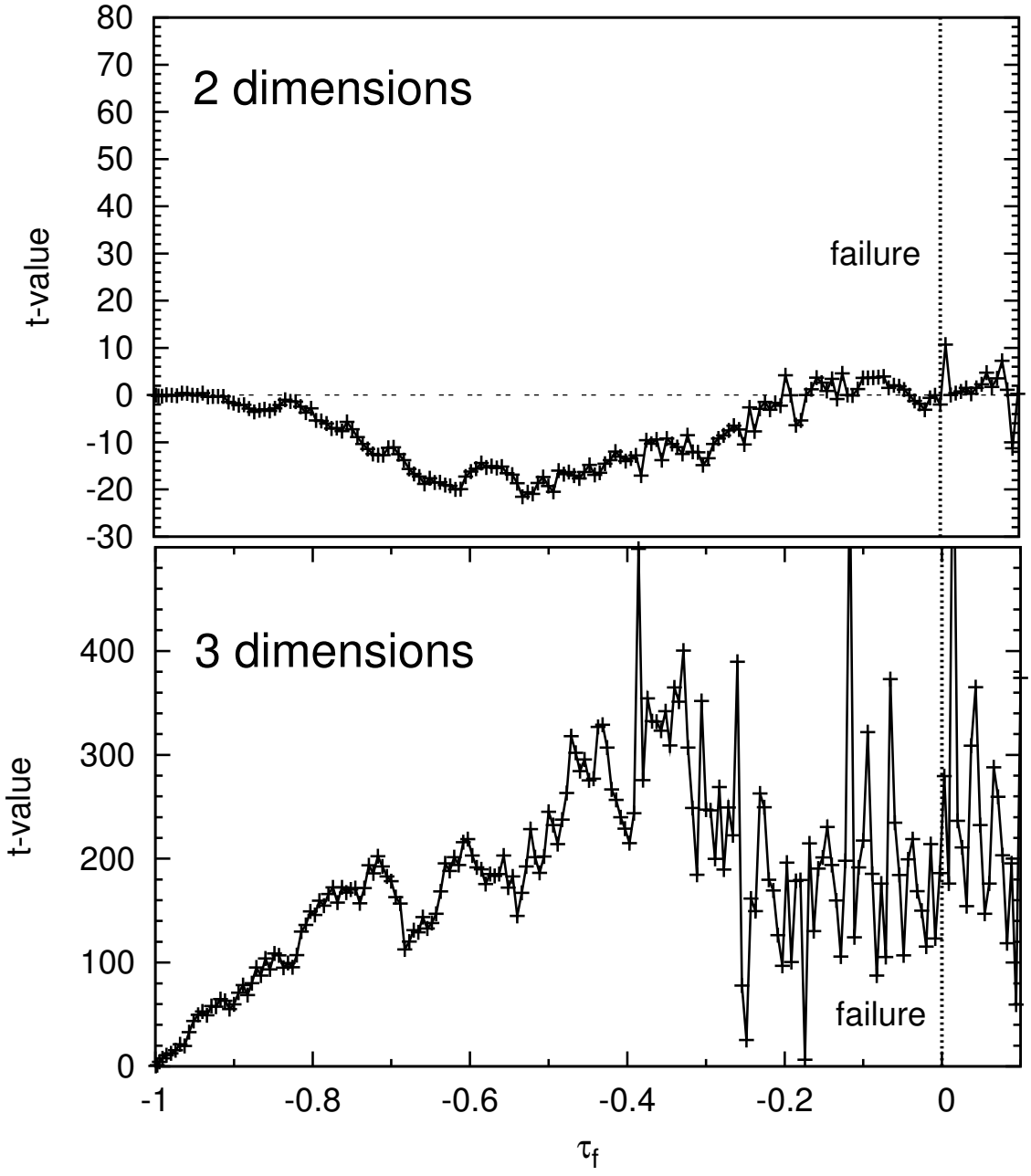

Figure 10.5: Values from the t-test. Upper figure: values for the two dimensional system with $N = 1024$ particles; bottom: values for the three dimensional system with $N = 16875$ particles.

10.6 Precursors

In three dimensions one observes also precursors of failure. Are these precursors similar to precursors in two dimensions? As seen in Fig. 10.3, their number is much higher in three dimensions. Therefore their characteristics might be different. This section contains material on two important aspects of precursors. In Sec. 10.6.1 the properties at precursors in three dimensions are examined for one example precursor. Thereafter Sec. 10.6.2 examines one precursor with two different simulation codes. It shows that the observation of precursors is not related to a specific simulation program.

10.6.1 Example of a precursor

Precursors are much more frequent in three dimensions than in two dimensions, but many principal features of precursors are similar. In this subsection one example of a precursor in three dimensions is investigated in detail. This precursor is the first of the two precursors indicated in Fig. 10.3 for the three dimensional system.

First, the evolution of the number of sliding contacts is inspected at the appearance of the precursor. It is captured by the rate of the contact status transitions $C \to S$ and $S \to C$ which are shown in Fig. 10.6. When the precursor appears, sliding contacts (S) become closed contacts (C). After the precursor, closed contacts start sliding again. This behavior was also observed for the precursor in two dimensions. The rise of the kinetic energy E_{kin} at the precursor is also shown in Fig. 10.6. At $f/f_0 = 1.8729$, E_{kin} rises by more than one order of magnitude. Note that the x-axis in Fig. 10.6 shows the external force f/f_0 instead of τ_f. In this way the values can be compared to the precursor in two dimensions in Sec. 6. For that precursor the values are given as a function of f/f_0. After the precursor in Fig. 10.6, E_{kin} decreases again. A snapshot of the simulation in Fig. 10.7, taken close to the maximum of E_{kin} in Fig. 10.6, shows that the particles which carry a high kinetic energy are concentrated in a small region of the system. Figure 10.7 shows only those grains which have above average kinetic energy. Only 143 particles meet this requirement, which is 0.85% of all grains. This cluster of particles is concentrated at the right sidewall, at the position of the precursor. The few grains at very different positions could be removed by further increasing the energy cutoff. Comparing Fig. 10.7 with Fig. 6.3 for the precursor in two dimensions, one can see that the precursors are localized in a very similar way. Although the dimensions of the three dimensional system are much smaller than those of the system in Fig. 6.3, the numbers of particles of the precursor is very similar: less than 1% of all particles have a kinetic energy E_{kin} above the global average, when the maximum kinetic energy is attained. In both cases the length of the high energy particles region at $E_{\mathrm{kin,max}}$ is about 15 particle diameters.

In the second half of Fig. 10.6, another increase in E_{kin} appears that makes the system become softer. At this transition, E_{kin} rises by roughly two orders of magnitude, and decreases then quickly by one order of magnitude. The increase is much slower than at the precursor and is related to a very limited number of contacts status changes. This is shown by the small values of the curves $C \to S$ and $S \to C$. Thus the limited number of contact status changes lead to a permanent increase in E_{kin}. Contact status transitions in two dimensions show a similar behavior: an example of a contact status transition in a small system with 16 particles has been investigated in Sec. 3.3 and the change of the kinetic energy is shown in Fig. 3.3. In that figure, the energy adjusts to a new value which depends on the new stiffness of the system. This is also observed in Fig. 10.6 for the three dimensional system. Note that the increasing number of contact transitions at $f/f_0 = 1.875$ are not a precursor, because the kinetic energy decreases quickly at that time. Thus the increase in transitions must be attributed

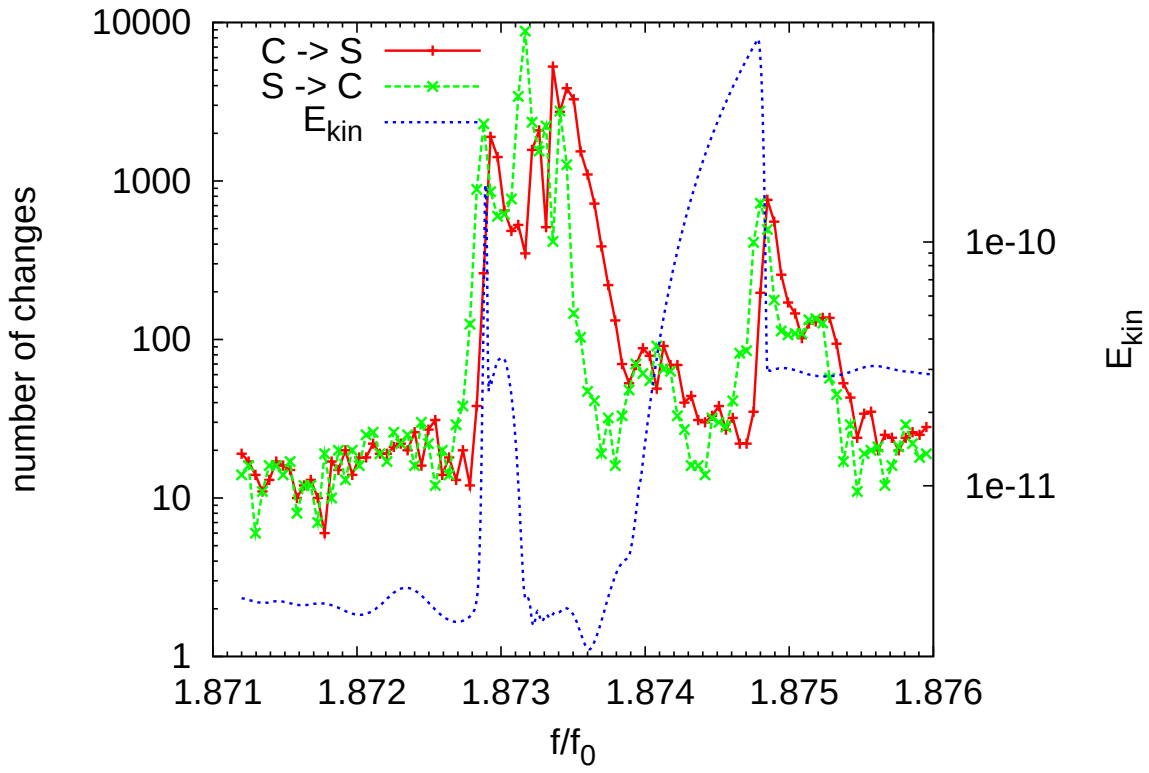

Figure 10.6: The first of the two marked precursors of failure in the 3D-simulation in Fig. 10.3. At the precursor at $f/f_0 = 1.8729$, the kinetic energy increases quickly, but decreases again after a very short time interval.

to vibrations that appear. Indeed, for the precursor at $f/f_0 = 1.8729$ it is also vibrations that cause the many contact changes.

This section showed that precursors of failure appear also in three dimensions, and they have very similar characteristics as in two dimensions. But can it be that these precursors are just and artifact of the simulation, and not a physical observation? By comparing two different simulation codes, the next section shows that exactly the same precursors can be observed with different simulation packages. Therefore the observed precursors are not an artifact of the simulation.

10.6.2 Precursors with different simulation codes

Precursors of the failure have been investigated for systems with different boundary conditions (rigid walls, membranes) and in systems of different dimensionality (two or three dimensions). Furthermore they can be observed in all the systems with at least about 100 particles, and do always occur in quasi-static simulations, independent of the rate at which the external forces are changed. The last but important thing that remains to be done is showing that the observed precursors do not depend on the simulation code and the integrator used for capturing the time evolution of Newton's equations of motion. This is the aim of this section. The results herein show that the same precursors occur also in calculations performed with other simulation packages. Specifically, one precursor in a small three

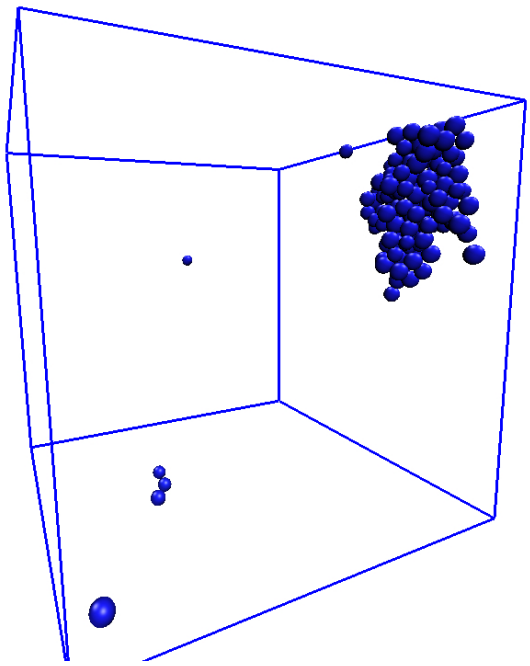

Figure 10.7: Grains with above average kinetic energy at a precursor in three dimensions. The boundary walls are indicated by the lines of intersection. The precursor is located at the right sidewall of the system. The high energy grains shown in the figure constitute a very small fraction, which is 0.85% of all grains. These particles carry more than 95%(!) of the total kinetic energy in the system, showing that the rise of the kinetic energy is concentrated in a very small region.

dimensional system with $N = 94$ particles is simulated with the code used throughout this thesis, and also with the Pasimodo simulation package. The results obtained from the two codes are then compared.

The Pasimodo-code was developed at the Institut für Technische und Numerische Mechanik at the University of Stuttgart by Florian Fleissner and coworkers. The package is intended to solve particle based problems. One simulation method therein is molecular dynamics, which is the method used in this thesis. Recall that molecular dynamics means that the motions of the particles are described by solving the particles' equations of motion. The method has been discussed in Chap. 2. For integrating the differential equations of motion, different methods can be used. The simulation package Pasimodo has several integrators on hand. For this comparison the Newmark integrator is chosen, while in this thesis the velocity Verlet integrator was taken. The main difference to the Verlet integrator is that the Newmark integrator solves the equations of motions *iteratively*. It is therefore an *implicit* method. Its advantage aver the explicit Verlet algorithm is that one can tune the length of one time step (or let it be controlled by the integrator). Specifically, the implicit method allows for small time steps when the kinetic energy is high, and tunes the time step to large values when the energy gets low again. This reduces the number of time steps and makes the simulation run faster. However, the advantage of a larger time step comes at the price of a larger number of computations required at each time step: at each step, a minimum number of iterations is needed.

The two very different integrators of the two simulation packages lead to very similar results concerning the precursors of failure. Figure 10.8 compares the kinetic energy at one example precursor between the two simulation results. It shows that the evolution of the energy is very similar, although in the Pasimodo simulation the precursor appears a little earlier; the difference is $\Delta f/f_0 = 0.06$. This difference might just be a consequence of the different integrators, and maybe also due to a different organization of the data. Figure 10.8 also shows that the appearance of a precursor coincides with a decrease of the number of sliding contacts.

But is the precursor in the two figures exactly the same, or is the similar shape of the two maxima a mere coincidence, with different granular behavior behind? We might first inspect in more detail the maximum of the Pasimodo simulation. Five snapshots of the system in Fig. 10.9 resolve the time of the maximum in E_{kin} with more spatial and temporal detail. The figures show only those particles which have $E_{\mathrm{kin}} > 10^{-8}$. The first three sketches in the upper row show the high energy grains when E_{kin} rises, and the two figures in the lower part show the particles with high energy when E_{kin} decreases again. The last figure in the upper row is taken at the maximum of E_{kin} in Fig. 10.8. The five figures show that one particle carries most of the energy, while all other particles have far less energy. From the first until the third figure, the single particle gains energy: the color of the particle changes from blue over green to yellow. In the third figure, the single yellow particle carries over 90% of the total kinetic energy of the system. Thereafter, in the snapshots in the second row of Fig. 10.9, the energy is dissipated in a vibration wave radiated outward.

A comparison with the McNamara package shows that the precursor observed is exactly the same. By inspecting the kinetic energy at the maximum E_{kin}, the same single particle is identified carrying almost all the energy. Similarly to the Pasimodo simulation, the single particle has more than 90% of the total E_{kin} at the peak in Fig. 10.8 at $f/f_0 = 1.7$. This shows that the precursors, observed in this thesis for different configurations, boundary conditions, and dimensionality, are not an artifact but a feature of granular systems submitted to a uniaxially increasing force.

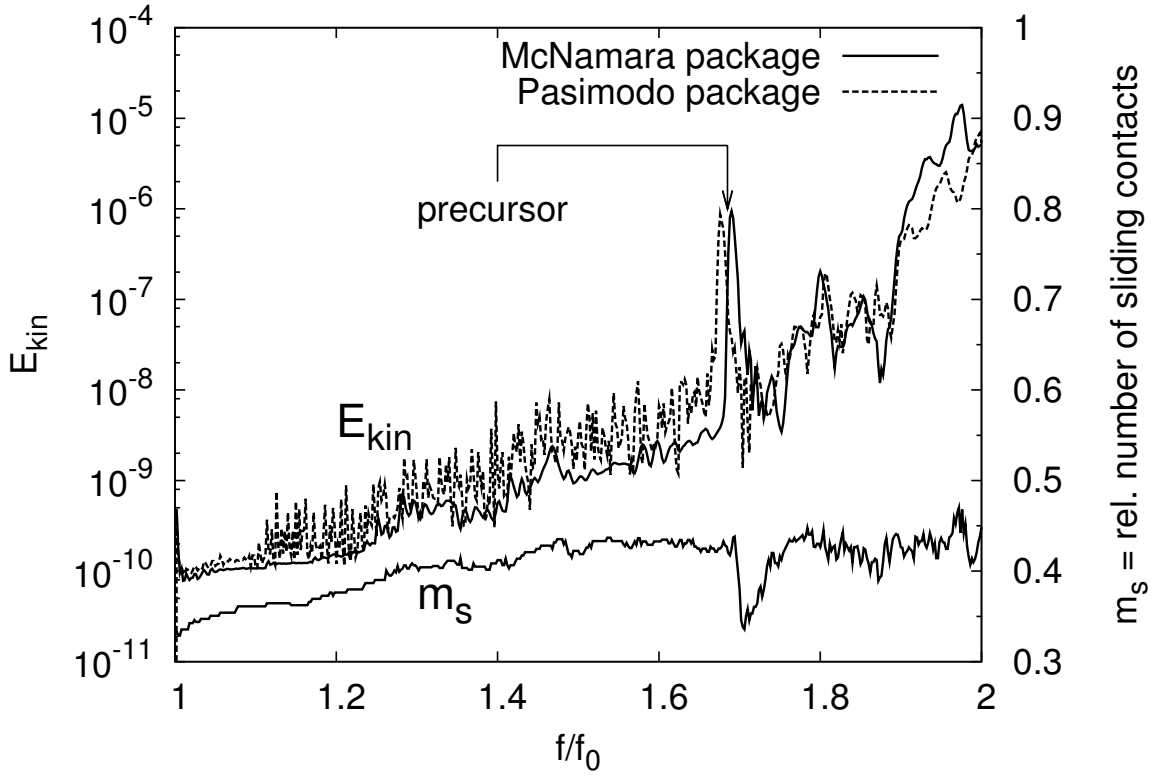

Figure 10.8: Kinetic energy in a system with $N = 94$ particles simulated with two different simulation packages.

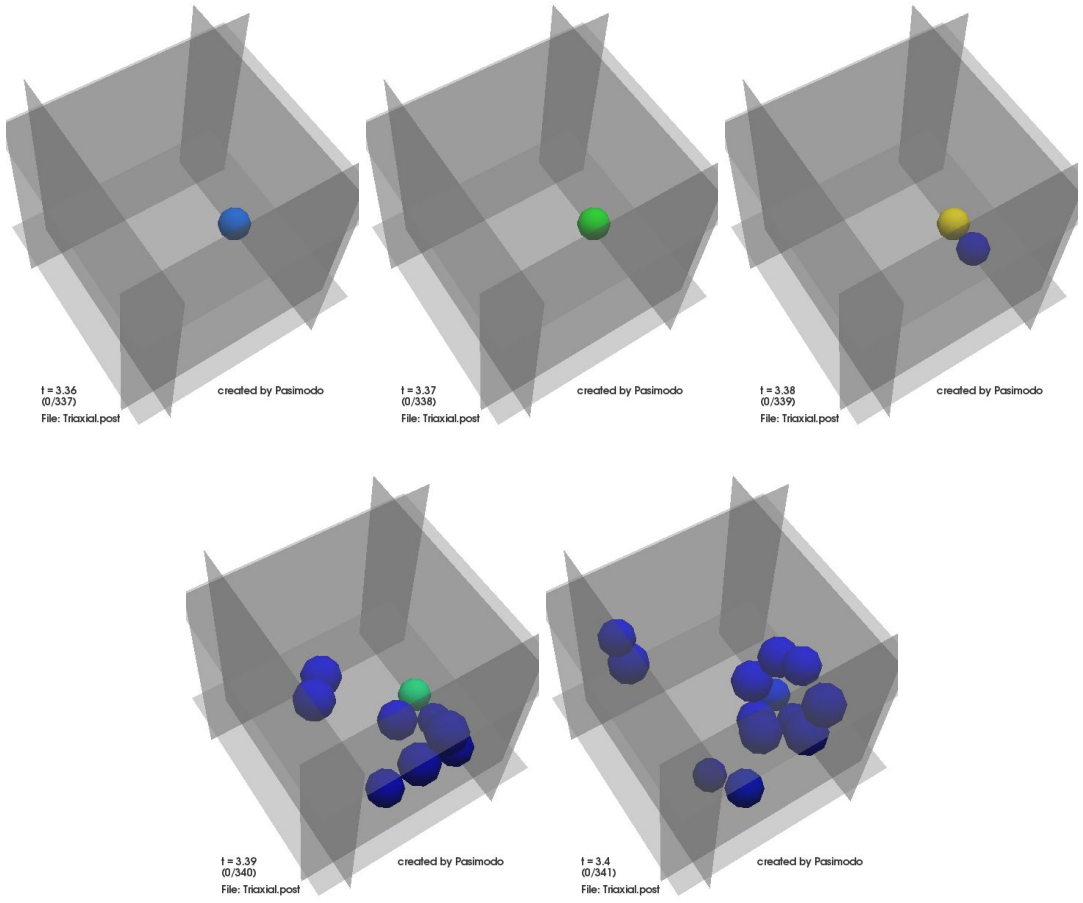

Figure 10.9: Precursor of failure in a system with $N = 94$ particles, simulated with the Pasimodo simulation package. The grey planes show the boundary walls. Only the particles with high kinetic energy E_{kin} are displayed. All particles in the figures have kinetic energies above 10^{-8}. Blue particles have medium high energy, and green and yellow particles have very high energies. The three figures in the top row show the evolution when the kinetic energy is increasing. The increase in energy is concentrated at one particle. The third figure is taken at the maximum energy at the precursor in Fig. 10.8. At this time, the yellow particle has an energy $E_{\mathrm{kin}} = 8 \times 10^{-7}$, while the total energy is $E_{\mathrm{kin}} = 8.64 \times 10^{-7}$. Thus almost all the energy is carried by one particle. When the kinetic energy decreases again in the figures in the bottom row, the energy is dissipated through a vibration wave which is radiated outward. Unfortunately the number of particles in the system is too small to resolve this wave in much detail.

10.7 Conclusion

The comparison of two and three dimensional systems shows that many aspects of the weakening and the failure of granular systems appear in two as well as in three dimensions. From these aspects, one important feature is the number of sliding contacts m_s, which rises linearly with increasing external force. This number attains a maximum at about half of the peak stress attained at the failure. After this maximum, m_s decreases again. At the failure, m_s quickly increases, and a decrease follows when the system stabilizes again within a very short period. After this decrease, most contacts are nonsliding, although the decrease is less pronounced in three dimensions.

Precursors of failure occur in all examples shown. In both two and three dimensions, they are characterized by a decrease in m_s, accompanied by an increase in the kinetic energy. This increase is localized, with the highest kinetic energy appearing in a very small region. The kinetic energy per particle in this region is much higher than anywhere else in the system, concentrating more than 90% of the energy in about one percent of all particles. This process is always accompanied by a vibration, appearing directly after the precursor of failure. Although the precursor lasts only for a very short time, the dissipation of the concentrated kinetic energy takes much longer, and the long range vibrations are damped only slowly.

The most important difference between two and three dimensions is the observed clustering tendency of sliding contacts, investigated by the t-test method. While in two dimensions sliding contacts tend to repel each other in the first half of the simulation, involving a rather even spatial distribution, in three dimensions there is a smooth transition from a random distribution to increasing clustering until the failure. This shows that, although many features are similar in two and three dimensions, some details of three dimensional behavior cannot be captured by two dimensional model systems. When precursors appear, the t-values are distorted, and no general trend is visible any more.

Another aspect is the number of precursors that appear. In the two dimensional system this number is very limited. Although the small system size might play a role, a similar small number of precursors is observed in a two dimensional system with 16384 particles in Fig. 5.5 in Sec. 5.4. In three dimensional systems of that size, the number of precursors is much larger, and the temporal distance between two precursors is much smaller.

Precursors are not an artifact, but they are always observed in all simulations of granular media, if the simulations are quasi-static. They are observed for simulations with different simulation packages, and they appear independently from the integrator used for solving the equations of motion. The observation of the precursors of failure in a variety of different simulations is one very important result of this thesis and stresses the observation that precursors do always appear prior to the failure.

Chapter 11

Summary

This work investigates granular assemblies subjected to increasing external forces in the quasi-static limit. In this limit, the system's evolution depends on static properties of the system, but is independent of the particles' inertia. At the failure, which occurs at a certain value of the external forces, the particles' motions increase quickly. In this thesis, the properties of granular systems during the weakening process and at the failure are investigated with the Discrete Element Method (DEM). Unlike continuum approaches, in the DEM each particle is represented by one element with certain properties. This method is combined with an analytical description and with numerical simulations of the granular systems. Although many results are obtained for systems with rigid boundaries in two dimensions, several aspects of granular behavior are investigated under different conditions: systems with rigid wall boundaries are compared to systems with membrane boundaries. Two and three dimensional systems with rigid wall boundaries show the dependence of weakening and failure on dimensionality. This enables one to separate the general granular behavior from individual trends. A comparison between two independently developed computer codes shows that the obtained results are a true physical property of our granular model, and are not due to a particular numerical procedure.

The dependence of the results on the system size is a further important aspect. Since the size of a grain introduces a characteristic length, small systems and large systems behave differently. For some of the investigated properties, an average over many small systems is equal to the value of one large system, but this is not always the case. Thus the system size dependence of granular properties is nontrivial. This work investigates small systems with only 16 particles but also large systems with more than 10^4 particles. Different aspects of granular behavior are investigated in different chapters. Chapter 1 introduces the reader to granular media, and Chap. 2 provides the theoretical framework for understanding the results in the following chapters.

Chap. 3 considers the failure and triggers of failure in small systems with only 16 particles. This size is small enough to identify single particle contact changes and investigate their meaning for weakening and failure. The stability of the systems is calculated from the knowledge of the contact structure, i.e. from position and orientation of the contacts (geometric aspects) and their states (mechanical aspect). From this structure, the stiffness matrix is constructed, and a scalar stiffness is deduced. Changes in the stiffness can in this way be related to changes in the interparticle contact structure. A contact status change always appears at the beginning of the failure, decreasing the stiffness of the system. Thus, this contact status change is at the origin of failure. Through the change, the stiffness either becomes negative (instability), zero (null-mode motion), or very low. In the latter case the transition from a higher stiffness before the change to the low stiffness afterwards is rather slow. During the transition, a subsequent contact status change leads to the failure of the

system. The results in Chap. 3 show that the stiffness matrix approach is successful in describing weakening and failure of granular systems. Thus Bagi's [20] definition of stability, which is based on the stiffness matrix description, is a useful concept for a more precise definition of jamming than the qualitative jamming diagram in Fig. 1.1.

In Chap. 4 the failure is investigated in more detail. Several publications show that there is a minimum number of interparticle contacts for which the system can stabilize the external forces at the boundaries. This limit, the so-called *isostatic limit*, defines the minimum number of contacts required for stability of a frictionless granular system. When friction comes into play, the counting of contacts becomes more complex: closed contacts contribute two stability conditions, and sliding contacts contribute one condition for stability. However, the results in Chap. 4 show that the failure of a granular system does not coincide with the minimum number of constraints required for stability, at least not based on the global comparison of constraints and degrees of freedom presented there. When a system fails, a shear band appears, where the particles' kinetic energy is higher than elsewhere in the system. This immediately suggests evaluating the number of constraints in that region to be a promising route for refinement.

Many aspects of the softening of granular systems on the way to the failure are explained in Chap. 5. The main result therein is that the softening of a granular assembly can be divided in two periods of different granular behavior. In the first period, many contacts become sliding, while in the second period the number of sliding contacts decreases. Also precursors of failure appear in the second period. They can be noticed as plunges in the number of sliding contacts, followed by a fast recovery. The evolution of sliding contacts can be fully understood in terms of contact status transitions. In the beginning of the simulation, most frequently a closed contact becomes a sliding contact. At the transition between the two periods, the number of sliding contacts becomes maximal. At this maximum, the inverse transition from sliding to closed is equally likely. Increasing the force further, another transition comes into play: sliding contacts disappear. This means the total number of contacts decreases. Finally, at the failure, all contact status transitions become equally likely. This behavior is a consequence of the global rearrangement involving a large number of grains. The spatial organization of sliding contacts also changes during the simulation. In the first period, sliding contacts tend to distribute evenly over the system, while they tend to cluster in the second period. This tendency increases until the failure, where the sliding contacts are finally concentrated in a diagonal band.

Chapter 6 examines more closely the precursors mentioned in Chap. 5. These are localized instabilities, i.e. a negative local stiffness appears in the system. Consequently, the kinetic energy rises locally very quickly, and decreases again when, after a very short interval of time, stability is recovered. Due to the localization, the kinetic energy is much lower than at the failure. One can more easily identify precursors by the sudden plunge of the number of sliding contacts. This decrease is always temporary, and it can be understood in terms of contact status transitions: when a precursors appears, contacts become nonsliding in the region of the vibration wave, which is initiated by the precursor and radiated outward. When the vibration disappears, these contacts start to slide again. Changes in the contact structure are mainly transitional, therefore the importance of precursors for the internal structure is much smaller than the general trend, which depends on the external force.

Chapter 7 examines closely the organization of motions, first observed in Chap. 5. While the system is stable, the two most important relative motions are the sliding of particles and the rolling of grains at their point of contact. This chapter shows that the latter motions do concentrate in bands appearing roughly at the angle $\pi/4$ relative to the direction of increasing force. Such rolling bands were also observed by Kuhn and Bagi [83]. The organization of rolling in bands increases as failure

approaches. As the number of bands decreases, the distance between the rolling bands increases. Eventually only very few rolling bands remain, and one of them becomes the shear band which appears at the failure. Thus the rolling motions are concentrated within the shear band, contributing to the process of reorganization. The direction of the shear band found here is similar to the Mohr-Coulomb direction of failure. The latter is also obtained from the principle of least dissipation rate of Török [93]. Another important finding is the correlation of rolling and sliding motions. This correlation is stronger in the simulation beginning and at failure, and it is weaker at the maximum number of sliding contacts.

Chapter 8 discusses the influence of the boundary conditions on the results presented in the foregoing chapters. Specifically, results obtained in systems with membrane boundaries are compared to results in systems with rigid wall boundaries. The comparison reveals that many details of the softening process and the failure are qualitatively independent of the boundary conditions. One example is the number of sliding contacts attaining a maximum before the failure, and disemboguing into a sharp maximum at the failure. The maximum always divides the softening process in two periods. On the contrary, the spatial organization of sliding contacts depends on the boundary conditions. Applying membrane boundary conditions leads to a constantly increasing clustering tendency with increasing force, which decreases again only at the failure of the system. When rigid walls boundaries are applied, sliding contacts tend to repel each other in the first period of the simulation, resulting in a more homogeneous distribution of sliding contacts. In the second period until the failure, sliding contacts show an increasing tendency to cluster. In both rigid walls and membrane conditions the sliding contacts concentrate at the failure in the shear band that develops. This suggests that the process of failure might be similar in both cases.

A further important finding, explained in Chap. 9, is that the critical force at failure depends on the interparticle friction coefficient μ. When this coefficient is increased, the system fails at a higher value of the external force. A higher μ involves also a stronger decrease in the number of contacts M before failure, while the number of sliding contacts M_s involved in the weakening is lower. A very important finding is that while M, M_s vary considerably, the global hyperstatic number $\mathcal{H}$ observed at failure is almost independent of μ. This suggests that failure might be better characterized by μ-independent properties.

Chapter 10 shows the behavior of granular systems in three dimensions. Applying similar boundary conditions as in two dimensions (rigid walls on every side of the system), important system characteristics can easily be compared. The comparison reveals that the approaching of failure in three dimensions is in some respects similar to two dimensions, but it has also some different features. One common observation is the initially linear increase in the number of sliding contacts m_s. At the maximum m_s, the behavior becomes different: m_s decreases very quickly in three dimensions, while the decrease in two dimensions is smooth. The spatial organization of sliding contacts is also different: they always tend to cluster in three dimensions, while in two dimensions they only cluster in the second period before failure. Precursors are observed in both two and three dimensions. In both cases, their characteristics are similar, but their number is much higher in three dimensions.

At least three main results can be distilled from this thesis. First, organization and clustering of sliding and rolling motions starts a long time before the failure is approached. Thus, in a macroscopic constitutive model, not only the number of sliding motions, but also their organization has to be taken into account. Second, precursors of the failure are always observed, *independent of the boundary conditions and the dimensionality*. In the literature, precursors of granular avalanches have been reported by several authors. The findings of this thesis show that the precursor phenomenon is more general and applies to rigid wall and membrane boundary conditions as well. Although from the

limited number of examples it is impossible to draw a general conclusion, most probably precursors of failure occur for any kind of boundary conditions and for any load protocol. Third, the thesis provides new insight into the nature of failure: in small systems, failure is connected to the appearance of instability and an exponential rise in the kinetic energy. In large systems, vibrations, appearing at precursors, become larger close to failure. Thus the system explores an increasing part of phase space. These vibrations are physical, and not an artifact of the simulation: they appear in the same way after localized instabilities as they also do after the failure, when the system comes back to rest. These vibrations are important for failure in large systems. This importance might trigger future investigations of granular media.

What are the perspectives for future work? First, the global hyperstatic number $\mathcal{H}$, defined in Sec. 2.7 and investigated in Sec. 4.1, could be locally defined. The hyperstatic number compares the number of constraints with the number of degrees of freedom. The refinement to a local definition is promising because sliding and rolling motions organize in localized diagonal bands close to failure. Thus failure might be a local happening, and calculating $\mathcal{H}$ in these regions might give further insight to what precisely happens at failure. For example, the mystery of failure being approximately an isostatic transition ($\mathcal{H} = 0$) in small systems, but hyperstatic ($\mathcal{H} > 0$) in large systems, could probably be explained by this approach: the isostatic region might be localized. Second, the number of precursors could be counted for each type of boundary conditions, and the rise in this number until failure could be evaluated. Also the position of subsequent precursors could be related to each other. Are the positions correlated? This would be interesting to know. Note that for this purpose it would be advisable to control the boundary motions (i.e. the strain) instead of the external forces (i.e. the stress). This increases the resolution close to the failure, where most precursors occur.

Last but not least, a few more words about the jamming diagram, introduced in Fig. 1.1 should be said, linking the results of this thesis with this diagram. Granular systems belong generally to the blue plane in the jamming diagram, defined by the density and the external force, which is the load. Considering the systems here, at least one more parameter must be introduced to fully pin the shaded jamming surface. This parameter is the *interparticle friction coefficient* μ. When it is reduced, the maximum supported load decreases. As the results in Chap. 9 show, the type of failure transition also changes qualitatively from $\mu = 0$ to $\mu \to \infty$ (See Fig. 9.1). For small μ, the hyperstatic number $\mathcal{H}$, which reflects the number of stabilizing contact forces, evolves smoothly and continuously at the failure. For $\mu > 0.3$, this number plunges suddenly at the failure. If the simulations are not quasi-static, the parameter *load protocol* must also be added to the list, because failure appears at a higher load when the external force is quickly increased. In the jamming diagram, the precise meaning of the axis *load* is also not clear. Most probably the authors mean a deviator stress which is applied to the system. This would be a good specification, because failure is most frequently identified with the point of maximum deviator stress. However, the maximum stress might depend on the dimensionality. Consequently the jamming surface in the diagram proposed by Liu and Nagel is only unique when a specific set of parameters is chosen. But then the same set of parameters must be applied to all systems (i.e. to grains, bubbles, glasses). Further investigation is needed to identify if the jamming diagram in the proposed form relates the granular failure to the glass transition in a favorable and unique way.

Appendix A

Params

In this section the parameters for the different investigations are given. Not all parameters do change. The ones that always remain are shown in Tab. A.1. Parameters which depend on system size or boundary conditions are adjusted to appropriate values. They are given in Tab. A.2.

The parameters D_R, D_T depend on system size N, because the aperiodic limit, in which local oscillations are replaced by exponential relaxation to equilibrium, depends on N. This limit can be calculated from Eq. 2.1. With $k_n \equiv k_R$ and $\gamma_n \equiv D_R$, the homogeneous part of that equation is

$$m\ddot{x} + D_R\dot{x} + k_R x = 0. \tag{A.1}$$

To prevent misinterpretation, the particles' overlap, denoted D_n in Eq. 2.1, is named x. (The inhomogeneous part would be $F_n^0 = k_r x$.) Equation A.1 depends on position and velocity of the two particles in touch. It describes the relative motion of the two body system. Thus mass m is the reduced mass $m = \frac{m_1 m_2}{m_1+m_2}$. With the ansatz $x = e^{i\omega t}$ one obtains the solutions

$$\omega = \frac{iD_R}{2m} \mp \sqrt{-\frac{D_R^2}{4m^2} + \frac{k_R}{m}} = i\omega_D \mp \sqrt{\omega_0^2 - \omega_D^2}. \tag{A.2}$$

where $\omega_0 = \sqrt{k/m}$ and $\omega_D = D_R/(2m)$. In the aperiodic limit $\omega_0 = \omega_D \Longrightarrow D_R = \sqrt{2k_R m}$. Thus D_R depends on mass m. The size of the system being constant, m decreases with increasing number of particles: $m \sim 1/N$. This means $D_R \sim 1/\sqrt{N}$, i.e. the value for damping decreases with N increasing. The systems are prepared with D_R, D_T close to the aperiodic limit, in which the system is critically damped and converges to equilibrium in the fastest possible way. Note that D_R, D_T are the damping constants at single contacts, meaning that short range vibrations of high frequency are quickly damped. On the other hand long range vibrations decay much slower. The reason is that relative particle motions decrease with increasing wavelength, thus the damping term becomes small.

parameter	value	details
density	1	particle density
Lx	1	length of the simulation box in x-direction
Ly	1	y-direction
muwall	0	friction coefficient for wall-particle contacts
Fx	0.8	force on walls in x-direction
Fy	0.8	in y-direction (increasing during simulation)
kR	1600	particle stiffness normal to particle surface
kT	1600	tangent to particle surface
g	0	gravitation constant
Droll	0	friction coefficient for rolling
Dtwist	0	friction coefficient for twisting (only in three dimensions)

Table A.1: Parameters which are identic for all systems.

parameter	values	details
dimension	2,3	dimension of space (2D or 3D)
Lz	0,1	length of the simulation box in z-direction (0 in 2D, 1 in 3D)
Fz	0,0.8	force on walls in z-direction (0 in 2D, 0.8 in 3D)
mu	0–2	friction coefficient for particle-particle contacts
Membrane	0,1	1=set membrane, 0=unset Membrane
dfextdt	1.28e-4,1.28e-3	slope α in Eq. 2.71 for $N \leq 100$, slope for $N > 100$
DR	see text	damping coefficient normal to particle surface
DT	see text	tangent to particle surface

Table A.2: Parameters taking specific values which depend on boundary conditions, system size, and dimension (2D or 3D).

Appendix B

CPU time

This section contains hints about the CPU time spent on the simulations. We will discuss the principal dependency of the time needed on system size, stiffness, and the rate at which the external forces are increased during a simulation. The rate $\dot{f}_{\text{ext}}$ is inverse proportional to the total simulation time. Next, the CPU time scales linear with the number of particles, as the integration of the equations of motion and the calculation of the forces take most of the time. Then we have the parameter particle stiffness, and the CPU time spent is proportional to the square-root of it. The calculation of the boundary conditions might scale linearly (membrane) or constant (rigid walls), depending on complexity. One simulation step is 0.01 of the average vibration frequency at a contact (i.e. of $\sqrt{m_{min}/k_n}$, where k_n is the normal contact stiffness and m_{min} is the minimum mass a grain can have. Note that due to the fact that m_{min} decreases with increasing number of particles N, the scaling is more than linear in N.). We have the following dependencies on system size N, particle stiffness $k_n = k_t$, and rate of increasing external force $\dot{f}_m athrmext$:

$$T_{sim} \sim N^{\frac{3}{2}}, \sqrt{k_n}, \frac{1}{\dot{f}_{ext}} \tag{B.1}$$

The simulation run time for some parameter sets shows Tab. B.1.

N	time	rel. time	k_n	$\dot{f}_{ext}$
4096	184h (Core2Quad Q6600 @2.40GHz)	1	1600	$1.28 \cdot 10^{-2}$
20164	1080h (Core2Quad @2.4GHz)	5.87	1600	$1.28 \cdot 10^{-2}$
20164	155h (Core2Quad @2.5GHz)	0.84	1600	$6.40 \cdot 10^{-2}$
20164	55h	0.30	160	$1.28 \cdot 10^{-2}$
20164	106h (Core2Quad @2.5GHz)	0.57	160	$6.40 \cdot 10^{-2}$

Table B.1: Simulation times for some values of N, k_n, and $\dot{f}_{\text{ext}}$.

Appendix C

Comparison of results with two different simulation packages

C.1 The two codes

The code used for this investigation is written by Sean McNamara It is a package optimized for efficient quasi-static simulations, i.e. for small changes in the particle positions. In the following we will name this simulation code after its purpose: QSP – *q*uasi-static *s*imulation *p*ackage. Most of the time the neighbors of the particles remain unchanged, thus the neighbor list must be updated only rarely.[1] As the neighbor search scales more than linear with the number N of particles, the seldom update optimizes the runtime of the code. If the list was updated at each step, this procedure would set the time needed for simulating systems with large numbers of particles.

The other code, Pasimodo, is written by Florian Fleissner at the ITM (Institut für technische und numerische Mechanik) at the university of Stuttgart. It is a simulation package for particle based methods such as molecular dynamics. The Pasimodo package is not specifically optimized for quasi-static simulations, and in this comparison the neighbor list was updated at each time step (but it is also sparsely calculated in an up to date version). The advantage of Pasimodo is its flexibility considering boundary conditions and particle shape, and it can be run in parallel. This brief comparison however is restricted to the serial version of the code.

When comparing different codes, one usually wants to use the same set of parameters and the same parameter values. This approach was hindered at one point: the integration algorithm. Although the Pasimodo package supports in general an integrator similar to the one used in QSP, it did not work for all sets of parameters. Therefore a different integrator had to be taken. In the QSP package, the velocity Verlet integrator is implemented, which integrates the equations of motion in an explicit way. In Pasimodo, an iterative algorithm, called Newmark, integrates the equations of motion implicitly. This integrator has one advantage and one disadvantage. The advantage is that the integrator can adjust the time step to meet a desired integration accuracy for a given problem. In general, if the particle velocities are small, the time step is large, and when the motions increase, the time step is reduced in given bounds. This flexibility comes at the price of a higher number of calculations at each time step, because the implicit calculation requires in each integration step a minimum number of iterative solutions, increasing the computation time. Thus for quasi-static simulations, in which

[1] One update is done, depending on the particle motions, after some thousands or millions of integration time steps.

most of the time the kinetic energy is low, the implicit Newmark integrator might not be the optimum choice.

C.2 The system

The three dimensional example system consists of $N = 94$ spheres, delimited by rigid walls on each side. The setup of the system is explained in the beginning of Chap. 10. The input is an xml-file generated by Pasimodo, and it contains the parameters and particle positions for both simulations. For the QSP run, the data structure is converted to the input file format.

C.3 Relaxation of the system

To avoid additional parameters, the time step for the Newmark integrator was set to the value of the velocity Verlet algorithm ($\Delta t = 7.63 \times 10^{-6}$). As mentioned above, the Newmark integrator can handle a variable time step and might then perform much better.

The first test compares the evolution of the system's kinetic energy during the relaxation procedure as described in Sec. 2.10. Here, the external forces during compressing are set to $f_0 = 1$ (while they are $f_0 = 0.8$ throughout the thesis). For simplicity, neither the center of mass nor the individual particle motions are damped by viscous terms other than the ones in Eqs. 2.1, 2.3. Figure C.1(a) shows the kinetic energy E_{kin} as a function of time for two versions of both codes. Three curves show a very similar behavior, but one curve is very different. It shows an exponential decrease of E_{kin} to 10^{-24}. This difference can be explained by two things. First we observe that rotating the system by $\pi/2$ along one coordinate axis leads to different results with the same code. This shows that the result depends on the organization of the particle data in the simulation code. Second a granular gas has irreversible microscopic dynamics [100]. Tiny differences in position and momentum after the first few time steps can grow much faster than linear with time. In conclusion, the relaxation process, where a granular gas is compressed to form a solid, is not appropriate to compare different simulations. Thus one of the configurations obtained at the end of the relaxation procedure is fixed as starting configuration for all following simulations.

C.4 Simulation of weakening and failure

The force on the boundary walls is increased in one direction while on the other boundaries the forces remain constant. The rate at which the external force is increased is set to $\alpha = 0.2$ in Eq. 2.71, and the simulation is running for $t = 5$ time units. Figure C.1(b) shows the resulting evolution of the kinetic energy. It evolves similarly for both packages. In the Pasimodo package, the time step could not be fixed in this case, so it varies within certain bounds. Nonetheless the evolution is similar. Failure announces itself at the end of the simulation at $f/f_0 = 2$, while the dip at $f/f_0 = 1.7$ is a precursor of failure. Although the precursor appears at slightly different times in the simulations, there is no obvious time shift in the data later on. The reason is most probably that the precursor depends on the local spatial structure, while failure depends on the positions of all the particles. The two curves are in good agreement, and at all values f/f_0, the differences are within one order of magnitude.

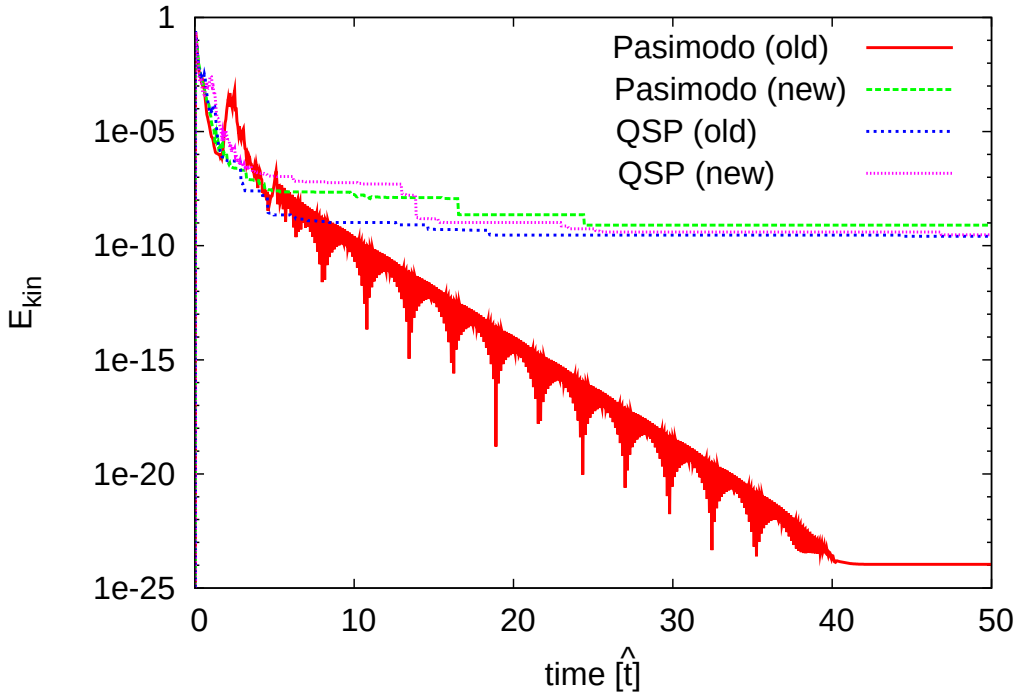

(a) Kinetic energy of a $N = 94$ particles system during the relaxation. The labels "new" and "old" denote the new and the old version of the simulation packages.

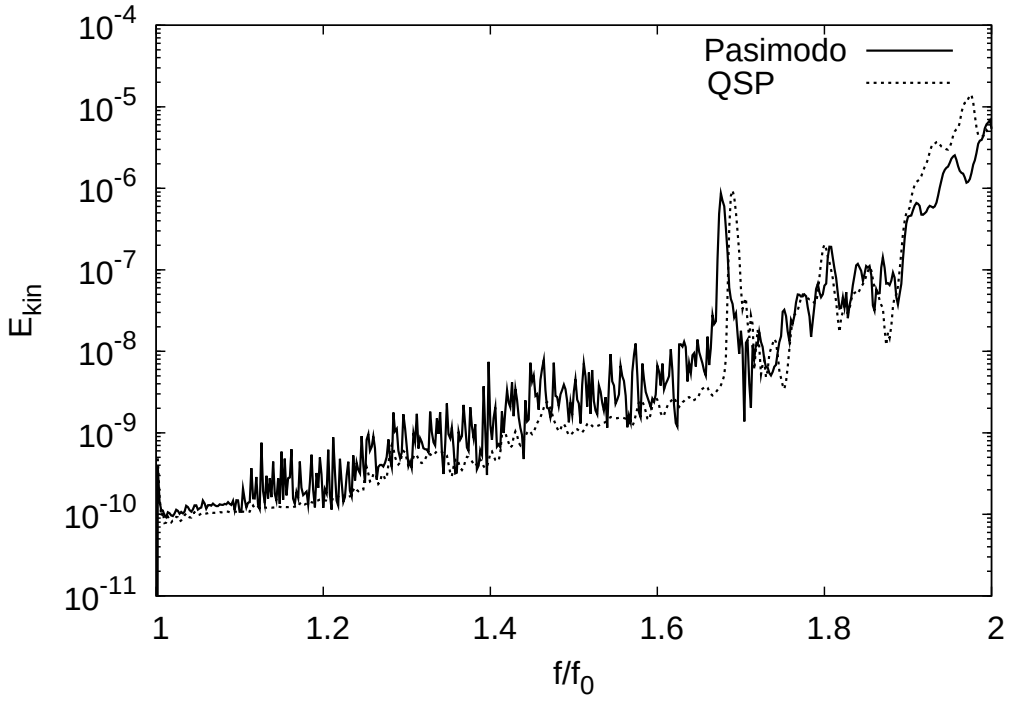

(b) Kinetic energy during compression in one direction. The initial configurations are identic. The time evolution is very similar.

Figure C.1: Kinetic energy of the system with $N = 94$ particles. Top: E_{kin} during the preparation. Bottom: E_{kin} during the loading.

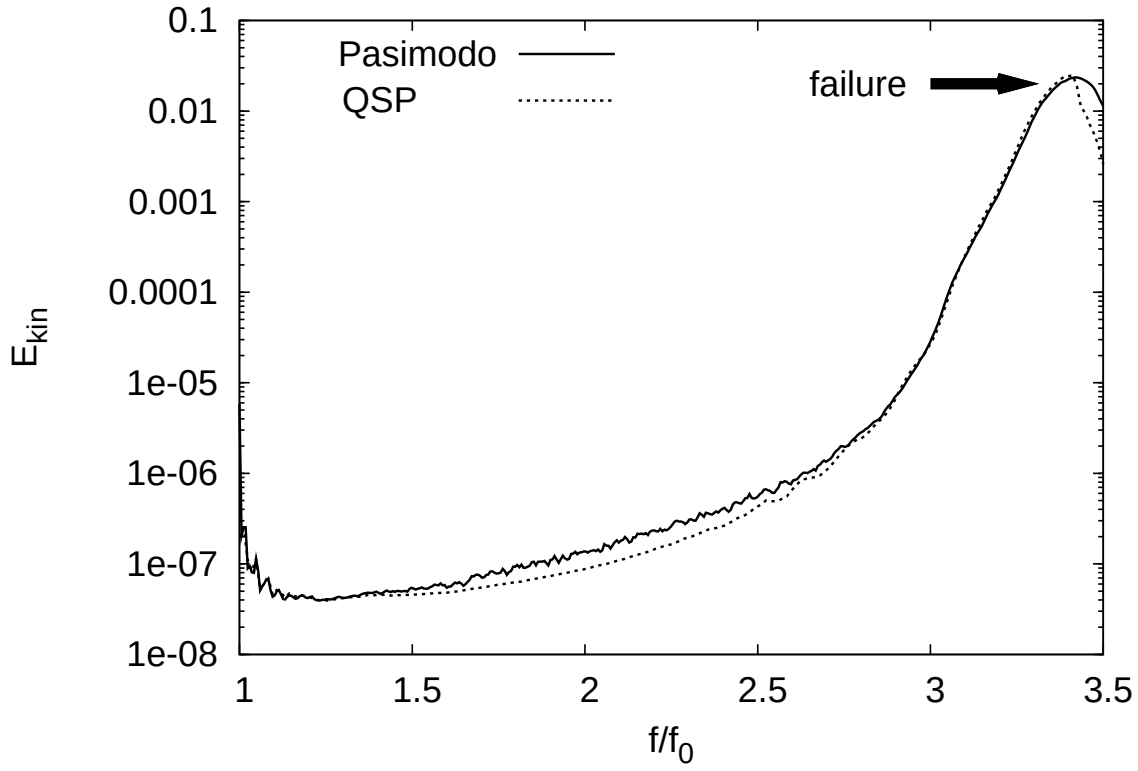

Figure C.2: Simulation of weakening and failure in a $N = 10260$ particle system in three dimensions.

C.5 Example of a larger system

Figure C.2 shows the kinetic energy for one simulation with $N = 10260$ particles until the failure, which is marked by a heavy arrow. Here the integrator used in Pasimodo is the Verlet, and the time step is the same as in QSP.[2] [3] The curves obtained with the two simulation packages are very similar, with the curve from Pasimodo showing slightly higher values between $f/f_0 = 1.2$ and $f/f_0 = 2.7$. At the failure the two curves collapse. The discrepancy right after the failure, at the end of the scale in the figure, arises because the dimensions of the system change, while the rigid walls in the Pasimodo simulations are constant in size and thus not large enough to keep all particles together: some of them escape to the void outside.

[2]The error on the first time step calculation of the Verlet method is of Δt^3, Δt being the time step. The same accuracy applies to the velocity Verlet integrator used in QSP.

[3]Note that the curves in Fig. C.2 show the sum of kinetic energy of all particles and walls, whereas the results presented in all other figures show the kinetic energy of the particles only. The mass of all walls is $m_{\mathrm{walls}} = 0.04$, and the mass of all particles is about $m_{\mathrm{p}} = 0.36$. Thus the walls' energy contributes a non-negligible value to the curves.

	relaxation	triaxial compression
N = 94		
QSP	9min (Core2Quad Q6600 @2.4GHz)	1.0 min (Core2Quad Q6600 @2.4GHz)
Pasimodo	2.5 - 2.75h (Core2 6600 @2.4GHz)	6.5min (Xeon E5530 @2.4GHz)
N = 10260		
QSP	-	1h35min
Pasimodo	-	6h35min

Table C.1: Comparison of the runtime of the quasi-static simulation package (QSP) and Pasimodo. In the $N = 94$ particle simulations, the neighbor list is updated every time step in Pasimodo. Thus the simulations take significantly longer. The Newmark integrator is used for solving the equations of motion. The time step during relaxation is the same in Pasimodo and in QSP. During the compression, the time step in Pasimodo is flexible. A problem with the integration accuracy during triaxial compression necessitated this flexible time step (at a fixed time step, the simulation got stuck at a certain point during simulation). The $N = 10260$ particles system is simulated with a more recent version of Pasimodo in which the neighbor list is only sparsely updated. Furthermore the Verlet integrator is used instead of the Newmark integrator. The timestep of Pasimodo and QSP are the same. Still the runtime is different. The reasons must be the higher versatility in particle shape, positions, frames of reference, etc. in Pasimodo. There might also be an effect of a different organization of the data.

C.6 Runtime comparison

While QSP is optimized for quasi-static simulations, Pasimodo is not optimized in the version used for this comparison (a newer version needs to update the neighbor list only from time to time, which significantly reduces the runtime). Table C.1 shows the runtime results for both codes on the corresponding architectures. The relaxation procedure is $t = 50$ time units, while the compression simulation lasts for $t = 5$, which is reflected by the shorter runtimes. The adaption of QSP to quasi-static simulations leads to a significant shorter runtime in comparison to the more flexible Pasimodo package. The difference between the two packages is roughly one order of magnitude.

List of Figures

List of Tables

Bibliography

[1] A. J. Liu and S. R. Nagel, "Nonlinear dynamics: Jamming is not just cool any more," *Nature*, vol. 396, pp. 21–22, 1998.

[2] M. A. Aguirre, N. Nerone, I. Ippolito, A. Calvo, and D. Bideau, "Granular packing: influence of different parameters on its stability," *Granular Matter*, vol. 3, pp. 75–77, 2001.

[3] F. Darve, G. Servant, F. Laouafa, and H. D. V. Khoa, "Failure in geomaterials: continuous and discrete analyses," *Computer Methods in Applied Mechanics and Engineering*, vol. 193, no. 27-29, pp. 3057 – 3085, 2004. Computational Failure Mechanics for Geomaterials.

[4] C. F. Moukarzel, "Isostatic phase transition and instability in stiff granular materials," *Physical Review Letters*, vol. 81, pp. 1634–1637, Aug 1998.

[5] L. Rothenburg and N. P. Kruyt, "Critical state and evolution of coordination number in simulated granular materials," *International Journal of Solids and Structures*, vol. 41, no. 21, pp. 5763 – 5774, 2004. Granular Mechanics.

[6] C. Maloney and A. Lemaître, "Universal breakdown of elasticity at the onset of material failure," *Physical Review Letters*, vol. 93, p. 195501, Nov 2004.

[7] M. R. Kuhn and C. S. Chang, "Stability, bifurcation, and softening in discrete systems: A conceptual approach for granular materials," *International Journal of Solids and Structures*, vol. 43, no. 20, pp. 6026 – 6051, 2006.

[8] E. Somfai, M. van Hecke, W. G. Ellenbroek, K. Shundyak, and W. van Saarloos, "Critical and noncritical jamming of frictional grains," *Physical Review E*, vol. 75, no. 2, p. 020301, 2007.

[9] L. P. Kadanoff, "Built upon sand: Theoretical ideas inspired by granular flows," *Reviews of Modern Physics*, vol. 71, pp. 435–444, Jan 1999.

[10] H. M. Jaeger, S. R. Nagel, and R. P. Behringer, "Granular solids, liquids, and gases," *Reviews of Modern Physics*, vol. 68, pp. 1259–1273, Oct. 1996.

[11] M. E. Cates, J. P. Wittmer, J.-P. Bouchaud, and P. Claudin, "Jamming, force chains, and fragile matter," *Physical Review Letters*, vol. 81, pp. 1841–1844, Aug 1998.

[12] J.-P. Bouchaud, M. Cates, and P. Claudin, "Stress distribution in granular media and nonlinear wave equation," *Journal de Physique I*, vol. 5, pp. 639–656, 1995.

[13] J. Wittmer, M. Cates, and C. P., "Stress propagation and arching in static sandpiles," *Journal de Physique I*, vol. 7, pp. 39–80, 1997.

[14] F. Krzakala and J. Kurchan, "Landscape analysis of constraint satisfaction problems," *Physical Review E*, vol. 76, no. 2, p. 021122, 2007.

[15] S. Torquato, T. M. Truskett, and P. G. Debenedetti, "Is random close packing of spheres well defined?," *Physical Review Letters*, vol. 84, pp. 2064–2067, Mar 2000.

[16] S. Torquato and F. H. Stillinger, "Multiplicity of generation, selection, and classification procedures for jammed hard-particle packings," *Journal of Physical Chemistry B*, vol. 105, pp. 11849 – 11853, 2001.

[17] S. Hyun, A. M. Karlsson, S. Torquato, and A. G. Evans, "Simulated properties of kagom and tetragonal truss core panels," *International Journal of Solids and Structures*, vol. 40, no. 25, pp. 6989 – 6998, 2003. Special issue in Honor of George J. Dvorak.

[18] A. Donev, S. Torquato, F. H. Stillinger, and R. Connelly, "Jamming in hard sphere and disk packings," *Journal of Applied Physics*, vol. 95, no. 3, pp. 989–999, 2004.

[19] A. Donev, S. Torquato, F. H. Stillinger, and R. Connelly, "A linear programming algorithm to test for jamming in hard-sphere packings," *Journal of Computational Physics*, vol. 197, no. 1, pp. 139 – 166, 2004.

[20] K. Bagi, "On the concept of jammed configurations from a structural mechanics perspective," *Granular Matter*, vol. 9, p. 109, 2007.

[21] C. Moukarzel, "Isostaticity in granular matter," *Granular Matter*, vol. 3, p. 41, 2001.

[22] C. S. O'Hern, S. A. Langer, A. J. Liu, and S. R. Nagel, "Random packings of frictionless particles," *Physical Review Letters*, vol. 88, p. 075507, Jan 2002.

[23] C. S. O'Hern, L. E. Silbert, A. J. Liu, and S. R. Nagel, "Jamming at zero temperature and zero applied stress: The epitome of disorder," *Physical Review E*, vol. 68, p. 011306, Jul 2003.

[24] E. Stein, R. Borst, and T. J. Hughes, eds., *Encyclopedia of Computational Mechanics, Volume 1: Fundamentals; Chapter 11: Discrete Element Methods*. Wiley and sons, Ltd., 2007.

[25] V. Frette, K. Christensen, A. Malthe-Sørenssen, J. Feder, T. Jøssang, and P. Meakin, "Avalanche dynamics in a pile of rice," *Nature*, vol. 379, pp. 49–52, Jan. 1996.

[26] A. Daerr and S. Douady, "Two types of avalanche behaviour in granular media," *Nature*, vol. 399, pp. 241–243, May 1999.

[27] Y. C. Zhou, B. H. Xu, A. B. Yu, and P. Zulli, "Numerical investigation of the angle of repose of monosized spheres," *Physical Review E*, vol. 64, p. 021301, Jul 2001.

[28] L. Staron, J.-P. Vilotte, and F. Radjai, "Preavalanche instabilities in a granular pile," *Physical Review Letters*, vol. 89, p. 204302, Oct 2002.

[29] L. Staron, J.-P. Vilotte, and F. Radjai, "Multiscale analysis of the stress state in a granular slope in transition to failure," *Eur. Phys. J. E*, vol. 18, pp. 311–320, 2005.

[30] T. Scheller, C. Huss, G. Lumay, N. Vandewalle, and S. Dorbolo, "Precursors to avalanches in a granular monolayer," *Physical Review E*, vol. 74, no. 3, p. 031311, 2006.

[31] V. Y. Zaitsev, P. Richard, R. Delannay, V. Tournat, and V. E. Gusev, "Pre-avalanche structural rearrangements in the bulk of granular medium: Experimental evidence," *Europhysics Letters*, vol. 83, no. 6, p. 64003 (6pp), 2008.

[32] R. Fischer, P. Gondret, B. Perrin, and M. Rabaud, "Dynamics of dry granular avalanches," *Physical Review E*, vol. 78, no. 2, p. 021302, 2008.

[33] M. A. Aguirre, A. Calvo, I. Ippolito, A. Medus, and M. Mancuso, "Rearrangements in a two-dimensional packing of disks," *Physical Review E*, vol. 73, no. 4, p. 041307, 2006.

[34] J. R. Williams and N. Rege, "Coherent vortex structures in deforming granular materials," *Mechanics of cohesive-frictional materials*, vol. 2, p. 223, 1997.

[35] T.-T. Ng, "Triaxial test simulations with discrete element method and hydrostatic boundaries," *Journal of Engineering Mechanics*, vol. 130, no. 10, pp. 1188–1194, 2004.

[36] M. R. Kuhn, "A flexible boundary for three-dimensional dem particle assemblies," *Engineering Computations*, vol. 12, p. 175, 1995.

[37] F. Alonso-Marroquín, *Micromechanical investigation of soil deformation: incremental response and granular ratcheting*. PhD thesis, Institut für Computeranwendungen 1, Universität Stuttgart, Stuttgart, Feb 2004.

[38] T. S. Majmudar, M. Sperl, S. Luding, and R. P. Behringer, "Jamming transition in granular systems," *Physical Review Letters*, vol. 98, no. 5, p. 058001, 2007.

[39] I. Agnolin and J.-N. Roux, "Internal states of model isotropic granular packings. i. assembling process, geometry, and contact networks," *Physical Review E*, vol. 76, no. 6, p. 061302, 2007.

[40] J.-N. Roux, "Geometric origin of mechanical properties of granular materials," *Physical Review E*, vol. 61, pp. 6802–6836, Jun 2000.

[41] M. Wyart, S. R. Nagel, and T. A. Witten, "Geometric origin of excess low-frequency vibrational modes in weakly connected amorphous solids," *Europhysics Letters*, vol. 72, pp. 486–492, Nov. 2005.

[42] W. G. Ellenbroek, E. Somfai, M. van Hecke, and W. van Saarloos, "Critical scaling in linear response of frictionless granular packings near jamming," *Physical Review Letters*, vol. 97, no. 25, p. 258001, 2006.

[43] Z. Zeravcic, W. van Saarloos, and D. R. Nelson, "Localization behavior of vibrational modes in granular packings," *Europhysics Letters*, vol. 83, no. 4, p. 44001, 2008.

[44] S. McNamara, R. Garcìa-Rojo, and H. J. Herrmann, "The stress-strain curve of cyclic loading: microscopic, analytical results," in *Powders and Grains* (R. Garcìa-Rojo, H. J. Herrmann, and S. McNamara, eds.), pp. 295–299, Taylor and Francis Group, London, 2005.

[45] S. C. McNamara and H. J. Herrmann, "Quasirigidity: Some uniqueness issues," *Physical Reviev E*, vol. 74, no. 6, p. 061303, 2006.

[46] P. Lotstedt, "Mechanical systems of rigid bodies subject to unilateral constraints," *SIAM Journal on Applied Mathematics*, vol. 42, no. 2, pp. 281–296, 1982.

[47] B. Winkler, *Computational Condensed Matter Physics, Lecture manuscripts of the 37th IFF Spring School March 06-17, Jülich, 2006*, ch. B.3 Molecular Dynamics Simulations. Schriften des Forschungszentrums Jlich, Reieh Materia und Material 32, 2006.

[48] M. P. Allen, *Computational Soft Matter: From Synthetic Polymers to Proteins, Lecture Notes, pp. 1-28*, vol. 23. John von Neumann Institute for Computing, Jülich, NIC Series, 2004.

[49] L. Verlet, "Computer experiments on classical fluids: I. thermodynamical properties of lennard-jones molecules," *Phys. Rev.*, vol. 159, p. 98, Jul 1967.

[50] J. G. Berryman, "Random close packing of hard spheres and disks," *Physical Review A*, vol. 27, pp. 1053–1061, Feb 1983.

[51] N. Xu, J. Blawzdziewicz, and C. S. O'Hern, "Random close packing revisited: Ways to pack frictionless disks," *Physical Review E*, vol. 71, p. 061306, Jun 2005.

[52] S. Ouaguenouni and J.-N. Roux, "Compaction of well-coordinated lubricated granular pilings," *Europhysics Letters*, vol. 32, no. 5, pp. 449–453, 1995.

[53] H. A. Makse, N. Gland, D. L. Johnson, and L. M. Schwartz, "Why effective medium theory fails in granular materials," *Physical Review Letters*, vol. 83, pp. 5070–5073, Dec 1999.

[54] I. Agnolin and J.-N. Roux, "Internal states of model isotropic granular packings. ii. compression and pressure cycles," *Physical Review E*, vol. 76, no. 6, p. 061303, 2007.

[55] P. R. Welker and S. C. McNamara, "What triggers failure in frictional granular assemblies?," *Physical Review E*, vol. 79, no. 6, p. 061305, 2009.

[56] R. Garcìa-Rojo, S. McNamara, and H. J. Herrmann, "Sliding and localization in a biaxial test of granular material," in *Powders and Grains* (R. Garcìa-Rojo, H. J. Herrmann, and S. McNamara, eds.), pp. 705–708, Taylor and Francis Group, London, 2005.

[57] C. Stolz, "On micro-macro transition in non-linear mechanics," *Materials*, vol. 3, no. 1, pp. 296–317, 2010.

[58] F. Nicot, L. Sibille, F. Donze, and F. Darve, "From microscopic to macroscopic second-order work in granular assemblies," *Mechanics of Materials*, vol. 39, no. 7, pp. 664 – 684, 2007.

[59] F. Dedecker, M. Chaze, P. Dubujet, and B. Cambou, "Specific features of strain in granular materials," *Mechanics of Cohesive-frictional Materials*, vol. 5, no. 3, pp. 174–193, 2000.

[60] S. McNamara, R. García-Rojo, and H. Herrmann, "Indeterminacy and the onset of motion in a simple granular packing," *Physical Review E*, vol. 72, p. 021304, Aug 2005.

[61] G. Combe and J.-N. Roux, "Strain versus stress in a model granular material: A devil's staircase," *Physical Review Letters*, vol. 85, pp. 3628–3631, Oct 2000.

[62] J.-N. Roux and G. Combe, "Quasistatic rheology and the origins of strain," *Comptes Rendus Physique*, vol. 3, no. 2, pp. 131 – 140, 2002.

[63] F. Alonso-Marroquín, S. Luding, H. J. Herrmann, and I. Vardoulakis, "Role of anisotropy in the elastoplastic response of a polygonal packing," *Physical Review E*, vol. 71, p. 051304, May 2005.

[64] J.-N. Roux, "The nature of quasistatic deformation in granular materials," in *Powders and Grains* (R. Garcìa-Rojo, H. J. Herrmann, and S. McNamara, eds.), pp. 261–265, Taylor and Francis Group, London, 2005.

[65] S. Luding and H. J. Herrmann, "Micro-macro transition for cohesive granular media," in *Zur Beschreibung komplexen Materialverhaltens* (S. Diebels, ed.), pp. 121–134, Institut für Mechanik, 2001.

[66] M. Kuhn, "Scaling in granular materials," in *Powders and Grains* (R. Garcìa-Rojo, H. J. Herrmann, and S. McNamara, eds.), pp. 115–122, Taylor and Francis Group, London, 2005.

[67] A. J. Liu and S. R. Nagel, eds., *Jamming and Rheology*. New York: Taylor and Francis, 2001.

[68] J. H. Snoeijer, W. G. Ellenbroek, T. J. H. Vlugt, and M. van Hecke, "Sheared force networks: Anisotropies, yielding, and geometry," *Physical Review Letters*, vol. 96, no. 9, p. 098001, 2006.

[69] R. García-Rojo, F. Alonso-Marroquín, and H. J. Herrmann, "Characterization of the material response in granular ratcheting," *Physical Review E*, vol. 72, p. 041302, Oct 2005.

[70] F. Alonso-Marroquín and H. J. Herrmann, "Ratcheting of granular materials," *Physical Review Letters*, vol. 92, p. 054301, Feb 2004.

[71] F. Radjai, D. E. Wolf, M. Jean, and J.-J. Moreau, "Bimodal character of stress transmission in granular packings," *Physical Review Letters*, vol. 80, pp. 61–64, Jan 1998.

[72] M. Wyart, L. E. Silbert, S. R. Nagel, and T. A. Witten, "Effects of compression on the vibrational modes of marginally jammed solids," *Physical Review E*, vol. 72, p. 051306, Nov 2005.

[73] A. Getis and B. Boots, *Models of Spatial Processes*. Cambridge: Cambridge University Press, 1979.

[74] V. Gibiat, E. Plaza, and P. De Guilbert, "Acoustic emission before avalanches in granular media," *Journal of the Acoustic Society of America*, vol. 123, p. 3142, 2009.

[75] N. Nerone, M. A. Aguirre, A. Calvo, D. Bideau, and I. Ippolito, "Instabilities in slowly driven granular packing," *Physical Review E*, vol. 67, p. 011302, Jan 2003.

[76] S. Kiesgen de Richter, *Etude de l'organisation des réarrangements d'un milieu granulaire sous sollicitations mécaniques*. PhD thesis, Institut de physique, Université de Rennes 1, Rennes, France, Nov 2009.

[77] L. Staron, F. Radjai, and J.-P. Vilotte, "Granular micro-structure and avalanche precursors," *Journal of Statistical Mechanics: Theory and Experiment*, vol. 2006, no. 07, p. P07014, 2006.

[78] R. C. Hidalgo, C. U. Grosse, F. Kun, H. W. Reinhardt, and H. J. Herrmann, "Evolution of percolating force chains in compressed granular media," *Physical Review Letters*, vol. 89, p. 205501, Oct 2002.

[79] X. Jia, "Codalike multiple scattering of elastic waves in dense granular media," *Physical Review Letters*, vol. 93, p. 154303, Oct 2004.

[80] A. Guarino, A. Garcimartín, and S. Ciliberto, "An experimental test of the critial behaviour of fracture precursors," *European Physical Journal B*, vol. 6, p. 13, 1998.

[81] S. A. M. El Shourbagy, S. Okeda, and H.-G. Matuttis, "Acoustic of sound propagation in granular materials in one, two, and three dimensions," *Journal of the Physical Society of Japan*, vol. 77, no. 3, pp. 034606–034606, 2008.

[82] I. Agnolin and N. Kruyt, "On the elastic moduli of two-dimensional assemblies of disks: Relevance and modeling of fluctuations in particle displacements and rotations," *Computers and Mathematics with Applications*, vol. 55, no. 2, pp. 245 – 256, 2008. Modeling Granularity, Modeling Granularity.

[83] M. R. Kuhn and K. Bagi, "Contact rolling and deformation in granular media," *International Journal of Solids and Structures*, vol. 41, no. 21, pp. 5793 – 5820, 2004. Granular Mechanics.

[84] A. S. J. Suiker and N. A. Fleck, "Frictional collapse of granular assemblies," *Journal of Applied Mechanics*, vol. 71, no. 3, pp. 350–358, 2004.

[85] I. Agnolin and J.-N. Roux, "On the elastic moduli of three-dimensional assemblies of spheres: Characterization and modeling of fluctuations in the particle displacement and rotation," *International Journal of Solids and Structures*, vol. 45, no. 3-4, pp. 1101 – 1123, 2008.

[86] P. R. Welker and S. C. McNamara, "Approaching failure: aspects of weakening in granular assemblies," *Granular Matter*, 2010.

[87] S. Luding, "Introduction to discrete element methods," *European Journal of Environmental and Civil Engineering*, vol. 7, p. 785, 2008.

[88] S. Luding, "Cohesive, frictional powders: contact models for tension," *Granular Matter*, vol. 10, p. 235, 2008.

[89] R. M. Nedderman, *Statics and kinematics of granular materials*. Cambr. Univ. Press, 1992.

[90] J.-P. Plassiard, N. Noura Belheine, and F.-V. Donzé, "A spherical discrete element model: calibration procedure and incremental response," *Granular Matter*, vol. 11, p. 293, 2009.

[91] S. Luding, "Anisotropy in cohesive, frictional granular media," *Journal of Physics Condensed Matter*, vol. 17, pp. 2623–+, June 2005.

[92] N. Estrada, A. Taboada, and F. Radjaï, "Shear strength and force transmission in granular media with rolling resistance," *Physical Review E*, vol. 78, no. 2, p. 021301, 2008.

[93] J. Török, L. Brendel, and D. E. Wolf, "Shear band patterns in biaxially sheared granular media," in *Powders and Grains 2009* (M. Nakagawa and S. Luding, eds.), pp. 417–420, AIP, 2009.

[94] H. J. Herrmann, "Structures in deformed granular packings," *Granular Matter*, vol. 3, pp. 15–18, 2001.

[95] S. Fazekas, J. Török, J. Kertész, and D. E. Wolf, "Morphologies of three-dimensional shear bands in granular media," *Physical Review E*, vol. 74, p. 031303, Sep 2006.

[96] J. Török, S. Krishnamurthy, J. Kertész, and S. Roux, "Self-organization, localization of shear bands, and aging in loose granular materials," *Physical Review Letters*, vol. 84, pp. 3851–3854, Apr 2000.

[97] J. Török, T. Unger, J. Kertész, and D. E. Wolf, "Shear zones in granular materials: Optimization in a self-organized random potential," *Physical Review E*, vol. 75, no. 1, p. 011305, 2007.

[98] H. Parisch, *Festkörper-Kontinuumsmechanik*. Stuttgart: Teubner, 2003.

[99] G. Fischer, *Lineare Algebra*. Braunschweig: Vieweg, 2002.

[100] S. McNamara and M. Mareschal, "Lyapunov spectrum of granular gases," *Physical Review E*, vol. 63, p. 061306, May 2001.

Acknowledgments

I want to thank my supervisor Sean McNamara for providing the topic and guiding me through the process of generating the results of this thesis. Without his continuous support and the innumerable comments on various aspects of this work, this thesis would not have been possible in its present form. For my visits in Rennes he provided his help for organizing a place to stay, and he created a nice and friendly atmosphere during my stays there. I also want to thank his family, especially for the nice and interesting trip to Lannion!

I am grateful to Rudolf Hilfer for writing the proposal of the SFB project, which provided the funds necessary to carry out my work at the Institute of Computational Physics (ICP). Fruitful discussions led to new ideas and physical insight. The opportunities for traveling enabled the continuous personal exchange with Sean McNamara and the participation at different conferences.

I want to express my thanks to Prof. Wunner, who accepted to act as a referee of this thesis.

I would like to express my gratitude to Christian Holm, the head of the ICP since 2009, for creating a nice and friendly environment in which it was always a pleasure to work. His large group, consisting of very different people, enabled many discussions on a broad range of topics, which were not necessarily of physical origin.

I also want to thank my office mates along the almost four years at the institute. These are Sean McNamara, Christian Kunert, Oliver Hönig, Shervin Rafatnia, Oliver Dommert, Rudolf Weeber, Sofia Kantorovich, and Nadezhda Gribova. It was always a pleasure to work together and discuss interesting and also important things.

Thanks also to all people at the ICP for the nice barbecues and the various discussions at lunch time. Thank you for the possibility to taste a variety of different cakes at certain opportunities, such as birthdays and farewell parties!

I acknowledge the support of this work by the Deutsche Forschungsgemeinschaft (DFG) through "Sonderforschungsbereich 716: Simulationen mit großen Teilchenzahlen".

Furthermore I also want to thank all my friends for supporting me along the way and for the discussions on several aspects of life. Their different viewpoints are always helpful for getting a more objective view of life. I also thank Tina for supporting me during the (almost) whole period, and for helping me whenever I was in trouble. She enriched my life in various respects.

Last but not least I am indebted to my family for their continuous support and their help during my several relocations.